DOE/HTGR-85-062
ORNL-6192

DE-1302-1

24

I-23105

GAS-COOLED REACTOR PROGRAMS

HIGH-TEMPERATURE GAS-COOLED REACTOR TECHNOLOGY DEVELOPMENT PROGRAM ANNUAL PROGRESS REPORT FOR PERIOD ENDING DECEMBER 31, 1984

AUTHORS/CONTRACTORS

P. R. Kasten et al., Oak Ridge National Laboratory

Oak Ridge National Laboratory
Oak Ridge, Tennessee 37831
operated by
MARTIN MARIETTA ENERGY SYSTEMS, INC.
for the
UNITED STATES DEPARTMENT OF ENERGY
July 1985

Printed in the United States of America. Available from
the U.S. Department of Energy
Technical Information Center
P.O. Box 62, Oak Ridge, Tennessee 37830

DISCLAIMER

ORNL--6192

TI85 029603

DOE/HTGR-85-062
ORNL-6192
Distribution
Category UC-77T

GAS-COOLED REACTOR PROGRAMS

HIGH-TEMPERATURE GAS-COOLED REACTOR TECHNOLOGY DEVELOPMENT PROGRAM ANNUAL PROGRESS REPORT FOR PERIOD ENDING DECEMBER 31, 1984

Paul R. Kasten, Program Director

P. L. Rittenhouse, Base Technology Program Manager

D. E. Bartine, Physics and Shielding Program Manager

J. P. Sanders, Component Flow Testing Program Manager

Date Published — July 1985

Prepared by the
OAK RIDGE NATIONAL LABORATORY
Oak Ridge, Tennessee 37831
Operated by
MARTIN MARIETTA ENERGY SYSTEMS, INC.
for the
U.S. DEPARTMENT OF ENERGY
under Contract No. DE-AC05-840R21400

CONTENTS

SUMMARY

1. MANAGEMENT ACTIVITIES (WBS* 0100.02, 1000.01, 1000.02)

The activities performed in management areas emphasized: (a) management of the ORNL activities under the National High Temperature Gas Cooled Reactor (HTR) Program; (b) maintenance of the Summary Level Program Plan (SLPP) of the National Program with particular regard to the ORNL work efforts; (c) interfacing with other Program participants in those areas where coordinated effort is required; (d) installation of electronic information transfer capability among Program participants; and (e) maintenance of the Tower Shielding Facility (TSF) for possible future HTR Shielding experiments.

2. PROGRAM REQUIREMENTS MANAGEMENT AND EVALUATION ACTIVITIES (WBS 0200.01)

ORNL participated in the National HTR Program Requirements Management (PRM) Task Force which addresses plant-level requirements, plant-level studies, and selection of the reference HTR concept for initial deployment. Primary activities completed during CY 1984 included development of proposed criteria for use in the concept selection process, evaluation of technical issues, and evaluation of the economic performance of the various HTR design concepts. During CY 1984, the PRM Task Force reduced the number of HTR design concepts being evaluated from about sixteen to four. ORNL made a preliminary estimate of the R&D costs associated with the Base Technology areas for concrete, metals and ceramics, graphite, fuel and fission product behavior; the preliminary R&D cost estimates varied only about 10% among the four concepts.

3. ECONOMIC STUDIES AND EVALUATIONS (WBS 1000.01)

A number of economic studies and evaluations were completed during FY 1984. Early in the year, ORNL responded to a Congressional subcommittee request for comments on a modular HTR Program and associated key development needs. Throughout the year, ORNL reviewed and commented on the economic ground rules and cost bases employed in the evaluation of HTR concepts. These ground rules and cost bases are generally well

*The Work Breakdown Structure (WBS) follows those numbers given in the Summary Level Program Plan (SLPP) of the National HTR Program; the SLPP is issued by the U.S. DOE and coordinated by GCRA with specific input by the various program participants. The WBS number for the ORNL work is identified at the beginning of each work area.

established, but changes and updates do occur and ORNL is involved in that process. During the last three months of CY 1984, ORNL participated as a member of a task force evaluating operating and maintenance O&M costs of various HTR concepts. ORNL calculated the O&M costs based on input from other Program participants using an ORNL-developed computer code.

A summary evaluation was performed relative to avoidance of graphite burning in HTRs, considering use of plant design features and the coating of graphite with silicon carbide as alternative approaches. It was recommended that air ingress be limited by plant design features, which concurs with the approach being used in the National HTR Program.

In December an invited seminar was presented at the Japan Atomic Energy Research Institute Open Seminar on R&D of the Multipurpose VHTR. The title of the paper was "New Approaches in the U.S.A. for High-Temperature Gas-Cooled Reactors."

4. INTERNATIONAL TECHNOLOGY TRANSFER (WBS 1400.01)

The activities described in this section involve international technology transfer in the areas of fuels, fission products, graphites, structural materials, physics, performance, and safety. Transfer of information in the first three areas above is covered under the U.S./Federal Republic of Germany (FRG) Fuel, Fission Product, and Graphite Subprogram. Structural materials technology transfer is handled through the U.S./FRG/Switzerland (CH) Materials Subprogram. Cooperation and information transfer in HTR physics, performance, and safety areas is governed by a separate AVR/KFA/ORNL agreement.

5. FUEL MATERIALS AND FISSION PRODUCT BEHAVIOR (WBS 1601)

The Fuel Materials and the Fission Product Performance Verification Programs at ORNL are part of a national fuel and fission product behavior effort in close cooperation with GA.

The ORNL fuel materials program is directed towards irradiation testing of GA-fabricated fuel in capsules designed and assembled at ORNL and operated in ORNL reactors. In addition, extensive PIE is conducted on the irradiated fuel in special facilities developed for this purpose.

Irradiation of capsules HRB-17 and -18, which comprise the hydrolysis experiment on reference UCO fuel particles, has been delayed until further justification of the experiment is completed. Progress during 1984 included completion of capsule fabrication, fuel-loading and final assembly; QA/QC audits and documentation; and completion and initial checkout of moisture generation-injection and gas analysis instrumentation. Installation at the HFIR site was initiated but halted due to the delay. The unirradiated capsules will remain in storage until needed.

Primary PIE efforts were concentrated on GA-fabricated fuels irradiated in capsules HRB-16 and R2-K13. German fuels from experiments FRJ2-P23, FRJ2-P25, and DR-S6 (Section 4.2); and ORNL-fabricated fuel irradiated in capsule HT-35. A final report was prepared by GA which documents the ORNL PIE efforts in capsule HRB-15a. In addition, a report was prepared by ORNL on the PIE results obtained on a variety of advanced HTR coated particle designs utilizing ZrC coatings. At the end of this reporting period only German irradiated fuels remain in storage at the HRLEL.

The IMGA facility was available about 60% of this report period; however, a major failure of the automated particle handler occurred in the last part of 1984. Instead of repairing the old device, we will decontaminate the IMGA cubicle and install the new automated particle handler fabricated in 1980. This will be a priority item in 1985. The upgraded PGA system was put into operation and used successfully to measure fission gas inventories in irradiated fuels from U.S. experiments HT-34, HT-35, HRB-16, R2-K13, and from German experiments FRJ2-P23 and DR-S6. Data from these measurements were in good agreement with existing models for predicting stable fission gas inventories.

A series of tests were conducted to determine the utility of a thermal gradient tube and to gain insight about the chemical forms of iodine and cesium vaporized from graphite. The usefulness of this method under HTR conditions was adequately demonstrated.

A diffusion coefficient of plutonium in graphite was determined using a source pellet in conjunction with a test pellet that was initially free of plutonium. After exposure under the test conditions, the concentration profile of plutonium in the test pellet provided a value for the coefficient. This coefficient and the plutonium vapor measure are necessary to determine the plutonium transport to the coolant.

6. GRAPHITE (WBS 1602)

The principal problem facing the Graphite Program at the beginning of this fiscal year was providing of a nuclear-quality Stackpole 2020 graphite for use in the Core Support Performance Test (CSPT). The ordinary off-the-shelf 2020 graphite exhibits high levels of catalytic impurity combined with a high level of presumed inhibitor impurity (silicon) in an uncontrolled fashion. Two lots of so-called nuclear-quality graphite were received from Stackpole during the past year, both from the same raw material source. The impurity levels remained high and unpredictable. A third lot is now in preparation. The problem appears to be associated both with raw material and its graphitization, and steps are being taken to follow both the selection of raw materials and the graphitization procedure to identify and remove the problem.

TEST ZERO of the CSPT was conducted in the Component Flow Test Loop (CFTL) during the period November 1983 to April 1984. TEST ZERO of the CSPT had two principal objectives. The first was to demonstrate continuous maintenance of impurity concentrations in helium during accelerated

oxidation of a graphite structure at 7.24 MPa. The second was to measure the rate of graphite corrosion by careful determination of the carbon monoxide produced during time intervals of two or three days using an overall material balance of the fill and vent streams.

Both of these objectives were met during the conduct of the test. The impurity control and measurement systems operated satisfactorily. Oxidation rates were measured at a sensitivity of less than 1 $\mu g/h\text{-}cm^2$ at a moisture concentration of 20 ppm in the helium. Surface corrosion rates in the range of 0.05 to >1.2 mg/h were observed for the graphite structure of 1.2 m^2 area.

Fracture mechanics studies have been continued, primarily now concerned with identifying the tensor (orientation) properties. Grade AGOT, a highly anisotopic extruded material, was employed because of the near isotropy of Great Lakes grade H451. The results lead to the conclusion the stress intensity factor K_{IC} is isotropic, and the observed anisotropy rests entirely in the crack-generations flaw field.

The effect of irradiation on the thermal expansion coefficient, particularly above the irradiation temperature, has been investigated for two graphites, H451 and Sigri grade ASRIRV. The experiment sought to find a closure of the crystallite c-axis voids at the irradiation temperature when damage was sufficient to close the voids at that temperature. The anticipated result was obtained, i.e., the thermal expansion from room temperature to the irradiation temperature remained low until the irradiation temperature was reached. Above this temperature the thermal expansion exceeds 20 $\mu m/m\text{-}K$ in all directions, indicating the c-axis expansion component of the crystallites is predominant in all directions with accommodation. On cooling and reheating, the expansion coefficient remains low indicating the accommodating voids have reformed and the c-axis expansion is again accommodated. We conclude any temperature surge in a reactor containing highly damaged graphite will cause significant dimensional changes in the material.

Calculations of the first four moments of the Weibull distribution have been essentially completed. These moments can be used for goodness-of-fit tests as well as for generating sampling statistics. The present calculations were performed to provide high precision values for the moments in the region above m (Weibull exponent) = 20. The closest approach to normality occurs at very low m-values, near m = 5, and continues to depart ever more drastically as m approaches infinity.

7. METALLIC MATERIALS (WBS 1603)

The overall objective of this task is to develop the metallic materials data base and the technology needed for the design, manufacture, and licensing of HTR components. Under Reactor System Materials the initial phase of an effort to characterize the fracture mechanics behavior of Inconel 718 was completed. Also, the compatibility of power and control

rod cladding with boronated graphite was studied. No compatibility problems were found at 700°C, but evidence of considerable solid-state reaction was found at 810°C.

Creep, aging, and fatigue studies of Reactor Vessel Materials was continued. Primary emphasis was on Hastelloy X; work on all other alloys was in a "phase-out" period. Both creep test and aging times for Hastelloy X specimens now exceed 50,000 h. High-cycle fatigue tests were conducted on solution-annealed Hastelloy X at 650°C; cyclic life times obtained at 650°C tended to be somewhat higher than at 760°C. Strain-controlled creep-fatigue interaction testing of Hastelloy X at 760°C was continued. The linear damage summation method for assessing creep-fatigue damage was found to be inappropriate for Hastelloy X.

In the area of Heat Transport Materials, the development of procedures for the internal bore welding of the steam generator superheater tube-to-tubesheet joint was continued. It was determined that a multipass welding technique with filler wire addition will be necessary for the tube-to-tubesheet welds. Creep and aging studies of 2 1/4 Cr-1 Mo steel steam generator tubing material were also continued. Creep test times approached 70,000 h. Studies of decarburization effects, creep-fatigue interactions, and the high temperature fracture mechanics behavior of 2 1/4 Cr-1 Mo were begun. Finally, the decarburization kinetics of 2 1/4 Cr-1 Mo in HTR-helium were derived for the temperature range 430 through 650°C.

Limited effort was devoted to several tasks on Advanced Metallic Materials. Creep tests were conducted on two of the GASM alloys and on several modified versions of Inconel 617. Three experimental nickel aluminide alloys were exposed to dry HTR-helium for 2500 h at 950°C; all of these alloys were superior to the Inconel 617 control specimens in terms of oxidation and carburization resistance. Work toward the development of design methodologies for very high temperature continued.

8. CERAMICS (WBS 1604.01)

In the bottom head region of the core outlet plenum, pads fabricated from hard ceramic materials and separated by interface materials are used to support the graphite posts that support the core. One candidate ceramic pad material was investigated: fused silica. Test articles of this material were in the form of right circular disks having a central cylindrical hole extending vertically through each disk. By using a specially designed test fixture, which incorporated either flat or conical platen sets, these pads were subjected to mechanical loadings at room temperature representative of loadings that would be induced in the ceramic pads due to thermal gradients. A woven silica fabric (Siltemp) was used as the interface material between the pads and loading platens to provide a more uniform loading environment and to permit more pad rotational freedom. Strain and displacement data as a function of load were collected for each of fifteen tests. Acoustic emission data were obtained from each of the pads during testing.

Creep tests for four grades of silica were performed in a helium atmosphere. Results characteristic of ceramic materials were obtained, and both scatter and anomolous behavior was observed.

9. CONCRETE MATERIALS QUALIFICATION (WBS 1605.01)

Design optimization studies at GA Technologies Inc. (GA) have indicated that a significant size reduction (≈1.3 m) in the Prestressed Concrete Reactor Vessel (PCRV) can be obtained by using 55-MPa concrete in conjunction with 13.3-MN capacity prestressing tendons. A 3-phase test program has been developed and evaluated to demonstrate the required high strength (≥63.4 MPa) concrete material systems using aggregate materials selected to provide bounds on achievable material properties. Factors related to the production of high-strength concrete have been reviewed. Phase I of the study concerned the material selection-evaluation, optimum cement content determinations, aggregate and fly ash evaluation testing, and final aggregate selection. Test results indicated that concretes having the desired compressive strengths are easily achievable utilizing any of the aggregate materials evaluated and that the incorporation of fly ash into the concrete mixes imparts several benefits.

10. REACTOR INTERNALS SUBSYSTEM DESIGN (WBS 5210.03)

Phase II of the HTGR bottom reflector and core support block neutron streaming experiment was completed. The measurements were taken, the experiment was analyzed, and draft documentation was completed for both the measurements and the analysis. The results generally confirmed results predicted during the analysis of the lower core support structure of the large HTGR. Insufficient flux reduction was achieved by the few variations in the boronated graphite shield pin layers. A major shield redesign effort is indicated.

A preliminary analysis of the shield designs for small HTR concepts was completed. The results indicated potentially high flux levels in the lower regions of the two concepts studied due to fission neutron and gamma-ray production in the fuel discharge chutes which penetrate the lower core support structure. In addition, the fissions in the fuel discharge chutes and the location of the steam generator may lead to high flux levels and dose rates in the steam-generator cavity of the side-by-side concept. This work indicates that more detailed analyses are required.

Capability has been added for the three-dimensional analysis of the core neutronics and heat removal. Parametric studies were completed for the 2240-MW(t) HTGR core with HEU fuel. Studies were also performed for the 1170-MW(t) annular pebble bed core. The effect of the recirculation of the pebbles on power density peaking was shown. The control was studied for several core designs and the increased reflector rod worth with reduced core thickness was calculated.

An investigation of 3-D hexagonal methods for HTGR large core physics calculations was made, and a generalized depletion/perturbation theory method was with special attention paid to the nodal method implemented for the GA FEVER-M1 code.

Available experimental data for simple graphite-moderated LEU fuel were evaluated and compared with calculations based on the ENDF/B-V cross-section data. Some of the problems associated with the processing of these data have been isolated and resolved.

1. MANAGEMENT ACTIVITIES
(WBS 0100.02, 1000.01, and 1000.02)

P. R. Kasten

Management activities are associated with planning, leading, organizing and controlling the ORNL activities under the National HTR Program. This effort includes annual planning and control relative to the Summary Level Program Plan (SLPP) work breakdown structure of the National Program, and the task includes the preparation of change proposals and the maintenance of cognizance of the overall work of the National Program with respect to that work which influences or is influenced by the ORNL activities. Management activities are also associated with interfacing with other program participants, particularly in those areas where a coordinated effort is being carried out. Specifically, the ORNL technology development efforts are part of a coordinated effort with GA Technologies Inc., (GA), and frequent meetings and interactions were held with GA covering the various technology areas. Interfacing activities largely involve interactions with the U.S. DOE, both in the Oak Ridge Operations Office (ORO), and in the Washington office, Gas-Cooled Reactor Associates (GCRA), the General Electric Company (GE), and Combustion Engineering (CE), and GA.

A new activity has been the installation of electronic information transfer capability among ORNL and other National Program participants. The data acquisition system of the Component Flow Test Loop (CFTL) has been used to provide this facility. This system is a PDP-11/34 computer with extensive storage capacity in the form of mountable disk packs and backup magnetic tape units. There are currently four RK07 disk units on the computer. The computer is accessible through two dial up ports at present. This capacity can be increased to three dial up ports with

available equipment. Any one port can be set to transmit at either 300 baud or 1200 baud. The two 212 Bell System modems will automatically detect the transmission rate of incoming calls and set itself appropriately. The port speed can be set either at the computer or through a remote command. Software presently exists on the system that will facilitate the input or recovery of electronic information in standard, sequential, ASCII coding. Files, i.e., letters, documents, or tables, can be stored on the disks using either a TExt Editor and COrrector program (TECO) or a Peripheral Interchange Program (PIP). Using the above system, we have established the capability for electronic information transfer between ORNL and GCRA, GA, and DOE (Washington and Oak Ridge).

Facilities development is also under this activity; in this area we assist in maintaining the Tower Shielding Facility (TSF) so that it will be available for future HTR shielding experiments. The TSF is jointly maintained by the HTR and Liquid Metal Reactor programs.

2. PROGRAM REQUIREMENTS MANAGEMENT AND EVALUATION ACTIVITIES (WBS 0200.01)

P. R. Kasten

During the last year, a Program Requirements Management (PRM) Task Force was organized within the National HTR Program to address plant level requirements, plant level studies, and selection of the reference HTR concept for initial deployment. ORNL is a member of that task force, as are the other major participants of the National Program; DOE chairs the group. Activities carried out included development of criteria to be used in the concept selection process, evaluation of technical issues and evaluation of the economic performance of the various HTR design concepts.

The initial emphasis was on the development of criteria against which various HTR design concepts could be evaluated. ORNL developed a proposed set of criteria for concept evaluation based on judgment, and these are given in Table 2.1. Two essential features identified were: "1 Overall Economics" and "II Practical Ability to Build a Plant." As given in Table 2.1, the first item pertains to the economic performance of the reactor concept considering factors such as (a) the economics under normal reactor operations and (b) the economics associated with real and perceived investment risks. A subset of the second item is the economics associated with real and perceived public safety concerns.

The second item pertains to the practicality of either building a commercial plant or of building a demonstration plant that precedes a commercial plant. This recognizes that if the perceived economics appear attractive and yet it is not possible to introduce the concept into the power generation industry, then it is not a practical system.

Table 2.1. Proposed criteria for HTR concept evaluation

Criteria		
I. Overall economics		
A. Normal economics	B. Investment risk economics (including Public Safety economics)	Practical ability to build plant
Important		
Capital costs	Costs associated with reactor accidents	Availability of financing
Availability	Costs associated with delays in reactor construction (technical or licensing delays, including those associated with concerns about plant safety)	Availability of vendor Availability of technology Ability to meet needs of utilities/generation companies/users
Fuel cycle costs	Costs associated with actions by regulatory bodies (e.g., PUC)	Ease of licensing Public acceptance
Operating and maintenance costs	Costs associated with evacuation planning, deviations from normal maintenance, effluent release, waste disposal	
Desirable		
Ease of siting	Ease of waste disposal	Low R&D requirements
High thermal efficiency	High resistance to sabotage	
High fuel utilization	Low proliferation concerns	
High versatility relative to applications	Ease of fuel recycle	
Ease of dismantling		

The important factors considered under "normal economics" are listed in Table 2.1 as: capital costs, availability, fuel cycle costs, and operating and maintenance costs. The estimated contribution of an item to total power cost is the criterion of merti, relative to overall cost as a criterion. In the case of capital, fuel cycle, and O&M costs, these costs are the normal estimated values for a nominal availability. For availability, it is necessary to consider the unique ability of a concept to provide a different than nominal availability factor, and this factor should then be used in calculating power costs. Probability distribution values could be utilized, but there appears to be more uncertainty in estimating distribution values than in estimating mean values.

Costs associated with accidents can also be estimated, as indicated in Item I(B) of Table 2.1. For example, the effective cost of an extreme accident is related to the probability of the accident times the sum of the cost of cleanup plus the investment cost payments during downtime plus the cost of replacement power. Multiplying the latter sum by the probability of a specific accident during the lifetime, divided by the power that the plant would have generated, gives the equivalent power cost of the accident.

The second item under investment risk economics, and probably more important than the effective cost of a specific accident, is the effective cost of a delay in plant construction. This requires knowledge of the investment cost required to get a plant into operation under planned circumstances, the probability that the plant will be build in a longer period of time than that planned, and the effects of such delays on investment costs. With this information, investment costs due to construction delay can be estimated in terms of unit power costs; the cost of replacement power needed during the delay period should be considered.

Similarly, unit power costs can be calculated for items such as plant construction delays due to regulatory requirements, evacuation planning requirements, or deviations from normal maintenance procedures.

There are difficult evaluations required in this process for determining mean delay values (or probability distributions for plant construction delays) on which associated power costs associated with certain

events can be evaluated, but the process does permit a consistent, relative evaluation in terms of total power costs as the criterion of merit.

With regard to the practical ability to build a plant, the proposed criterion of merit is the probability that a commercial plant would be built (item II in Table 2.1). There are six "important" criteria listed for item II, and these illustrate some of the factors that need to be considered. For example, the availability of financing can be related to the ability of a utility to include costs in the rate base, which in turn influences the probability of building a specific plant; alternatively, financing by the government is related to the national interest, which involves political factors.

The availability of technology is a factor that influences the ability to build a plant on a given schedule. The ability to meet the needs of utilities is influenced by a comparison of a given power source with alternatives in terms of advantages and risks. Ease of licensing and public acceptance can be factored into these items, or these attributes can be considered as separate items as listed in Table 2.1.

Evaluation of the above factors (and others, since the list is incomplete) in terms of the probability of being able to proceed in a practical way with plant construction is a difficult task, but the process does put information into a format that is meaningful for the comparative evaluation of reactor concepts on a consistent basis. In fact, the economic evaluation itself should also be considered from the viewpoint of how estimated economics influence the probability of being able to construct a specific plant.

Table 2.1 also lists some desirable criteria; however, if all possible factors are included in the evaluation process, the process will become too burdensome and will lose its usefulness. At some level, subjective evaluations are made. However, the various items can be evaluated relative to the probability of being able to build a plant, and this procedure will provide a consistent concept evaluation. The key to valid evaluations is, of course, bringing appropriate decision-making expertise into the process of judging relative probabilities.

This information was provided by ORNL as input to the PRM Task Force; input was also obtained from other Task Force members. The concept evaluation criteria eventually adopted by the PRM was issued by GCRA as report GCRA-84-009, "Concept Evaluation Plan for Small HTGRs," October 31, 1984.

ORNL has continued to participate in the PRM Task Force activities, attending and contributing to meetings pertinent to understanding the various HTR design concepts in sufficient detail so that evaluations and rating of concepts could be performed. In July, the PRM Task Force reduced the number of HTR concepts being evaluated from about sixteen to four; the four remaining are the 250-MW(t), side-by-side, steel-vessel concept; the 250-MW(t), vertical-in-line, steel-vessel concept; the 1260-MW(t), annular-core, prestressed-concrete-reactor-vessel (PCRV) concept; and the 1170-MW(t) cylindrical-core, PCRV concept. Later in the year, ORNL provided preliminary cost estimates for base technology research and development (R&D) requirements for the above four HTR concepts; these estimates cover the areas of concrete, metals and ceramics, graphite, fuels, and fission product behavior. The preliminary R&D estimates varied by only about 10% among the four concepts, so it does not appear that technology R&D costs should impact the concept choice.

3. ECONOMIC STUDIES AND EVALUATIONS (WBS 1000.01)

H. I. Bowers and P. R. Kasten

3.1 INTRODUCTION — P. R. Kasten

During the past year, there has been continuing review of the economic ground rules and cost bases being used in the National HTR Program. These ground rules are generally well established, but changes and updates do occur, and ORNL is involved in that process (see Section 3.2). We have also been involved in the comparison of power costs from modular HTRs versus alternative energy sources. During the last three months of CY 1984, ORNL participated as a member of the Task Force evaluating operating and maintenance (O&M) costs of HTR concepts (see Section 3.3); our continuing role in the Task Force is to calculate O&M costs based on input from other Task Force participants, using the OMCOST computer code (developed at ORNL for light water reactors) with appropriate modifications.

Early in CY 1984, ORNL responded to a Congressional subcommittee request concerning the practicality of modular HTRs and associated key development needs; the ORNL response is summarized below in Section 3.4. In September, ORNL summarized an evaluation of how graphite burning is best avoided in HTRs considering plant design as one approach and coating of graphite with SiC as another approach. Results of this study are given in Section 3.5. Late in the year, ORNL was invited to present a seminar at the Japanese Atomic Energy Research Institute Open Seminar on their Very High Temperature Reactor (VHTR) Program. The abstract of the paper presented is given in Section 3.6.

3.2 HTR ECONOMIC GROUND RULES AND COST BASES — H. I. Bowers

ORNL reviewed and evaluated the HTR economic ground rules and cost bases as proposed and used by GCRA and other Program participants. This is a continuing activity, and updates are incorporated as needed. The program ground rules and cost bases are issued in draft GCRA reports entitled "Economic Ground Rules of the HTGR Program" (Report GCRA-83-008) and "Cost Estimating and Control Procedure" (Reports HP 20901 and HP 20902).

Revision 2 of report GCRA-83-008 was the pertinent report at the beginning of CY 1984. Overall, ORNL found the economic ground rules to be thorough, appropriate, and generally excellent, although there are some specific concerns. Examples of proposed changes by ORNL are as follows:

- The producer price index for industrial commodities is inappropriate for adjusting cost estimates to January 1984. It was recommended that sector-specific indexes, such as the Handy-Whitman index for nuclear power plant construction costs, be used for adjusting earlier cost estimates to the current year. In the absence of sector-specific indexes, the Gross National Product Implicit Price Deflator was recommended as being more appropriate than the producer price index.
- The cost of money appears low, and it was recommended that it be increased to a value more consistent with recent experience;
- An escalation rate of 1%/year for coal, oil, gas and U_3O_8 should be included in the ground rules. The price of U_3O_8 and the cost of separative work to be used in comparative evaluations were recommended to be \$35/lb U_3O_8 and \$100/kg separative work unit, respectively.
- Comments were provided concerning contingency funds evaluation, overall contingency considerations, and meaningful estimates of contingency;
- Comments were provided relative to making the HTR economic ground rules consistent with those used for LWRs and coal plants (or vice versa); and
- Comparisons based on experience were provided, showing that the "indirect cost" percentages for the "best experience" PWRs are significantly higher than those in the HTR ground rules.

We also reviewed the economic ground rules and cost estimating procedures for the HTGR Program issued as report, GCRA HP-20902, Rev. 4, October 4, 1984; Rev. 5 (Draft), December 14, 1984; and report GCRA HP-20901, Rev. 1, September 24, 1984. These economic ground rules and procedures again are thorough and appropriate, and their use should simplify and improve the preparation and comparison of economic studies prepared for the HTR Program. Nonetheless, we question the use of a higher return on bonds than on the return of common stocks for the long term beyond 2000.

We also recommend that documentation of construction cost estimates should include estimates of labor manhours and commodities (e.g., concrete, steel, piping, electrical wiring, etc.) to assist in judging the reasonableness of cost estimates. In addition, some of our previous comments still apply, e.g., the "indirect cost" percentages for first units of plants are not consistent with previous experience cited above.

3.3 ESTIMATES OF HTR O&M COSTS — H. I. Bowers

ORNL participated in a National HTR Program Task Force for evaluating the O&M costs of HTR concepts. Information provided by other participants was utilized with cost estimating procedures developed by ORNL for the computer code OMCOST (an ORNL computer code for calculating O&M costs). Primary participants were GE, GCRA, GA, ORNL, and Bechtel Group, Inc. Plant concepts under consideration were, first, a 4-reactor (steel vessel concept), 1-turbine generator modular HTR plant [387 MW(e)] with on-line refueling; and, second, a 1-reactor (PCRV) concept, 1-turbine generator, integrated HTGR plant [428 MW(e)] with off-line refueling. ORNL provided a preliminary estimate of O&M costs using the staffing and maintenance requirements recommended by other members of the Task Force.

The cost accounting breakdowns and cost estimates are given in Table 3.1. The direct costs encompass those expenses defined in nuclear power generation accounts 517 to 532 of Federal Energy Regulatory Commission (FERC) code of accounts (18 CFR 101). The indirect costs

Table 3.1. Estimated total annual nonfuel operation and maintenance costs

(January 1985 dollars)

	Integrated HTGR (PCRV)	Modular HTR (steel vessel)
Plant capacity, MW(e)	428	379
Capacity factor, %	75	75
Annual generation, 10^6 MWh	2.812	2.490
Onsite staff	222	257
Direct costs (10^6 $/year)		
Onsite staff	9.8	11.3
Maintenance materials		
Fixed	2.1	2.5
Variable	0.8	0.9
Subtotal	2.9	3.4
Supplies and expenses		
Fixed	3.6	3.6
Variable	0.3	0.3
Subtotal	3.9	3.9
NRC fees	1.0	1.0
Offsite support services	2.5	2.5
Subtotal direct costs		
Fixed	19.0	20.9
Variable	1.1	1.2
Subtotal direct costs	20.1	22.1
Indirect costs (10^6 $/year)		
Administrative and general	2.0	2.1
Insurance	4.5	4.5
Subtotal indirect costs	6.5	6.6
Total direct and indirect costs (10^6 $/year)		
Fixed	25.5	27.5
Variable	1.1	1.2
Total	26.6	28.7
Unit costs (mills/kWh)		
Fixed	9.1	11.0
Variable	0.4	0.5
Total	9.5	11.5

encompass administrative and general accounts 928 to 932 as allocated to generation. Variable costs were allocated in two subaccounts; namely, variable maintenance materials and variable supplies and expenses. All other accounts were considered to be fixed expenses.

Estimates of O&M costs were developed for the two plant concepts considered here. A weighted average of all personnel, namely, crafts, technical, engineering, and administrative and supervisory, was used in estimating the annual salary expense for nuclear power plant personnel.

The annual cost of maintenance material was estimated to be 90% of the annual cost of the total maintenance labor including supervision, crafts, instrumentation, and control (at 80% plant capacity factor). The estimates for supplies and expenses were based on judgment and comparison with LWRs. Under NRC fees, an estimated annual fee for routine inspections was included (such as those for safety, environmental and health physics inspections). Off-site support services were based on the full-time services of a 25-person engineering staff. Estimates were included for the premiums associated with liability insurance and property damage insurance. Administrative and general expenses were estimated to be 10% of the total direct O&M costs.

The summary of O&M cost estimates is given in Table 3.1; the total direct and indirect costs were $26.6M/year for the integrated HTGR (PCRV with prismatic fuel), $28.7M/year for the four-reactor modular HTR (steel vessel with pebble fuel). The estimated unit costs are 9.5 mills/kWh and 11.5 mills/kWh, respectively. The higher costs for the modular HTR were primarily due to higher personnel requirements for reactor operation, maintenance, and security. The results given are those initially estimated by ORNL.

3.4 ORNL RESPONSE TO CONGRESSIONAL SUBCOMMITTEE REQUEST CONCERNING MODULAR HIGH TEMPERATURE GAS COOLED REACTORS — P. R. Kasten

Early in CY 1984, ORNL responded to a request of the Subcommittee on Energy Research and Production, U.S. House of Representatives Committee on Science and Technology; the request concerned the practicality of HTRs

having a very high degree of inherent safety (passive safety), and the key research and development needs of such a reactor concept. The ORNL response was given in a hearing report;[1] excerpts are as follows.

> "The modular high-temperature gas-cooled reactor (HTR) is a concept that shows promise of achieving the ultra-safe features which are desired. In fact, the ability to limit fuel temperatures under loss of cooling conditions for modular HTRs has been demonstrated in the Arbeitsgemeinschaft Versuchsreaktor (AVR) in the Federal Republic of Germany. In experiments following full power operation where the helium circulators were turned off, the main circuit coolant valves were closed, and the control rods were not inserted into the reactor, the AVR fuel temperatures remained well below values at which fuel coating damage and fission product release would occur.
>
> "Design features required for an ultra-safe HTR are a low core power density, a negative temperature coefficient of reactivity, and the ability to transfer by passive means a limited amount of decay heat to a heat sink outside the reactor core. All these features are attainable in HTRs. Further, experimental information obtained to date, while not extensive, indicates that fuels can be fabricated in commercial equipment which will have excellent fission product retention characteristics, that fuel temperatures can be cycled from 1100°C to 1600°C for a limited number of cycles without significant deterioration in fuel coatings, and that reactor depressurization during normal reactor operations leads to a very low release of fission products. However, further experimental information is still needed, and not all the significant parameter values have been explored.
>
> "In addition to being ultra-safe, HTRs also need to be economically competitive with alternative energy sources. A modular HTR tends to have relatively high costs for the nuclear steam supply system (NSSS) because of the low power density and the low power level; however, most of the capital investment lies in the balance-of-plant (BOP) costs, which are normally greatly influenced by the NSSS requirements. With an ultra-safe HTR, however, it should be possible to markedly reduce that influence because of a reduction in safety-related systems, resulting in less costly BOP construction. Further, shop fabrication of the relatively small-sized components used in modular HTRs should increase plant availability and improve economic performance. Overall, an ultra-safe HTR appears possible to develop in which licensing concerns are reduced and simplified and BOP costs are reduced. At the same time, experimental verification of such performance is needed.

"Key technical areas which need to be investigated for the modular HTR are:

- The determination of fission product retention by the fuel coatings, graphite, and metal surfaces during and subsequent to extreme accident conditions;
- The design of the modular HTR plant in sufficient detail to permit an estimate of plant costs, based on features which limit fuel temperatures under accident conditions, facilitate shop fabrication, and reduce BOP costs;
- The performance of the plant as a function of design, size [e.g., reactor power of 100—500 MW(e)] and the extent and choice of engineered safety features for comparison purposes;
- The design and evaluation of pebble-bed fuel handling systems;
- The core reactivity coefficients associated with high temperatures and with water ingress, and the development of transport methods to calculate radiation source terms for pebble-bed reactors;
- Verification that the thermal transients which could take place in heat exchanger components can be accommodated;
- Determination of experimental shielding factors so that designs are developed which lead to low radiation damage of the pressure vessel and other components over the plant lifetime;
- Verification that steel pressure vessels will be satisfactory for modular HTR service, and evaluation of steel and prestressed concrete vessels for modular HTR use;
- Design of a helium circulator which does not permit water to enter the core region, e.g., a gas/magnetic bearing circulator; and
- Selection of a reflector graphite which will last the life of the plant without replacement."

3.4 EVALUATION OF WAYS TO INVESTIGATE GRAPHITE BURNING IN HTRs — P. R. Kasten

The response of HTRs to air ingress has often been raised by others as a concern. During the first part of the year, Alvin Weinberg met with GA and University of San Diego personnel and discussed this concern. Based on those discussions, Alvin Weinberg proposed[2] that coating graphite components with SiC would protect graphite from oxidation, and alleviate concerns about graphite burning.

ORNL performed a cursory evaluation of whether SiC coating was a practical way to limit graphite oxidation. However, coating fuel elements (pebble or prismatic) with a material such as SiC does not assure that the coating will always be present. In fact, it is unlikely that SiC will remain in place, since graphite shrinks during irradiation, and SiC is relatively stable. Further, in the case of pebble-bed fuel, dropping a coated sphere would probably cause cracking of the SiC on the surface of the ball. Overall, it is unlikely that SiC would be always present as a protective layer for graphite fuel elements; depending on such a layer would lead to an impractical quality assurance requirement.

While there are modifications of surface coatings that might improve the protective capability of SiC (such as placing the SiC layer a small distance inside the outer surface of a pebble fuel element), a more practical approach is to limit the amount of air available to the fuel element under all circumstances.

Serious oxidation of graphite and resulting fission product release can occur only if there are multiple ruptures in the primary system, there is no forced cooling to maintain graphite at low temperatures, and there are many multiples of one confinement volume of air available for reacting with the graphite. If there is forced cooling capability, core temperatures can be reduced below 400°C in a few hours; the rate of graphite oxidation at temperatures below 400°C is not a safety concern.

If natural circulation effects take place, the flow rate of air to the core is limited to such small values that it would take many hours for one confinement volume of air to flow into the core. Complete reaction of the oxygen content of one confinement volume of air with graphite liberates only about 0.64 MW(t) for the present U.S. modular HTR concept. This is quite small compared with decay heat generation, which liberates roughly 6 MWh during the first 1.5 h after reactor shutdown, and roughly 42 MWh during the first 24 h after reactor shutdown.

While more than one confinement volume might be available for reaction, the use of one confinement volume provides a basis for evaluating consequence and understanding the magnitude of temperatures under specified conditions. Assuming that one confinement volume of air reacts

completely with graphite, it is estimated that the mass of graphite reacting would be about 250 kg, or about 0.41% of the total graphite inventory (excluding reflector). On the basis of pebble bed fuel with a 5-mm unfueled region at the outer surface of the pebble (present design of pebble fuel), about 23% of the core graphite is associated with the outer unfueled portion of the pebble. Thus, there should be no release of fission products if 0.41% of the core graphite were to oxidize; in fact, reaction with several containment volumes should be permissible.

Air ingress to the reactor region may be reduced by using a silo-type placement; the present modular HTR designs involve this type of reactor embedment.

Because of the apparent low-probability event of air ingress to the core, the apparent limited consequences, and the ability to lower the consequences further by plant design changes, it appears that the best way to limit graphite burning is by limiting air ingress through plant design rather than by depending upon a SiC coating of graphite as a protective medium.

This conclusion does not mean that the present design is not adequate; in fact, it appears that the probability for air ingress is very low. At the same time, if graphite oxidation due to possible air ingress must be further limited, the ORNL study concluded that the preferred approach is through plant design changes.

3.5 SEMINAR ON U.S. HTR PROGRAM PRESENTED AT JAERI — P. R. Kasten

In response to an invitation from JAERI to present a paper at the JAERI annual open seminar on the Research and Development of the Multipurpose VHTR in December of 1984, a joint paper with GA and GCRA was prepared. The title and authors of the paper are as follows: "New Approaches in the USA for High-Temperature Gas-Cooled Reactors" by Paul R. Kasten, Oak Ridge National Laboratory; A. J. Neylan, GA Technologies, Incorporated; and S. R. Penfield, Jr., Gas-Cooled Reactor Associates. The paper was presented by Paul R. Kasten at the Japan Atomic Energy Research Institute Annual Open Seminar held in Tokyo, Japan, December 12, 1984. The abstract for the paper is as follows:

"Several concepts are being evaluated in the U.S. HTR* Program to explore designs which might improve the commercial viability of nuclear power. The general approach is to reduce the reactor power and increase the ability to use inherent features for removing heat following extreme accidents. The unit size and design of these concepts are constrained so that extreme accidents do not result in significant release of radioactivity from the reactor plant. Through the greater reliance on inherent safety features in small HTRs, it should be possible to minimize the amount of nuclear grade components required in the balance-of-plant, which could lead to an economic system. Four HTR concepts are presently being evaluated within the U.S. Program, and these concepts are briefly summarized. A modular HTR using a steel pressure vessel, which is very similar to one of the four HTR concepts being evaluated within the U.S. National program, is presented as an example of a specific concept to illustrate the features and performance of HTRs having a high degree of inherent safety."

3.6 REFERENCES

1. Fiscal Year 1985, Department of Energy Authorization Hearings before the Subcommittee on Energy Research and Production of the Committee on Science and Technology, U.S. House of Representatives, 98th Congress, Second Session, February 7, 8, 9, 1984, [No. 89] Vol. IV, U.S. Government Printing Office, Washington, D.C., 1984, pp. 201—228.

2. Alvin Weinberg to P. R. Kasten, personal communication, February 1984.

---

*HTR is a generic term applying both to prismatic-fueled (HTGR) and pebble bed fueled (PBR) reactors.

4. INTERNATIONAL TECHNOLOGY TRANSFER (WBS 1400.01)

J. C. Cleveland, W. P. Eatherly, M. J. Kania,
P. L. Rittenhouse, and R. P. Wichner

4.1 AVR/KFA/ORNL COOPERATION ON HTR PHYSICS, PERFORMANCE AND SAFETY — J. C. Cleveland, B. R. Becker, D. L. Moses and D. R. Vondy

The Project Work Statement (PWS) for the AVR/KFA/ORNL cooperative effort in HTR Physics, Performance and Safety was established within the frame of the U.S. DOE/Federal Republic of Germany Ministry for Research and Technology (BMFT) Umbrella Agreement. The PWS was developed in the period May through August 1983, approved by DOE in February 1984, and approved by BMFT in May 1984. The objectives are: (1) to develop further understanding of small HTRs through computational simulation and reactor experimentation, and (2) to further validate reactor physics and thermal hydraulic analysis tools for modular HTRs against experimental data. The focus is on AVR performance in the area of steady-state core neutronics and on the AVR response (both neutronic and thermal hydraulic) to operating transients, safety tests, and hypothetical accidents.

4.1.1 Core Physics Analyses

Computations of cross sections for AVR fuel were initiated in late 1984 and detailed results will be reported during 1985. Using a one-dimensional transport "cell" model, few group cross sections reaction rates, k-infinite and temperature coefficients (hot and cold) will be determined for HEU/Th fuel and for LEU fuel. A comparison will be made of results obtained using libraries derived from ENDF/B-IV with results obtained using libraries derived from ENDF/B-V. Such an analysis of the impact of new nuclear data (i.e. ENDF/B-V) on computed physics parameters is of interest to KFA and AVR. These cross sections will be used later by ORNL in AVR core analyses and the impact of the new libraries on computed core parameters will be examined. Results will also be compared with AVR performance.

4.1.2 Implementation of the KFA THERMIX-KONVEK Code

An area of interest to ORNL and the DOE HTR program was to obtain the THERMIX-KONVEK HTR thermal hydraulics code from KFA and make this code useful in the HTR Program. THERMIX-KONVEK is a two-dimensional pebble bed reactor thermal hydraulics code which has been developed by KFA and used for steady-state and transient analyses (normal operational transients as well as accident conditions). Analyses of both pressurized and depressurized conditions can be performed. The code has been used extensively for analyses of various pebble fueled HTR concepts and for the AVR and THTR. THERMIX has also been used in a coupled version with other models of various primary and secondary system components for simulation of THTR plant response to various operational transients and accidents. Furthermore, the code has been coupled to REACT for analyses of water and air ingress accidents in pebble fueled reactors.[1]

THERMIX-KONVEK was received from KFA in June 1984. The code was installed on ORNL's computer, and sample problems were executed successfully. At the Request of GA Technologies (GA), and with concurrence from KFA, the code was provided to GA in January 1985. ORNL also provided GA with descriptions of IBM system routines that must be included for successful execution of the code but could not be provided by KFA along with the THERMIX-KONVEK subroutines. Further information provided to GA included:

- a tape and listing of an exact copy of the original tape as received from KFA;
- A tape, listing and compilation of the code as installed at ORNL and a printout of all changes relative to the original version; and
- results of a steady-state sample problem and a transient sample problem.

4.1.3 Analysis of the Thermal Response of the AVR to a Hypothetical Depressurized Core Heatup Accident

This analysis was performed as one of ORNL's commitments in the PWS. The AVR staff was interested in having ORNL perform an independent

analysis of this accident using independent thermal hydraulic tools (i.e., not THERMIX-KONVEK) for comparison with analyses of this accident by AVR and KFA.

One motivation for performing these analyses at this time is that the AVR has many design features which are similar to those of modular HTR concepts being developed both in the U.S. and in the Federal Republic of Germany. The AVR staff is examining the possibilities of performing additional experiments at the AVR to demonstrate important features of that reactor which provide it with a high degree of safety. In particular, AVR staff is considering performing depressurized core heatup tests. Such tests would provide data which might be used for verification of reactor analysis tools for actual reactor conditions with irradiated materials. They would also constitute an integral test of important HTR safety features.

4.1.3.1 Summary and Conclusions of ORNL's Analyses of a Hypothetical Core Heatup Accident at the AVR

The analyses reported here assume an instantaneous depressurization and loss of forced convection with the reactor initially operating at full power [46 MW(t)] with a gas outlet temperature of 950°C. A scram is assumed to occur at accident initiation. Because the primary system is assumed to be depressurized during the accident, convective heat removal is neglected. This is a conservative assumption relative to core temperature predictions. The analyses were carried out in two dimensions (r-z) using the ORNL HEATING-6 general purpose heat transport code.[2] Of key interest in this analysis was the fuel temperature and the time the fuel experiences above normal temperatures. Major factors affecting the predicted fuel and vessel temperatures were also identified.

Results of ORNL's calculations show that the response of the core temperatures is very slow with the peak fuel temperature increasing only 25°C in the first half hour following accident initiation and only 100°C in the first two hours following accident initiation. Assuming that the outer pressure vessel can be kept fairly cool (near 100°C) by the containment spray ("water sprinkle") cooling system, which cools the outer surface of the steel containment shell, or by other means, the highest temperature

reached in the fuel is in the range of 1320°C to 1350°C and occurs 15 to 20 hrs after accident initiation. Further, for the first several days (~10 days) after accident initiation, the maximum fuel temperature is not dependent on the rate of heat removal through the outer vessel wall.

The inner vessel could reach a maximum temperature of 640 to 790°C, about 500 to 600 h after accident initiation. This maximum temperature of the inner vessel is sensitive to the conductivity of the first biological shield. If this conductivity is decreased from 1.0 W/m-K to 0.5 W/m-K, the temperature of the inner reactor vessel is increased by 50°C at 150 h into the transient, and the subsequent maximum temperature of the inner vessel is increased by 150°C. The thermal properties of the first biological shield are not well known. If depressurized core heatup experiments are to be performed at the AVR, methods of obtaining better values for the thermal properties (e.g., thermal conductivity and thermal diffusivity) of the first biological shield should be investigated. This would allow a more accurate prediction of vessel temperature response.

For the postulated accident, the heat must be removed through the side reflector, and so the side reflector thermal conductance is an important parameter relative to the time fuel is above normal temperature. For example, these analyses showed that the time for which the peak core temperature remains above normal operating temperature would double if the conductivity of the inner 50 cm of the side reflector were about 50% lower (which is generally within the range of various reported nominal and conservative values for reflector conductivity). On the other hand, peak fuel and vessel temperatures are not very sensitive to side reflector conductivity. This decrease of 50% in the conductivity of the inner 50 cm of the side reflector increased the peak fuel temperature only 25°C, and had essentially no effect on peak vessel temperature. Time at temperature could be a significant factor relative to fission product retention.

No analysis has been done here to estimate the fission product release from the fuel which would result from this hypothetical heatup accident. It is relevant here to note that the peak temperatures which would be reached in the hypothetical core heatup accident calculated here are higher (by roughly 200°C to 250°C) than those experienced in earlier

AVR experiments which involved pressurized core heatup (without insertion of the control rods) under conditions that allowed significant heat removal from the core by natural convection. Further, with a depressurized core heatup, the fuel would remain at above normal temperature longer than it did in the pressurized heatup experiments. (In the earlier experiments, the fuel exceeded normal temperatures by, at most, 60°C.)

The peak temperatures predicted here for a depressurized core heatup are quite a bit below the 1600°C limit nominally considered as an interim design limit for modular HTRs (using TRISO coated fuel) to assure acceptably low fission product release under accident conditions.

4.1.3.2 Results

The reference case assumed an instantaneous depressurization and a loss of forced convection of primary coolant with the reactor initially at full power conditions, which are 46 MW(t) and 950°C core outlet temperature. A scram was also assumed at accident initiation. Other ORNL analyses of AVR flow reduction experiments, which involve stopping of the circulators following the initial flow reduction with the reactor pressurized, show that the reduced rate of heat removal from the core rapidly drives the reactor subcritical without control rod insertion, due both to the increase in core temperature coupled with the negative temperature coefficient of reactivity, and due to the transient increase in Xenon concentration due to the decreasing flux. Under depressurized conditions, the core would be driven subcritical more rapidly because the rate of heat removal by natural convection would be even lower.

This reference case assumed that a water spray system, which is available to cool the outer surface of the steel containment shell using water stored above the containment, would provide sufficient cooling of the region between the steel containment and the outer pressure vessel of the reactor to maintain the surface of this outer pressure vessel at approximately 100°C. This assumption avoided the complicated task of modeling natural convection, heat radiation and conduction, and heat capacity in the geometrically complicated region between the outer pressure vessel and the steel containment. The impact of this assumption on the predicted

peak fuel temperature was analyzed in an additional case discussed later. Because the primary system was assumed to be depressurized, heat removal from the core by natural convection was neglected. Therefore, the only means of heat removal from the core considered in this case are the heat transport mechanisms of conduction and radiation outward from the core, reflector and core barrel, through the thermal shield, inner vessel, first biological shield, and ultimately through the outer vessel.

Figure 4.1 shows the predicted radial temperature distribution through the core, reflector, thermal shield, the inner and outer vessels and the biological shield at several times during the transient. The radial profiles are plotted for the axial plane in which the highest core temperature occurs at that point in time. The highest temperature is near the top of the pebble bed at normal operation which represents the initial condition for this accident, and moves downward toward the core midplane as the transient progresses. Figure 4.2 shows the peak fuel temperature versus time. For this reference case, a peak fuel temperature of 1320°C occurs at approximately 17 h into the transient, and decreases very slowly after that time.

As mentioned above, for this reference case it was assumed that the outer surface of the outer pressure vessel could be held at 100°C by some means (e.g., the "water sprinkle" system). Supplementary analyses were performed to scope the effect of this assumption on computed fuel temperature. Figure 4.2 compares the peak fuel temperature for the reference case with the peak fuel temperature computed under the assumption that no heat is removed through the outer vessel (i.e., adiabatic heatup), and Fig. 4.3 shows the radial temperature profiles for this adiabatic heatup case. Note that for the first several hours, the peak fuel temperature is essentially the same for both cases. This derives from the fact that significant quantities of heat can be removed through the outer vessel only after the temperature in the thermal shield, the inner pressure vessel, and the first biological shield have increased significantly to set up temperature gradients that support heat transport. During the first several hours, the primary effect is a temperature redistribution with those regions which are initially relatively cool (i.e., the lower core region, the side and

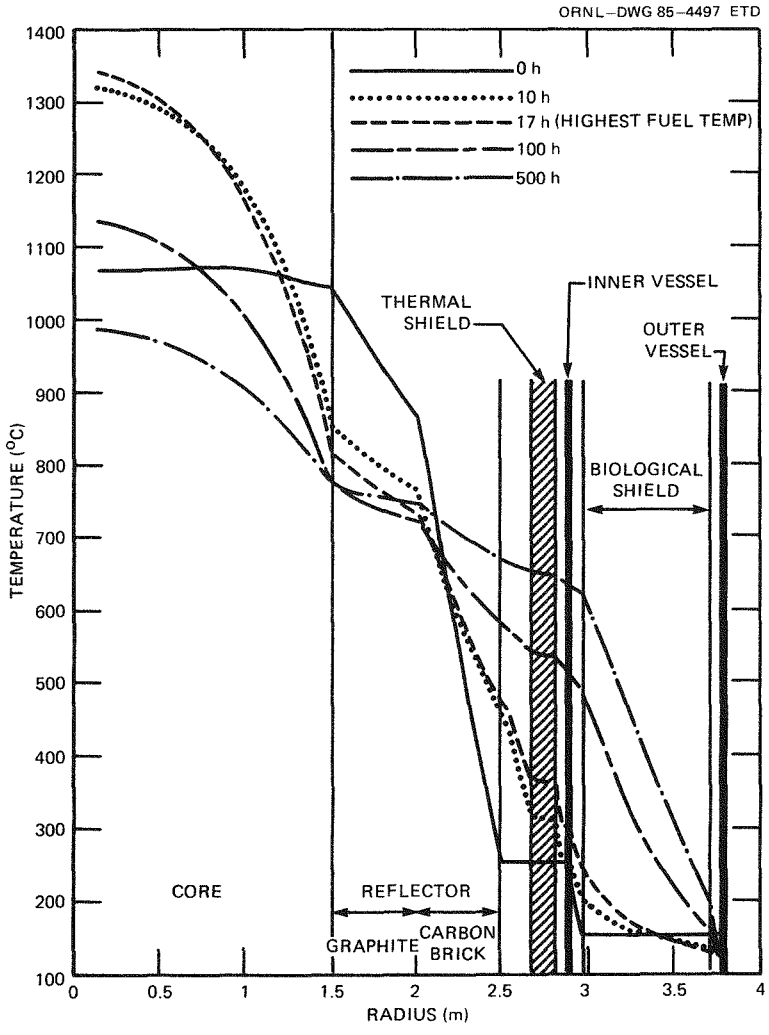

Fig. 4.1. Temperature distribution during depressurized core heatup in AVR with heat rejection through outer vessel (no cooling by interspace cooler).

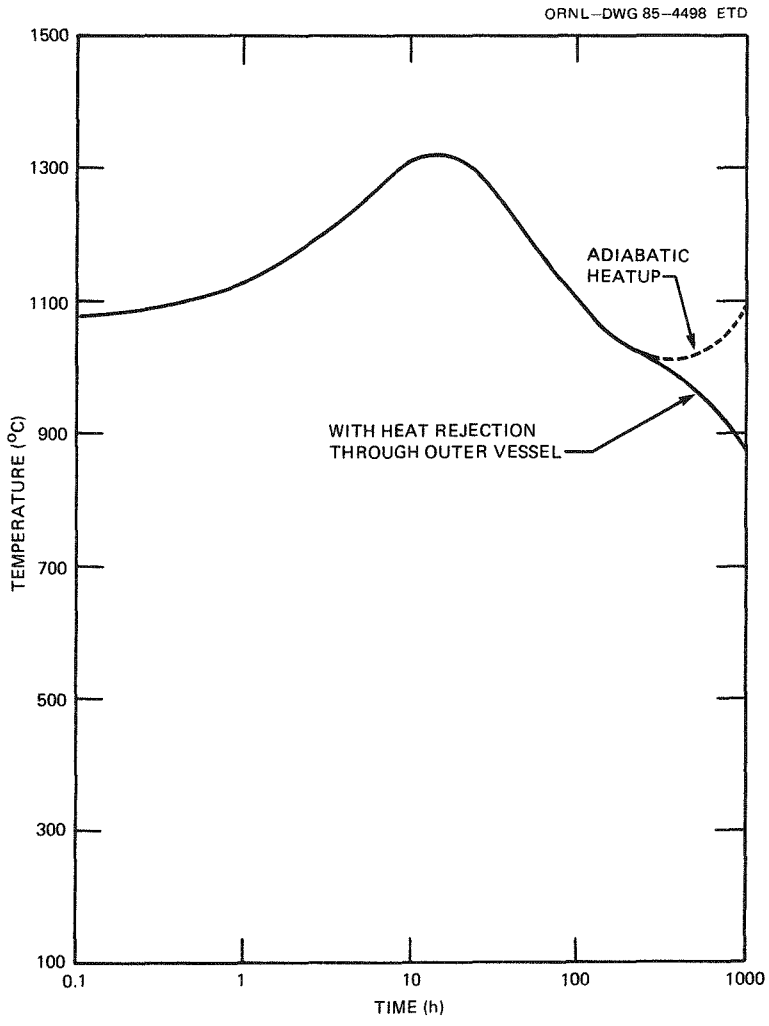

Fig. 4.2. Peak fuel temperature in depressurized core heatup in AVR.

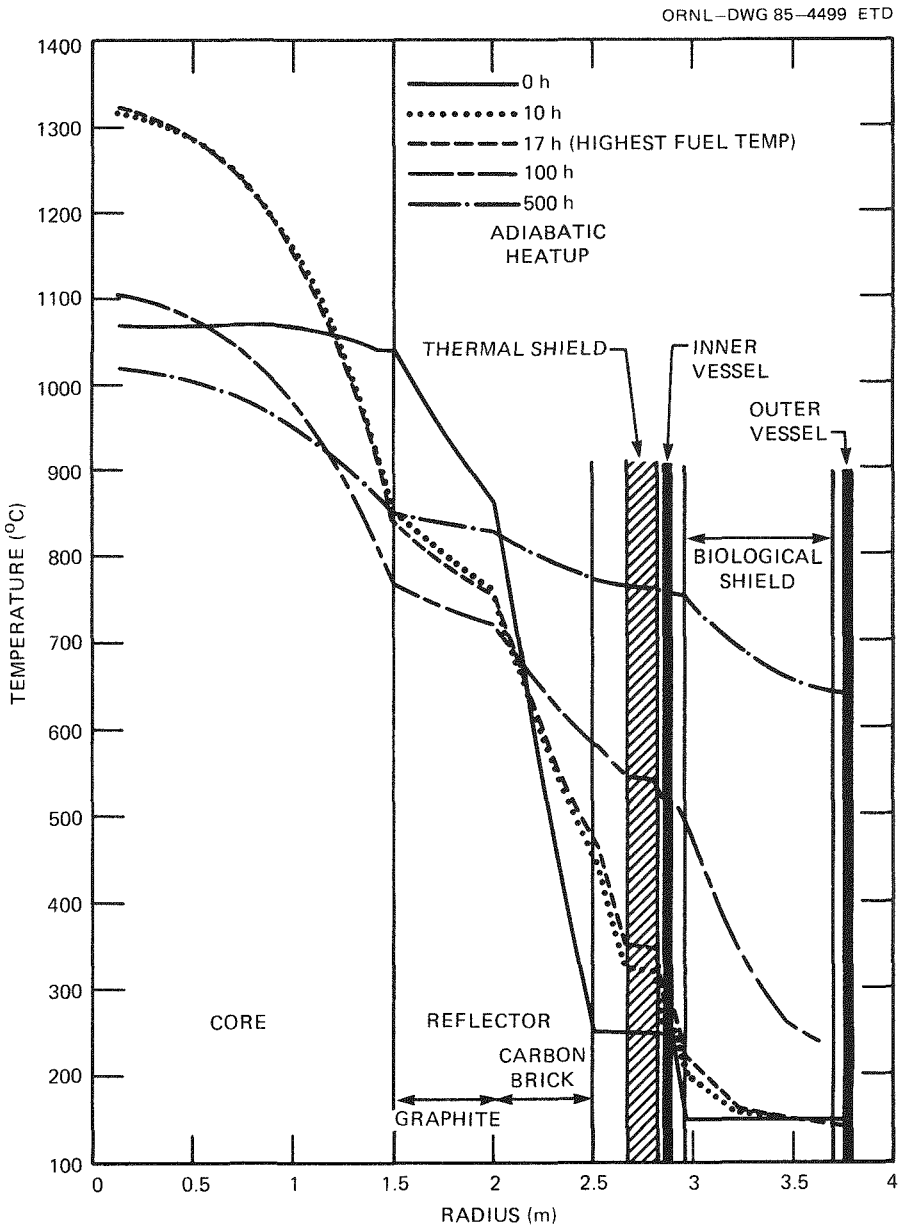

Fig. 4.3. Temperature distribution during depressurized core heatup in AVR (adiabatic heatup).

lower reflectors, the biological shield, and the pressure vessels) undergoing a slow temperature increase. The fuel temperature peaks relatively early (at approximately 17 h) into the transient. Thus, the inaccuracies introduced by assuming the outer vessel is held at 100°C are of little importance during the period when the fuel temperature is peaking. Any inaccuracies in the predicted temperatures of the fuel, biological shield,

and pressure vessels caused by this assumption would become significant only later in the transient when temperatures in the outer regions of the reactor have increased.

A variation in the reference case was analyzed to determine the sensitivity of peak fuel and vessel temperatures, as well as the time which the peak fuel is above normal temperature to the conductivity of the side reflector. Results show that a decrease of about 50% in side reflector conductivity (relative to the values used in the reference case) approximately doubles the length of time that the peak fuel temperature is above its value during normal operation. The lower value for side reflector conductivity increased the peak fuel temperature by only 25°C and had essentially no effect on peak vessel temperature.

With the level of effort expended for this analysis, no overall claim of conservatism can be made in the prediction of core temperatures because of the wide range of uncertainty associated with various input parameters (e.g., decay heat generation and conductivity of the bed of irradiated pebbles). Areas where conservatism has been applied are noted. However, it is important to note that assumptions and input parameters which would yield conservative predictions of core temperature will not necessarily yield conservative predictions of vessel temperature. For example, small convective currents between the core barrel and the thermal shield, and between the thermal shield and the inner vessel would provide an additional means of transferring heat from the core to the vessel. Further, a low value for conductivity of the first biological shield will tend to increase the peak vessel temperature. This conductivity is not well known. A decrease of 50% in the conductivity of this biological shield resulted in an increase of 150°C in the predicted value of the peak vessel temperature, but this decrease had essentially no effect on peak fuel temperature. Therefore, if this accident is to be analyzed further, it is recommended that the effects on the inner vessel temperature be considered in more detail.

The effect on predicted fuel temperature of applying a different correlation for effective pebble bed conductivity was also investigated. The results shown in Figs. 4.1 and 4.2 were obtained using a correlation by Schürenkramer.[3] Figures 4.4 and 4.5 show the same case except using a

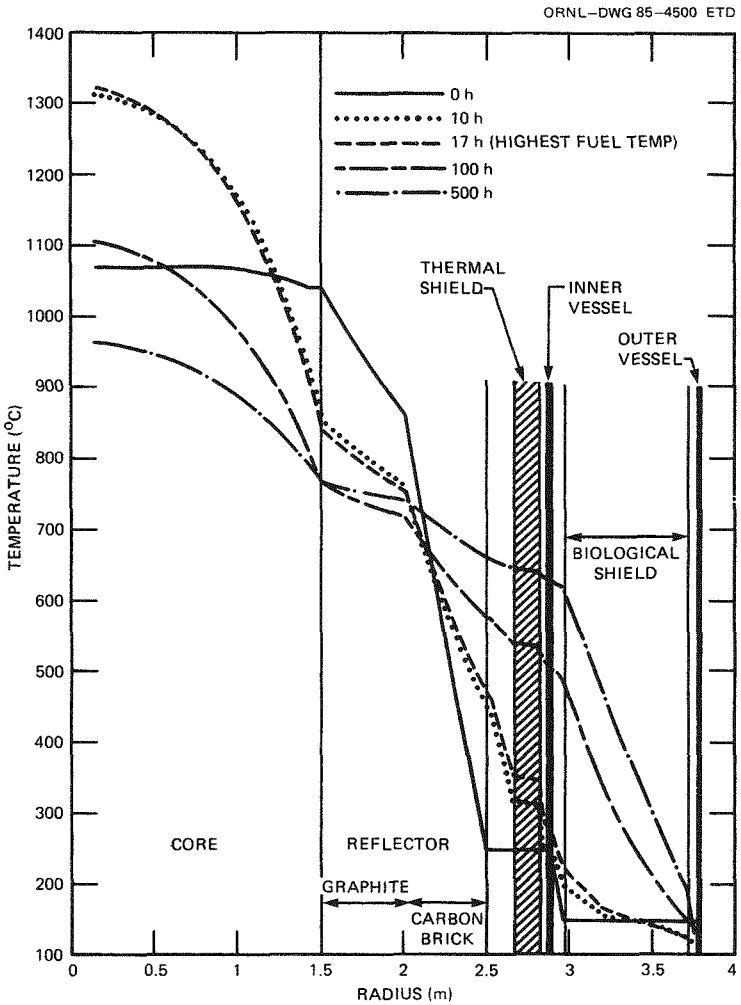

Fig. 4.4. Temperature distribution during depressurized core heatup in AVR with heat rejection through outer vessel (using correlation for effective conductivity of pebble bed from Ref. 4).

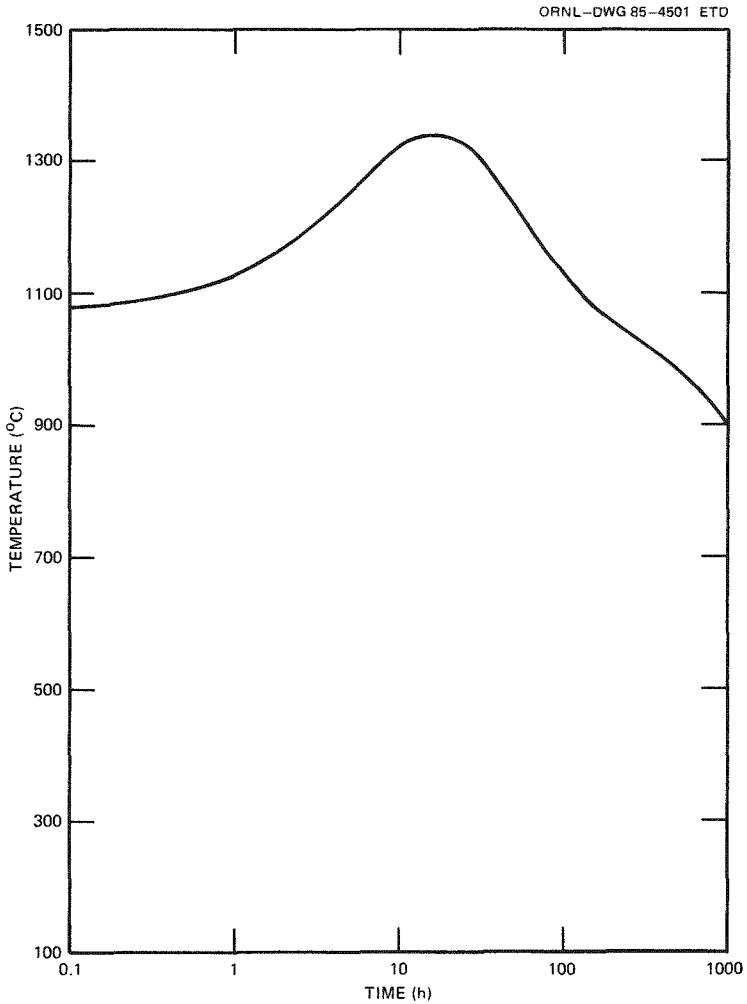

Fig. 4.5. Peak fuel temperature in depressurized core heatup in AVR with heat rejection through outer vessel (using correlation for effective conductivity of pebble bed from Ref. 4).

correlation for the effective bed conductivity by Petersen. The difference in peak temperature resulting from these two correlations was 20°C, with the correlation by Petersen predicting the higher core temperatures and predicting that the fuel remains at high temperatures for a longer time.

4.2 FUELS AND FISSION PRODUCTS — M. J. Kania and R. P. Wichner

This work is being performed under the Fuel, Graphite, and Fission Product Subprogram, which is one of several programs included under the Umbrella Agreement between the United States and the FRG. The fuel development work covered in this subprogram is being performed by ORNL, GA, and KFA-Jülich. Only PWS FD-20 remains as an active project work statement in the fuel development area between ORNL and KFA.

4.2.1 PWS FD-20 — M. J. Kania and G. A. Moore

Irradiated fuels from three German experiments were subjected to postirradiation examination (PIE) at ORNL under Project Work Statement (PWS) FD-20. Unbonded particles were obtained through chemical deconsolidation on a total of seven irradiated compacts: experiment FRJ2-P23/Compact 14, experiment FRG2-P-25/Compacts 32, 27, 21, and 13, and DR-S6/Compacts 19 and 22. About 1500 to 2000 particles from each compact were shipped from the Kernforschungsanlage (KFA)-Jülich, FRG.

Characteristics of each of the particle batches irradiated in the different compacts are provided in Table 4.1. The unbonded particles from the FRJ2-P25 compacts contained a small number of laser failed particles from various batches along with a larger number of test particles from batch EO 1607. The particles that failed prior to irradiation were included to assess fission gas release during in-reactor operation.

4.2.2 Gamma Spectrometry Measurements (IMGA Examinations)

Irradiated Microsphere Gamma Analyzer (IMGA) examinations were performed on approximately 1600 particles from each of the four compacts from experiment FRJ2-P25 and the single compact from FRJ2-P23. Three hundred particles from each of the two compacts from DR-S6 were examined. A

Table 4.1. Particle batch characterization from Set 2 fuels of PWS FD-20

Experiment/ compact	Particle batch	Coating type	Kernel type[a]
FRJ2-P23/14	EO 1607	Triso	$(Th,U)O_2$ — HEU
FRJ2-P25/32	EO 1607	Triso	$(Th,U)O_2$ — HEU
	HT-174	Triso	UCO — LEU[b]
FRJ2-P25/27	EO 1607	Triso	$(Th,U)O_2$ — HEU
	EO 1607	Triso	$(Th,U)O_2$ — HEU
FRJ2-P25/21	EO 1607	Triso	$(Th,U)O_2$ — HEU
	EO 1232	Biso	$(Th,U)O_2$ — HEU
FRJ2-P25/13	EO 1607	Triso	$(Th,U)O_2$ — HEU
	EO 1338	Triso	UC_2 — HEU
DR-S6/19	EO 403/405	Triso	UC_2 — HEU
DR-S6/22	EO 403/405	Triso	UC_2 — HEU

[a] HEU = High Enriched Uranium, ^{235}U enrichment >90%.
LEU = Low Enriched Uranium, ^{235}U enrichment <20%.

[b] ^{235}U enrichment is 20.08%.

[c] ^{235}U enrichment is 9.5%.

reduced number of particles from DR-S6 were examined because of the long period of time (about eight years) between the reactor discharge and the IMGA examination. Specific gamma energy peaks selected from the full gamma energy spectrum of each particle were set to coincide with measurements made at KFA-Jülich. Peak areas along with corresponding isotope branching ratios were used to calculate fission and activation product activities. All were corrected back to the specific reactor discharge date for each experiment.

Tables 4.2 through 4.4 present the analyses of the IMGA examination data on the three experiments. Results are presented in the form of a measured minimum, maximum, and mean activity, and the population standard deviation. The latter was calculated assuming the distribution of activity values was normal. Also shown are the results of the gamma spectrometry measurements performed at the KFA-Jülich for experiments FRJ2-P23 and -P25 fuels. The IMGA-derived activity ratios $^{134}CS:^{106}Ru$, $^{137}Cs:^{106}Ru$, and $^{134}Cs:^{137}Cs$ are also presented. The range in activity ratios represents the total population examined from each compact, and the mean measured ratio was used as the normalization constant for each histogram.

Table 4.2. Results of IMGA examination on 1567 particles from batch E0 1607 irradiated in Compact 14 of experiment FRJ2-P23

Isotope	Activity/heavy metal (Bq/g)			s (%)	KFA-Jülich results
	Minimum	Maximum	Mean		
^{134}Cs	10.6	27.0	13.5	5.58	15.2
^{137}Cs	9.7	24.1	12.0	5.14	13.7
^{106}Ru	12.7	31.7	17.2	6.94	19.9
^{144}Ce	207.1	476.7	245.8	6.05	301.0
^{154}Eu	0.21	0.60	0.29	9.70	
$^{134}Cs/^{106}Ru$	0.617	0.992	0.786	6.41	0.76
$^{137}Cs/^{106}Ru$	0.561	0.896	0.697	6.26	0.69
$^{134}Cs/^{137}Cs$	1.08	1.18	1.13	1.54	1.11

The analysis of FRJ2-P23/Compact 14 revealed a uniform performance for the particle population of 1567. The shape of the activity ratio distributions were indicative of no failed fuel particles present. The counting error associated with each cesium:ruthenium ratio was on the order of 5.1% and for the $^{134}Cs:^{137}Cs$ it was about 0.5%. These numbers are in general much smaller than the error associated with the actual burnup measurement of the fuel. This is apparent by the relatively broad range of activity ratios for $^{134}Cs:^{106}Ru$. A possible reason for this would be a significant "softening" of the flux spectrum due to the geometry of the irradiation compact.

The analyses of the fuels from experiment FRJ2-P25 indicate that a number of failed particles were present in each of the particle populations from Compacts 32, 27, and 21. In Compact 32, one particle of the 1605 examined was physically separated as failed during the IMGA examination run. Further study of the data set for this particle revealed a very low inventory of ^{232}Th as compared to the test set batch E0 1607. The differences were more than a factor of ten. The laser failed particles in this compact contained UCO kernels so there was no ^{232}Th present in them. We cannot at this time speculate to which particle batch this

Table 4.3. Results of IMGA examinations on 6,588 particles from batch E0 1607 irradiated in Compacts 32, 27, 21, and 13 of experiment FRJ2-P25

Isotope	Activity/heavy metal (Bq/g)			s (%)	KFA-Jülich results
	Minimum	Maximum	Mean		
Compact 32 (1604 particles)					
^{134}Cs	0.36	19.22	9.88	6.45	9.66
^{137}Cs	0.44	21.67	10.91	5.65	11.8
^{106}Ru	11.24	31.29	14.95	7.83	16.3
^{144}Ce	75.27	411.32	211.67	6.54	238.0
^{154}Eu	0.11	0.47	0.23	18.08	
$^{134}Cs/^{106}Ru$	0.03	0.848	0.662	6.94	0.59
$^{137}Cs/^{106}Ru$	0.038	0.918	0.732	6.49	0.72
$^{134}Cs/^{137}Cs$	0.810	1.06	0.905	2.51	0.82
Compact 27 (1695 particles)					
^{134}Cs	6.60	26.79	13.32	4.46	13.4
^{137}Cs	6.49	24.72	12.46	3.98	14.2
^{106}Ru	13.55	33.74	17.00	6.41	17.3
^{144}Ce	188.29	467.34	236.82	5.12	282.0
^{154}Eu	0.23	0.60	0.31	8.97	
$^{134}Cs/^{106}Ru$	0.376	0.949	0.786	6.03	0.77
$^{137}Cs/^{106}Ru$	0.370	0.888	0.735	5.78	0.82
$^{134}Cs/^{137}Cs$	1.02	1.11	1.07	1.46	0.94
Compact 21 (1659 particles)					
^{134}Cs	4.86	25.70	12.43	8.37	12.8
^{137}Cs	5.00	25.70	12.45	8.18	13.6
^{106}Ru	8.39	34.26	16.24	8.83	16.6
^{144}Ce	127.16	479.34	236.94	8.23	257.0
^{154}Eu	0.15	0.65	0.30	9.49	
$^{134}Cs/^{106}Ru$	0.555	0.873	0.766	3.97	0.77
$^{137}Cs/^{106}Ru$	0.570	0.874	0.767	3.59	0.82
$^{134}Cs/^{137}Cs$	0.954	1.05	0.999	1.85	0.94
Compact 13 (1630 particles)					
^{134}Cs	3.82	21.48	10.44	5.67	10.8
^{137}Cs	4.61	25.94	12.76	5.33	14.1
^{106}Ru	6.00	34.23	16.73	6.19	14.7
^{144}Ce	81.84	499.27	237.58	6.11	261.0
^{154}Eu	0.01	0.56	0.27	8.00	
$^{134}Cs/^{106}Ru$	0.552	0.704	0.624	3.79	0.73
$^{137}Cs/^{106}Ru$	0.677	0.855	0.763	3.39	0.96
$^{134}Cs/^{137}Cs$	0.785	0.854	0.818	1.60	0.77

Table 4.4. Results of IMGA examination of 600 particles from batch EO 403/405 irradiated in Compacts 19 and 22 from experiment DR-S6

Isotope	Activity /heavy metal (Bq/g)			s (%)
	Minimum	Maximum	Mean	
Compact 19 (300 particles)				
^{134}Cs	4.37	11.77	6.74	11.75
^{137}Cs	4.30	11.76	6.48	11.41
^{106}Ru	19.52	65.05	34.83	15.67
^{144}Ce	16.91	108.48	55.55	26.76
^{154}Eu	0.14	0.38	0.22	13.45
$^{134}Cs/^{106}Ru$	1.52E−1	2.57E−1	1.95E−1	8.71
$^{137}Cs/^{106}Ru$	1.43E−1	2.51E−1	1.88E−1	8.75
$^{134}Cs/^{137}Cs$	9.91E−1	1.09	1.04	2.23
Compact 22 (300 particles)				
^{134}Cs	1.21	6.91	4.77	11.03
^{137}Cs	1.31	7.75	5.38	10.64
^{106}Ru	8.96	59.85	34.89	15.39
^{144}Ce	13.60	82.93	46.36	27.39
^{154}Eu	0.04	0.25	0.16	12.38
$^{134}Cs/^{106}Ru$	1.30E−1	2.22E−1	1.67E−1	9.47
$^{137}Cs/^{106}Ru$	1.45E−1	2.42E−1	1.89E−1	9.27
$^{134}Cs/^{137}Cs$	8.47E−1	9.36E−1	8.86E−1	2.29

particle belongs, but we believe it to be neither HT-174 nor EO 1607. For Compact 27, four particles of the 1695 examined were isolated during the examination run. All four particles experienced significant cesium inventory losses. Unfortunately, the laser-failed batch in Compact 27 was the same as the test batch EO 1607. Therefore, it is difficult to assign these four particles as belonging to the laser failed group. Due to the excellent performance of the test batch EO 1607 in experiment FRJ2-P23 and the remaining compacts from this experiment, we believe that these four particles do indeed belong to the laser failed group. In Compact 21, one particle of 1660 examined was isolated as failed during the examination run. Further examination of this particle data set revealed that it was not a mixed oxide particle as no ^{232}Th was evident in the gamma energy spectrum. The laser failed set of particles contained in this compact

were from batch EO 1232, which had a mixed oxide kernel. Therefore, the laser failed particles should also contain some evidence of ^{232}Th. Again, we are not sure of the origin of this particle with the exception that it does not appear to be from either the test set or the laser failed set.

During the examination of 1630 particles from Compact 13 of FRJ2-P25, a total of 11 particles were physically separated as inert. These 11 had counting rates that were less than the minimum limit initially set for particle detection at the start of the examination run. Upon closer examination, we found these to be actual fuel particles but with relatively low activities. The 11 particles were separately examined by gamma spectrometry. Analyses of the individual spectra indicated that the particles contained no evidence of ^{232}Th. Therefore, all were identified as belonging to the laser failed batch EC 1338. The kernel material for this batch was UC_2.

Analyses of Compacts 19 and 22 from experiment DR-S6 did not indicate any difference in performance between the two sets of particles. Both exhibited the same activity ratio distribution shape with slightly different mean activity ratio values. Only 300 particles were examined from each compact and none was detected as being significantly different than the majority.

A summary of the performance characteristics for each of the three experiments is presented in Table 4.5. None of the 1567 particles of batch EO 1607 examined from experiment FRJ2-P23/Compact 14 had significantly different performance characteristics than the majority of particles. For the 6588 particles of batch EO 1607 examined from experiment FRJ2-P25, only four particles exhibited significant cesium loss to be classified as failed. These four particles are thought to be part of the laser failed particle set (failed prior to irradiation) included in Compact 27. In the visual examination of these four particles no evidence of the laser hole was evident; only low magnifications, less than 10×, were used. The 600 particles of batch EO 403/405 from experiment DR-S6 also exhibited uniform performance and none showed any evidence of significant cesium loss.

Table 4.5. Summary of performance characteristics for set 2 fuels examined with the IMGA under PWS-20

Experiment/ compact	Number examined	Number failed	Failure fraction[a] (%)	
			$\eta(50)$	$\eta(95)$
Batch EO 1607				
FRJ2-P23/14	1567	0	0.00	1.91E−3
FRJ2-P25/32	1604	0	0.00	1.86E−3
/27	1695	4	0.24	<6.50E−3
/21	1659	0	0.00	1.81E−3
/13	1630	0	0.00	1.84E−3
Batch EO 403/405				
DR-S6/19	300	0	0.00	9.92E−3
DR-S6/22	300	0	0.00	9.92E−3

[a]Numbers in parentheses represent confidence level in percent.

4.2.3 Mass Spectrometry Measurements (PGA Examinations)

Postirradiation Gas Analyzer (PGA) examinations were conducted on a small number of particles selected from the general population of particles from experiments FRJ2-P23 and DR-S6. Twelve particles from the single compact of FRJ2-P23 and twelve particles from each of the two compacts of DR-S6 were analyzed in the PGA system for their stable xenon and krypton gas inventories.

For Compact 14 of FRJ2-P23, inventories of ^{84}Kr, ^{86}Kr, ^{134}Xe, and ^{136}Xe were measured; and for Compacts 19 and 22 of DR-S6 only the krypton isotopes were measured. The mean value of six measurements (six different particles) for each set of fuels is presented in Table 4.6. It should be noted that for each set of fuels the measured gas release data exhibited consistency from particle to particle. Table 4.6 also presents a comparison between the PGA measured release and the calculated total gas inventory generated for each isotope of interest. The ratio of the PGA measured release-to-calculated inventory provides a fractional release value which is then compared to predicted release fractions. The predicted

Table 4.6. Comparison between calculated and measured stable fission gas inventories from selected particles from German irradiation experiments FRJ2-P23 and DR-S6

	Stable fission gases (n mol)				Mean measured		Predicted[a]	
	^{84}Kr	^{86}Kr	^{134}Xe	^{135}Xe	Kr	Xe	Kr	Xe
Particle Batch EO 1607, Experiment FRJ2-P23/Compact 14								
Measured, %	1.48	2.40	7.56	11.49				
Calculated, %	2.55	4.91	18.49	28.57				
Fraction released	0.58	0.49	0.41	0.37	0.52	0.40	0.84	0.84
Particle Batch EO-403/-405, Experiment DR-S6/Compact 19								
Measured, %	2.13	3.43						
Calculated, %	2.03	3.82	19.95	34.42				
Fraction released	1.05	0.90			0.95		0.91	0.69
Particle Batch EO-403/-405, Experiment DR-S6/Compact 22								
Measured, %	0.37	0.55						
Calculated, %	1.75	3.32	16.65	28.57				
Fraction released	0.21	0.17			0.18		0.27	0.20

[a]Predicted fractional release values provided by H. Nabielek, HBK-Projekt, Kernforschunsanlage (KFA) Jülich, Republic of Germany.

fractional release values were derived from $(Th,U)O_2$ particle performance model and provided by H. Nabielek, Kernforschungsanlage (KFA) Jülich.

The IMGA examination data and the PGA gas release data have been provided to H. Nabielek, KFA-Jülich. Remaining fuels from experiment FRJ2-P25 that have not been examined with the PGA system are presently being held in storage at the HRLEL until a decision is made whether the measurements are needed or not.

4.3 GRAPHITE — W. P. Eatherly and R. A. Strehlow

Results were received from KFA, Jülich, FRG on the effect of helium pressure on oxidation of graphite by steam. The results were compared with predictions based on the ORNL model. Although the total oxidation

was significantly higher (about of factor of 6) than had been anticipated, presumably due to impurities in the graphite, the penetration depths were in satisfactory agreement. The penetration depth is the distance into the porous graphite at which the total oxidation is 1/e of that at the surface.

The results are shown in Table 4.7 for oxidation at 1000°C with a steam pressure of 50 kPa.

Table 4.7. Penetration depths of oxidation as a function of total pressure

Helium pressure (MPa)	KFA (mm) experimental	ORNL (mm) calculated
0.4	2.7	4
1.5	1.0	
4.0		0.4
5.5	0.5	

The agreement appears to be quite satisfactory. A more complete analysis and comparison is planned contingent on receipt of additional details from the KFA. The current results indicate that the model used to calculate oxidation at pressures of interest in the HTR is valid.

4.4 STRUCTURAL MATERIALS — P. L. Rittenhouse

4.4.1 US/FRG/CH Material Subprogram

A meeting of the US and FRG Materials Subprogram managers was held at ORNL on November 7–8, 1984. The meeting covered progress and plans relative to HTR materials development under the US/FRG Umbrella Agreement on Gas-Cooled Reactor Technology. The Subprogram meeting was productive and met all requirements concerning review of progress of individual Project Work Statements (PWSs), planning, and updating of the Subprogram Plan. Cooperation in most of the PWS areas was deemed satisfactory to very good over the past years. Areas where difficulties remain were identified and suggestions were made for their resolution.

A revised Subprogram Plan and minutes of the meeting were prepared and distributed after approval by the Subprogram managers. Representatives of US, FRG, and CH sponsoring organizations are to review the revised Plan prior to formal approval.

4.4.2 Fatigue Round-Robin — J. P. Strizak

Experimental variables such as specimen design, mode of test control, strain and load measurement, environment, cyclic frequency, and waveform are important factors in obtaining and evaluating low-cycle fatigue and creep-fatigue data. The objective of the subject round-robin under PWS M-1 is to compare and assess experimental equipment and test methods being employed for low-cycle fatigue and creep-fatigue testing in the United States and West Germany in order to recommend test practices, improve data confidence, and provide a basis for possible future cooperation in high-temperature fatigue programs. GA Technologies, General Electric Company, and Oak Ridge National Laboratory are joined in this task by Gesselschaft für Hochtemperatur-Technik GmbH/Interatom GmbH (GHT/IA), Hochtemperatur-GmbH (HRB), and Kernforschungsanlage Jülich GMbH (KFA) in West Germany.

The participants have conducted a series of fully reversed strain-controlled low-cycle fatigue tests on a single heat of solution annealed alloy 800H hot rolled bar stock provided by KFA. Testing was done at 850°C in air. The data are presently being compiled and will be reviewed before considering extension of the round-robin to include creep-fatigue and high-cycle fatigue.

Differences in fatigue life and hardening behavior (Figs. 4.6 and 4.7, respectively) have been observed which are larger than the scatter in the data of the individual laboratories. Similar comments have been received concerning the data generated in West Germany. The test results and data evaluation methods will be compared in detail on the basis of cycles to failure, cycles to crack initiation, hardening or softening curves and the shape of hysteresis loops.

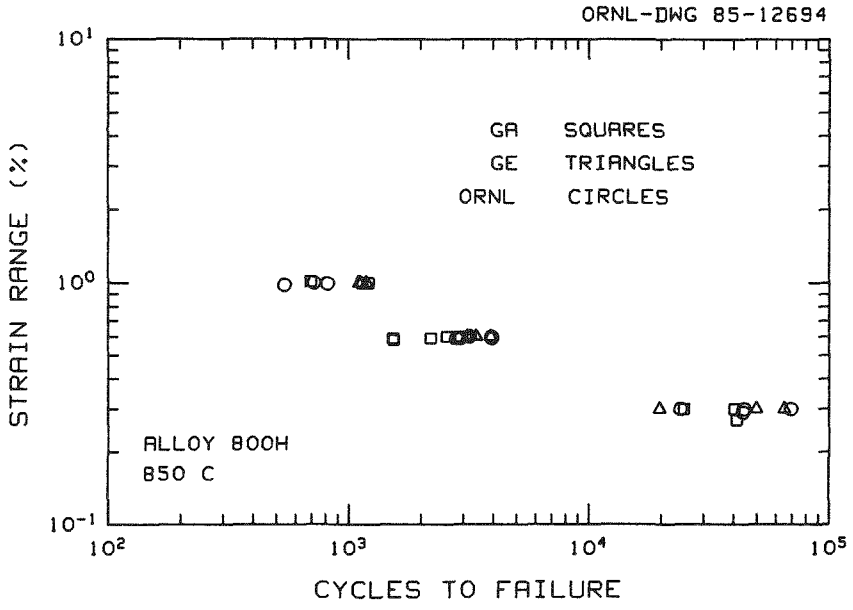

Fig. 4.6. Fatigue lives determined by U.S. participants in PWS M-1 round-robin.

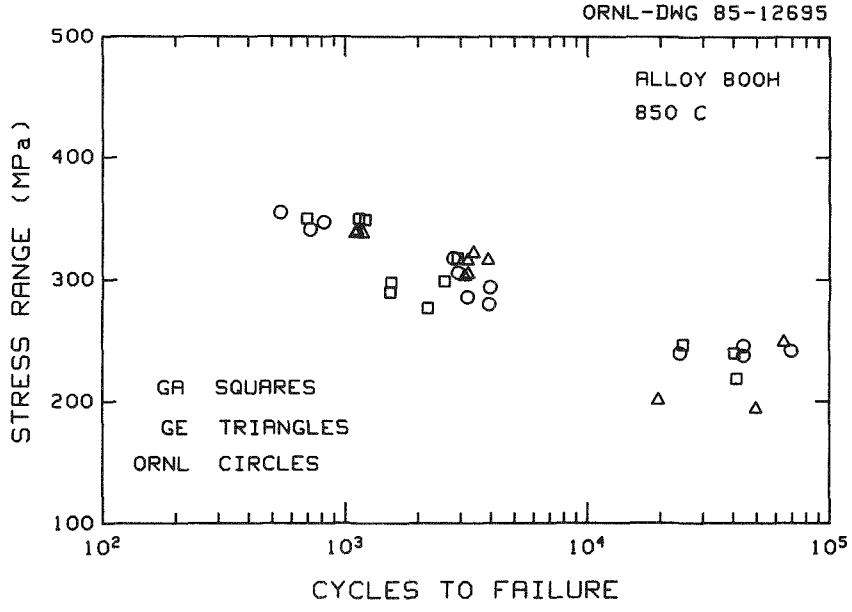

Fig. 4.7. Hardening behavior determined by U.S. participants in PWS M-1 round-robin.

4.4.3 Fracture Mechanics Round-Robin — J. P. Strizak and J. J. McGowan

Experimental variables such as specimen type, mode of test control, strain, load, and crack length measurement, strain rate, and test material are important factors in obtaining and evaluating J-integral R-curves. The objective of the subject round-robin under PWS M-5 is to compare and assess equipment and test methods being employed for J-integral testing, and evaluation procedures (e.g., compliance method, multi-specimen method, potential drop method, frame method, etc.) in the United States, West Germany, and Switzerland in order to recommend test practices, improved data confidence, and provide a basis for possible future cooperation in high-temperature fracture mechanics programs. GA Technologies, General Electric Company, and Oak Ridge National Laboratory are joined in this task by Gesellschaft für Hochtemperatur-Technik GmbH/Interatom GmbH (GHT/IA), Hochtemperatur-Reaktorbau GmbH (HRB), and Kernforschungsanlage Jülich GmbH (KFA) in West Germany, and Eidenössisches Institut für Reaktorforschung (EIR) in Switzerland.

Recently the participants conducted room temperature tests on a single heat of alloy 800H. The data will be compiled and reviewed before considering extension of the round-robin to elevated temperatures. Tests performed at ORNL are discussed below.

J-Integral fracture toughness specimens (1 TCS and 1/2 TCS)[4] were fabricated with the T-L orientation[5] from the alloy 800H provided by KFA. The specimens had 10% side groves on each side, and were tested in broad-line displacement control at a rate of 5 μm/s. The single-specimen unloading-compliance technique was used to determine the crack length change during the test. With this technique, small unloadings (~15% of the previous load) were performed at regular displacement intervals to determine the specimen elastic compliance. The crack length was then uniquely determined from the compliance. The load line displacement was measured with a strain-gage clip gage resting on knife edges. The J-Integral was calculated using the modified Ernst[6] procedure. The value of the fracture toughness was calculated from J_{Ic} using the equation $K_{Jc} = \sqrt{E\ J_{Ic}}$, and the tearing modulus (T_{avg}) was calculated from the

average slope of the J-Δa curve (dJ/da) between the 0.15 and 1.5 mm offset lines, and the equation

$$T = \frac{E}{\sigma_f^2} \frac{dJ}{da}$$

where E is the Young's modules and σ_f is the flow stress.

Two differing procedures were used to calculate J_{Ic} and T_{avg}. The first method used a linear regression of the J-Δa pairs between the 0.15 and 1.5 mm offset lines as proposed in ASTM Standard E-813.[4] The second method uses a power law fit to the J-Δa pairs up to the 1.5 mm offset lines as proposed by Loss.[7]

The results of the J-Integral tests are listed in Table 4.8. Note that the agreement is very good between the two size specimens, both for J_{Ic} and T_{avg}. However, the table also illustrates a large difference between the measured ductile crack growth (Δa_m) and the predicted ductile crack growth (Δa_p) from the unloading-compliance technique. This problem was likely caused by the large amount of arm bending and plasticity observed during testing. The specimen size was inadequate to measure the high toughness of the 800H material in the present material condition. The specimen measurement capacity (ASTM E-813) was J_{Ic} = 325 kJ/m^2 for the 25.4 mm-thick specimen and J_{Ic} = 165 kJ/m^2 for the 12.7 mm-thick specimen. However, the measured value of J_{Ic} was above 1000 kJ/m^2.

Table 4.8. Alloy 800H fracture toughness tests

Specimen	Test temperature (°C)	Thickness (mm)	Side groves (%)	$(a/W)_1$	Ductile Δa_m	Ductile $\Delta a_p - \Delta a_m$	J_{Ic} (kJ/m^2)		$K_{J_{Ic}}$ MPa$\sqrt{m}$		T_{avg}		Flow stress MPa	Yield stress MPa	Young's modulus GPa
							Power law	E-813	Power law	E-813	Power law	E-813			
800H3	24	25.4	20	0.623	5.060	−0.964	1061	1014	467	457	520	516	409	233	206
800H4	24	25.4	20	0.630	4.684	−1.087	1139	1104	484	477	480	475	409	233	206
800H9A	24	12.7	20	0.585	4.773	−0.594	1229	1136	503	484	495	507	409	233	206

4.5 REFERENCES

1. R. Moormann und K. Petersen, *REACT/THERMIX-Ein Computercode zur Berechung der storfallbedingten Graphitkorrosion in Kugelhaufenreaktoren*, Jül-1782, April 1982.

2. D. C. Elrod et al., "HEATING-6: A Multidimensional Heat Conduction Analysis with the Finite Difference Formulation, included in SCALE: A Modular Code System for Performing Standardized Computer Analyses for Licensing Evaluation," ORNL/NUREG/CSD-2, March 1978.

3. M. Schürenkramer, *Theoretische und experimentelle Untersuchungen der Naturkonvektion im Kern des Kugelhaufen-Hochtemperaturreaktors*, Jül-1912, April 1984.

4. "Standard Test Method for J_{Ic}, A Measure of Fracture Mechanics, E813-81," *Annual Book of ASTM Standards*, ASTM, 1984, Vol. 03.01, pp. 763–781.

5. "Plane-Strain Fracture Toughness of Metallic Materials, E399-81," *Annual Book of ASTM Standards*, ASTM, 1981, pp. 588–618.

6. H. A. Ernst, "Material Resistance and Instability Beyond J-Controlled Crack Growth," Elastic Plastic Fracture: Second Symposium, Volume I — *Inelastic Analysis*, ASTM, STP-803, 1983, pp. I-191 — I-213.

7. F. J. Loss,ed., "Structured Integrity of Water Reactor Pressure Boundary Components," Annual Report FY 1979, USNRC Report NUREG ICR-1128, 1979.

5. FUELS AND FISSION PRODUCT BEHAVIOR (WBS 1601)

M. J. Kania and W. P. Wichner

5.1 INTRODUCTION

The High Temperature Reactor (HTR) Fuel Materials Program and the Fission Product Performance Verification Program at ORNL continue as part of a national fuel and fission product development effort in cooperation with GA Technologies Inc. (GA). ORNL has been assigned, and has assumed the "Lead" Laboratory Role in this area based on recommendations from the DOE.

5.1.1 Fuel Materials Qualification Program — M. J. Kania

The Fuel Materials Qualification Program is conducted in close cooperation with GA. The ORNL portion is directed towards irradiation testing of GA-fabricated fuel in capsules designed and assembled at ORNL and operated in ORNL reactors. We also conduct extensive postirradiation examinations (PIE) on this fuel in special examination facilities developed for this purpose. The GA responsibilities include interface with core designers and development of fuel performance models with data derived from the irradiation tests at ORNL. GA Technologies also has the responsibility for fuel manufacturing, process development, and quality control.

In addition to the cooperation with GA, the ORNL fuels program includes specific cooperative tasks with the German Nuclear Research Center [Kernforschungsanlage (KFA)] at Jülich. The cooperation with KFA is part of the formal agreement between the U.S. and the West German (FRG) governments for gas-cooled reactor development. Only one active area of cooperation existed in the fuel development area during this year, and the work performed in this area is presented in Sect. 4.2 of this report.

5.1.2 Fission Product Transport and Behavior — R. P. Wichner

A series of tests were conducted to assess the utility of a thermal gradient tube (TGT) and to gain insight on the chemical forms of iodine and cesium vaporized from graphite. These tests illustrated the utility of the TGT under HTR test conditions.

It is necessary to know plutonium vapor pressure and the effective diffusion coefficient of plutonium in graphite to determine the rate and amount of plutonium transport to the coolant. A pellet transfer method, in which plutonium was supplied from a source pellet to a plutonium-free test pellet, was used to determine the diffusion coefficient in graphite. A plot of the plutonium profile in the test pellet provided a value for the diffusion coefficient.

5.2 IRRADIATION CAPSULE ASSEMBLY AND OPERATION — C. D. West

5.2.1 Hydrolysis Experiments HRB-17 and -18 — R. L. Senn and M. J. Kania

Irradiation of the two capsules, HRB-17 and -18, was placed on "Hold" in September 1984 by DOE until further justification for the hydrolysis experiment was completed. This experiment, described in a previous progress report[1] was designed to evaluate the performance of failed reference HTR-SC/C fuel when subjected to moisture levels simulating various water ingress events. In a reactor operating environment, fissile UCO kernel material undergoes hydrolysis when subjected to moisture; this results in a substantial increase in fission gas release. Progress during 1984 included completion of capsule fabrication, fuel loading, and final assembly of HRB-17 and -18; quality assurance and quality control (QA/QC) documentation; plus completion and initial checkout of moisture generation-injection and gas analysis systems.

Prior to termination of efforts in September, installation of the capsule control and monitoring instrumentation had begun at the HFIR site. These instruments have been stored for future use. The completed capsules also remain in storage.

5.2.1.1 Capsule Fabrication and Assembly

Fabrication, fuel loading, and final assembly of the two capsules for this experiment were completed in June 1984. Each capsule is as identical as possible and contains the following test materials:

- six fuel rods, each "seeded" with five test UCO particles designed to fail within the first irradiation cycle,
- one Incoloy-clad unbonded particle tray experiment,
- one niobium-clad graphite diffusion sample experiment, and
- piggy-back samples consisting of niobium-encapsulated UCO particles or short silver dosimeter wires.

An audit was conducted in July 1984 in the areas relating to the QA/QC implementation of management, design, procurement, fabrication, installation, and modifications. In the opinion of the auditor, the Engineering Technology Division (ETD) engineering staff had met all essential requirements in accordance with the ORNL Quality Assurance Program.

5.2.1.2 Moisture Generation and Gas Analysis Systems

Operation and routine testing of the moisture generation-injection system indicated discrepancies in measurements between the capacitance-type and electrolytic-type moisture analyzers in the system. They were not in agreement nor did they agree with the dew point of the gas stream based on moisture generator temperature. To eliminate this, a thermocouple was placed directly within the saturated gas stream in order to provide a more accurate temperature measurement as the basis for the dew point. This temperature was then closely calibrated with the response of the electrolytic-type moisture analyzer using known gas samples. The capacitance-type moisture analyzer will remain in the system, but this instrument will be used only as a prompt warning if the moisture system becomes unstable. This instrument provides a relatively fast response.

The gas chromatograph and accompanying SpectraPhysics integrator, which serve as the gas analysis system, have been operated successfully with neon/helium sweep gas mixtures simulating in-reactor operation. The problem with accurate hydrogen detection and measurement was resolved by

returning to the palladium probe that had been originally procured for this measurement. By moving the probe to the gas chromatograph offgas stream and by correcting a small leak and some unstable electronics, the detector now provides a satisfactory measurement of hydrogen content.

In August 1984, the instrumentation for the moisture generation-injection system and the gas analysis systems was moved to the HFIR site for installation. Installation of these systems with sweep gas flow lines and reactor control and monitoring instrumentation also began in August. This work was superseded in September, and all the instrumentation stored for subsequent use.

5.3 POSTIRRADIATION EXAMINATION OF IRRADIATION EXPERIMENTS

Efforts have concentrated on GA-fabricated fuels irradiated in capsules HRB-16 and R2-K13, German fuels irradiated in experiments FRJ2-P23, FRJ2-P25, and DR-S6 (see Section 4.2), and ORNL-fabricated fuels irradiated in capsule HT-35. In addition, a final report was prepared that documents the postirradiation examination (PIE) results obtained on a variety of advanced HTR particle designs utilizing ZrC coatings. At the end of this report period, only the German irradiated fuels from Set 3 under the US/FRB cooperative agreement remained in PIE at the High-Radiation Level Examination Laboratory (HRLEL).

5.3.1 Capsule HT-35 — M. J. Kania

Irradiation experiment HT-35 was designed to answer a number of questions relating to HTR fuel performance that arose during the post-irradiation examination (PIE) of fuel from previous experimental capsules. Capsule HT-35 was a joint ORNL and GA test and was irradiated for a total of 2140.5 h of full reactor power (100 MW) between August 17, and November 19, 1980.

Capsule HT-35 has received a very low priority during the PIE phase because of its emphasis on Biso-coated fuel and the fact that this type of coating has not been of interest to the HTR Program since 1981. All planned examinations are now complete on the fuel from this capsule and in

most cases the results have been reported previously. A detailed description of the capsule design and operating history were reported in a previous progress report.[2] Capsule disassembly and meterology of the graphite and fuel components have also been reported.[3] Examination of the SiC coatings from inert (carbon) particles before and after irradiation using Transmission Electron Microscopy (TEM) have also been reported.[4] Similar TEM examinations on the SiC coatings removed from irradiated fuel particles, along with fission product retention investigations using IMGA[5] were reported in a previous annual report.[6]

The results of the examinations addressed two specific objectives of capsule HT-35. They were:

- Objective 1: assess the irradiation performance of Biso-coated fertile particles with PyC coatings deposited in the 0.13-m-diam furnace using standard coating gases diluted with CO_2, and
- Objective 2: compare the irradiation performance of dense UC_xO_y - kernels with the performance of Weak-Acid Resin derived (WAR) Uc_xO_y kernels in Triso-coated particles.

5.3.1.1 Objective 1: Irradiation Performance of CO_2 Diluted Coatings

Prior to capsule HT-35, good irradiation performance had been observed with a single batch of particles (OR-2013) that was fabricated in a laboratory-scale (2.5 cm-diam) coating furnace using CO_2 as a diluent for the coating gas. The reason for the favorable performance relative to other batches irradiated in the same capsule was never fully understood. Thus, part of the development portion of the ORNL Fuels Program included a careful study of the fabrication parameters associated with such coatings.[7] Some of these particle batches were included in HT-35 to assess their irradiation behavior. The excellent performance of the previous batch OR-2013, in capsules HT-18 and HT-19,[8] was based solely on visual examination. A small number of particles from this batch, irradiated in capsule HT-34, showed the same excellent performance relative to visual observations. However, PGA examinations[9] showed that fission gas retention was

not better than with other particle batches fabricated without using the CO_2 diluent. In addition, PyC deposition studies[7] on these coatings showed no apparent advantage with this fabrication technique.

Nine different Biso-coated fertile particle batches from capsule HT-35 were examined for fission gas content using the PGA device to assess their irradiation performance. All of the batches were selected from the two high-temperature, high-fluence magazines of the capsule. Four batches (A-914, A-915, A-919, and A-935) were fabricated using the CO_2 diluent, and the remaining five batches were fabricated using standard procedures. Gas inventories for the stable fission gas isotopes ^{84}Kr, ^{86}Kr, ^{134}Xe, and ^{136}Xe were measured on four to six particles from each batch. A comparison of the total krypton and xenon gas inventories, measured for the CO_2 diluted versus the non-CO_2 diluted particles, are shown in Figs. 5.1 and 5.2, respectively. The irradiation positions shown are symmetric to the reactor horizontal midplane (HMP) with respect to temperature, fertile burnup, and neutron fluence accumulation[2] (i.e., position 24 is equivalent to position 29, 23 to 30, 21 to 32, and 20 to 33).

As illustrated in the two figures, both the total krypton and total xenon inventories for the CO_2 diluted PyC coatings are, on the average, nearly twice the values for the non-diluted coatings. This is consistent at all the equivalent irradiation positions. The shaded regions in each figure represent calculated gas inventories based on cesium inventory data provided for each particle batch. The cesium measurements were performed with the IMGA system prior to the PGA measurements. The model, which is used for estimating stable fission gas inventory released from the fertile kernel, is based on empirical data from Biso-coatings fabricated without CO_2 dilution. With few exceptions, the diluted particle contained fission gas inventories greater than predicted. Those particles that exhibited krypton inventories less than predicted, as shown in Fig. 5.1, also contained lower than predicted xenon inventories, as shown in Fig. 5.2.

5.3.1.2 Objective 2: Dense UC_xO_y versus WAR UC_xO_y Kernel Performance

A comparison of the irradiation performance of the dense UC_xO_y fissile fuel kernels with that of the WAR derived UC_xO_y kernel was initially undertaken to assist in the selection of a reference fissile fuel kernel.

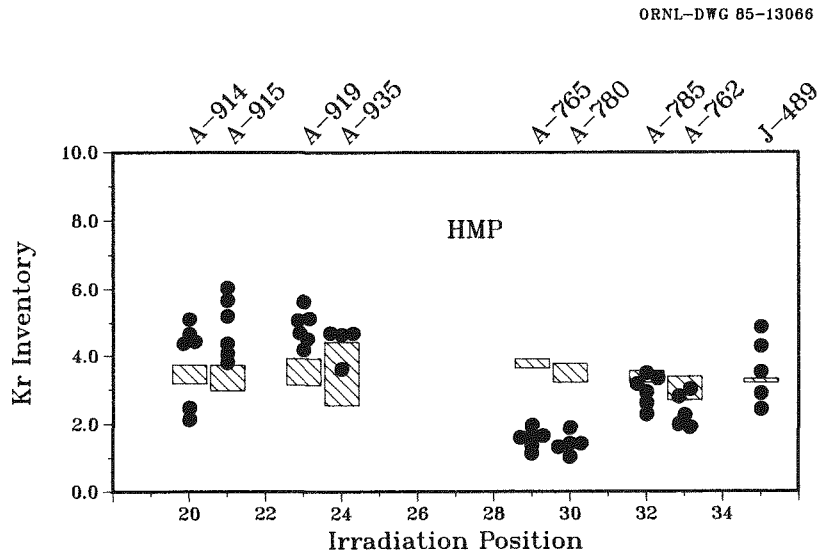

Fig. 5.1. Krypton gas retention in biso-coated ThO_2 particles irradiated in capsule HT-35.

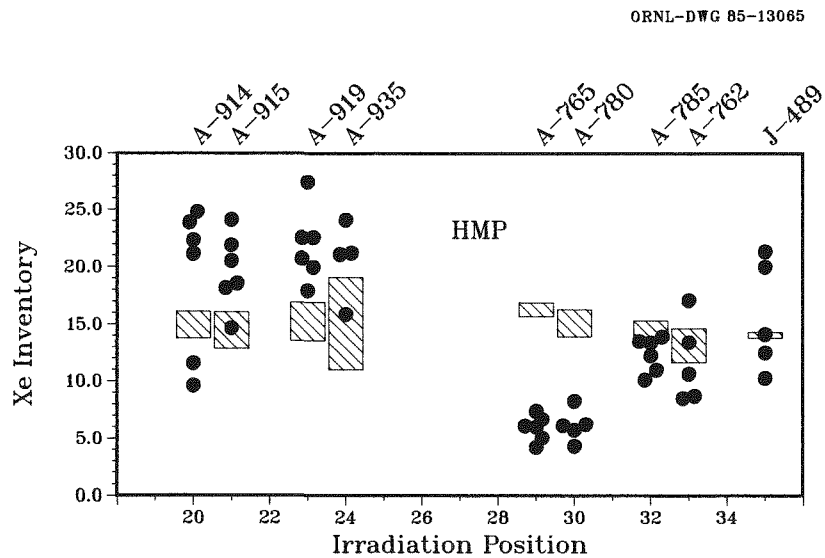

Fig. 5.2. Xenon gas retention in biso-coated ThO_2 particles irradiated in capsule HT-35.

This comparison is somewhat academic at this time, since dense UC_xO_y was chosen as the reference fissile fuel for the LEU/Th fuel cycle for the HTGR-SC/C lead plant.[10]

Particle batch A-976 was the first test batch of dense UC_xO_y fissile kernels, fabricated in a 0.13 m-diam coating furnace, to be included in an irradiation experiment. The 7% enriched fissile kernel material for this batch had a preirradiation density of 10.98 Mg/m^3 compared to about 3.5 Mg/m^3 for the WAR kernels. All particles of test batch A-976 were irradiated in bonded fuel rod specimens located in six irradiation positions (three in high-temperature region and three in the low-temperature region). After irradiation all six fuel rods were electrolytically deconsolidated to obtain unbonded particles for further PIE.

Unbonded particles from irradiation position 31 in the high-temperature region and 44 in the low-temperature region were metallographically examined. Figure 5.3 exhibits the typical appearance of batch A-976 particles from position 31. The kernel material of the two particles in Figs. 5.3(a) and 5.3 (b) appears very similar to high-burnup UO_2 kernels with the characteristic formation of large fission gas bubbles. Particles in this position achieved a burnup of 20.4% FIMA and a neutron fluence of 8.64×10^{25} neutrons/m^2. Time averaged operating temperatures were 1295°C for the rod centerline, and 1195°C for the rod surface. Both particles show significant kernel swelling, and kernel migration is evident. This is characterized by the position of the kernel next to the inner-PyC coating layer in the particle shown in Fig. 5.3(a). In each particle, a significant amount of fission product attack of the SiC coating was noted. This is exhibited in the high magnification (500×) views in Figs. 5.3(c) and 5.3(d). In both particles, the area of fission product attack extend more than half-way through the nominal 35 μm-thick SiC layer. No electron microprobe examinations were conducted on these particles; however, the appearance of the SiC attack is similar to that observed due to the fission product palladium.[11]

The appearance of batch A-976 particles irradiated in position 44, illustrated in Fig. 5.4, were much different than those irradiated in

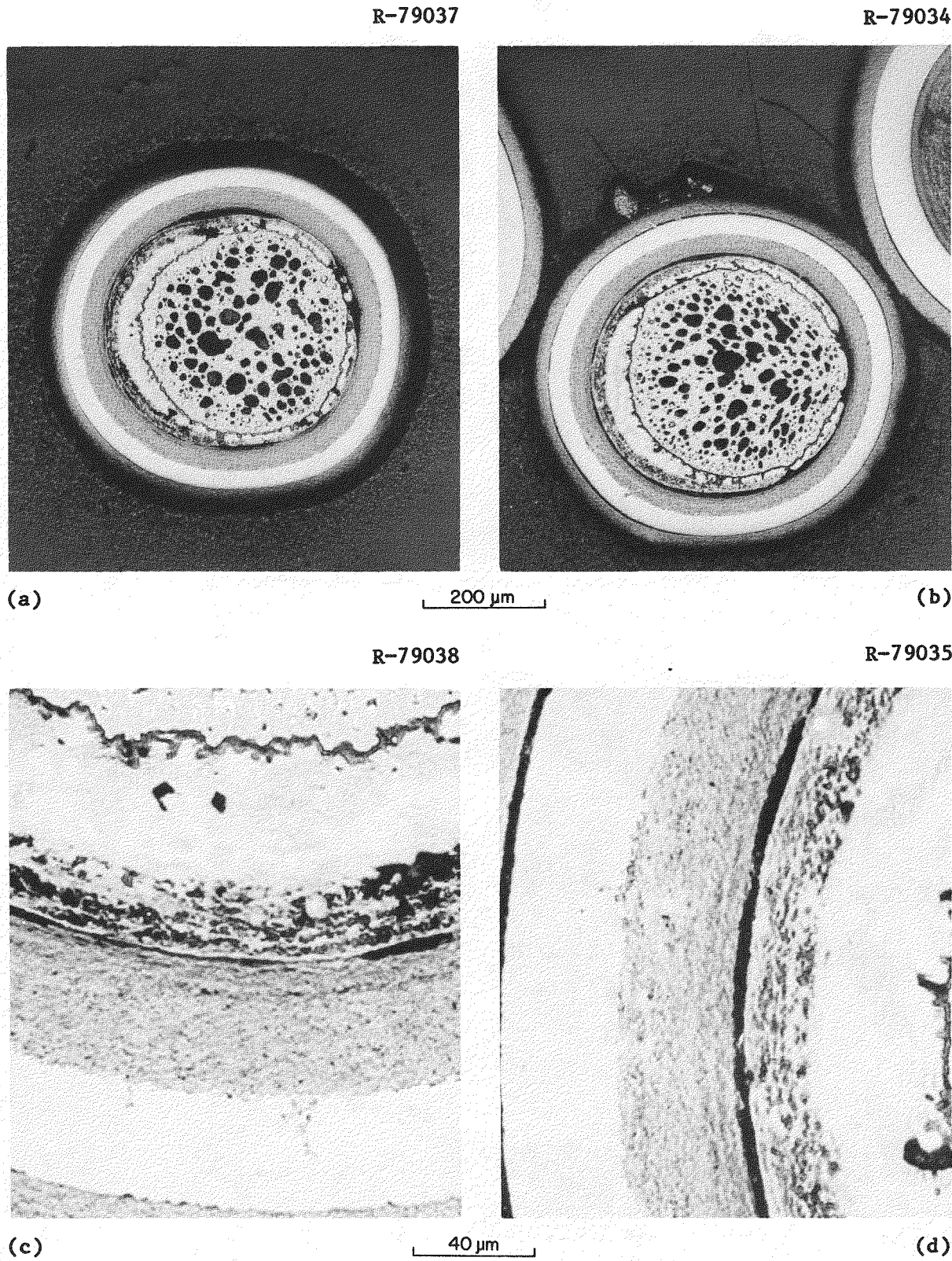

Fig. 5.3. UC_xO_y Triso-coated particles irradiated in high-fluence, high-temperature region, position 31, of capsule HT-35.

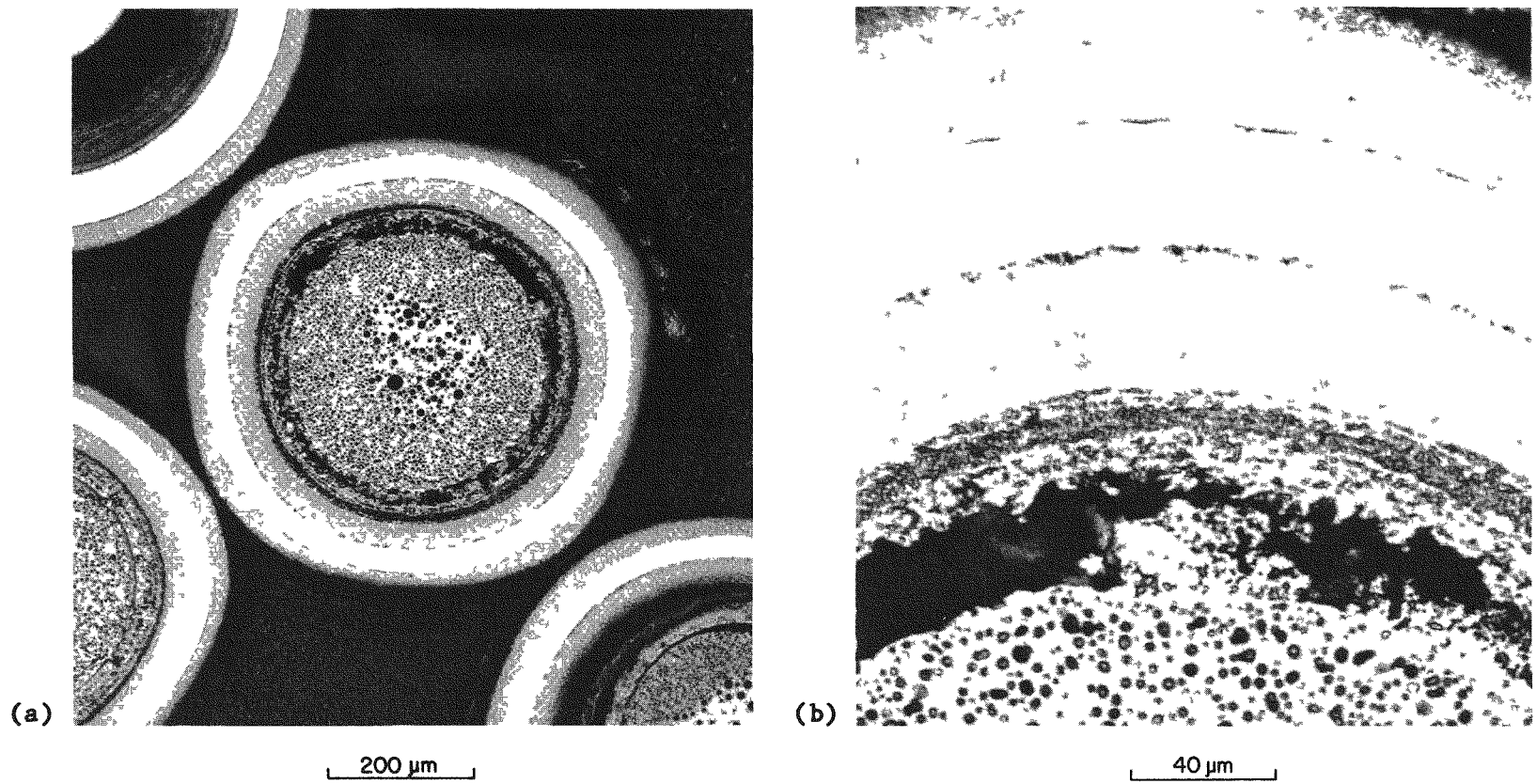

Fig. 5.4. UC_xO_y triso-coated particle irradiated in low-fluence, low-temperature region, position 44, of capsule HT-35. (a) Typical particle appearance. (b) Silicon carbide layer.

position 31. Fuel from position 44 achieved a burnup of 16.3% FIMA and accumulated a neutron fluence of 6.17×10^{25} neutrons/m^2. Time averaged fuel rod centerline and surface temperatures were 1010°C and 915°C, respectively. The fuel particle shown in Fig. 5.4(a) is typical of the appearance of all particles from this low-temperature irradiation position. Large numbers of small gas bubbles were present throughout the kernel in contrast to the kernel appearance in Fig. 5.3(a). This is most likely due to the higher burnup and the 200°C higher irradiation temperature in position 31 compared to position 44. No evidence of kernel migration was present. Figure 5.4(b) shows the typical appearance of the SiC layer for the particles from position 44. No evidence of fission product attack of the SiC layer was observed in any of the particles examined.

Figure 5.5 shows a comparison of an irradiated WAR derived kernel from capsule HRB-10[12] and a dense UC_xO_y kernel from HT-35. The difference in appearance of the two kernels is quite dramatic. Both were UC_xO_y initially, but the WAR kernel had a density of 3.7 mg/m^3 compared to the dense UC_xO_y kernel with a density of 10.98 mg/m^3. The irradiation temperatures of both particles were nearly the same, 1290°C and 1250°C; however, the burnup of the HEU WAR kernel was 80.4% FIMA and the LEU UC_xO_y kernel achieved only 20.4% FIMA. Both kernels exhibited kernel migration and some SiC-fission product interaction.

As indicated, all planned PIE work for the fuels irradiated in capsule HT-35 has been completed. Work is now in progress to complete the final report on this last in the HT-series of irradiation experiments.

5.3.2 Capsule HRB-15A — M. J. Kania

Capsule HRB-15A was designed to evaluate the irradiation performance of a variety of reference and experimentally coated particle fuel types to peak irradiation conditions expected in a large HTGR. The final report[13] describing this irradiation capsule has been completed by GA. The abstract of that report is provided as follows:

R-78767

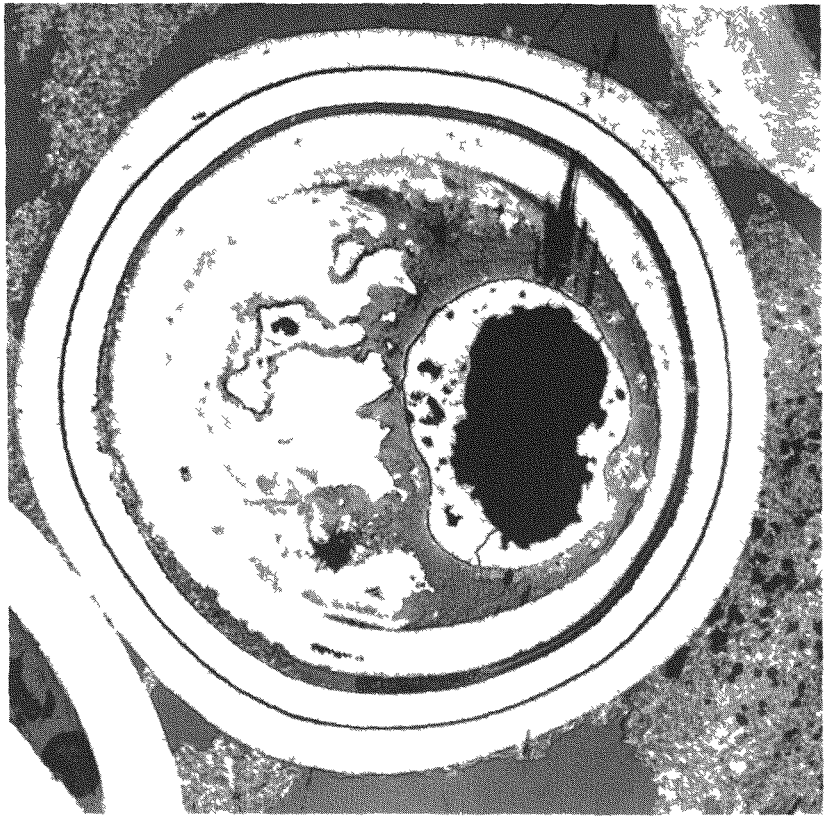

(a)

R-69574

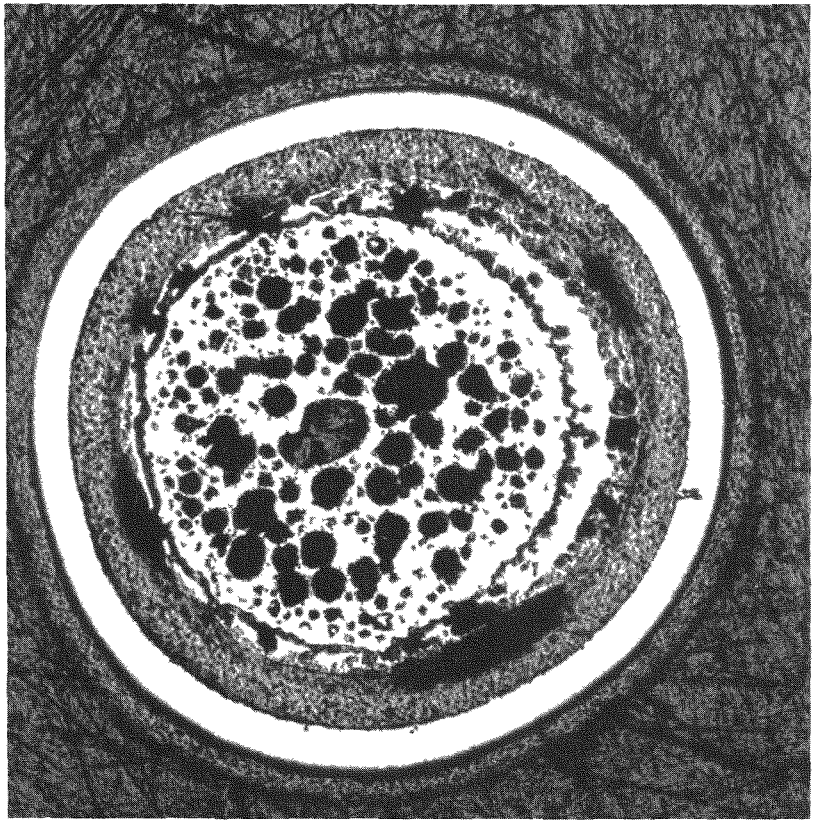

(b)

Fig. 5.5. Comparison of the appearance of an irradiated WAR derived HEU kernel from capsule HRB-10. (a) With a dense LEU UC_xO_y kernel from capsule HT-35. (b) In text.

Capsule HRB-15A, carried out jointly by GA Technologies (GA) and Oak Ridge National Laboratory (ORNL), successfully irradiated a variety of LHTGR reference and experimental fuel particle types to peak exposures of 6.5×10^{25} n/m^2 $(E > 29fJ)_{HTGR}$ fast fluence, 29% FIMA fissile burnup and 6.4% FIMA fertile burnup, and a time-average irradiation temperature of ~1100°C. The capsule was irradiated in ORNL's High Flux Isotope Reactor for ~6 months in 1980 and early 1981, followed by an extensive post-irradiation examination involving equipment and expertise at both GA and ORNL. Some of the conclusions reached as a result of the HRB-15A irradiation are these:

1. The HRB-15A fuel rods were in excellent condition following irradiation. Their integrity was good, with little to no debonding, cracking or chipping.
2. Candidate TRISO-coated LEU $UC_{0.5}O_{1.5}$, UC_2, UO_2 and UO_2^* fuel particles performed adequately for the HTGR steam cycle application.
3. The SiC coatings on the two $UC_{0.5}O_{1.5}$ TRISO batches in HRB-15A were least retentive of ^{110m}Ag during irradiation in comparison to other TRISO fissile particle types. Ceramographic results showed that severe degradation of the SiC layers by fission product attack had occurred in 70% of these particles with much deeper penetration than in other TRISO batches. No preirradiation processing anomalies or postirradiation microstructural defects that would explain the relatively poor performance of the SiC layers on these particles were identified.
4. Large diameter (nominal 600 μm kernel) ThO_2 particles tested in HRB-15A were judged unacceptable for use in an all-TRISO separable fuel system because of high PyC and SiC failure levels.
5. ZrC barrier layers in two ZrC-TRISO-coated fissile particle batches in HRB-15A showed superior resistance to chemical attack by fission products compared to that of SiC. However, one of the ZrC-TRISO batches was poorly retentive of silver and europium, and fuel rods containing both batches had the highest end-of-life fission gas release values.
6. Performance models for defective particles were shown to be overly conservative by results on faceted and thin buffer ThO_2 particles in which less than 2% pressure vessel failure was observed in the latter type compared to predictions of 20—35%. Consistent with these results and other irradiation data, a new assumed SiC strength of 350 MPa (51 ksi) is currently in use in the TRISO pressure vessel performance models.

7. The failure rate of OPyC coatings on TRISO particles in HRB-15A was found to increase as the particle diameter increased, exceeding Weibull theory estimates by roughly 30%. For a fast fluence of 6.4×10^{25} n/m^2 (E > 29 fJ)$_{HTGR}$ at 1130°C nominal irradiation temperature, the OPyC failure level increased from zero at approximately 600 μm total particle diameter to about 26% at 1014 μm.

5.3.3 Capusle HRB-16 — M. J. Kania, G. A. Moore, L. G. Shrader, and N. M. Atchley

Capsule HRB-16 was discharged from the HFIR on December 23, 1981, after completing an 8-cycle irradiation for nearly 4082 h of full reactor power (100 MW). All fuel irradiated in this capsule was fabricated by GA. The capsule was shipped to the HRLEL for disassembly and detailed PIE. A selected number of fuel rods and unbonded particles from Tray-positions were returned to GA for examination. Full capsule disassembly including graphite component and fuel meterology, capsule and graphite sleeve gamma spectrometry, and photographic documentation were completed.[14] A total of six fuel rods were subjected to an electrolytic deconsolidation and the fuel from four of these rods were examined with the IMGA system, the PGA, and with selected metallography. An additional seven fuel rods were used for detailed metallographic examinations. A summary report documenting the work performed at ORNL was prepared and provided to GA. The final report on the HRB-16 irradiation experiment will be prepared by GA.

Six HRB-16 fuel rods (1, 4, 12, 15, 17, and 18) were electrolytically deconsolidated to recover unbonded particles for IMGA and PGA examinations. Analysis of the electrolyte solutions revealed excessive quantities of uranium present for a number of the rods. A close examination of the unbonded particles did not exhibit excessive chemical attack on a large number of failed coatings in the questionable sets of particles. These observations, together with the IMGA and PGA results suggested that the high concentration of uranium was most likely due to contamination.

IMGA examinations were conducted on a variety of unbonded fissile and fertile particles. Fuel types examined were LEU UO_2^* fissile from rods 1, 4, and 12, and LEU UCO fissile from rod 17, ThO_2 fertile particles from rods 4, 12, and 17, the HEU mixed oxide $(Th,U)O_2$ particles from trays 10, 11, and 12, and the HEU UC_2 fissile from tray 20. Particle batch types

contained in each irradiation position with the number of particles examined from each position are provided in Table 5.1. In addition, a small number (10 to 12) of particles from each set were reexamined with IMGA prior to fission gas inventory measurements with the PGA system.

Table 5.1. Unbonded particles irradiated in fuel rods and loose particle trays of capsule HRB-16 examined and analyzed with IMGA

Position	Kernel-coating batch	Number of particles
	Fissile particles	
Rod 1	UO_2^*-Triso/6152-06-010	640
Rod 4	UO_2^*-Triso/6152-04-010	289
Rod 12	UO_2^*-Triso/6152-03-010	453
Rod 17	UCO-Triso/6157-11-010	439
Tray 10	$(Th,U)O_2$-Triso/6155-01-030	72
Tray 11	$(Th,U)O_2$-Triso/6155-01-030	85
Tray 12	$(Th,U)O_2$-Triso/6155-01-030	90
Tray 20	UC_2-Triso/6161-23-020	108
	Fertile particles	
Rod 4	ThO_2-Triso/6252-12COMP	1088
Rod 12	ThO_2-Triso/6252-12COMP	661
Rod 17	ThO_2-Triso/6262-12COMP	1088

Analysis of the fissile particle performance for capsule HRB-16 was derived from the ^{137}Cs:^{106}Ru activity ratio distributions. A summary of this analysis is presented in Table 5.2. Failed particles were indicated by low ^{137}Cs inventory as compared to ^{106}Ru inventory. The data describe the number of particles examined, number failed, mean failure fraction (number failed/number examined), and the failure fraction at the 95% confidence level. The UO_2^* fissile particle (ZrC-buffered UO_2 fuel kernels)

Table 5.2. Irradiation performance of fissile fuel particles from fuel rod positions 1, 4, 12, and 17 of capsule HRB-16

Fuel rod/ kernel	Number examined	Number failed	$^{137}Cs:^{106}Ru$ Ratio		Failure fraction	
			Measured	Calculated	Mean	η(95%)
$1/UO_2^*$	640	0	1.779×10^{-1}	1.784×10^{-1}	0	4.7×10^{-3}
$4/UO_2^*$	289	0	1.301×10^{-1}	1.349×10^{-1}	0	1.0×10^{-2}
$12/UO_2^*$	453	1	1.019×10^{-1}	1.165×10^{-1}	2.2×10^{-3}	1.0×10^{-2}
17/UCO	439	8	1.265×10^{-1}	1.479×10^{-1}	1.8×10^{-2}	3.5×10^{-2}

irradiated in fuel rod 1 exhibited the best performance. The mean measured failure fraction was 0% since no failures were detected in 640 examinations. This yielded a failure fraction of 0.5% at the 95% confidence level. Fissile fuel from the other three fuel rods exhibited failure fractions in the range of 1 to 3.5% at the 95% confidence level. The reference UCO particle design irradiated in rod 17 had the poorest performance with a failure fraction of 3.5%. In rod 4, no failed UO_2^* were detected, but the particle population size of 289 limited the failure fraction to about 1% at the 95% confidence level.

Silver retention studies were conducted on the UO_2^* and UCO fissile particle types from rods 12 and 17, respectively. Large within batch particle to particle variations were observed with the UCO fuel but not with the UO_2^* fuel. Silver retention, comparing the measured to calculated inventories of isotope ^{110m}Ag, was only at the 50 to 60% level for the best performing UO_2^* particles. This was attributed to uncertainties in the inventory calculations rather than to failed particles. In the case of the UCO particles, mean retention was only at the 27% level and this was attributed to the condition of the SiC coating relative to fission product attack. Figure 5.6 describes the cesium and silver retention data obtained on the two fuels studied. For both fuels, cesium retention is very high and exhibits very small within batch variation in measured inventories.

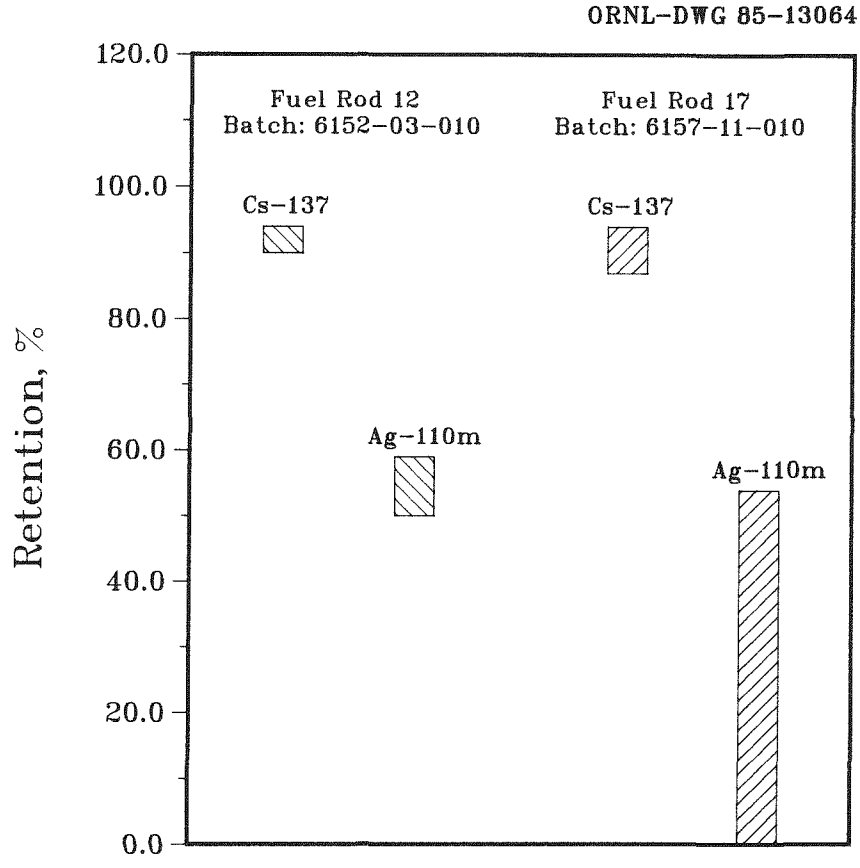

Fig. 5.6. Within batch particle-to-particle variation in ^{110m}Ag and ^{137}Cs retention for UO_2^* Triso-particles from rod 12 compared to UCO Triso-particles from rod 17 irradiated in capsule HRB-16.

A performance analysis was also performed on the fertile particles based on the ^{137}Cs:^{106}Ru activity ratio distribution obtained from particles from rods 4, 12, and 17. A total of 2837 fertile particles were examined from the three rods and only one particle, from rod 17, was classified as failed. The calculated failure fraction with a 95% confidence level was 1.6×10^{-3}, and the mean measured failure fraction was 3.5×10^{-4}. A summary of fertile particle performance assessment is shown in Table 5.3.

PGA fission gas release measurements were conducted on failed and non-failed particles from fuel rods 4, 12, and 17, and from particle trays

Table 5.3. Irradiation performance of fertile fuel particles from fuel rod positions 4, 12, and 17 of capsule HRB-16

Fuel rod/ kernel	Number examined	Number failed	$^{137}Cs:^{106}Ru$ ratio		Failure fraction	
			Measured	Calculated	Mean	η(95%)
4/ThO_2	1088	0	8.555×10^{-1}	8.942×10^{-1}	0	$<2.7 \times 10^{-3}$
12/ThO_2	661	0	8.530×10^{-1}	8.378×10^{-1}	0	$<4.5 \times 10^{-3}$
17/ThO_2	1088	1	8.849×10^{-1}	9.230×10^{-1}	9.2×10^{-4}	$<1.6 \times 10^{-3}$

10, 11, 12, and 20. (Failed particles were recovered only in rod 17 and trays 11 and 12.) Fission gas release data on fuel particles exhibiting significant cesium release were within range of values recorded for non-failed particles. Such data were recorded for particles with outer PyC coatings as well as for particles with the outer PyC coatings removed. These results indicate differences in failed fuel fractions based on gaseous fission product release, such as in-reactor R/B measurements, and fractions derived from metallic fission product release, based on gamma spectrometry results.

Metallography examinations did not reveal any unexpected irradiation behavior. The behavior of fissile fuel kernels and fission products during irradiation followed trends observed in previous capsule experiments. Oxide kernels without a ZrC-buffer coating exhibited kernel migration; however, the rare earth fission products were retained. Carbide kernels were not observed to migrate; however, they did not retain their rare earth fission products. The addition of the ZrC layer on the UO_2 kernel was effective in eliminating kernel migration. Severe SiC corrosion was observed in the UCO particles in all fuel rods examined. This corrosion was characteristic of the chemical attack produced by the fission product palladium as shown in Fig. 5.7. This conclusion was based on metallography results since no electron microprobe examinations were performed on the HRB-16 fuel.

R-79421

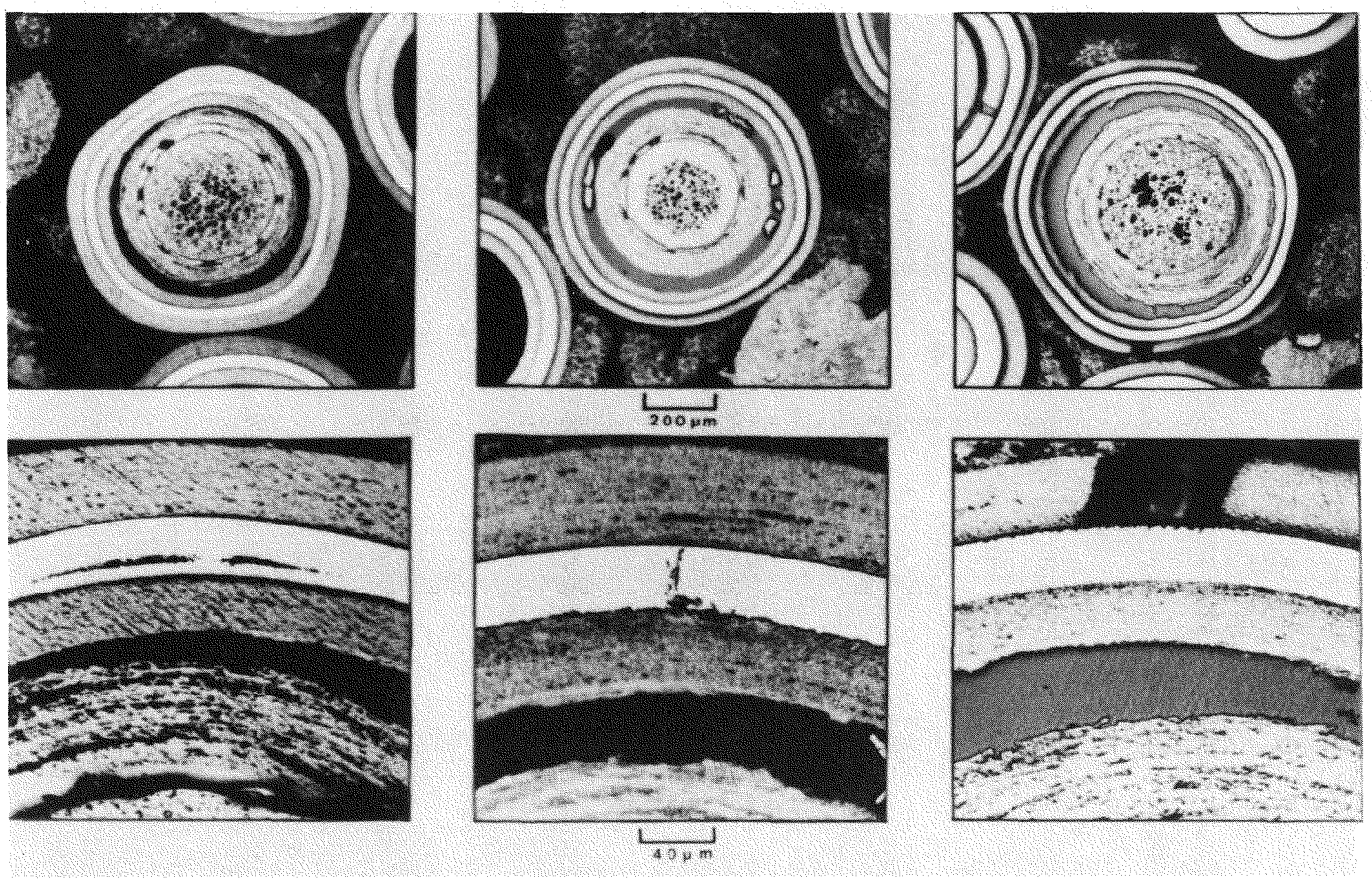

Fig. 5.7. UCO fissile particles irradiated in fuel rod 6 of capsule HRB-16 to a burnup of 26% FIMA and an accumulated fluence of 5.6×10^{25} neutrons/m^2.

Generally, the UO_2^* fissile particle types appeared to have the best irradiation performance in capsule HRB-16, and the UCO fissile particle type exhibited the poorest performance. The UCO fissile particle batch tested in this capsule was fabricated in production-scale equipment and in production-size batches. All other fissile particle batches were fabricated in laboratory-scale equipment. The majority of the evidence presented indicated that fuel performance was more closely related to coating performance than to fuel kernel type. Palladium attack, based on metallographic examinations, was more extensive in SiC coatings from the UCO particles than any other of the fissile fuel type tested.

5.3.4 Capsule R2-K13 — M. J. Kania and G. A. Moore

Irradiated fuel rods 2B2 and 3A1 from capsule R2-K13 containing GA fabricated fuel were subjected to detailed PIE at ORNL. Each fuel rod was first subjected to a 25 h acid leach to determine the number of particles with total coating failure. The measured thorium and uranium concentrations together with individual fissile and fertile particle burnups were used to estimate this number. The previously reported results[15] are summarized in Table 5.4. For fuel rod 2B2, which maintained a mean operating temperature of 1190°C, the number of particles having total coating failure at EOL represented 1.4% of the fissile fuel and 0.4% of the fertile fuel. For rod 3A1, with a mean operating temperature of 985°C, approximately 0.3% of the fissile fuel and 0.1% of the fertile fuel had particles with total coating failure.

Table 5.4. Summary of 25 h acid leach results for fuel rods 2B2 and 3A1 irradiated in capsule R2-K13

Fuel rod	Batch	Number of particles		Particles with total coating failure (%)
		Total	Failed	
		Fertile particles		
2B2	6252-12COMP	716	3.0	0.42
3A1	6252-12T 04 B2	706	0.8	0.11
		Fissile particles		
2B2	6157-11-020	1363	19.7	1.44
3A1	6157-11-020	1364	4.5	0.33

Both fuel rods were subjected to an electrolytic deconsolidation after the acid leach. The unbonded fissile and fertile particles obtained from the deconsolidation were used in the IMGA analysis. Analysis of the electrolyte solution revealed a large actinide concentration (uranium and thorium) for fuel rod 2B2, while only detection level concentrations were recorded for the sample from rod 3A1. Based on EOL burnup in rod 2B2, the actinide concentration represented 4.3 ± 1.1 fertile particles (0.6% of total number) and 235 ± 25 fissile particles (17.2% of total number). Both values were much higher than indicated by the 25 h acid leach results.

Results of the IMGA analysis on the fissile particles are shown in Table 5.5 for specific fission product activity and fission product activity ratios. Shown are a summary of the IMGA measurements along with the calculated activities and ratios provided by KFA-Jülich.[16] Both fuel rods contained the same Triso-coated UCO fissile particle batch 6157-11-020. Activity ratio histograms for ^{134}Cs:^{106}Ru, ^{137}Cs:^{106}Ru, and ^{134}Cs:^{137}Cs measured on the total particle population examined are provided in Fig. 5.8 for rods 2B2 and 3A1.

Table 5.5. Fission product activities and activity ratios measured on fissile particles from fuel rods 2B2 and 3A1 irradiated in capsule R2-K13

Isotope	IMGA derived activity[a] (Bq)		KFA calculation (Bq)
	Minimum	Maximum	Mean
Rod 3A1 (1115 particles examined)			
^{134}Cs	7.75×10^{6}	2.78×10^{7}	1.08×10^{7}
^{137}Cs	3.91×10^{6}	1.50×10^{7}	5.64×10^{6}
^{106}Ru	1.74×10^{7}	5.52×10^{7}	2.61×10^{7}
^{134}Cs:^{106}Ru	4.05×10^{-1}	5.03×10^{-1}	4.14×10^{-1}
^{137}Cs:^{106}Ru	2.03×10^{-1}	2.72×10^{-1}	2.16×10^{-1}
^{134}Cs:^{137}Cs	1.85	2.05	1.91
Rod 2B2 (962 particles examined)			
^{134}Cs	1.98×10^{5}	3.08×10^{7}	1.16×10^{7}
^{137}Cs	1.32×10^{5}	1.47×10^{6}	5.75×10^{6}
^{106}Ru	1.13×10^{7}	9.24×10^{7}	$^{2\sim70} \times 10^{7}$
^{134}Cs:^{106}Ru	1.13×10^{-2}	8.64×10^{-1}	4.30×10^{-1}
^{137}Cs:^{106}Ru	6.40×10^{-3}	3.77×10^{-1}	2.13×10^{-1}
^{134}Cs:^{137}Cs	1.47	2.34	2.02

[a]Activity ratios presented have dimensions Bq/Bq.

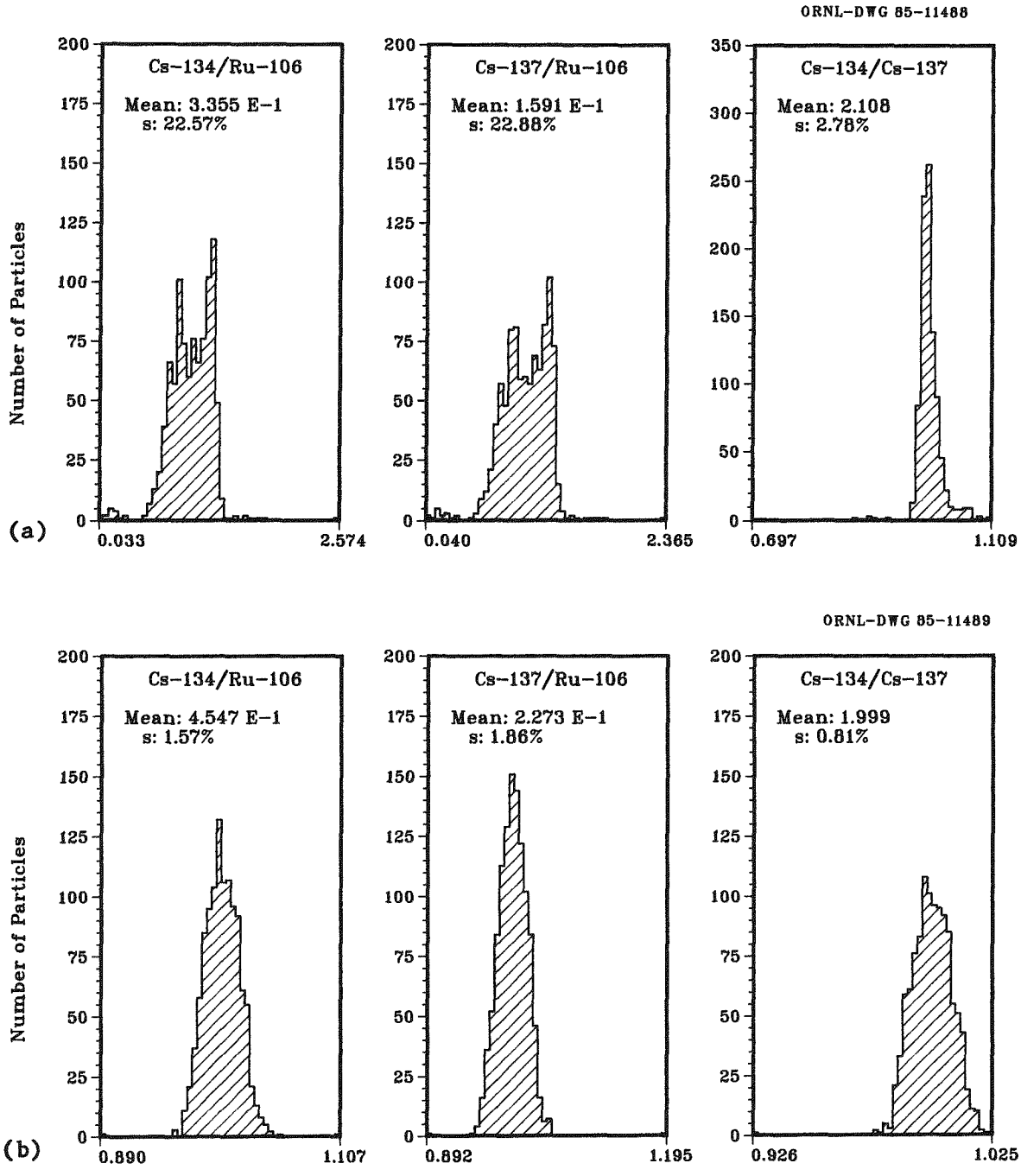

Fig. 5.8. Activity ratio histograms derived from the IMGA examination of UCO fissile particles of batch 6157-11-020 irradiated in capsule R2-K13: (a) population size of 962 particles from rod 2B2, and (b) population size of 1115 particles from rod 3A1.

Agreement between the IMGA-derived mean activities and the KFA calculations were within +2% for ^{134}Cs and ^{137}Cs in rod 3A1. The ^{106}Ru activity, as measured, was about 7% less than calculated. For rod 2B2, the measured cesium activities were low by 32% for ^{134}Cs and 35% for ^{137}Cs. The ^{106}Ru activity was within + 12% of the calculated value for rod 2B2. Measured activity ratios ^{134}Cs:^{106} and ^{137}Cs:^{106}Ru also indicated good agreement with similar calculated ratios in rod 3A1, but poor agreement in rod 2B2. The measured ^{134}Cs:^{137}Cs activity ratio was in good agreement with calculated value in both fuel rods.

Results of the IMGA analysis on fertile particle from rods 2B2 and 3A1 are presented in Table 5.6. Calculated activities again were provided by KFA-Jülich.[16] The fertile particle batch in rod 2B2 (6252-12COMP) was a composite batch of several different Triso-coated particle batches. One of these was batch 6252-12T-04B2, which was irradiated in fuel rod 3A1. The activity ratios derived from IMGA measurements on the total fertile particle population examined are provided in Fig. 5.9 for rods 2B2 and 3A1.

Table 5.6 Fission product activities and activity ratios measured on fertile particles from fuel rods 2B2 and 3A1 irradiated in capsule R2-K13

Isotope	IMGA derived activity[a] (Bq)			KFA calculation (Bq)
	Minimum	Maximum	Mean	Mean
Rod 3A1 (612 particles examined)				
^{134}Cs	2.45×10^{6}	6.05×10^{6}	2.87×10^{6}	4.50×10^{6}
^{137}Cs	2.00×10^{6}	4.98×10^{6}	2.35×10^{6}	4.04×10^{6}
^{95}Zr	5.19×10^{7}	1.29×10^{8}	6.13×10^{7}	1.01×10^{8}
^{134}Cs:^{95}Zr	4.43×10^{-2}	4.99×10^{-2}	4.69×10^{-2}	4.46×10^{-2}
^{137}Cs:^{95}Zr	3.62×10^{-2}	4.10×10^{-2}	3.84×10^{-2}	4.00×10^{-2}
^{134}Cs:^{95}Zr	1.19	1.27	1.22	1.11
Rod 2B2 (579 particles examined)				
^{134}Cs	2.67×10^{6}	6.84×10^{7}	3.23×10^{6}	4.58×10^{6}
^{137}Cs	2.06×10^{6}	5.20×10^{6}	2.46×10^{6}	3.88×10^{6}
^{95}Zr	5.57×10^{7}	1.38×10^{8}	6.54×10^{7}	9.52×10^{7}
^{134}Cs:^{95}Zr	4.64×10^{-2}	5.31×10^{-2}	4.95×10^{-2}	4.81×10^{-2}
^{137}Cs:^{95}Zr	3.54×10^{-2}	3.99×10^{-2}	3.76×10^{-2}	4.08×10^{-2}
^{134}Cs:^{95}Zr	1.28	1.36	1.32	1.18

[a]Activity ratios presented have dimensions Bq/Bq.

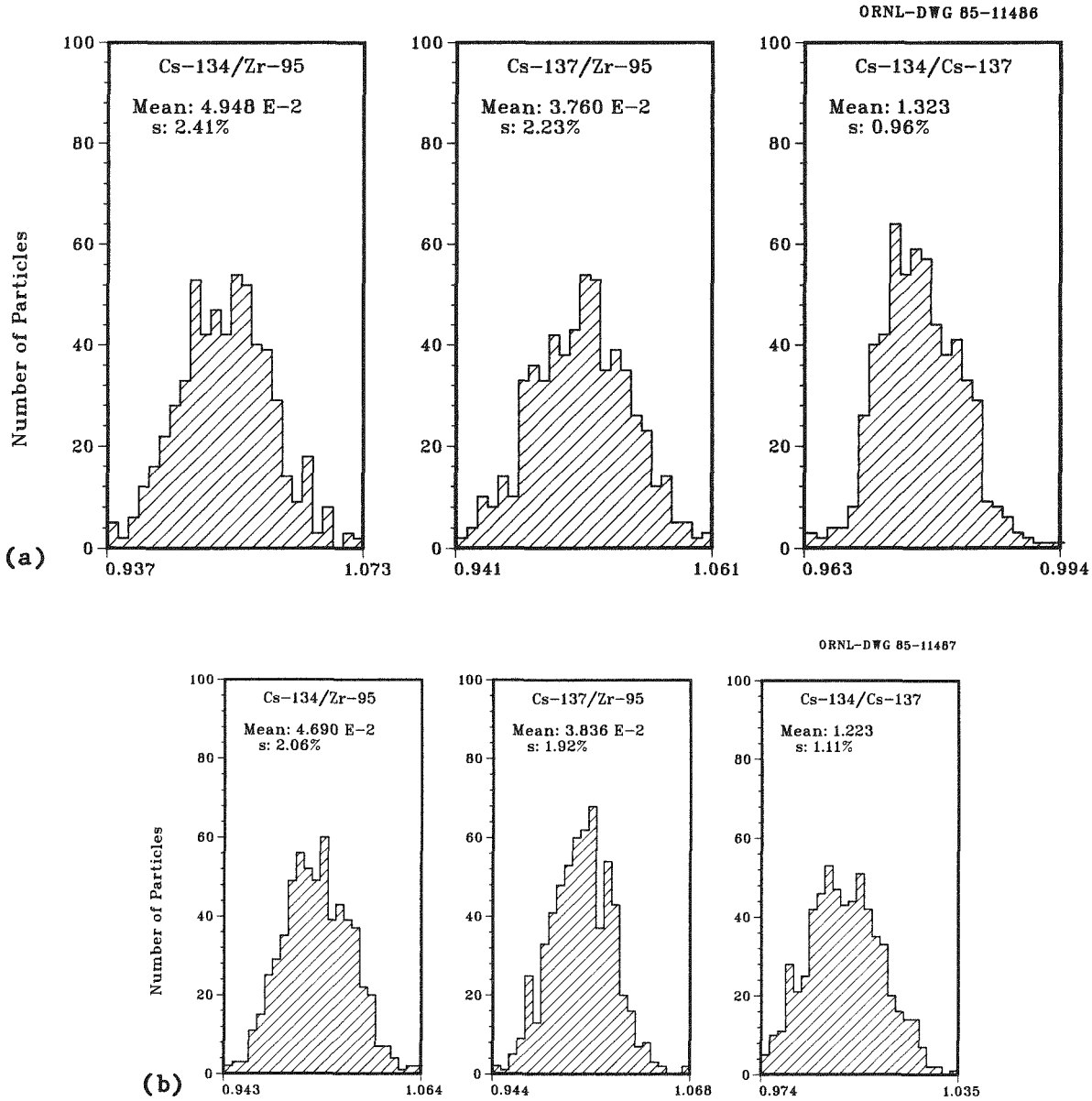

Fig. 5.9. Activity ratio histograms derived from the IMGA examination of ThO_2 fertile particles irradiated in capsule R2-K13: (a) population size of 579 particles of batch 6252-12T 04 B2 from rod 2B2, and (b) population size of 612 particles of batch 6252-12COMP from rod 3A1.

The comparison between measured and calculated activities for the fertile particles is poor as shown in Table 5.6. For the three isotopes listed, the measured activities are 30 to 40% less than the calculated values. Activity ratio comparisons, however, show much better agreement. The large difference between the measured and calculated activities, in this case, do not indicate a large quantity of failed fuel present. Rather, it suggests that significant errors exist either in the input data for the calculations or in the calibrations used with measuring technique. By using the activity ratios, rather than the absolute inventory data, these large differences can be eliminated.

The results of a performance assessment on both the fissile and fertile particle batches irradiated in capsule R2-K13 are provided in Table 5.7. For the fissile fuel, it was assumed that the calculated cesium inventories and the measured ruthenium activities were most accurate. For the fertile fuel, only the activity ratio data was used. Performance was based on the ^{137}Cs retention of each of the subject fuels. The ^{137}Cs:^{106}Ru activity ratio was used for the fissile fuel, and the ^{137}Cs:^{95}Zr activity ratio was used for the fertile. In rod 3A1, only one of 1115 particle examined had significant cesium loss compared to ruthenium. Rod 2B2 in contrast, has 953 of 962 particles examined with cesium loss greater than 10%. The ^{137}Cs retention of the fissile fuel from this rod was only 65.4% compared to 97.8% in rod 3A1. Some fuel particles from rod 2B2 experienced >97% cesium loss.

No failed fertile particles were detected during the IMGA examination of the unbonded particle populations. The activity ratio distributions of Fig. 5.9 illustrate this as each histogram shown is quite symmetric with no particles with low activity ratios present. The distributions shown in Fig. 5.8 are much different. Figure 5.8(a) presents nonsymmetric cesium distributions for rod 2B2 where large cesium loss was measured. Figure 5.8(a) presents symmetric cesium distributions; however, a single particle with a low activity ratio is clearly evident to the far left in each distribution shown.

Table 5.7. Performance assessment of the UCO fissile and ThO_2 fertile particles irradiated in fuel rods 2B2 and 3A1 of capsule R2-K13

Fuel rod (batch)	Measured ratio / Calculated ratio[a]			Number of particles		^{137}Cs Mean retention (%)
	Minimum	Maximum	Mean	Examined	Failed[b]	
Fissile particles						
3A1 (6157-11-020)	0.88	1.17	0.98	1115	1	97.8
2B2 (6157-11-020)	0.026	1.55	0.65	962	953	65.4
Fertile particles						
3A1 (6252-12T 04 B2)	0.91	1.03	0.96	612	0	96.0
2B2 (6252-12COMP)	0.87	0.98	0.92	579	0	92.2

[a]Fissile: ^{137}Cs:^{106}Ru: Rod 3A1 = 0.232. Rod 2B2 = 0.243. Fertile: ^{137}Cs:^{95}Zr: Rod 3A1 = 0.040. Rod 2B2 = 0.041.

[b]Failed particle defined as having activity ratios <10% of the mean ratio.

Additional examinations were performed on 50—100 unbonded particles in an attempt to understand the performance differences observed for the fissile fuel of rod 2B2. The data from the 25 h acid leach suggested that about 1.4% of the particles were failed. However, the IMGA analysis indicated over 99% of the particles were deficient in their cesium inventory. In addition, large actinide concentrations were discovered in the electrolyte solution from the deconsolidation of this rod.

Four metallographic mounts were prepared; one for each of the particle types from the two rods. Two were fissile and two were fertile. Photographs from metallographic examination of fissile batch 6157-11-020 from rod 2B2 are shown in Fig. 5.10. The particle shown in Fig. 5.10(a) is typical of all 100 particles from this metallographic mount. As shown along the outer surface of the SiC layer, a chemical attack is present

R-79116

(a) 200 μm

R-79117

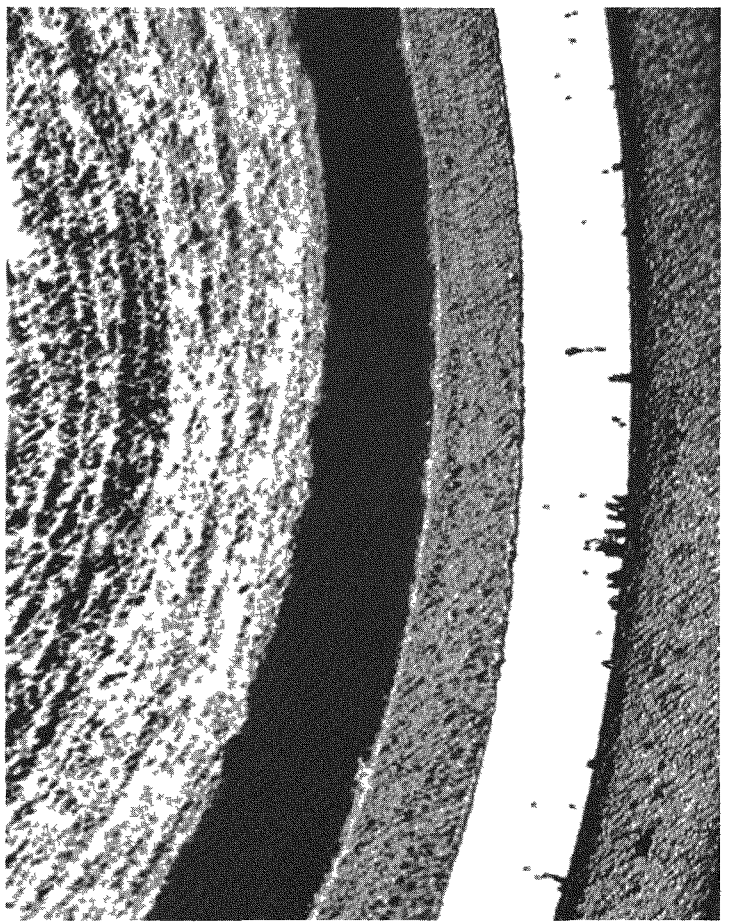

(b) 40 μm

Fig. 5.10. Typical appearance of fissile batch 6157-11-020 irradiated in fuel rod 2B2 of experiment R2-K12 after electrolytic deconsolidation and IMGA examination. Chemical attack beginning at the outer circumference of the SiC appears uniformly distributed around particle and was present on all particles examined. (a) Optical photograph, 150×. (b) High magnification of a portion of the SiC layer from particle shown in (a), 1000×.

circumferentially along this layer. The attack appears to begin at the outer surface and work inward into the SiC. Figure 5.10(b) is a high magnification view of one section of the SiC layer. The attack extends more than halfway through the nominal 35-μm-thick coating. This type of attack was present in all the particles from rod 2B2 that were examined. This was true of fertile particles as well as fissile; although the attack was not as pronounced. This type of chemical attack was not present in either particle type from fuel rod 3A1.

At this time, we have no definitive cause for the chemical attack of the SiC layer of particles in rod 2B2. However, it does appear likely that the fuel rod was damaged somehow during the deconsolidation procedure after the acid leach work was completed. Further analyses of the electrolyte solution from each rod are underway to confirm the high actinide concentrations initially detected.

All PIE work on the GA fuels from R2-K13 has now been completed. This included long-term acid leaching, fuel rod deconsolidation, IMGA examinations, stable fission gas inventory measurements, and metallography of the unbonded particles. A final report documenting the results of this effort is now in progress.

5.3.5 HTR Fuel Performance Assessments — M. J. Kania and F. J. Homan

A report[17] describing the irradiation performance of different types of HTR fuel particles with advanced ZrC-coating designs was prepared. This report documents the results of PIE conducted on these fuels at ORNL. The advanced fuel coatings were fabricated at Los Alamos National Laboratory and at GA, and irradiated in experimental test capsules during the time period of April 1975 through January 1981. The abstract of this report is provided as follows:

> During the past 25 years of fuel development for the High-Temperature Gas-Cooled Reactor (HTGR) the Triso particle has evolved as the favored design to optimize economics and performance. The Triso particle consists of a kernel (fissile or fertile), a buffer [porous pyrocarbon (PyC)], an inner PyC layer, a dense SiC layer, and an outer PyC layer. The SiC layer is the primary barrier to the release of both metallic and gaseous fission products from the particle. Consideration has been given to replacing the SiC layer with ZrC for applications

requiring very high fuel operating temperatures. Zirconium carbide is more refractory than silicon carbide (3540°C melting temperature compared with 2700°C for SiC) and denser (6.73 g/cm^3 compared with 2.217 for SiC) and therefore has the potential for being a better fission product barrier. Other designs using ZrC have also been considered and tested. The testing done to date on HTGR fuel particles with ZrC coatings has been very limited compared with the testing done on the Triso particle design. Most of the data have been collected on isolated specimens included in experiments planned to test reference designs. This report reviews all the irradiation testing data collected within the U.S. program on HTGR fuel particles with ZrC coatings. Fission product retentiveness of particles with ZrC coatings has generally been inferior to that of similar particles with the Triso design, but it is emphasized that the fabrication of ZrC coatings has not been optimized to nearly the extent of that of SiC coatings.

5.4 EQUIPMENT DEVELOPMENT AND MAINTENANCE — M. J. Kania

The IMGA, PGA, X-radiography facility, and the shielded electron microscope are important systems which are totally integrated into the PIE effort on HTR fuels at ORNL. Although these systems are used in the routine PIE of HTR materials, they continue to require maintenance and upgrading to maintain their reliability and capabilities.

5.4.1 Irradiated-Microsphere Gamma Analyzer (IMGA) — M. J. Kania and G. A. Moore

During this year, the availability of the IMGA system was nearly 60%, which was down slightly from the previous year. Equipment failure associated with the automated particle handler device accounted for the majority of the downtime. HRLEL maintenance requirements, beyond our control, was also a contributory factor. The most significant problems this year were the hardware and electronics associated with the automated particle handler. The singularizer portion of the particle handler failed completely, and attempts to re-build component parts and install them remotely proved unsuccessful. We have concluded that the singularizer is beyond remote repair and will require a major effort to fabricate and install a device of the same design. Therefore, decontamination of the

IMGA cubicle has begun, and preparations are being made for the installation of the new automated particle handler device, which was fabricated some years ago. Installation will begin in January 1985 and be completed in June 1985.

Despite problems with the automated particle handler a significant number of examinations were completed this year with the IMGA system. GA fabricated fuels irradiated in capsules R2-K13 and HRB-16 were examined, plus German fuels from experiments FRJ2-P23, FRJ2-P25, and DR-S6 under the US/FRG cooperative program (see Section 4.2). Fuel rod deconsolidations were performed on the U.S. fuel, and the German fuel was received in unbonded form. Analysis of the results of these examinations were reported in Section 5.3. A third set of irradiated German fuels were received and are being held in storage at the HRLEL until the IMGA examinations can begin.

Work has progressed slowly on the introduction of the ND-6700 system to replace the TP-5000 system presently being used for pulse height analysis with the IMGA. This work has been slowed due to lack of manpower and the need to proceed with scheduled IMGA examinations to meet other commitments. Programming of the operation of the automated handler was written in FORTRAN IV, but operation under ND-6700 control was not accomplished. Software development and installation of ND-6700 system to replace present system will be a priority item in FY 1985. The new automatic particle handler software will be designed specifically to run on the ND-6700 system.

5.4.2 Postirradiation Gas Analyzer (PGA) — M. J. Kania and L. G. Shrader

During the past year, the upgraded PGA system was put into operation. The upgraded PGA employs an IO-200 quadruple mass spectrometer connected to a high vacuum chamber in which single irradiated HTR coated particles are broken and their fission gases quantitatively measured. The chamber is configured with a capacitance manometer which measures the increase in chamber pressure when a particle is broken. Fission gases released from the particle are fed through a series of sized orifices into the spectrometer. The orifices are small enough to ensure a sufficient pulse duration while not permitting isotopic mass separation. The spectrometer is

interfaced with a DEC LSI-11/23 microcomputer for data acquisition, analysis, and storage. Vacuum is supplied by a 150 L/s turbomolecular pumping system.

The system has been available for approximately 40% of the year. This is the first year of operation and several problems have surfaced that deal with the operation of the quadrupole spectrometer. The most serious problem has been the calibration of the device. Procedures, which proved successful initially, have become increasingly difficult to use as the instrument ages. Recent investigations have revealed that this is due to contamination of the spectrometer sensor. Procedures are available to eliminate this contamination, but they require short-term annealing at 800°C. Since the spectrometer is located in a radiation environment, decontamination and removal from this environment is necessary before the anneal can take place. Although time-consuming, this procedure will be implemented on a regular basis.

Irradiated GA fuels from capsules HT-34, HT-35, R2-K13, and German fuels from experiments FRJ2-P23 and DR-S6 have been evaluated in the PGA. In general the results from these analyses are in good agreement with empirically-derived models used to predict stable fission gas inventory within coated particle fuels.

5.4.3 X-Radiography Facility — M. J. Kania

The high-voltage power supply system purchased for the upgrade of the x-radiography facility was checked out on-site during this year. During this checkout, it was discovered that the system was built around a generator with a maximum current output rated at 25 mA. The original specification called for a generator with a capacity of 40 mA to meet the load characteristics of our high-voltage 160 kV x-ray tube. Due to the limitation on load current, the x-ray system was rejected so that the original procurement specifications could be met. Our specifications will be reviewed and returned for bid.

5.4.4 Shielded Electron Microprobe — J. M. Keller and M. J. Kania

During this report period the shielded electron microprobe facility located in the HRLEL has not been available for use. The existing facility

has not been maintained during the past two years, and no significant upgrade was been employed to maintain its compatibility with existing electronic data analysis techniques. Therefore, a significant upgrade of this facility was initiated in November 1985 to make the system operational and to bring it up, as much as possible, to current standards.

5.5 FISSION PRODUCT TRANSPORT AND BEHAVIOR — R. P. Wichner

5.5.1 Thermal Gradient Tube Tests and Assessment of Iodine and Cesium Chemical Forms Evolved From Graphite — O. K. Tallent

A test series was conducted to assess the utility of a thermal gradient tube (TGT) for use in possible future fission product transport experiments.[18] The device, which has its advantages and disadvantages, has been used extensively to aid in species identification in tests conducted under non-HTR conditions. In addition, the tests were used to gain some insight about the chemical forms of iodine and cesium vaporized from graphite. Specifically, these scoping tests were conducted using a simulated fission product source that consisted of a graphite sample laced with cesium and iodine and heated to 1400°C.

A schematic of the TGT is shown in Fig. 5.11. Helium, with a controlled oxygen potential, passed over the fission product source at a flow ~1 cm^3/s and subsequently through the TGT, which consisted of a graphite tube held at ~1000°C at the inlet and ~100°C at the outlet.

The notion that the iodine chemical form is predominantly cesium iodide was in vogue at this time despite an abundance of contrary empirical evidence. Therefore, most of the tests were conducted using a cesium iodide source with additional cesium to bring the Cs/I ratio approximately to 10. Typical TGT deposition profiles for two such tests are shown in Fig. 5.12. This figure shows a peak, which is predominantly cesium iodide, that moves downward with time from an early location at ~850°C to a subsequent location in the TGT at ~350°C. Other tests indicated that perhaps 10% of the iodine appears in locations indicative of a molecular iodine deposit with the balance forming a condensed cesium iodide deposit.

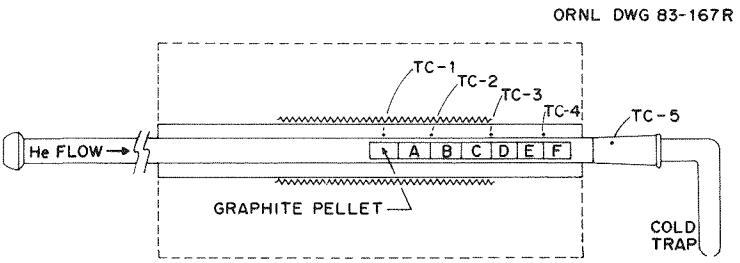

Fig 5.11. Thermal gradient tube (TGT) schematic.

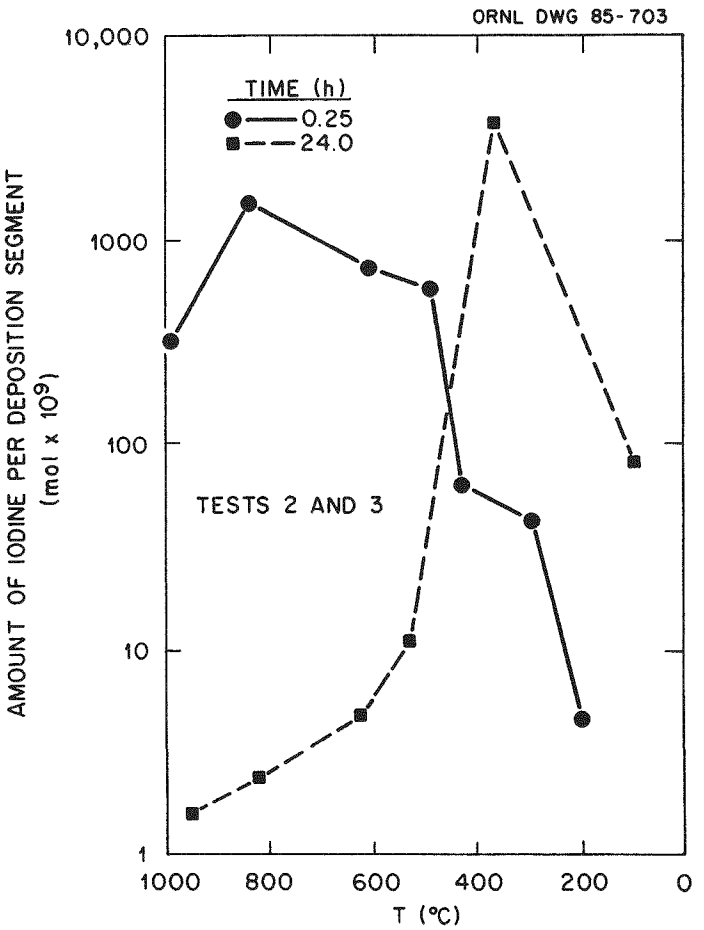

Fig. 5.12. Adsorption of iodine from CsI-Cs_2O_3 source, Cs/I mole ratio = 10, on graphite thermal gradient tube. Cover gas: 1% carbon monoxide.

Other tests using a molecular iodine source were also performed for comparison. In addition, the effect of varying the oxygen potential, by adjusting the carbon monoxide partial pressure, was investigated.

These tests illustrated the potential utility of the TGT device under HTR test conditions. However, further calibration runs would be required to gain confidence in the interpretation of observed deposition peaks in terms of specific fission product species.

5.5.2 Diffusion of Plutonium in H451 Graphite at 1000 to 1350°C — O. K. Tallent

To determine the rate and extent of plutonium transport to the coolant gas, it is necessary to know the plutonium vapor pressure and the effective diffusion coefficient of plutonium in graphite. We have previously reported our study of the vapor pressure of the adsorbed plutonium,[19] and a previous study of uranium as a stand-in for plutonium[20] allowed development work to be conducted and equipment to be tested without the constraints of alpha glove-box containment.

A pellet transfer method, in which plutonium was supplied from a source pellet into a second, initially plutonium-free test pellet, was used for diffusion coefficient determination in graphite.[21] Data were collected to determine the penetration profiles of the plutonium into the test pellets as a function of temperature. The plutonium concentrations in the source pellets are considered to have remained essentially constant, since these concentrations were large compared to the concentrations diffusing into the test pellets. The transfer of plutonium across the plane of contact between pellets provided an almost constant plutonium concentration on the test pellet outer surface.

The source pellets were placed in contact with the test pellets for the diffusion tests. Both pellets were inserted into a tightly fitting cylindrical opening in a 2-×2-×1.25-cm graphite block, such that the plane of contact between the pellets was approximately in the center of the block, which was then placed in a 2.54-cm-diam alumina tube in a horizontal tube furnace and heated. Heating periods ranged from 0.4 to 8.0 d at 1000, 1200, or 1350°C. A 0.4-cm^3/s (STP) flow of helium gas purified over titanium sponge at 400°C was passed through the tube during the heating

period. The pellets were then cooled to room temperature and analyzed to determine the concentration profile in the test pellet. A typical profile for a test series run using 0.1% CO in the cover gas is given in Table 5.8.

If a constant surface concentration of the test pellet during the test is assumed, which appears reasonable for the test parameters employed, the plutonium concentration profile may be expressed as

$$1 - \left(\frac{C(x,t)}{C_o}\right)^2 = \text{erf}\left(\frac{x^2}{Dt}\right) \qquad (1)$$

where C_o is the surface concentration and C(x,t) is the plutonium concentration in the pellet as a function of time. Using Eq. (1), a plot of the left term of Eq. 1 as a function of x^2 yields a straight line with slope equal to 1/4 Dt, where D is the effective diffusion coefficient for plutonium in graphite for the given test conditions. A typical profile is illustrated in Fig. 5.13 for 7-d test at 1000°C.

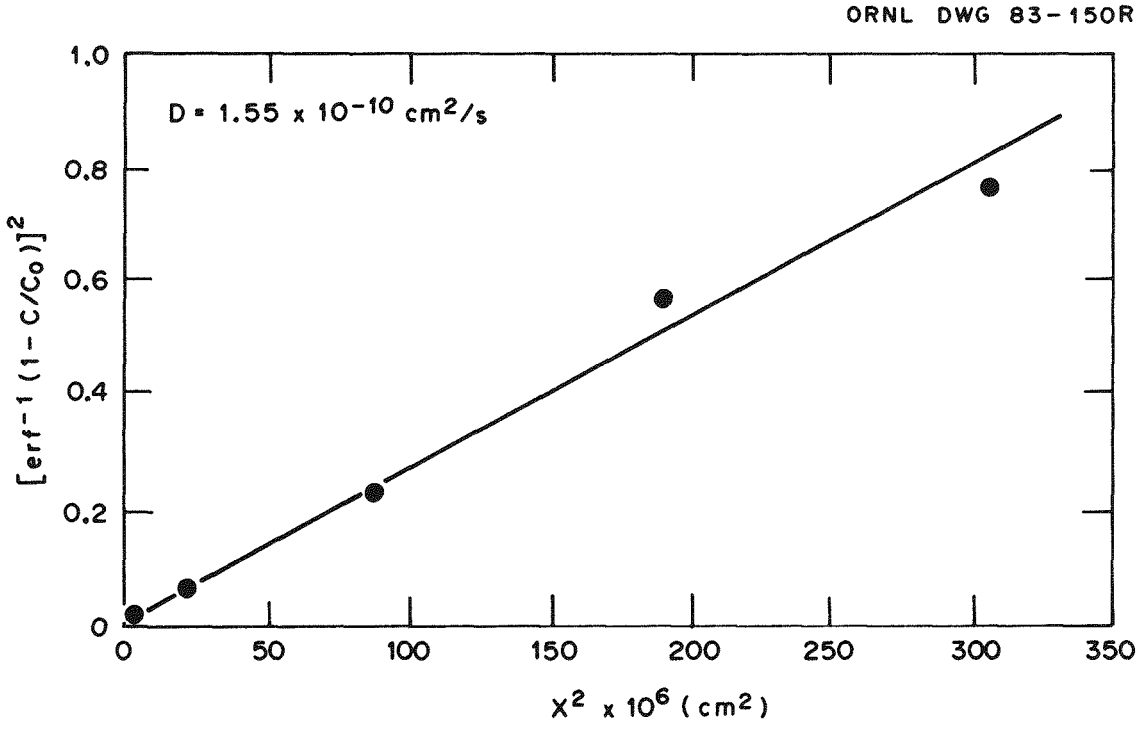

Fig. 5.13. Penetration profile for the diffusion of plutonium in H-451 graphite at 1000°C for 7 d.

Tests conducted between 1000 and 1400 K indicated that the effective diffusion coefficient of plutonium in H451 graphite may be expressed as

$$\log_{10} D = -1.60 - \frac{9893}{T} \qquad (2)$$

where D is given as cm/s and T in degrees K.

Table 5.8. Penetration of plutonium in H-451 graphite; helium–0.1% carbon monoxide cover gas

Temperature (°C)	Time (d)	Penetration distance (cm)	Plutonium concentration [(g/cm^3) × 10^6]
1000	6.75	0.0067	174.65
		0.0177	26.03
		0.0274	18.00
		0.0381	24.34
1000	7.0	0.0087	66.53
		0.0124	16.28
		0.0255	12.58
		0.0315	7.35
1200	3.8	0.0025	61.79
		0.0122	31.95
		0.0224	13.97
		0.0323	15.00
		0.0436	21.31
1200	8.0	0.0074	22.40
		0.0125	16.60
		0.0215	15.13

5.6 REFERENCES

1. R. L. Senn, "Hydrolysis Experiments HRB-17 and HRB-18," pp. 8–9 in *High-Temperature Gas-Cooled Reactor Technology Development Program Annual Progress Report for Period Ending December 31, 1982*, ORNL-5960, June 1983.

2. T. N. Tiegs, I. I. Siman-Tov, and M. J. Kania, "Capsule HT-35," pp. 23–27 in *High Temperature Gas Cooled Reactor Technology Development Program Annual Report for Period Ending December 31, 1980*, ORNL-5753, August 1981.

3. M. J. Kania and T. N. Tiegs, "Capsule HT-35," pp. 16–21 in High Temperature Gas Cooled Reactor Technology Development Program Annual Report for Period Ending December 31, 1981, ORNL-5871, June 1982.

4. R. J. Lauf, "Irradiation Behavior of Pyrolytic Silicon Carbide," pp. 72–73 in *Proceedings of 41st Annual Meeting of Electron Microscopic Society of America held in Phoenix, Ariz.*, on Aug. 8–12, 1983, ed. G. W. Bailey, San Francisco Press, San Francisco, CA, 1983.

5. M. J. Kania and K. H. Valentine, *The Irradiated Microsphere Gamma Analyzer (IMGA) System — An Integrated System for HTGR Fuel Performance Assessments*, ORNL-5606, November 1980.

6. M. J. Kania, F. J. Homan, and R. J. Lauf, "Capsule HT-35," pp. 131–142 in *High Temperature Gas Cooled Reactor Technology Development Program Annual Report for Period Ending December 31, 1983*, ORNL-6053, June 1984.

7. D. P. Stinton and W. J. Lackey, "Deposition and Characterization of Pyrocarbon Coatings Produced by Use of CO_2 Dilution," *Am. Ceram. Soc. Bull.*, **61**(8), 1982.

8. E. L. Long et al., "Irradiation Performance of HTGR Biso Fertile Particles in HFIR Experiments HT-17, -18, and -19," ORNL/TM-6414, November 1978.

9. M. J. Kania, B. A. Thiele, and F. J. Homan, "Irradiation-Induced Permeability in Pyrocarbon Coatings — Final Report of Work Conducted Under PWS FD-12," ORNL/TM-8348, October 1982.

10. R. F. Turner et al., *Selection of LEU/Th Reference Fuel for the HTGR-SC/C Lead Plant*, GA-A17123, May 1983.

11. T. N. Tiegs, "Fission Product Pd-SiC Interaction in Irradiated Coated Particle Fuels," *Nuclear Technology*, **57**, pp. 389–398, June 1982.

12. F. J. Homan et al., *Irradiation Performance of HTGR Fuel Rods in HFIR Experiments HRB-9 and -10*, ORNL-5254, April 1978.

13. J. W. Ketterer er al., *Capsule HRB-15A Postirradiation Examination Report*, GA Technologies Inc., GA-A16758, July 1984.

14. M. J. Kania, "Capsule HRB-16," pp. 19–21 in *High Temperature Gas Cooled Reactor Technology Development Program Annual Progress Report for Period Ending December 31, 1982*, ORNL-5960, June 1983.

15. M. J. Kania, "Capsule R2-K13," pp. 162–167 in *High Temperature Gas-Cooled Reactor Technology Development Program Annual Progress Report for Period Ending December 31, 1983*, ORNL-6053, June 1984.

16. W. A. Kuehnlein, unpublished data Kernforschungsanlage Jülich, Institut fur Reaktorwerkstoffe.

17. F. J. Homan and M. J. Kania, "Irradiation Performance of HTGR Coated Particle Fuels with ZrC Coatings," ORNL/TM-9085, January 1985.

18. O. K. Tallent et al., *Analysis of Iodine and Cesium Chemical Forms Evolved from Graphite Surfaces at Temperatures for 425 to 1400°C*, ORNL/TM-9213 (to be issued).

19. O. K. Tallent, R. P. Wichner, R. L. Towns, and T. T. Godsey, *Vapor Pressure of Plutonium Carbide Adsorbed on Graphite*, ORNL/TM-9161, 1984.

20. O. K. Tallent, R. P. Wichner, and R. L. Towns, *Diffusion of Uranium in H-451 Graphite at 900 to 1400°C*, ORNL/TM-8205, March 1983.

21. O. K. Tallent, R. P. Wichner, and T. T. Godsey, *Diffusion of Plutonium in H-451 Graphite at 1000 and 1350°C*, ORNL/TM-9376 (to be issued).

6. GRAPHITE (WBS 1602)

W. P. Eatherly

6.1 INTRODUCTION — W. P. Eatherly

In 1984, the graphite program continued its concentration on fracture mechanics and statistics, increasingly focused on the development of failure criteria for the material under at least uniaxial but nonuniform stress fields. Such criteria are equally applicable to either a prismatic or pebble bed core; for the two applications, the problem simply transfers from the fuel element to the reflector. Because of budget limitations, no irradiation experiments were performed; however, the delay of the creep experiments has caused increased concern with regard to overall program requirements.

At the beginning of this year, the necessity to obtain a nuclear-quality Stackpole 2020 graphite was an intense activity in order to provide a proper material for the Core Support Performance Test (CSPT). With the decision to delay the continuation of this test series for at least one year, the immediate pressure to obtain a satisfactory material was relieved. We were and are at this time strongly involved with the supplier on improving the manufacturing techniques, and therefore the program has continued at a high level of activity.

6.2 GRAPHITE MATERIALS — INTERNALS (WBS 1602.01)

6.2.1 Stackpole 2020 Improvement Program — R. A. Strehlow and W. P. Eatherly

Stackpole 2020 graphite has been selected as the material of choice for several applications as a permanent component in the reference design gas-cooled reactor.[1] Three shipments (lots) of 2020 graphite were received

at the Oak Ridge National Laboratory for tests and evaluation. Each of the lots consisted of three cylindrical billets measuring approximately 180 cm long by 25 cm diameter. The first lot was a standard or off-the-shelf 2020 graphite and was used in TEST ZERO of the CSPT series.[2] The second and third lots were the first iterations in the development of a nuclear-quality material by the manufacturer.

It had been recognized earlier that stock or off-the-shelf 2020 graphite was not a satisfactory material for application as a permanent component in a gas-cooled reactor because of agglomerated impurities in the graphite and the variability of impurities from billet to billet. The development plan involved the use of selected material to avoid the agglomerated impurity problem and a higher graphitization temperature to decrease the billet-to-billet variability. Nuclear-quality Lot 1, however, was found to have agglomerated impurities, but only after Nuclear Lot 2 had been committed. As a consequence, the differences between Lots 1 and 2 were not great.

The billets were cut to provide samples for analysis and pieces of appropriate size for the CSPT. The lots of nuclear-quality graphite were intended to provide the material for TEST ONE, the final test in the CSPT series, subject in part to the results of chemical analyses.

6.2.1.1 Cutting Plan for Chemical Analysis Specimens

The billet designations for the three lots of 2020 graphite are shown in Table 6.1.

Table 6.1. Billet designations of the three shipments of Stackpole 2020 graphite

Lot	Billet numbers
Off-the-shelf	148, 159, and 220
Nuclear Lot 1	21, 24, and 25
Nuclear Lot 2	20, 29, and 30

Each billet was cut normal to its axis into seven sections and the sections designated by the letters A through G. Sections B, D, and F were cut to a length of 483 mm and were reserved as stock for the CSPT series. Four sections of the nominal length of 100 mm from the regions of the billet immediately adjoining each of the 483-mm pieces were used to provide samples for analyses and tests. These were designated A, C, E, and G. This cutting pattern thus provided samples from four different regions along the axes of the billets.

The four 100-mm sections of each billet were used to provide specimens for physical and chemical testing. Each of the 100-mm sections was cut to provide a quadrant from which the samples for analyses and density measurements were taken. This cutting pattern permitted assessment of radial and axial variations of composition. Each of the billets provided approximately 216 samples for chemical tests as well as samples for physical testing. The cutting pattern was designed to provide a mapping of each billet that would permit an assessment to be made of the purity levels in each of the test pieces and to permit a choice to be made of representative pieces for the CSPT.

6.2.1.2 Method

All of the specimens for chemical analysis were weighed and the density of each was calculated. Four to six specimens from each section A, C, E, and G from all nine billets were submitted for chemical analysis of the inorganic components of ash formed by an air oxidation of the specimens at 800 to 850°C for 16 h. The analytical method used for the analysis of the ash was inductively coupled argon-plasma emission spectroscopy. The dominant or significant constituents were found to be calcium, aluminum, silicon, and iron.

The analytical results for the nine billets studied are summarized in Table 6.2. Nuclear Lot 1 graphite clearly had a significantly lower impurity level than did the off-the-shelf graphite and showed that the manufacturer was able to produce 2020 graphite with some control of impurities. The further improvement expected for Nuclear Lot 2, however,

Table 6.2. Billet summaries

		Off-the-shelf				Nuclear lot 1				Nuclear lot 2			
		148	159	220	Average	21	24	25	Average	20	29	30	Average
Density	$\bar{\chi}$	1.772	1.762	1.769	1.768	1.783	1.783	1.790	1.785	1.784	1.797	1.788	1.790
	σ (ν)*	0.039(4)	0.030(4)	0.010(4)		0.011(4)	0.013(4)	0.019(4)	0.011(4)	0.018(4)			
Ash	$\bar{\chi}$	0.22	0.22	0.12	0.19	0.11	0.10	0.10	0.10	0.14	0.13	0.12	0.13
	σ (ν)	0.09(16)	0.09(16)	0.04(16)		0.02(16)	0.02(16)	0.02(16)		0.02(24)	0.01(24)	0.02(24)	
Fe	$\bar{\chi}$	180	140	140	153	9.6	5.6	8.2	7.8	12.1	8.5	6.1	8.9
	σ (ν)	90(16)	60(15)	50(16)		3.0(16)	2.3(16)	3.5(16)		9.8(24)	6.7(24)	4.1(24)	
Si	$\bar{\chi}$	260	300	210	257	76	77	66	73	127	113	115	118
	σ (ν)	180(16)	90(16)	90(16)		32(16)	34(16)	36(16)		28(23)	16(24)	18(24)	
Si/Fe		1.4	2.1	2.3	1.7	7.9	13.8	8.0	9.4	10.5	13.3	18.9	13.3
Ca	$\bar{\chi}$	400	430	310	380	261	219	250	243	510	436	441	462
	σ (ν)	230(16)	260(16)	160(16)		53(16)	46(16)	76(16)		56(24)	11(24)	97(24)	
Al	$\bar{\chi}$	250	80	140	157	17	15	14	15.3	19	17	17	17.5
	σ (ν)	160(16)	50(15)	90(16)		4(16)	3(16)	4(16)		8(24)	3(24)	5(24)	
Ca/Al		1.6	5.4	2.2	2.4	15	15	18	16	27	26	26	26

*By section. $\bar{\chi}$ is the value of the mean with standard deviation σ obtained with ν specimens.

was not observed. For Nuclear Lot 2 the impurities appeared to be generally higher than for Lot 1, but especially so for calcium which, along with iron, can act as a catalyst for graphite oxidation.

Radial and axial variations of some of the impurities are shown in Tables 6.3 and 6.4, respectively. The radial variation that is distinct for the off-the-shelf grade was significantly reduced for Nuclear Lots 1 and 2 except for iron, which did show a gradient that is consistent with the diffusion of iron out of the graphite body. Axial variation showed an enhancement of calcium and aluminum at the ends of the billets.

In an effort to improve their purity, four of the 483-mm pieces from Nuclear Quality Lot 2 were returned to the manufacturer for regraphitization with more highly controlled conditions and materials. A portion of a print of an x-radiograph of a 6.5-mm slab from one of the regraphitized pieces is shown in Fig. 6.1. Agglomerated impurities or particles are evident.

Table 6.3. Radial impurity distributions (ppm) Stackpole 2020 graphite billet-to-billet statistics[a]

		Off-the-shelf	Nuclear Lot 1	Nuclear Lot 2
Iron:	Inner	153 ± 68(3)	10.0 ± 2.3(3)	14.6 ± 4.0(3)
	Middle	133 ± 25(3)	8.0 ± 2.5(3)	9.5 ± 3.7(3)
	Outer	170 ± 10(3)	5.1 ± 1.0(3)	2.5 ± 1.5(3)
	All	152 ± 40(9)	7.7 ± 2.8(9)	8.9 ± 5.9(9)
Calcium:	Inner	317 ± 40(3)	240 ± 28(3)	494 ± 40(3)
	Middle	283 ± 6(3)	242 ± 18(3)	465 ± 50(3)
	Outer	457 ± 102(3)	247 ± 35(3)	429 ± 37(3)
	All	352 ± 97(9)	243 ± 24(9)	462 ± 47(9)
Silicon:	Inner	153 ± 45(3)	53 ± 8(3)	118 ± 6(3)
	Middle	190 ± 69(3)	74 ± 11(3)	116 ± 7(3)
	Outer	333 ± 64(3)	89 ± 17(3)	121 ± 9(3)
	All	226 ± 98(3)	72 ± 19(9)	118 ± 7(9)
Aluminum:	Inner	273 ± 87(3)	14.4 ± 0.4(3)	19.8 ± 3.3(3)
	Middle	157 ± 95(3)	14.7 ± 1.2(3)	18.9 ± 1.4(3)
	Outer	147 ± 83(3)	17.7 ± 2.0(3)	13.9 ± 1.0(3)
	All	159 ± 78(9)	15.6 ± 2.0(9)	17.5 ± 3.3(9)

[a]In the form $\bar{x} \pm s$ (n), arithmetic mean ± standard deviation (number of specimens).

Table 6.4. Axial impurity distributions (ppm) Stackpole 2020 graphite billet-to-billet statistics[a]

			Off-the-shelf	Nuclear Lot 1	Nuclear Lot 2
Iron:	Section	A/G[b]	103 ± 45(3)	6.2 ± 2.7(3)	13.3 ± 8.1(3)
		C/E	147 ± 12(3)	6.6 ± 1.9(3)	8.1 ± 1.7(3)
		E/C	150 ± 26(3)	8.1 ± 1.8(3)	8.1 ± 1.8(3)
		G/A	217 ± 81(3)	10.3 ± 2.7(3)	6.1 ± 2.0(3)
		All	154 ± 59(12)	7.8 ± 2.5(12)	8.9 ± 4.7(12)
Calcium:	Section	A/G	567 ± 100(3)	295 ± 28(3)	563 ± 59(3)
		C/E	227 ± 35(3)	195 ± 23(3)	438 ± 46(3)
		E/C	240 ± 46(3)	198 ± 24(3)	413 ± 64(3)
		G/A	527 ± 211(3)	285 ± 29(3)	436 ± 115(3)
		All	390 ± 194(12)	243 ± 54(12)	462 ± 89(12)
Silicon:	Section	A/G	270 ± 10(3)	105 ± 10(3)	133 ± 17(3)
		C/E	210 ± 72(3)	56 ± 14(3)	106 ± 17(3)
		E/C	263 ± 67(3)	48 ± 9(3)	106 ± 3(3)
		G/A	310 ± 46(3)	82 ± 4(3)	129 ± 8(3)
		All	263 ± 59(12)	74 ± 25(12)	119 ± 17(12)
Aluminum:	Section	A/G	197 ± 103(3)	17.7 ± 0.6(3)	18.2 ± 3.3(3)
		C/E	70 ± 36(3)	12.7 ± 1.5(3)	15.9 ± 0.5(3)
		E/C	73 ± 35(3)	12.3 ± 1.5(3)	15.7 ± 1.7(3)
		G/A	290 ± 167(3)	19.3 ± 1.7(3)	20.1 ± 5.3(12)
		All	158 ± 129(12)	15.5 ± 3.4(12)	17.5 ± 3.3(12)

[a]In the form $\bar{x} \pm s\ (n)$

[b]The sections labeled A→G or G→A are end sections and C/E and E/C are internal in the billet.

Earlier work on some of the particulate impurities used energy-dispersive x-ray analysis and scanning electron microscopy. This work had shown the particles generally to contain calcium and silicon as principal constituents along with iron (in the case of off-the-shelf graphite). Some particles in both a sample of off-the-shelf and of nuclear-quality graphite contained large concentrations of titanium and vanadium. The particles were found to be about 0.33 mm in size and were not well crystallized.

The particles were assumed to be carbides of the inorganic elements present in the graphite. Further studies are planned both to identify these impurities and to determine ways of minimizing their possible effect

ORNL-DWG 85-14594

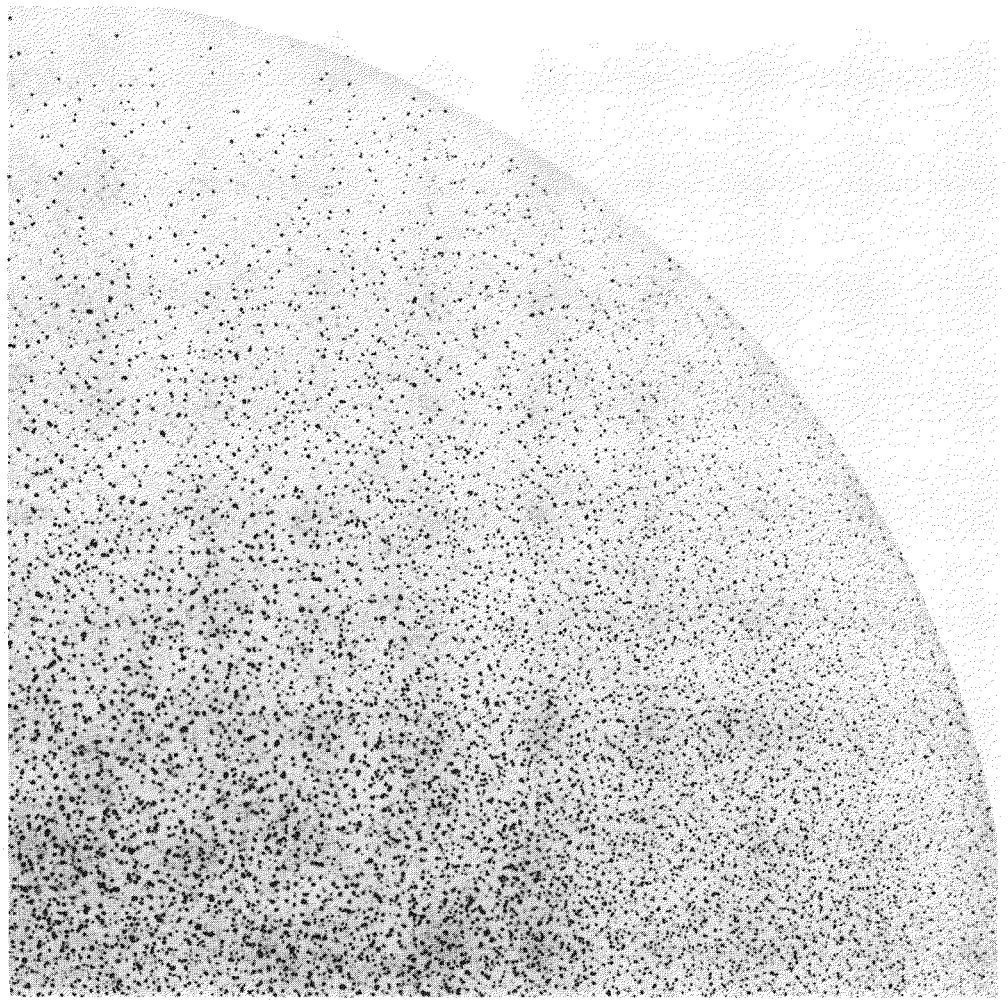

Fig. 6.1. Quadrant of radiograph of 1/4 in. thick slice of regraphitized Stackpole 2020 graphite, showing particulate impurities as dark spots.

on the graphite. It should be noted, however, that the improvement of purity achieved in all graphite received since Nuclear Lot 1 has resulted in a significant reduction of oxidation susceptibility.

6.2.2 Core Support Performance Test — J. P. Sanders and H. C. Young

Near the end of 1983, TEST ZERO, the second phase of the planned CSPT graphite oxidation test n the CFTL, had a continuous test run of about 500 h when it was halted by rapid plugging of the full-flow helium filter.[3]

By mid-January 1984, a replacement filter assembly and two modified helium heater assemblies were installed.[4] Loop operation was resumed on January 20, 1984. Operation was interrupted in mid-February by a fault in the variable frequency power supply for No. 3 circulator and damage to the gas lubricated bearings in No. 3 circulator.

A heat shield was installed in the No. 3 circulator pressure vessel in place of the circulator rotary assembly, and the remainder of TEST ZERO was completed with circulators No. 1 and 2. The two circulators operated continuously for the remainder of TEST ZERO, except for three unscheduled interruptions of less than 15 minutes each.

Moderate, but progressive, plugging of the full-flow helium filter was noted starting in early March 1984 and continuing through the end of TEST ZERO.

The specified goals for TEST ZERO were met, and TEST ZERO was formally completed on April 23, 1984. However, operation for further investigation of the graphite oxidation rate and the sensitivity of filter plugging to changes in gas chemistry and graphite temperatures were continued through May 16, 1984.

The TEST ZERO graphite was then removed for inspection and analysis. The vessel liner sections were removed and rebored in preparation for the planned TEST ONE.

The bearings in No. 3 circulator rotary assembly were repaired. The helium heaters were refurbished, and the filter elements for the full-flow helium filter were removed and replaced. Fabrication of the bellows sealed device for imposing an axial load on the TEST ONE graphite was completed.[5]

The modified vessel liners, No. 3 circulator rotary assembly, the helium heaters, the replacement filter assembly, and the graphite loading device were installed. The CFTL was evacuated and pressurized with low-pressure helium and will remain in readily reusable standby condition until FY 1986.

6.2.2.1 CFTL Operation — Circulators and Helium Heaters

Figure 6.2 presents a chronology of the circulator and helium heater operation during TEST ZERO. The circulators were manually stopped or

ORNL–DWG 84–5544A ETD

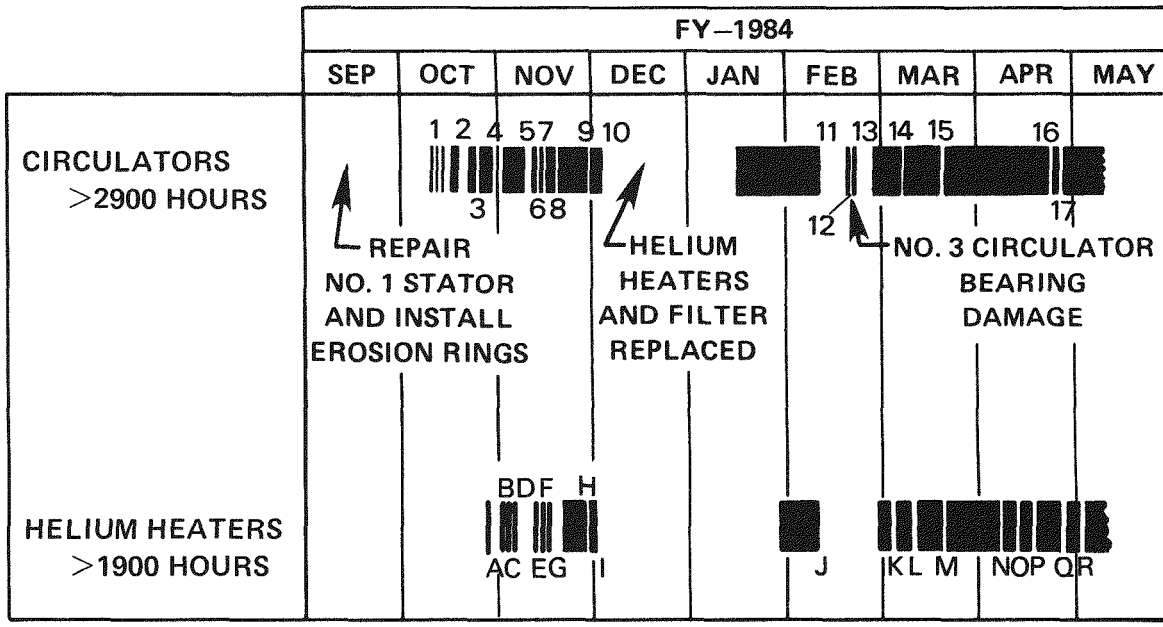

SCRAM NO	CIRCULATOR	CIRCULATOR DOWN TIME (h)
1	CIRC OPER & VIB CHECKS	1 0
2	VFPS* NO 1 FAULT	168 0
3	MAINT OF AUX CIRCUIT	0 1
4	VFPS NO 1 FAULT	100 0
5	Sch – Mfr INSP VFPS	48 0
6	VFPS NO 3 FAULT	3 0
7	VFPS NO 1 FAULT	0 1
8	CALIBRATING PRESS SWITCH	0 1
9	VFPS NO 3 FAULT	45 0
10	HELIUM FILTER PLUGGING	~(5 wks)
11	VFPS NO 3 FAULT	168 0
12	CIRC NO 3 BEARING PROBLEM	168 0
13	Sch – TO CHECK HEAT SHIELD	24 0
14	MAINT OF IDLE VFPS NO 3	0 1
15	MAINT OF IDLE VFPS NO 3	0 1
16	ADJ CIRC ΔP TRIP SET POINT	<0 1
17	Sch – TO EVACUATE LOOP	6 0

SCRAM NO	HELIUM HEATER
A	FUNCTION CHECK
B	FUNCTION CHECK
C	Sch – TO CHECK HELIUM BYPASSING HEATER
D	Sch – TO RAISE HIGH–TEMP SCRAM SETTING
E	FLUCTUATION IN HEATER CONTROL TE
F	DEFECTIVE GROUND FAULT INDICATOR
G	CIRC SCRAM NO 6
H	CIRC SCRAM NO 9
I	HELIUM FILTER PLUGGING – LOW HTR FLOW
J	CIRC SCRAM NO 11
K	Sch – GRADUAL FILTER PLUGGING
L	Sch – TO ADJ H_2 H_2O RATIO
M	CIRC SCRAM NO 15
N	Y–12 AIR FAILURE TO HELIUM FLOW VALVE
O	FAILURE AIR BLOWER IN INDUCTION VOLT REG
P	Sch – TO RUN 100°C GRAPHITE TEST
Q	Sch – TEST ZERO COMPLETED
R	Sch – POST TEST ZERO INVESTIGATION

*VARIABLE FREQUENCY POWER SUPPLY

Fig. 6.2. Operating history of the CSPT.

scrammed some 17 times over an 8-month operating period. Circulator operation was delayed for one hour or less after seven of these stops. Some inadvertent stops were caused by manual interruption of scram circuits during on-line maintenance. The addition of bypass circuits will eliminate some of these interruptions.

Six major interruptions in circulator operation were caused by faults in the variable frequency power supplies (VFPS) for the circulators. A change in the stop circuitry, recommended by the manufacturer of the power supplies, and replacement of solid-state components appeared to improve the reliability of VFPS No. 1 and 2. Preliminary discussion with the manufacturer were broached regarding upgrading of the printed circuitry, particularly in VFPS No. 3. VFPS No. 3 was manufactured in 1978 and was loaned to Mechanical Technology Inc., the circulator supplier, for use in testing the prototype circulator plus the two follow-on circulators at the supplier's site. VFPS No. 1 and 2 were manufactured and shipped directly to the CFTL site in 1981.

After Scram No. 11, caused by a fault in No. 3 VFPS, No. 3 circulator would not start. The journal bearing and pivoted pads on the impeller end were scored as shown in Fig. 6.3. The bearings were repaired by MTI, and No. 3 circulator rotary was assembled and bench tested in air in August 1984. The exact cause of the scoring is unknown; however, it is assumed that particles from the corrosion-erosion damage to the type 410 stainless steel impeller end rings[6] may have passed through the bearing.

The bearing damage to No. 3 circulator was discovered on February 22, 1984. TEST ZERO operation was resumed with circulator No. 1 and 2 on February 28.

The loss of forced convection heat transfer in a stopped circulator permits heat to be transported from the process helium; this will overheat the motor windings rapidly. Therefore, the rotary assembly was removed and a heat shield inserted into No. 3 circulator pressure vessel. The resistance of a stopped rotary assembly is about 80% of the head developed by one circulator. With the rotary assembly removed, two circulators can supply the required pressure rise and helium flow.

ORNL-PHOTO 6844-84

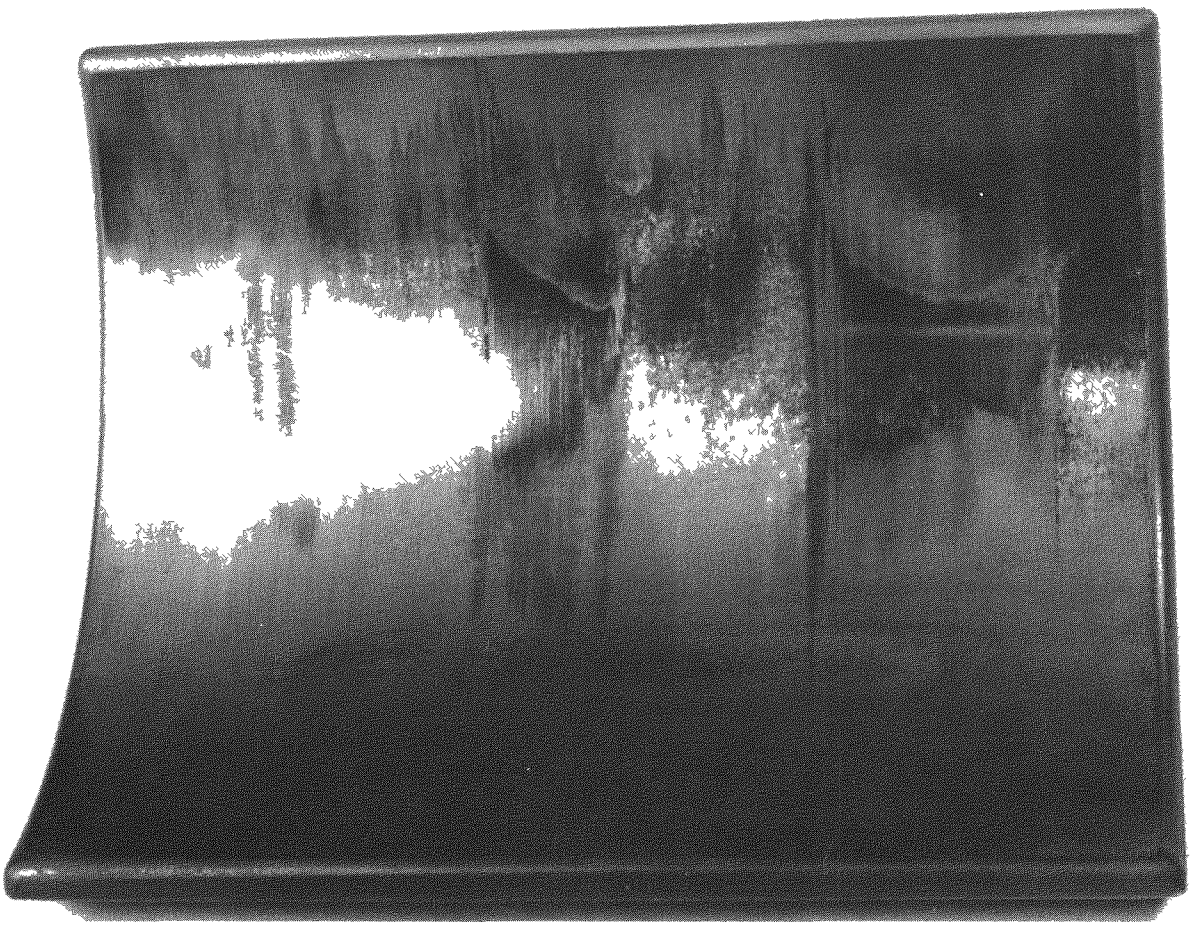

Fig. 6.3. Scored bearing pad for No. 3 circulator.

The temperature at the Teflon flange seal in circulator No. 3 pressure vessel was higher than expected as the loop helium approached the normal 427°C operating temperature. A method for the installation of a water-cooling coil at the flange end of the heat shield was considered; however, this modification would require additional downtime. The temperature of the Teflon flange seal was limited to a maximum of 175°C by maintaining the helium discharge temperature from No. 3 circulator pressure vessel at 335°C rather than the normal 427°C. The electrical power to the helium

heater was increased to provide the required 700°C graphite temperature. This required the addition of more heat with the helium heater and the removal of more heat with the air-cooled helium heat exchanger. The system operated satisfactorily in this mode through the remainder of TEST ZERO until the CFTL was shut down on May 17, 1984.

Circulator No. 1 and 2 have operated for approximately 2900 h in TEST ZERO and 1900 h in TEST P-1, plus approximately 200 h earlier shakedown operation for a total of 5000 h each. No. 1 circulator (the prototype) has been started about 260 times.

Helium heater operation is also shown in Fig. 6.2. This figure shows that electrical power to the heaters was interrupted (scrammed) 18 times over the 8-month operating period. However, the heaters and the attendant heater scram and alarm systems performed quite adequately. Four of the heater scrams occurred because the circulator scrammed. Seven heater power shutoffs were scheduled and were not actually emergency-type scrams.

A heater scram during unattended operation is actuated by either high or low heater helium outlet temperature, low helium flow through the heaters, low loop pressure, and loss of electrical power which could thermally shock the alumina parts of the heaters. A heater scram shuts off the electrical power to the heaters, closes the heater helium flow control valve, shuts off the air-cooling blower, and closes the air dampers to the helium-to-air heat exchanger.

During heater startup and during scheduled heater downtime, the voltage to the heaters is changed in very small increments and the heater helium outlet temperature permitted to reach equilibrium after each voltage change.

Scram E, shown in Fig. 6.2, was caused by fluctuations in heater helium outlet temperature beyond the set limits of the alarm and scram switches. A stainless steel thermocouple holder has been installed at the outlet end of each heater alumina shroud tube to eliminate direct radiation to the thermocouples from the high-temperature HT-molybdenum heater coil, and also to average fluctuations in heater helium outlet temperature caused by movement of the heater coil in the heater flow annulus.

Scram N resulted from failure of the instrument air supply to the heater helium flow control valve, which caused the valve to close. This type heater scram can be prevented by providing a backup nitrogen bottle system paralleled with the air supply system.

As indicated in Fig. 6.2, the original helium heaters that were used during TEST P-1 and during the early part of TEST ZERO were replaced with a modified heater in December 1983.[7]

The major change to the heater, Fig. 6.4, was a linear reduction in the cross-sectional area of the 5.4-mm HT-molybdenum wire to increase the electrical resistance at the lower temperature helium inlet end to provide more uniform heat generation over the heater length.

In June 1984, the heater assembly was removed from the bottom of the CSPT test vessel. The top of the alumina shroud tubes that form the flow annulus around the two HT-molybdenum heaters were cracked slightly. The stainless steel shim stock around each shroud tube held the shroud tubes intact. A small piece of alumina lodged in the flow annulus near the top of Heater No. 1. It caused the flow passage to be somewhat reduced at one side of the heater.

The alumina shroud tubes were removed, and a small amount of foreign material was attached to the surface of the HT-molybdenum heater element in a localized region about 100 mm from the heater inlet. Analysis indicated the material was melted alumina from the heater core mandrel. The helium flow passage was reduced in this region because the heater coil was not concentric. The eccentricity was apparently caused by radial movement of the coil due to a shortened horizontal section of the heater wire forming a pigtail from the electrode to the lowest turn. The HT-molybdenum heater coil appeared in excellent condition.

The HT-molybdenum wire was torch-heated in place near the pigtail at the bottom end, and the first or bottom turn of the coil rotated slightly to increase the center-to-center distance between the two 22-mm-diam TZM-molybdenum electrodes. Thus, the center alumina mandrel and heater coil were moved to a concentric position in the shroud tube. The surface of the HT-molybdenum was cleaned, and new alumina shroud tubes installed.

ORNL-PHOTO 6653-84

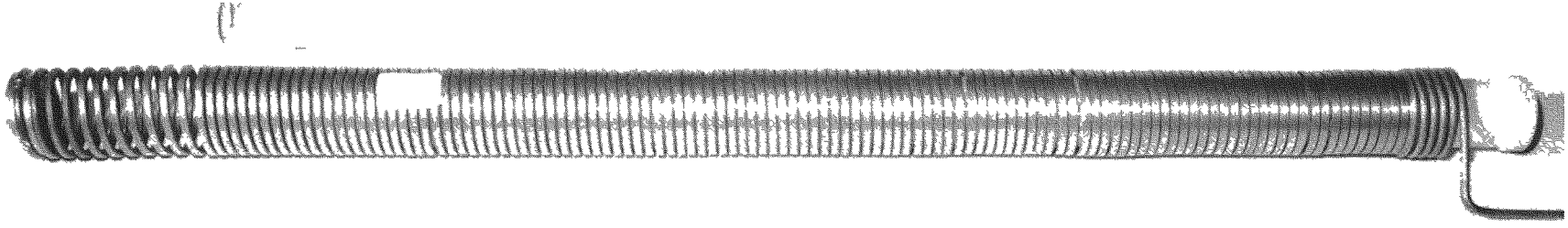

Fig. 6.4. Modified HT-Molybdenum heater element of CSPT.

Stainless steel thermocouple holders were installed on top of the shroud tubes. These are expected to eliminate radiant heating from the high-temperature heater wire on the heater helium outlet temperature thermocouples. These holders will also average the readings from the four exit thermocouples on each heater.

The original helium heaters operated for 120 h in TEST P-1 and 380 h in TEST ZERO. The modified heaters operated for 1820 h in TEST ZERO and have been reinstalled for use in TEST ONE.

6.2.2.2 TEST ZERO Operation

Referring to Fig. 6.2, especially continuous helium flow was provided by the circulators from a restart on February 28, 1984, until the completion of TEST ZERO; however, when the graphite temperature was increased on March 2, 1984, to 700°C after operating for 2 days at 650°C, it was noted that the differential pressure across the loop helium full-flow filter was gradually rising. Table 6.5 summarizes the progressive increase in filter differential pressure as operation continued. The magnitude of the pressure differential and the rate of increase was significantly less than the filter plugging experienced on December 1, 1983. On Saturday, March 3, operation of the helium heaters was temporarily discontinued. The filter differential pressure decreased from 46.7 to 45.9 kPa when the heaters were turned off. The circulators continued to operate over the weekend, and by Monday the filter differential had dropped to 40.7 kPa.

Since the pressure drop across the filter was still acceptable, plans were made to resume heater operation at a graphite temperature of 500°C at the existing loop moisture ~5 ppm and hydrogen ~450 ppm condition. If no filter plugging occurred, the plan was to operate at incrementally higher graphite temperatures to the original 700°C condition.

No filter plugging occurred at 500° and 600°C operation, even at a loop moisture concentration of 10 ppm, double that at which previous filter plugging had occurred. The heaters were again temporarily shutoff on March 7, and the loop was vented to reduce the hydrogen concentration to approximately 200 ppm and increase the moisture concentration to approximately 20 ppm. The helium heaters were again turned on March 16, and

Table 6.5. TEST ZERO summary of filter differential pressure history

Time period	Graphite temperature (°C)	Heater power (kW/htr)	Filter helium flow (ACFM)	Filter ΔP		Number circ. oper.	Concentration of gaseous impurities in loop, ppm			Filter rate of ΔP increase (kPa/hr)
				Initial (kPa)	Final (kPa)		Moisture	Hydrogen	Carbon monoxide	
12/2/83 to 1/26/84	Filter replaced									
1/20 to 1/31/84	427	0	840	17.4	17.4	3	50 to 11	394 to 486		0
1/31 to 2/10/84	700	116	840	17.4	18.2	3	15 to 5	486 to 271		~0
2/10 to 2/28/84	No. 3 circulator removed — installed heat shield									
2/28 to 2/29/84	260	0	770	13.7	13.3	2	3 to 6	211 to 219		~0
2/29 to 3/1/84	650	155	782	16.9	17.0	2	5 to 3	510 to 476		~0
3/1 to 3/3/84[a]	700	180	780	20.4	47.3	2	3 to 5	471 to 659		0.4 to 1.2
3/3 to 3/7/84	280	0	716	42.8	40.2	2	5 to 16	630		~0
3/7 to 3/9/84	500	79	350	15.3	14.9	2	8	494		~0
3/9 to 3/12/84	600	122	560	28.1	27.1	2	10	489		~0
3/12 to 3/16 Adj H_2 & H_2O	308	0	705	37.3	37.5	2	20	198		~0
3/16 to 4/5	650	160	705	36.9	36.8	2	20 to 5 to 18	200 to 180	5 to 82	~0
4/5 to 4/10	675	171	730	39.2	50.7	2	17 to 12 to 17	190 to 197	85 to 121	0.29
4/10 to 4/16	700	183	748	56.2	64.9	2	13 to 16	209 to 198	128 to 176	0.08
4/16 to 4/17	9	0		8.2	8.2	2	16 to 5	189	177	~0
4/17 to 4/18	650	161	735	62.7	62.2	2	12 to 19	186 to 165	166 to 160	~0
4/18 to 4/23	700	183	728	66.5	75.9	2	21 to 17	196 to 491	158 to 178	0.08
4/24 to 4/26 20% O_2	17	0		1.9	1.9	2	40 to 53		27 to 29	~0
4/26 to 5/14	700	183	710	75.5	100	2	8 to 20	184 to 185	1 to 135	0.06 to 0.08
5/14 to 5/15 H_2 1200 ppm	700	183	680	100.2	101.1	2	26 to 30	1199 to 1130	135 to 125	0.08
5/15 to 5/16 H_2 1200 ppm	725	196	652	115	129.2	2	24 to 18	1107 to 1071	132 to 144	0.9 to 0.6
	Heaters off at 15:55 on 5/16/84 Circulators off at 9:50 on 5/17/84									

[a]Filter again starting to plug.

operation resumed at a graphite temperature of 650°C. Operation continued at this graphite temperature for the remainder of March. The filter differential pressure remained essentially constant. Definite oxidation of the graphite was occurring as indicated by the increase in the carbon monoxide concentration.

Some difficulty was encountered in maintaining the moisture level because of partial plugging of the very small orifice in the hydrogen feed control valve to the copper-oxide moisture generator. The valve was cleaned several times. The valve has an upstream filter; however, it was believed that occasional flow reversals downstream of the valve were occurring when the supply pressure and volume flow of the helium carrier gas stream and the hydrogen gas stream were varied. A downstream filter will be installed in preparation for TEST ONE.

On April 5, the graphite temperature was increased from 650 to 675°C, the filter differential pressure increased.

At 700°C graphite temperature, the filter differential pressure increased at a rate of ~0.08 kPa/h over 6 days through April 16. The graphite was cooled to room temperature and again brought to 700°C through April 23, and the ~0.08 kPa/h rate of filter differential pressure recurred. The formal TEST ZERO was completed on April 23. Operation was continued in an attempt to determine the mechanism causing filter plugging. The graphite was then deliberately exposed to a "synthetic" air mixture of 20% O_2 and 80% helium at room temperature. After evacuating the loop and reestablishing the 10:1 hydrogen to moisture ratio and reestablishing the 700°C graphite temperature, the filter differential pressure again increased at approximately 0.08 kPa/h. On May 15, the hydrogen concentration was increased from ~200 to 1200 ppm while maintaining a graphite temperature of 700°C, the rate of differential pressure increase across the filter remained

On May 16 the graphite temperature was increased from 700° to 725°C, and the rate of increase in the filter differential pressure increased by a factor of 10.

By then, the filter differential pressure had exceeded the range of the differential pressure gage and the added system resistance was reducing the total circulator flow toward the surge region. The circulators were stopped on May 17, 1984, to conclude this TEST ZERO post-test operation.

The filter was removed and maintained under an inert atmosphere. Three of the seven filter tubes were given to the Metals and Ceramics Division for dissection and analysis. This analysis was not completed because of termination of funding for TEST ONE preparation. New filter tubes have been welded into the tube sheet and the filter assembly reinstalled into the CFTL filter housing. However, before resuming TEST ONE operation, it is recommended that the filter analysis be completed to determine if the existing 200 × 1400 wire mesh type filter elements should be replaced by a different type of filter element.

The bottom surface of the TEST ZERO support plate is about 38 mm above the outlet from the helium heaters. This surface indicated some erosion in the region directly impacted by high-velocity, high-temperature helium from the heater. It has been speculated that this carbon, which was eroded from the bottom of the support plate, may be the source of plugging in the CFTL full-flow helium filter during the latter phases of TEST ZERO. The support plate for TEST ONE is machined from type 304H austenitic stainless steel.

6.2.3 Summary of Results of TEST ZERO, Phase Two of the Core Support Performance Test Series — R. A. Strehlow and H. C. Young

6.2.3.1 Description of the Core Support Performance Test Series

The objective of the Core Support Performance Test (CSPT) is to perform an accelerated corrosion of the full-sized, loaded, graphite core support structure for HTGR under reactor conditions of pressure, temperature, and flow.

The Component Flow Test Loop facility in which the CSPT is conducted and the CSPT series has been described earlier.[8,9] The loop circulates helium with added and controlled impurities at a total flow of 1.7 kg/s. Part of this flow is directed past the graphite test structure at 700°C or higher and at a pressure of 7.24 MPa. The facility has a physical volume of 3.0 m^3 and permits the testing of graphite structures as large as 200 mm diam and 1.8 m in length. The summary of results of the first test in the CSPT series, TEST P-1, has been presented.

For TEST ZERO, impurities of moisture, hydrogen, and argon were added at controlled rates to the circulating helium. During the traverse of gas around the loop, the gas flowing past the graphite test piece was heated from 300°C to the test temperature of about 700°C. About two-thirds of the total flow was used as an attemperating flow to maintain the maximum design temperature of 600°C at the pressure boundary. Constant pressure was maintained by intermittent additions of helium to balance the flow that was used for analysis or was removed from the loop due to leaking or venting. Argon was used as a tracer to measure the total flow that leaked or was vented or withdrawn.

The essential information to be obtained in the CSPT series is the extent of graphite degradation that occurs in the seat-post region under these conditions of flow, temperature, pressure, and stress during the operating life of the reactor. The critical structural components will be tested under actual operating conditions with increased concentrations of oxidants used to increase the rate of corrosion to obtain meaningful data in a practical experimental test period of six months duration. In particular, the test will investigate the performance of the structure in that region of the seat-post interface where Hertzian stress occurs.

The CSPT is based on the kinetic expression for the oxidation of graphite that shows the oxidation or corrosion rate can be decreased by the addition of hydrogen. This permits independent control of the amount of diffusion (penetration oxidation), which is proportional to both the water concentration and the oxidation rate. Thus, accelerated corrosion can be obtained in which the extent of penetration is matched to that of a longer exposure. This matching is accomplished by considering the kinetic expression obtained for the specific material, the burnoff dependence, the diffusion processes, and the CO-shift reaction (which could affect the concentration gradients in the pores).

The calculated extents of burnoff and the penetration (depth at which the burnoff equals 1/e of that at the surface) are compared in Table 6.6.

Table 6.6. Calculated extents of burnoff and penetration 700°C, 7 MPa

	Burnoff 10^3 (g/cm^2)[a]	Penetration (mm)
Reactor — 30 years		
0.2 ppm H_2O	2.5	4—7
Test — 6 months		
20 ppm H_2O	0.9—3.6	4—15
50 ppm H_2O	1.3—13.0	5.4—15

[a]All at a hydrogen to steam ratio of 10.

6.2.3.2 Objectives of TEST ZERO

There were two principal objectives of TEST ZERO. The first was to demonstrate the ability to maintain specified levels of impurities in the helium during an accelerated oxidation of a graphite test structure. The second was to determine the amount of the carbon monoxide produced by the corrosion reaction during selected time intervals.

In addition to these two principal objectives, there were additional objectives for TEST ZERO. One was to compare the total oxidation with that predicted from small-scale, low-pressure laboratory measurements. Others were to determine any presence of adventitious material, to demonstrate installation and removal of the specimens, to measure corrosion rate behavior as it varies with time and other conditions of the test, to develop information for specification of quality assurance procedures for the final test, and to evaluate NDT (nondestructive test) capability. Some of these ancillary objectives are discussed below.

The graphite test structure for TEST ZERO was constructed from off-the-shelf Stackpole 2020 graphite without an external structural load. The structure consisted of four 480 mm by 196 mm diam right cylinders stacked in the CFTL liner. A stainless steel structure was positioned at the top of the column to prevent movement of the cylinders and to guide thermocouples that were inserted into the graphite stack.

Because of the presence of a black iron carbide and carbon powder that had formed during the conduct of TEST P-1,[10] the lowermost (upstream) piece of the test structure was modified to include a set of small test

coupons mounted in a machined channel in the test piece. It was expected that the coupons would be used to assess whether iron or other adventitious material had an effect on the corrosion of the graphite or if the powder might be deposited on the surface of the graphite specimens. The thirty-four coupons were of both off-the-shelf Stackpole 2020 and from the Lot 1 of nuclear quality Stackpole 2020.

The two principal objectives of TEST ZERO, to demonstrate operational capability of the CFTL and to measure an extent of oxidation, were both addressed by considering the chemical composition of the impurities in the CFTL during the test.

In TEST ZERO and the planned final test, oxidation of graphite by moisture in the presence of hydrogen to produce carbon monoxide is the basic corrosion reaction. By measuring the amount of carbon monoxide produced during the experiment, it is possible to calculate the total amount of oxidation that has occurred on the entire graphite test structure.

Controlled additions of moisture were made. The moisture is generated in trace levels of about 20 ppm (140 Pa) by diluting a mixture of hydrogen, at a level of 1 to 10% in helium with a larger flow of helium. This very dilute mixture of hydrogen in helium is then converted to moisture by passing the gas through a copper oxide bed held at a temperature of 500—550°C.

Hydrogen was held at a higher level of ten times the moisture by intermittent additions of a hydrogen-helium mixture. Argon was added intermittently and was also analyzed by gas chromatography. The decay of argon concentration with time permits a satisfactory measurement to be made of the total venting and leakage flows from the system. Carbon monoxide (CO) production was measured by analyzing the CO present in the loop continuously by gas chromatography and by adjusting this inventory for the amount lost or vented from the loop as measured from the argon loss.

6.2.3.3 TEST ZERO Operations and Studies

The operating experience for TEST ZERO is shown in Fig. 6.2. The total operating time of the circulators during TEST ZERO and additional

tests conducted after completion of TEST ZERO was 3270 hours with no significant interruption from February 28 to the close of the period of additional studies on May 17. The helium heaters accumulated 220 hours during the period of TEST ZERO. Five periods of operation occurred during TEST ZERO. These periods are described in Table 6.7.

Table 6.7. Dates of five time periods during the conduct of TEST ZERO

Period No.	Dates	Summary of operation
1	Nov. 14—Dec. 2, 1983	Startup, operation terminated after filter plugging occurred
2	Jan. 1—Feb. 11, 1984	Restart, operation terminated after power supply failure and impure helium found
3	Feb. 29—Mar. 28, 1984	Restart, operation terminated after filter plugging recurred
4	March 30—Apr. 23, 1984	Continued operation at 700°C and restarted for study of filter plugging at lower test structure temperatures
5	Apr. 24—May 16, 1984	Operation continued for additional tests after the objective of TEST ZERO were met

The leakage and venting rate was monitored by argon concentration measurements. Values of the leakage and venting rate indicated that the residual leakage of this system was approximately 0.02% per hour. Rates that were observed to be higher than this general level led to leak checking and correcting.

Analytical data showing both the performance of the systems and measurements of flow rates and total oxidation rate have been presented.[11] The operation and results during five periods of TEST ZERO operation are summarized as follows:

A. Test Period No. 1

The first period of the test was characterized by an increase in both water and carbon monoxide as the graphite was heated to 700°C. This is attributed primarily to outgassing processes. Evidence of oxidation was provided by a subsequent increase in carbon monoxide associated with a like decrease in moisture concentration.

The oxidation rate observed is much higher than had been anticipated in the design of the water vapor admission system, and this higher rate made it somewhat difficult to achieve a stable oxidation rate until the end of Period No. 4 of the test.

The first period of the test ended when the filter pressure drop began to increase rapidly; this led to the termination of the operation for replacement of the filter. Particulates found in the filter consisted of a partly magnetic powder that by analysis was found to consist of 30% carbon with the remainder being iron with some in the form of iron carbide, Fe_3C. After filter replacement, the test was restarted for the second period. The origin of the particulates was viewed as either residual particulates from TEST P-1 or a new phenomenon associated with the oxidation of the graphite test structure.

B. Test Period No. 2

A rapid oxidation occurred demonstrated by the decrease of moisture from 17 to 2 ppm and the increase in CO concentration from 2 to 20 ppm. This led to a decrease in the oxidation rate due to limited moisture after the initial part of the second period. The period ended with the failure of a circulator power supply February 10.

C. Test Period No. 3

After removal of the circulator and its replacement by a heat shield assembly, a restart resulted in a rapid increase in carbon monoxide level and simultaneously an increasing pressure drop across the filter. Although it appeared that corrosion of graphite was associated with the apparent plugging of the filter, a systematic study was designed to rule out several other possibilities. A staged

increase in temperature was conducted to see if other possible sources of particulate might be operative. Because the pressure drop across the filter did not increase significantly during a period of nearly full temperature but low graphite oxidation rate, the oxidation of graphite was believed to be associated with the generation of particulates.

D. Test Period No. 4

The fourth period was to obtain a steady state oxidation rate and develop additional operating experience. The temperature was raised from 600° to 675°C after it appeared that a steady state had been reached during the period from April 3 to April 5. A steady state again appeared to have been reached in the period from April 8 to April 10. At that time, the temperature was increased to 700°C. Moisture data once again reflected the oxidation behavior. A steady state was reached and maintained for four days ending on April 23; at this time the principal objectives of TEST ZERO had been met. Both during Periods Nos. 3 and 4, the oxidation rate of the graphite test structure decreased significantly.

From the carbon monoxide concentrations, the argon decay rate, and the moisture level, it is possible to calculate a global oxidation rate for the entire TEST ZERO graphite structure with a surface area of approximately 1.2 m^2. The results of these calculations are compared with modeled (predicted) data in Table 6.8. The initial oxidation rate is high, but the agreement with modeled results based on data from GA appears to be satisfactory. A generally decreasing oxidation rate with time was evident.

E. Test Period No. 5

Because of the smooth operation of the CFTL at the end of TEST ZERO, additional tests were conducted to provide additional data for specification of the final test, TEST ONE, and to simulate the effect of inadvertent or planned exposures or perturbations of operating conditions as well as to check for conformity with the expected hydrogen dependence in the kinetic expression.

One of the additional tests involved exposing the test structure to oxygen simulating an air exposure. The oxidation rate measured after this exposure and a reestablishment of oxidation conditions is shown in Table 6.8. It is evident that a significant increase in oxidation rate was occasioned by this "air" exposure. This result is attributed to iron impurities in the off-the-shelf graphite used for the test.

The coupons that had been installed in the test structure were removed and weighed. Nuclear quality material used as a reference showed no weight loss. The off-the-shelf 2020 grade showed weight losses as shown in Fig. 6.5. Preliminary examination indicated that the different levels of weight loss may be associated with the inorganic constituents or impurities of the graphite.

Table 6.8. Observed and modeled oxidation rates in TEST ZERO

Condition	mg/h-Pa(H_2O)[a]	Modeled
Initial, periods 1-3	≥0.55	0.20
After 2 days, periods 2, 3	0.22-0.30	
After 2 days, period 4	~0.10	
Steady state		0.05-0.07
After room temperature excursion		
Initial	0.21	
After 3 days	0.10	

[a]0.1 mg/h-Pa = 1.2 μg/h-cm^2, 20 ppm H_2O in CSPT.

6.2.3.4 Conclusions

The impurity control and measurement systems installed in the CFTL operated satisfactorily.

Oxidation rates were measured with a sensitivity of less than 1 μg/h-cm^2 at 20 ppm water concentration in the CSPT.

Scaling of oxidation rates from results on gram size thin species at one atmosphere pressure to 100 kg size and 7.24 MPa has been satisfactorily accomplished.

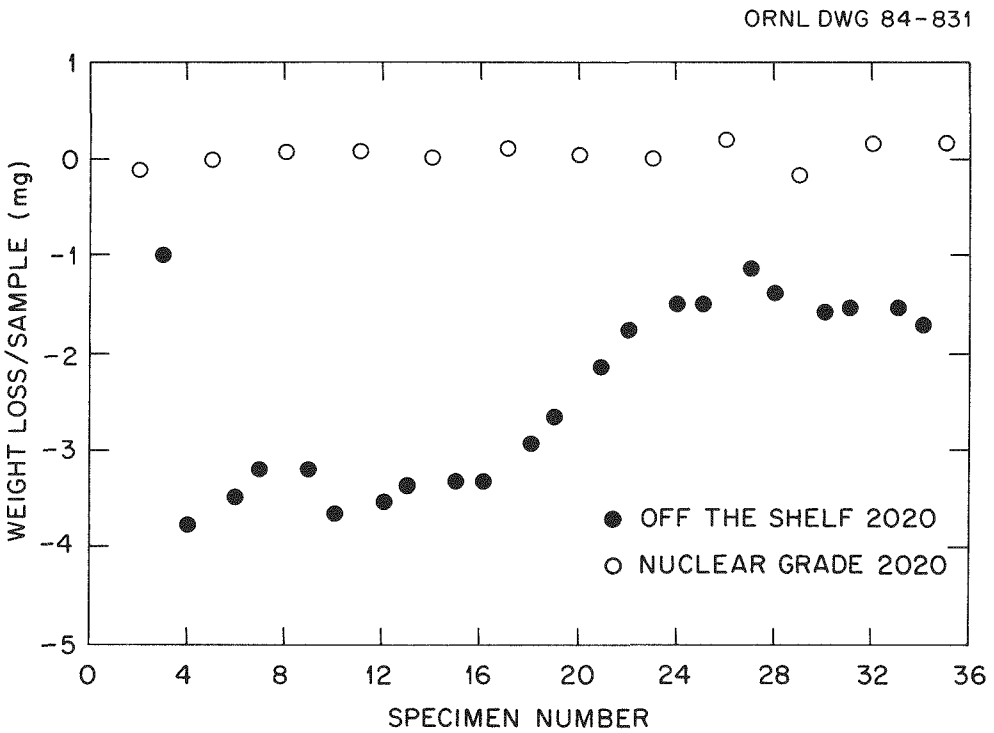

Fig. 6.5. Weight loss of graphite coupons, TEST ZERO.

Because of smooth operation of the CFTL, additional tests were conducted for three additional weeks.

The results of one of these tests showed that exposure to oxygen at low pressures will significantly increase the oxidation rate from its prior value.

6.3 GRAPHITE MATERIALS — CORE (W.B.S. 1602.02)

6.3.1 Fracture Toughness of Anisotropic Graphites — C. R. Kennedy

The strength of most grades of graphite tends to be anisotropic. The strength in the preferred c-axis direction is fairly weak compared to the preferred a-axis direction. The strength differences in the preferred directions are generally assumed to be a result of the much higher Young's modulus in the a-axis compared to the c-axis direction. The Griffith-Irwin expression for fracture,

$$\sigma_f = (G_{IC}E/2\pi c)^{1/2} = K_{IC}/(2\pi c)^{1/2} , \qquad (6.1)$$

is used to correlate the properties, where

σ_f = fracture stress,

G_{IC} = strain energy release rate,

E = Young's modulus,

c = radius of the critical defect,

K_{IC} = fracture toughness.

However, fracture toughness tests[12] of some fairly anisotropic electrode grades yielded results that indicated that the fracture toughness was essentially isotropic. To investigate this phenomenon further, a series of short-rod fracture toughness specimens was machined from a block of AGOT graphite with the specimen axis at 0, 30, 45, and 90° to the extrusion axis. Grade AGOT is almost identical to grade H327, which is used as a fuel block grade in Fort St. Vrain. The physical properties previously obtained from this block are given in Table 6.9 that demonstrates the degree of anisotropy. The short-rod specimens were made with the geometry to force the crack to propagate in either the direction normal to the theta vector or normal to the cross product of the axial and theta vector.

Table 6.9. Physical properties of AGOT graphite

	With grain	Against grain
Flexural strength (MPa)	12.3	7.8
Young's modulus (GPa)	13.0	6.7
Coefficient of thermal expansion (mm/m·K)	1.5	2.5
Electrical resistivity (μΩ-m)	5.0	9.1

Longitudinal and shear velocities of each specimen were measured and the elastic constants were calculated. These results are given in Fig. 6.6 comparing the actual results to predicted results using the Kennedy approximation[13] based upon the assumption that the shear velocity, C_{44}, does not vary with angle. The electrical resistivity was also measured using eddy-current techniques. The results are given in Fig. 6.7, also demonstrating the anisotropy of the AGOT graphite.

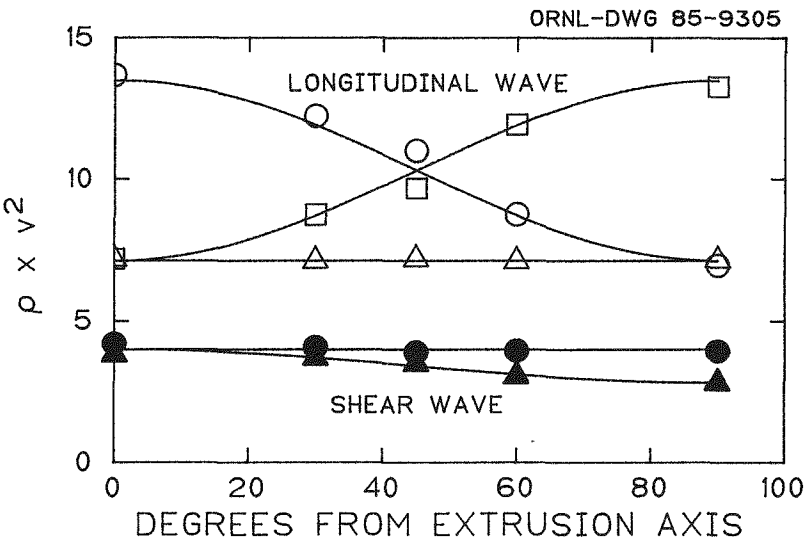

Fig. 6.6. The effect of orientation on the sonic velocity of grade AGOT graphite.

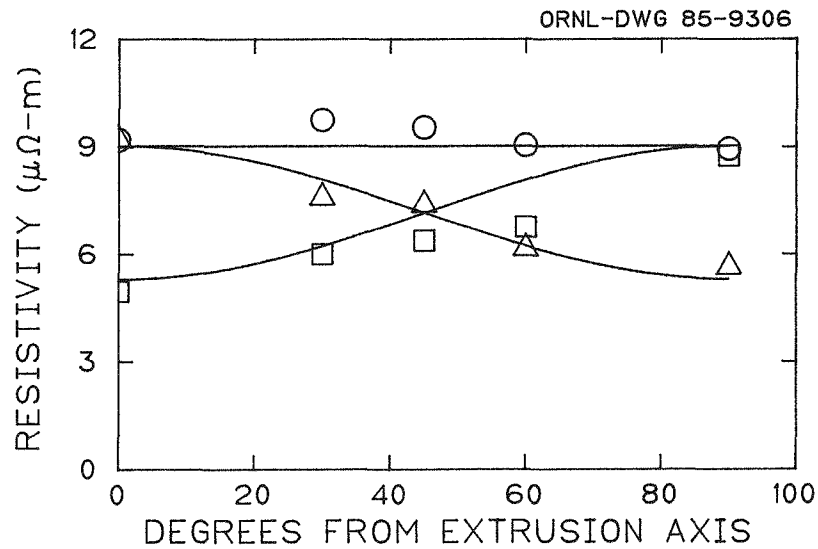

Fig. 6.7. The effect of orientation on the electrical resistivity in grade AGOT graphite.

The results of the test series do confirm those of E. P. Kennedy[12] that the fracture toughness was essentially isotropic. The ORNL AGOT results are shown in Fig. 6.8, actually indicating that there was even a slight reduction in the fracture toughness in the strongest direction. The calculated values of the strain-energy release rate, G_{IC}, are given in Fig. 6.9. As would be expected from Figs. 6.6 and 6.8, G_{IC} decreased significantly with increasing deviation from the extrusion axis for those specimens oriented with the crack normal to the cross product at the axial and theta vectar. These results are in sharp conflict with the initial assumption that the strength difference are related to the differences in Young's modulus. It is readily apparent that the fracture strength is not controlled by Young's modulus. It seems apparent from Eq. (6.1) that if K_{IC} is isotropic, the sole factor controlling the fracture strength is the defect size.

The defect size can be measured independently by sonic attenuation as has been previously demonstrated.[14] The results of sonic attenuation measurements as a function of angle are given in Fig. 6.10. This is a natural result of the projection of the filler particles with a high shape factor used to make grade AGOT. The ratio in strength can then be calculated using the square root of ratio in defect size from Fig. 6.10.

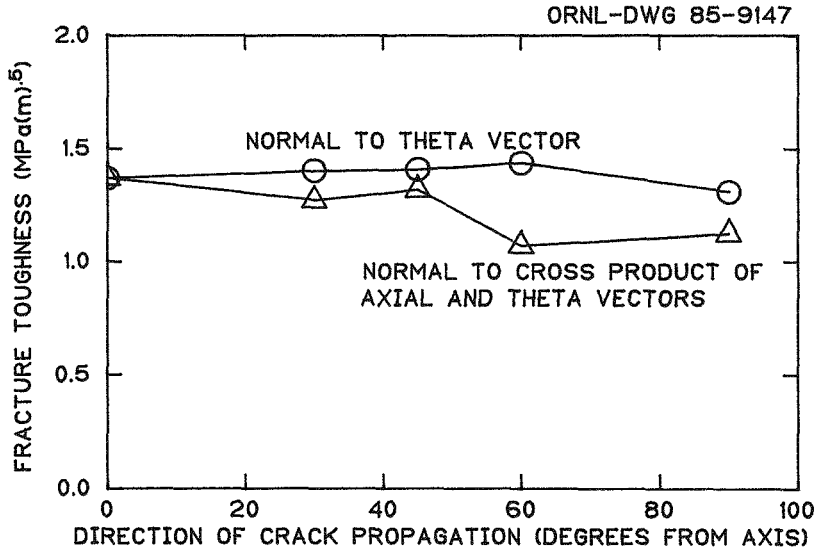

Fig. 6.8. The effect of orientation on the fracture toughness of grade AGOT graphite.

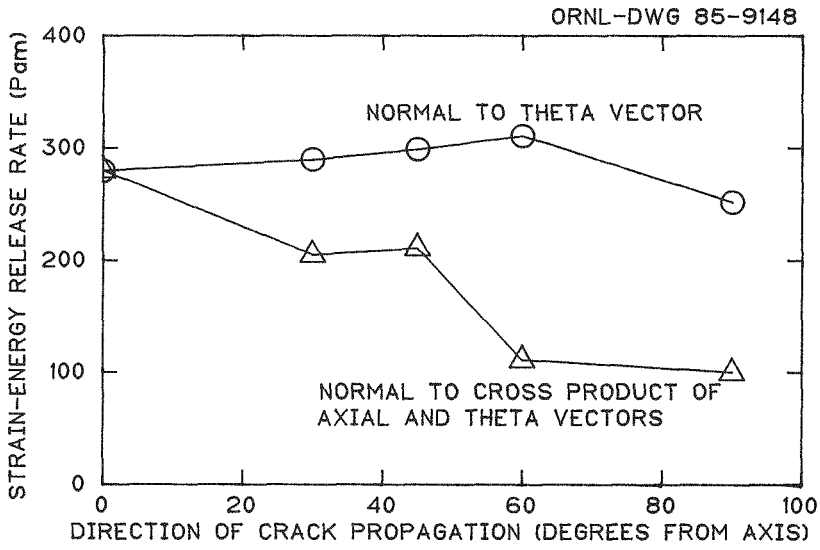

Fig. 6.9. The effect of orientation on the strain-energy release rate of grade AGOT graphite.

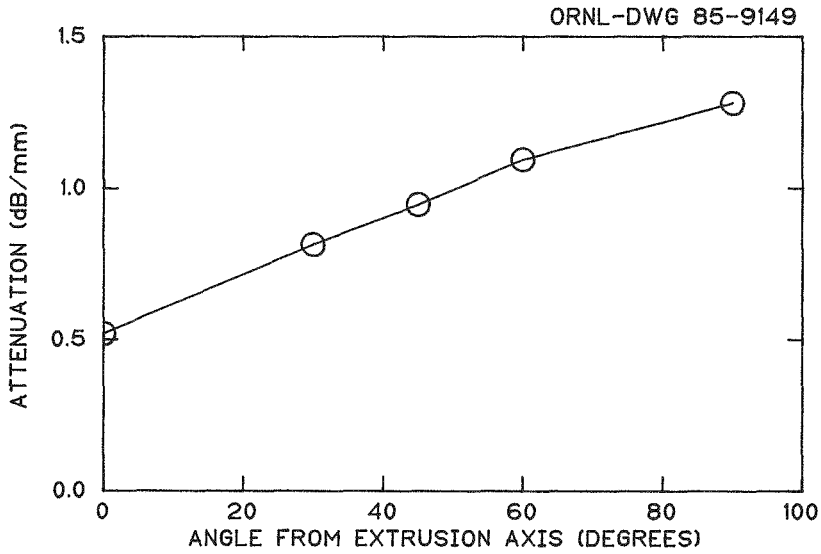

Fig. 6.10. The effect of orientation on the sonic attenuation in grade AGOT graphite.

The calculated value is 1.56 compared to a ratio of 1.57 from Table 6.9. The results from Fig. 6.9 also support the description by E. P. Kennedy of the significance of crack branching over tortuosity in increasing the energy for fracture. The increase in energy by the tortuosity factor is a result of forcing the crack to move up and around filler particles misaligned for each cleavage. Crack branching increases the energy required for fracture by reducing the stress intensity at the crack tip and by the actual increase in the number of fracture faces created by the branching. The case where the crack is propagating normal to the aligned particles, the increased tortuosity of the crack path would dominate as the energy absorbing mechanism. In the case where the crack is propagating parallel to the aligned particles, crack branching would dominate as the energy-absorbing mechanism. It seems to be clear that crack branching requires a much higher energy for fracture than does tortuosity.

These results are significant in that they show clearly that it is the defect size that controls the anisotropy in strength of graphite. This is in contrast to the past assumptions that variations in Young's modulus controlled fracture. It also seems apparent from these studies that crack branching is a significant factor in increasing the energy required for fracture.

6.3.2 Effect of Thermal Cycling Graphite Above the Irradiation Temperature — C. R. Kennedy

We have been careful not to exceed the irradiation temperature in measuring the coefficient of thermal expansion. However, now that all measurements have been made and the specimens have been brittle-ring tested, several specimens have had their expansion measured above the irradiation temperature. These experiments were performed on the hypothesis that the voids giving rise to the thermal expansion accommodation coefficient have been largely eliminated by the radiation-induced c-axis crystallite growth. When the specimens are cooled down to room temperature after irradiation, the voids presumably are regenerated or new voids created to accommodate the c-axis thermal contraction, thus reducing the bulk (macroscopic) coefficient of thermal expansion (CTE). However, when the specimens are heated to temperatures exceeding the

irradiation temperature, there should be an abrupt increase in the CTE as the accommodating voids are again eliminated. This is exactly what was observed and is shown in Figs. 6.11 through 6.14. The extent of the volume expansion occurring in the thermal cycle was found to be related to the volume change that had occurred during the irradiation. This expected result is shown in Fig. 6.15.

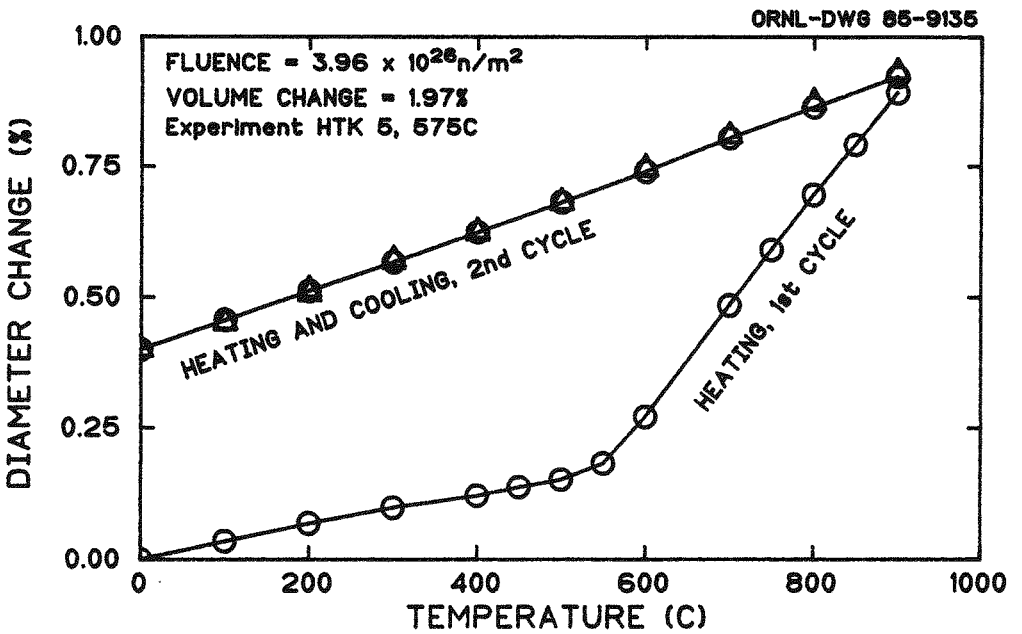

Fig. 6.11. The effect of heating irradiated grade ASR1RV graphite above the irradiation temperature.

An interesting observation is that the CTE above the irradiation temperature exceeds 20 μm/m-K in all directions. This is almost equal to the thermal expansion coefficient of the *c*-axis. Since the *a*-axis expansion coefficient is essentially 0, this implies that the bulk CTE is a result of *c*-axis-orientated crystals in series with no interaction between the *a*-axis material. When this condition occurs, it is certain that structural degradation has occurred. This also requires consideration of whether room-temperature evaluations of irradiated graphite really represent the physical properties of the material at the temperature of irradiation.

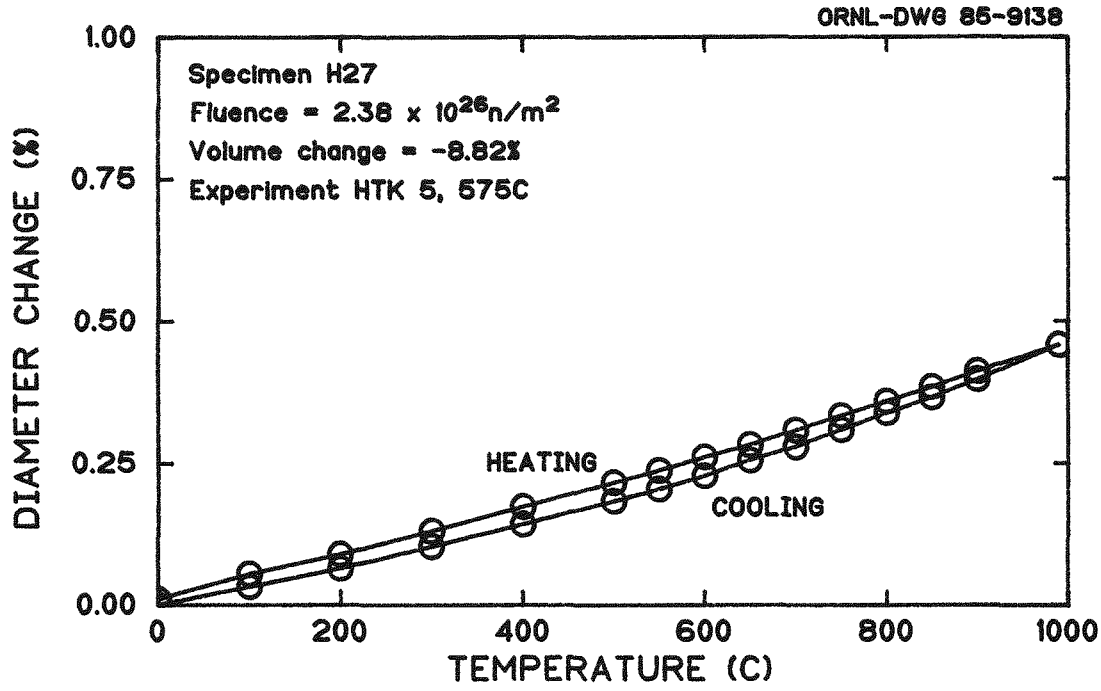

Fig. 6.12. The effect of heating irradiated grade H451 (426) above the irradiation temperature.

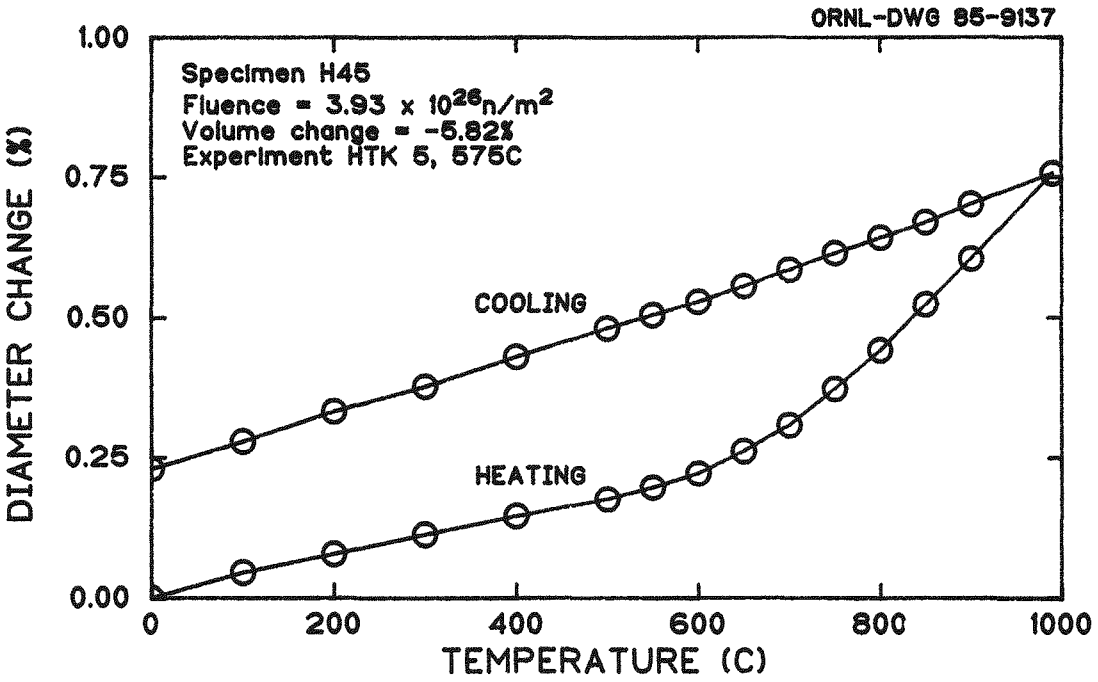

Fig. 6.13. The effect of heating irradiated grade H451 (426) above the irradiation temperature.

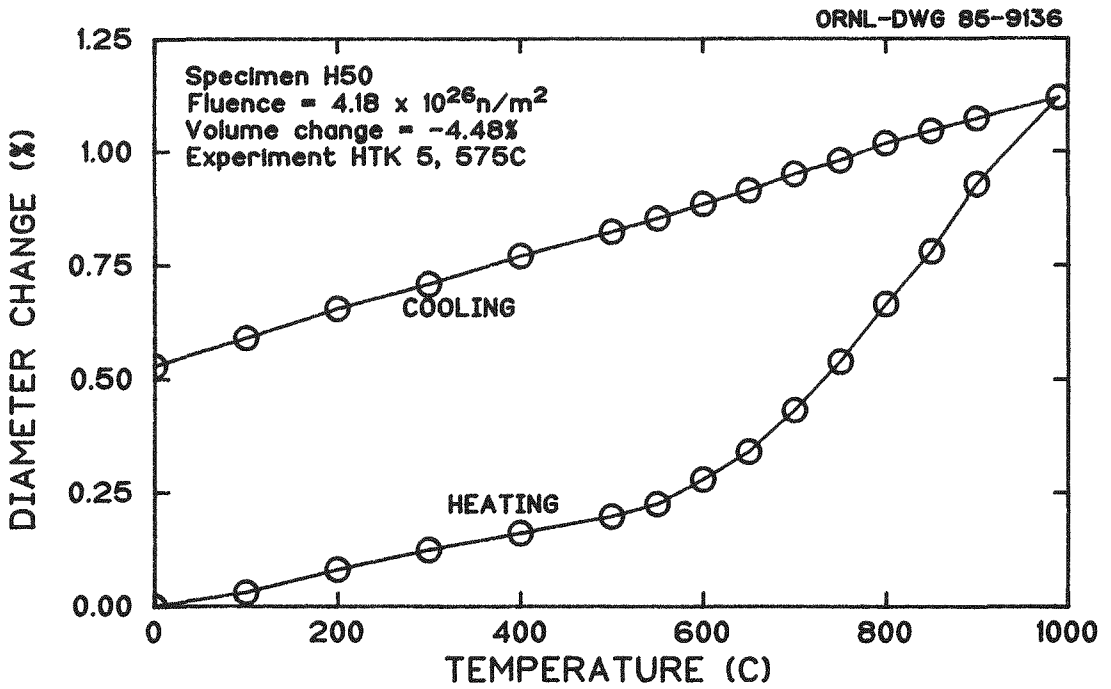

Fig. 6.14. The effect of heating irradiated grade H451 (426) graphite above the irradiation temperature.

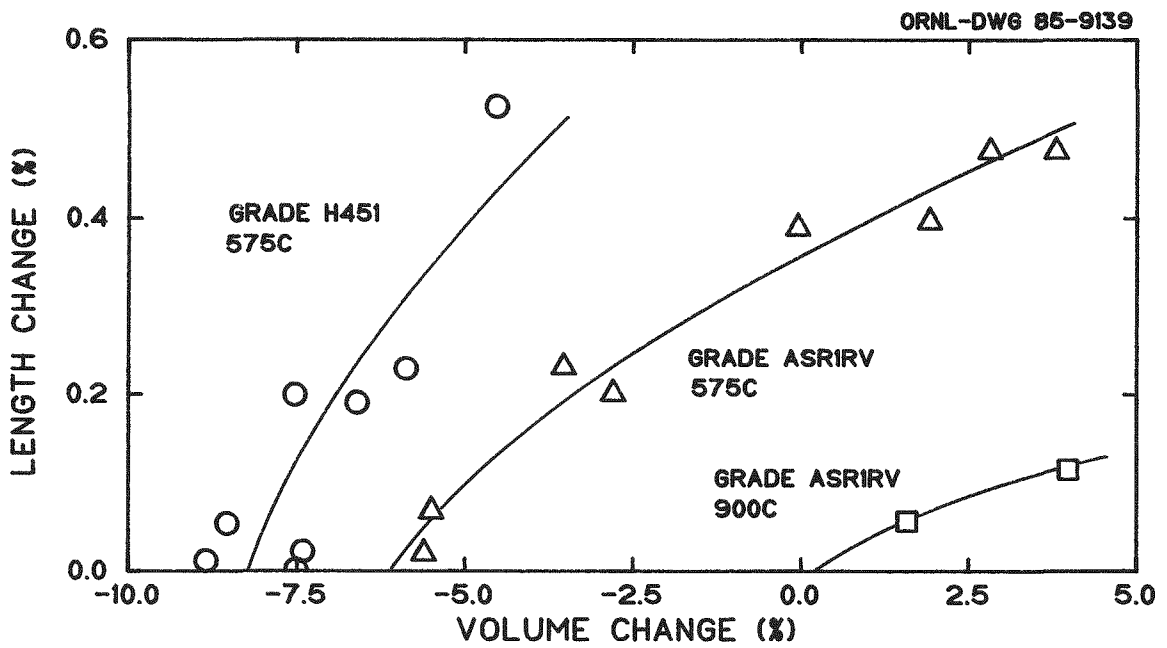

Fig. 6.15. The effect of volume expansion on the thermal cycle length change.

These studies also offer a chance to further confirm the actual irradiation temperature of each experiment. The HTK-5 results did not exactly agree with those of HTK-3, although they were supposed to have been run at the same temperature. Without calibration experiments, temperatures cannot be exactly determined; however, it is fairly clear from these experiments that HTK-5 ran about 50°C less than HTK-3. This is in good agreement with the dimensional change results. Estimates can be made that indicate the experiment temperatures were 630°C for HTK-3, 700°C for HTK-4, and 575°C for HTK-5.

Estimates of the operating temperature of HTK-6 cannot be made because most of the graphites did not exceed maximum densification and the effect is much smaller.

6.3.3. Development of H451I Graphite — C. R. Kennedy

Studies have indicated a potential need for greater strength in the radial direction of the high-temperature reactor reference graphite grade H451. A program to develop this grade has been initiated with the new material being fabricated by Great Lakes Research Corporation, nondestructively evaluated by the Oak Ridge National Laboratory (ORNL), and tensile tested by GA Technologies, Inc. Additionally, fracture-toughness testing and irradiation testing of representative billets were also performed at ORNL. The new grade of graphite is made with the same raw materials as H451 but with a finer particle size and by molding rather than extrusion. The new grade is designated H451I.

The concurrent development of nondestructive evaluation techniques with the development program and destructive testing is essential to define the limits of acceptability. Sonic and eddy-current testing techniques extended from fine-grained aerospace graphite evaluations were used to measure the conductivity, elastic constants, and sonic attenuation. These evaluations yield good estimates for both the mean strength and the variability in strength. Evaluation of larger billets demonstrates the inspectability of H451I and indicates that inspecting full-size billets should be feasible. The fracture toughness of H451I was found to be equal to or higher than standard H451. The irradiation characteristics at 600 and 900°C were equivalent to H451.

While the primary goal of demonstrating the feasibility of creating an improved H451 was accomplished, it must still be demonstrated that large full-scale billets can be reproducibly molded to meet specifications.

6.4 GRAPHITE TECHNOLOGY (W.B.S. 1602.03)

6.4.1 Higher Moments of the Weibull Distribution* — W. P. Eatherly

The calculation of the second, third, and fourth normalized central moments of the Weibull distribution has been completed. The central moments of the distribution are defined as

$$\mu_n = \theta^n \int_0^\infty (x - \mu)^n \, f(x) dx \quad , \qquad [6.2]$$

where μ_n is the n-th central moment, θ a scaling parameter, μ the mean, and $f(x)$ the probability density function (pdf). The variance is given by

$$\sigma^2 = \mu_2 \qquad [6.3]$$

and the normalized central moments by

$$\beta_n = \frac{\mu_n}{\sigma n} \, . \qquad [6.4]$$

Our objective is to calculate asymptotic values for β_n as the Weibull exponent m becomes large compared to unity.

We thus desire a series of the form

$$\frac{\mu_n}{\theta^n} = \sum_{i=0}^{\infty} c_{ni} \, z^i \qquad [6.5]$$

with

$$z \equiv \frac{1}{m} \, . \qquad [6.6]$$

---

*These studies are being jointly supported by the HTR Technology Program and the Ceramic Technology for Advanced Heat Engines Program.

It has been previously stated[15] that the coefficients of this series may be expressed in terms of the Riemann zeta-function, and when this is done the c_{ni} themselves turn out to be terminating series. Further, it is easily shown that the series starts at $i = n$. The final result of the calculations is to provide a series

$$\frac{\mu_n}{\theta^n} = \sum_{i=n}^{k} c_{ni}\ z^i + \frac{\hat{c}_{nk} z^{k+1}}{1 + 2z}\ , \qquad [6.7]$$

where the remainder term is given by

$$\lim_{k\to\infty} \hat{c}_{nk} = n\ , \qquad [6.8]$$

and we calculated the c_{ni} out to $k = 8$. For six decimal-place accuracy in the moments β_n, the remainder term becomes negligible at $m = 25$ for the second moment, $m = 100$ for the third, and $m = 200$ for the fourth.

We present the results of the calculations for selected values of m in Tables 6.10, 6.11, and 6.12. Table 6.10 presents various parameters associated with the moments up to the limits of quartic interpolation from 15-place tables[16] of the gamma function (1, 2; 0.005). Table 6.10 is not different from that given previously except that we have carefully truncated the results so that they are correct to within less than one unit in the last decimal place exhibited. Table 6.11 provides the results obtained from the asymptotic series and gives both the sum to eighth order (S_8) and this sum plus the remainder term (S_∞), both expressed to within one unit in the last place exhibited. Finally, Table 6.12 provides best values to six decimal places where these are available. It will be noted that the values from the tabled Γ-function and those from the asymptotic series overlap most weakly around $m = 20$.

A topical report covering these results in detail is in preparation.

Table 6.10. Normalized moments of the Weibull distribution for various values of the exponent m calculated by quartic interpolation on 15-place table of the Γ-function

m	μ/θ	σ/μ	β_3	β_4
1	1.	1.	2.	9.
2	0.886227	0.522723	0.631111	3.245089
3	0.892980	0.363447	0.168103	2.729464
4	0.906402	0.280544	-0.087237	2.747829
5	0.918169	0.229053	-0.254110	2.880290
6	0.927719	0.193774	-0.373261	3.035452
7	0.935438	0.168022	-0.463190	3.187182
8	0.941743	0.148369	-0.533727	3.327676
9	0.946965	0.132863	-0.590657	3.45521
10	0.951351	0.120310	-0.637637	3.57016
12	0.958286	0.101216	-0.71074	3.76697
14	0.963510	0.087371	-0.76509	3.92777
16	0.967580	0.076866	-0.80712	4.06076
18	0.970838	0.068621	-0.84063	4.1724
20	0.973504	0.061976	-0.86797	4.2670
25	0.978438	0.049902	-0.91846	4.4513
50	0.988844	0.025289	-1.0248	4.879
100	0.994326	0.012733	-1.081	5.1
200	0.997139	0.006390	-1.11	5.

Table 6.11. Normalized moments of the Weibull Distribution for various values of the exponent m calculated from the asymptotic series to eighth order (S_8) and with the correction term added (S_∞)

m	Order	β_3	β_4
10	S_8	-0.6	4.
	S_∞	-0.6378	3.6
20	S_8	-0.8678	4.3
	S_∞	-0.8679 65	4.267
50	S_8	-1.0248	4.8779
	S_∞	-1.0248 5300	4.8777 82
100	S_8	-1.0810 737	5.1234 5
	S_∞	-1.0810 7376 0	5.1234 456
200	S_8	-1.1100 166	5.2591 46
	S_∞	-1.1100 1656 9	5.2591 4541
500	S_8	-1.1276 6270 6	5.3427 698
	S_∞	-1.1276 6270 6	5.3427 6980 1
∞		-1.1395 4710 0	5.4000 0000 4

Table 6.12. "Best" values for the normalized moments and associated quantities of the Weibull distribution for varous values of the exponent m

m	μ/θ	σ/μ	β_3	β_4
1	1.	1.	2.	9.
2	0.8862 27	0.5227 23	0.6311 11	3.2450 89
3	0.8929 80	0.3634 47	0.1681 03	2.7294 64
4	0.9064 02	0.2805 44	-0.0872 37	2.7478 29
5	0.9181 69	0.2290 53	-0.2541 10	2.8802 90
6	0.9277 19	0.1937 74	-0.3732 61	3.0354 52
7	0.9354 38	0.1680 22	-0.4631 90	3.1871 82
8	0.9417 43	0.1483 69	-0.5337 27	3.3276 76
9	0.9469 65	0.1328 63	-0.5906 57	3.4552 1
10	0.9513 51	0.1203 10	-0.6376 37	3.5701 6
12	0.9582 86	0.1012 16	-0.7107 4	3.7669 7
14	0.9635 10	0.0873 71	-0.7650 9	3.9277 7
16	0.9675 80	0.0768 66	-0.8071 2	4.0607 6
18	0.9708 38	0.0686 21	-0.8406 3	4.1724
20	0.9735 04	0.0619 76	-0.8679 65	4.2670
25	0.9784 38	0.0499 02	-0.9184 55	4.4528
50	0.9888 44	0.0252 89	-1.0248 53	4.8777 82
100	0.9943 26	0.0127 33	-1.0810 74	5.1254 46
200	0.9971 39	0.0063 90	-1.1100 17	5.2591 45
500	0.9988 50	0.0025 61	-1.1276 63	5.3427 70
∞	1.	0.	-1.1395 47	5.4000 00

6.5 REFERENCES

1. J. P. Sanders and A. G. Grindell, "HTR Component Flow Test Loop Studies," pp. 23–91 in *High-Temperature Gas-Cooled Reactor Technology Development Program Annual Progress Report for Period Ending December 31, 1983*, ORNL-6053, June 1984.

2. R. A. Strehlow and H. C. Young, *Summary of Results of TEST ZERO, Phase Two of the Core Support Performance Test Series*, ORNL/GCR-84/6, August 1984.

3. H. C. Young, "Core Support Performance Test," p. 29 in *High-Temperature Gas-Cooled Reactor Technology Development Program Annual Progress Report for Period Ending December 31, 1983*, ORNL-6053, June 1984.

4. *High-Temperature Gas-Cooled Reactor Technology Development Program Annual Progress Report for Period Ending December 31, 1983*, pp. 46–56, ORNL-6053, June 1984.

5. *High-Temperature Gas-Cooled Reactor Technology Development Program Annual Progress Report for Period Ending December 31, 1983*, p. 60, ORNL-6053, June 1984.

6. *High-Temperature Gas-Cooled Reactor Technology Development Program Annual Progress Report for Period Ending December 31, 1983*, pp. 40–43, ORNL-6053, June 1984.

7. *High-Temperature Gas-Cooled Reactor Technology Development Program Annual Progress Report for Period Ending December 31, 1983*, pp. 48–51, ORNL-6053, June 1984.

8. J. P. Sanders, A. G. Grindell, and W. P. Eatherly, "High-Temperature Reactor Flow Test Loop Studies," pp. 175–94 in *High-Temperature Gas-Cooled Reactor Technology Development Program Progress Report for the Period Ending December 31, 1982*, ORNL-5960.

9. J. P. Sanders and A. G. Grindell, "High-Temperature Reactor Flow Test Loop Studies," in *High-Temperature Gas-Cooled Reactor Technology Development Program Progress Report for the Period Ending December 31, 1983*, ORNL-6053.

10. R. A. Strehlow and H. C. Young, unpublished data, December 1983.

11. R. A. Strehlow and H. C. Young, unpublished data, August 1984.

12. E. P. Kennedy, "Fracture Mechanics Analysis of Extruded Graphite," to be published in 17th Biennial Conference on Carbon Extended Abstracts, June 16–21, 1985, Lexington, Kentucky.

13. C. R. Kennedy, "Elastic Constants of Graphite," p. 437 in *13th Biennial Conference on Carbon Extended Abstracts, July 18–22, 1977, Irvine California.*

14. C. R. Kennedy, "The Evaluation of Fracture Strength by Sonic Testing," p. 536 in *15th Biennial Conference on Carbon Extended Abstracts and Program, June 22–23, 1981, Philadelphia, Pennsylvania.*

15. W. P. Eatherly, "Higher Moments of the Weibull Distribution," pp. 240–244 in *High-Temperature Gas-Cooled Reactor Technology Development Program Annual Progress Report for Period Ending December 31, 1983,* ORNL-6053, June 1984.

16. Milton Abromowitz and Irene A. Stegun, eds. *Handbook of Mathematical Functions With Formulas, Graphs, and Mathematical Tables,* Applied Mathematics Series 55, National Bureau of Standards, U.S. Government Printing Office, Washington, D.C., Third Printing, March 1965.

7. METALLIC MATERIALS (WBS 1603)

P. L. Rittenhouse

This work is directed toward the development of the metallic materials data base and technology needed for the design, manufacture, and licensing of HTR components. Tasks in progress emphasize alloys selected as reference materials for critical components (e.g., heat exchangers and reactor internals) of the HTR steam-cycle plant. Testing includes long-term creep and creep-rupture in HTR-He, low-cycle fatigue and creep-fatigue interactions, high-cycle fatigue, fracture mechanics, and thermal stability. All studies are closely coordinated with similar work being conducted by GA Technologies Inc. (GA) and General Electric (GE).

7.1. MATERIALS ENGINEERING (WBS 1603.01) - P. L. Rittenhouse

The ORNL Program is cooperating with GA in identifying Design Data Needs (DDN) for the reference HTR and preparing the Technology Development Program Plan needed to guide efforts on HTR metallic materials. Identification of requirements, criteria, and resultant DDN is the responsibility of GA; ORNL is responsible for developing the specifics of the experimental program to satisfy the DDN.

Work on the Technology Development Program Plan was initiated at the beginning of FY 1985 with the 2240 MW(t) integrated steam-cycle HTGR as the reference. An outline of the Plan was agreed between GA and ORNL, and a detailed example of requirements and other criteria was prepared by GA. However, work was halted in early December of 1984 in anticipation of the selection of a different reference HTR system. A new schedule for the Plan is expected to be established sometime early in 1985.

7.2 REACTOR SYSTEM MATERIALS (WBS 1603.02)

7.2.1 Fracture Mechanics Behavior of Inconel 718 - D. O. Hobson, R. K. Nanstad, and J. J. McGowan

The initial phase of an effort to characterize the fracture mechanics behavior of Inconel 718 was completed in FY 1984. The material studied was a 25.4 mm thick plate (Plate 4ACB) from a reference heat prepared by the DOE.[1] This plate had been annealed at 950-955°C for 45 minutes following rolling. Two independent chemical analyses are listed in Table 7.1. Miniature tensile specimens with transverse orientation were fabricated from the plate. These specimens were nominally 55 mm long, with a gage length of 32 mm and a diameter of 4.52 mm (resulting in a length/diameter ratio of 7/1). These specimens were tested at a 8.5 μm/sec displacement rate in an air furnace in conformance with ASTM Standard Test Method E-08. The results of the tests are listed in Table 7.2 and shown in Fig. 7.1. These tests did not use an extensometer; the 0.2% yield strength was estimated from crosshead motion.

Charpy V-notch specimens were fabricated from the plate with the T-L (axis in transverse direction, notch in longitudinal direction) orientation. Before testing, the impact test machine was calibrated with Watertown Arsenal standard specimens. The test procedure used electrical heating or cold gas (nitrogen) to adjust specimen temperature, and a calibrated contact thermocouple for determining specimen temperature. All

Table 7.1. Chemical analysis of alloy 718 reference material products

Element	Cabot	ORNL	Element	Cabot	ORNL
Ni	52.11	52.98	Ta	<0.10	0.03
Cr	18.01	18.11	Mn	0.30	0.31
Fe	19.03	18.62	Si	0.13	0.12
Cb+Ta	5.07	5.12	C	0.05	0.04
Ti	0.98	0.99	Cu	0.03	0.03
Al	0.60	0.62	B	0.004	ND
Mo	3.02	2.99	P	<0.005	0.004
Co	<0.05	0.06	S	<0.002	0.001

Table 7.2. Tensile properties of annealed 718 reference heat

Specimen identification	Test temperature °C	0.2% offset yield strength MPa	Ultimate Strength MPa	Elongation[a] %	Reduction in area %
7186A1	24	453	880	47.4	58.4
7186A2	24	443	862	48.4	59.7
7186A3	288	356	781	48.1	56.4
7186A4	288	359	781	46.8	58.0
7186B1	566	375	754	51.7	55.1
7186B2	566	374	751	52.7	54.6

[a] 7/1 length to diameter ratio

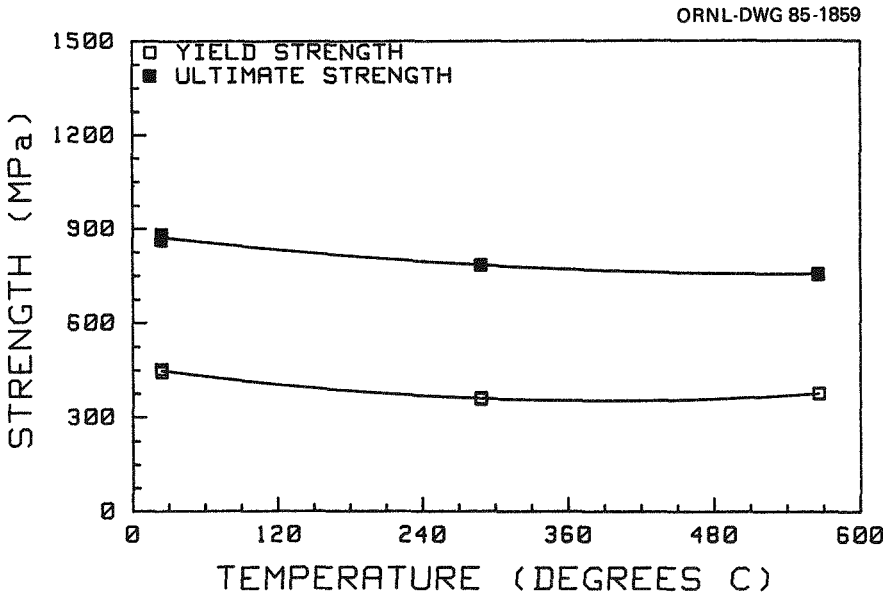

Fig. 7.1. Tensile strength of annealed alloy 718.

tests were conducted in less than 3 s after removal of the specimen from the temperature conditioning chamber. The tabulated results of the Charpy V-notch tests are listed in Table 7.3. The impact energy and lateral expansion results are shown in Figs. 7.2 and 7.3, respectively. Note that the energy and lateral expansion have only a moderate temperature dependence over the entire temperature range.

Table 7.3. Impact properties of annealed 718 reference heat

Specimen ID	Test temperature °C	Dial energy Joule	Lateral expansion mm	Fracture appearance % shear
7181B1	−129	131	1.567	100
7181B4	−101	136	1.516	100
7182A2	−73	125	1.506	100
7182A3	−45	125	1.524	100
7181B3	−18	144	1.689	100
7181A1	22	136	1.478	100
7181A2	52	151	1.745	100
7181A3	79	151	1.595	100
7181A4	121	149	1.758	100
7182A4	149	132	1.618	100
7182A1	177	141	1.709	100
7182B1	232	149	1.880	100
7181B2	288	158	1.842	100

J-integral fracture toughness specimens (1TCS) were fabricated from the plate with the T-L orientation. These specimens were 25.4 mm thick, had 10% side grooves on each side, and had been modified for load-line displacement measurement. The specimens were tested in load-line displacement control at a rate of 5 μm/sec. The single-specimen unloading compliance technique was used to determine the crack length change during the test. With this technique, small unloadings (~15% of previous load) were

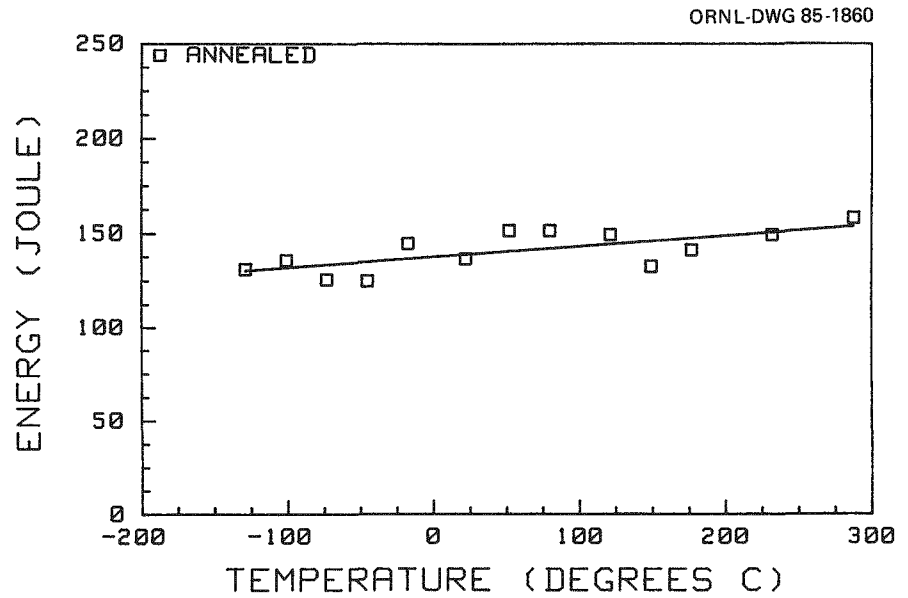

Fig. 7.2. Charpy V-notch energy of annealed alloy 718.

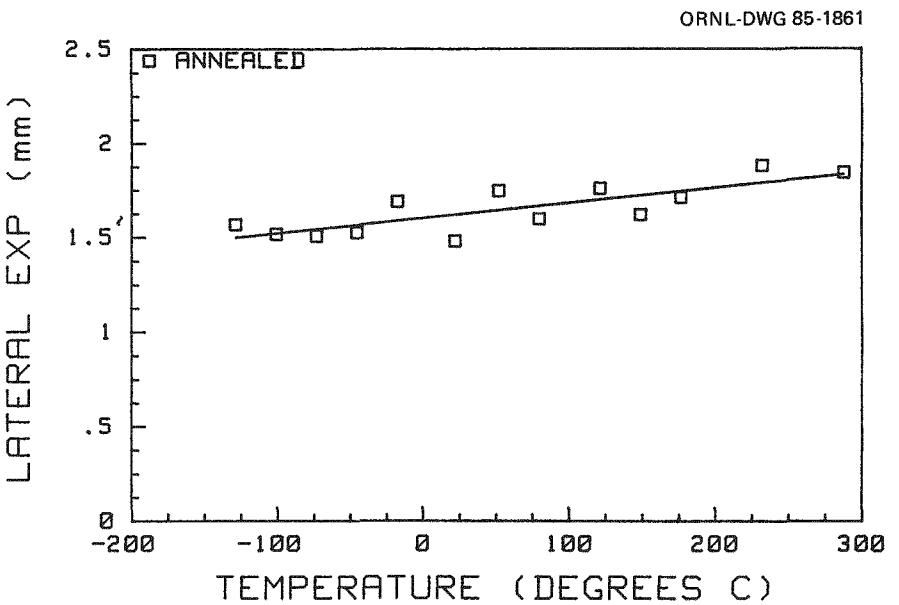

Fig. 7.3. Charpy V-notch lateral expansion of annealed alloy 718.

performed at regular displacement intervals to determine the elastic specimen compliance. The crack length can then be uniquely determined from the compliance. The load line displacement at room temperature was measured with a strain-gage clip gage resting on knife edges. The load-line displacement at elevated temperature was measured with a HITEC Proxicod Model B capacitative clip gage. The calibration change that occurred with clip gage cable movement caused some concern; and, the results at high temperature show a larger scatter than the room temperature results. The results of the fracture toughness tests are listed in Table 7.4 and shown in Fig. 7.4. The value of the fracture toughness (K_{Jc}) is calculated from the modified-Ernst J-Integral[2] using the equation $K_{Jc}=\sqrt{E\ J_{Ic}}$. In this equation, J_{Ic} is calculated via the power law procedure.[3] In Fig. 7.4, the upper bound is estimated by adding two standard deviations to the mean value; the lower bound is estimated by subtracting two standard deviations from the mean value. Due to the scatter at higher temperature, it is difficult to judge the temperature dependence of K_{Jc}; however, it appears it is not significant.

The values of the tearing modulus ($T\int avg$) are listed in Table 7.4 and shown in Fig. 7.5. The tearing modulus is given by

$$T\int avg = \frac{E}{\sigma_f{}^2}\frac{dJ}{da} \qquad [7.1]$$

where E is Young's modulus, σ_f is the flow strength and dJ/da is the slope of the J-Δa curve. Note that there is considerable scatter among the test values, especially at the higher temperatures. Upper and lower bounds are estimated in the same manner as with the K_{Jc} data. The temperature dependence of the tearing modulus does not appear to be significant.

The fatigue crack growth resistance was determined with 25.4 mm fracture toughness specimens (1TCS) fabricated from the plate with the T-L orientation. The specimens were not side grooved, but were modified for load line displacement measurement. These specimens were tested in load control at 10 H_z and a "load ratio" of R=0.1 (R is the algebraic ratio of

Table 7.4. Summary of fracture toughness parameters, annealed 718 reference heat

Specimen ID	Test temperature (°C)	$\frac{a_i}{w}$	Ductile Δa (mm)	J_{Ic} (kJ/m^2)	K_{Jc} (MPa$\sqrt{m}$)	T$\int$avg	Flow stress (MPa)	Young's modulus (GPa)
ID718 50	566	0.626	5.29	584	320	99	564	175
ID718 71	288	0.633	3.31	550	324	146	569	191
ID718 72	24	0.664	1.54	290	245	176	660	206
ID718 84	288	0.663	1.41	537	320	101	569	191
ID718 85	288	0.654	3.15	489	305	130	569	191
ID718 87	24	0.626	2.28	357	271	141	660	206
ID718 91	566	0.627	4.07	371	255	150	564	175
ID718 98	566	0.650	3.52	573	317	131	564	175
ID718148	288	0.651	3.41	372	267	138	569	191

minimum to maximum load in a fatigue cycle). The potential drop technique[4] was used to determine the crack length throughout the test. The results of the fatigue crack growth tests are shown in Fig. 7.6. The crack growth rate (da/dN) was determined by the secant method. Note the small amount of scatter in the data; this is primarily due to the accuracy of the crack length measurement technique and the homogeneity of the material. Using the data from this figure, a curve of the form $da/dN = (\Delta K)^m$ was determined by least square methods to the logarithms of a da/dN and ΔK. These curve fits are also shown on Fig. 7.6. Along with the curve fits from the fatigue crack growth data, the curve fits from James and Mills[5] are shown in Fig. 7.7. (The data from James and Mills[5] was produced from tests on annealed Inconel 718 at 40 H_z and R=0.05.) The comparison of the present study with this reference is very good.

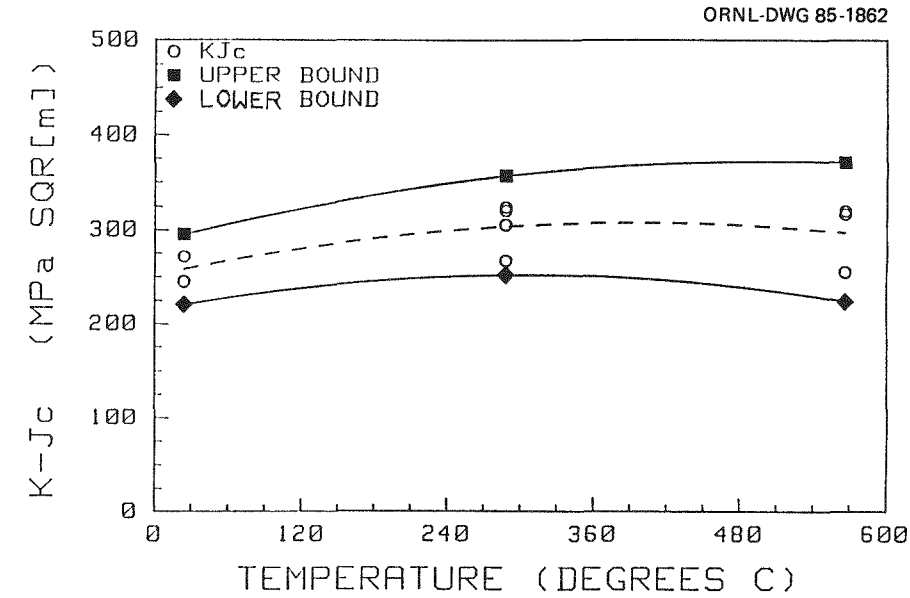

Fig. 7.4. Fracture toughness of annealed alloy 718.

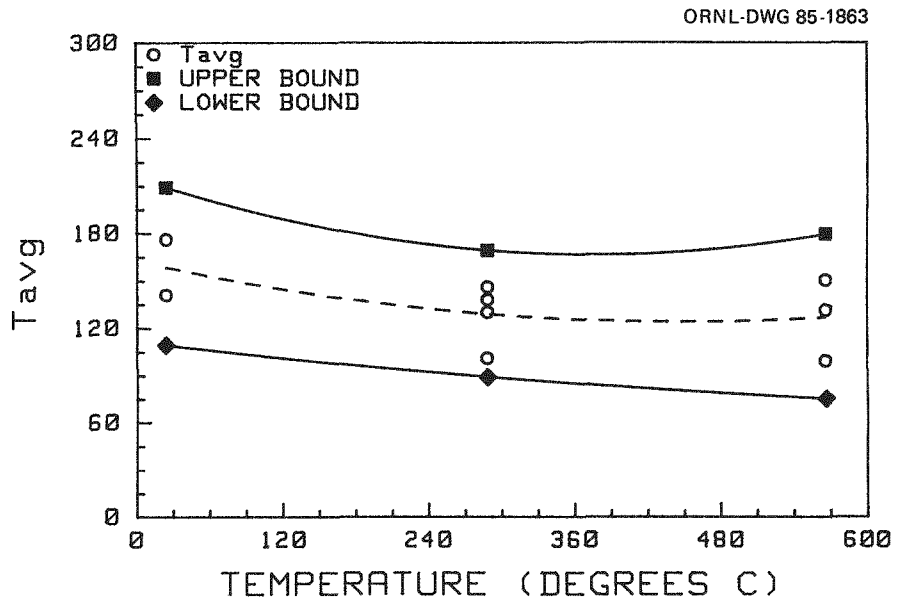

Fig. 7.5. Tearing modulus of annealed alloy 718.

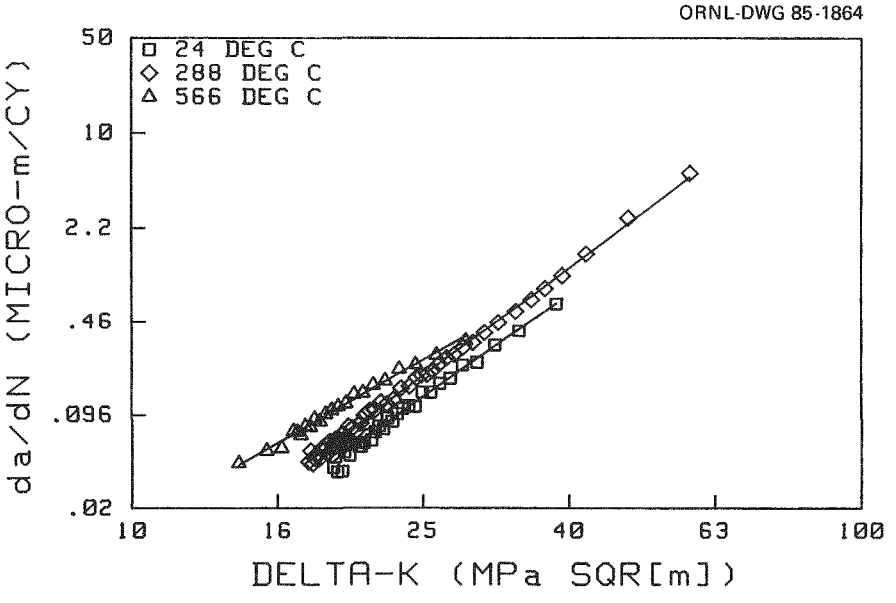

Fig. 7.6. Fatigue crack growth of annealed alloy 718.

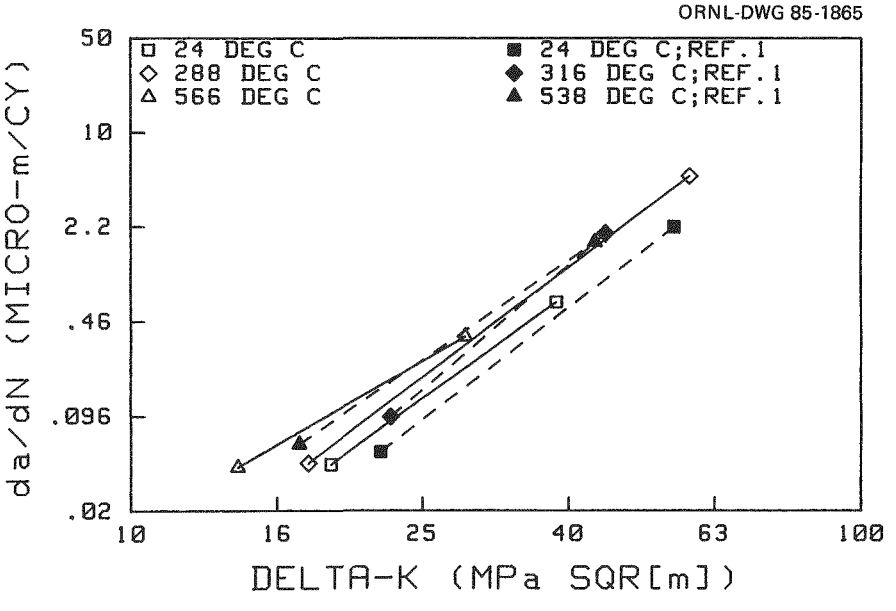

Fig. 7.7. Comparison of fatigue crack growth of annealed alloy 718 to Hanford data in reference 5.

Further work on the fracture mechanics behavior of Inconel 718 (e.g., aging effects) has been delayed to allow effort to be devoted to more pressing questions on the fracture behavior of 2 1/4 Cr-1 Mo steel.

7.2.2 Cladding - B_4C Compatibility - P. F. Tortorelli and J. H. DeVan

The power and control rods of the HTR consist of boron carbide-graphite compacts housed in metallic tubing. A study was performed to qualitatively assess the elevated temperature compatibility of boronated graphite with possible cladding materials (alloy 800H and type 316 stainless steel) in the absence of radiation. If severe, the reactions between this graphite and the cladding could cause detrimental carburization and self-welding of the two components.

The solid-state reactions between boronated graphite compacts and both type 316 stainless steel and alloy 800H were studied by placing duplicate stacks of these materials under a compressive load in flowing helium at 700 and 810°C, respectively. As described previously,[6] a load of approximately 10.3 MPa (1500 psi) was transmitted to each stack by use of a pneumatic ram passing into a chamber that rigidly held the specimen set in place. In general, the specimen stack in each test device consisted of alternating alloy 800H-graphite-type 316 stainless steel coupons that were periodically removed in order to follow the reactions as a function of time. After each exposure period, specimens were first checked visually and then cut, polished, and metallographically examined in cross section. In selected cases, electron probe microanalysis of polished cross sections and/or scanning electron microscopy of reacted surfaces were used to supplement the optical observations.

An evaluation of the data obtained for exposure times of 1000, 3000, 6000, and 10,000 h showed several consistent trends. At 700°C, the principal reaction with both alloys was limited oxidation (e.g., the oxide layer thickness was $\leq$25 μm after 10,000 h). However, at 810°C, three general types of reaction were observed. The first involved localized reactions at the sites at which B_4C particles were in contact with the alloy surfaces (see Fig. 7.8) and was more prevalent for type 316 stainless steel. The second type was carburization leading to precipitation of a

ORNL-PHOTO 5234-84

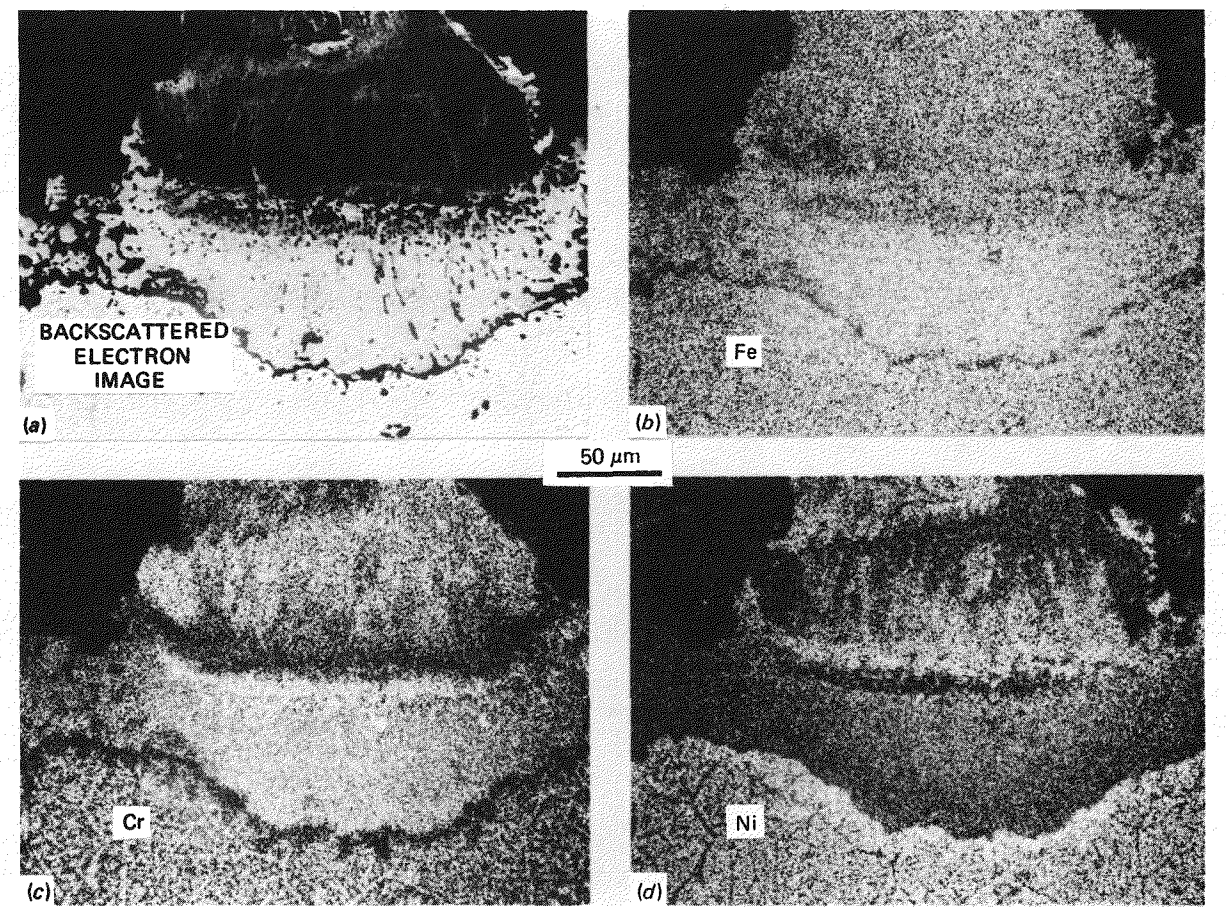

Fig. 7.8. Polished cross section of type 316 stainless steel exposed to boronated graphite for 6000 h at 810°C (a) electron image showing attachment of a B_4C particle, (b), (c), (d) elemental maps.

Y-194381

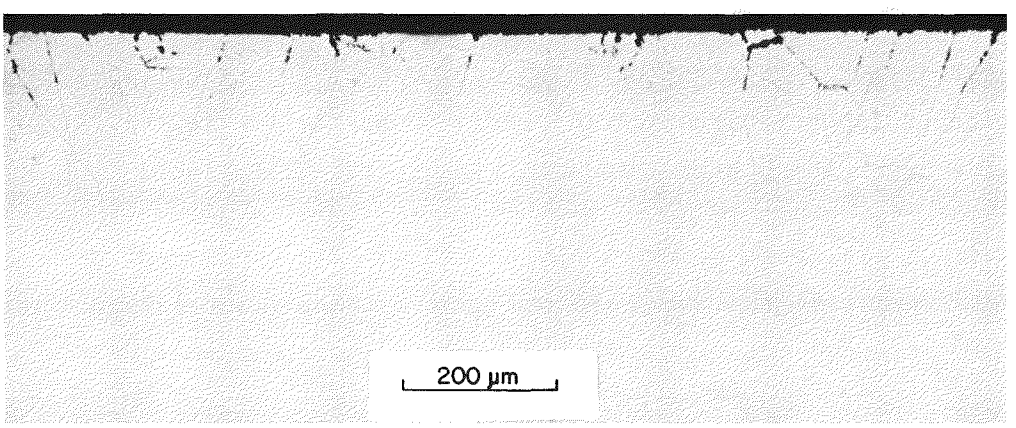

Fig. 7.9. Optical micrograph of a polished cross section of alloy 800H exposed to boronated graphite for 6000 h at 810°C.

chromium-carbide phase (also shown in Fig. 7.8). Since this precipitation extended over 200 μm into the alloy matrix after 10,000 h at 810°C, such a process is a compatibility concern. Third, as shown in Fig. 7.9, significant intergranular penetration occurred at this temperature, but only for the alloy 800H. Since the depth of intergranular penetration was normally less than that of the carburization process, this reaction can be considered a secondary one unless such penetration promotes crack initiation. At both 700 and 810°C, the extent of the corrosion reactions generally increased with time.

The results indicated that a main effect of the boron in the graphite was to accelerate the corrosion reactions at the sites where the B_4C particles were in contact with the metal surfaces. Such an observation is consistent with findings from another study,[7] which showed that as the percentage of boron in B_4C-graphite compacts increased, the extent of uniform and grain boundary penetration also increased. Furthermore, the same study revealed intergranular attack of higher nickel alloys, in agreement with the present work.

The qualitative findings from this study would seem to indicate that, while the corrosion reactions are relatively minor at 700°C, compatibility concerns arise when the exposure temperature for boronated graphite in contact with alloy 800H and type 316 stainless steel is raised to 810°C. In particular, welding of the clad material to the graphite and degradation of mechanical properties due to surface carburization and intergranular attack may necessitate an operating temperature closer to 700 than to 800°C. It is interesting, in this regard, to compare this temperature limit to one of approximately 600°C set by an earlier study[8] of graphite-stainless steel compatibility. In this previous work, significant carburization was observed at 700°C. It is thus possible that the present lack of carburization at 700°C may be due to the formation of an oxide layer which serves as a barrier to carburization.

7.3 REACTOR VESSEL MATERIALS (WBS 1603.03)

7.3.1 Creep and Aging Behavior of Hastelloy X and Alternate Alloys - H. E. McCoy

Hastelloy X (Ni-22% Cr-9% Mo-18% Fe-0.10% C) is the primary material being evaluated for Class B thermal barrier cover plates. Four heats of base metal and one heat of weld wire are being evaluated. Creep test times now exceed 50,000 h and samples have been aged 53,000 h. Inconel 617 (Ni-20% Cr-12% Co-9% Mo-0.06% C) is another material that had been considered for this application, and three heats of base metal and one heat of filler metal have been under study. Creep tests on this material have exceeded 30,000 h and samples have been aged 53,000 h. Inconel 618 (Ni-22% Cr-15% Fe-6% W-0.04% C) has also been evaluated in creep tests of about 15,000-h duration. Inconel 718 (Ni-18% Cr-19% Fe-5% Nb+Ta Mo-3%-0.05% C) base metal was evaluated in FY 1985 (for "reactor system" application). Creep tests and aging experiments reached in excess of 10,000 h. Two other alloys, Incoloy 802 (Fe-20% Cr-32% Ni-0.5% C) and HD 556 (Fe-22% Cr-20% Ni-20% Co-3% Mo-2.5% W-0.1% C), were evaluated only briefly, and this work has ceased. In fact, study of all of the materials above, except Hastelloy X, is in a "phase-out" period.

Many of the testing details were reported previously,[9] and the creep and aging environments are high purity helium with additions of impurities to the following partial pressures (Pa): 34.0 H_2, 3.2 CH_4, 1.9 CO, 0.2 H_2O, and <0.05 N_2. The test programs for each material included the preparation of weldments for test samples; machining creep and, usually, impact samples of base metal, weld metal, and transverse weld samples; aging of samples in HTR-He; short-term tensile and impact testing of samples in the as-received and aged conditions; and creep testing of as-received and aged samples in air and HTR-He environments.

The findings for Hastelloy X have been summarized.[10,11] The weldability of the alloy is good although there is a tendency under creep conditions for fracture to occur in the weld metal rather than in the base metal. The alloy is carburized at high temperatures in HTR-He, but the creep properties are equivalent in air and HTR-He. Aging has no detectable

effect on the creep properties. Aging affects the short-term tensile properties significantly with the property change of most concern being the fracture strain at ambient temperature. Fracture strains of only a few percent were noted after some aging treatments, and impact samples aged at corresponding conditions failed with energies as low as 6 J.

The experimental results for Inconel 617 and 618 are summarized in a recent topical report.[12] Inconel 617 has been studied more extensively than Inconel 618. Even though Inconel 617 was carburized during creep testing, there was no detectable difference in creep behavior in air and HTR-He environments. The creep characteristic of concern for Inconel 617 is the low fracture strain (1 to 2%, independent of environment) over the temperature range of 600 to 700°C. Higher strains were noted at higher temperature. The weldability of Inconel 617 was good, and the creep strength of the weld metal was only slightly less than that of the base metal. Aging caused some changes in tensile properties, but the property change of main concern was the reduction in fracture strain at ambient temperature. Elongation at fracture was reduced to about 10% and impact values were as low as 10 J. Inconel 617 has considerably higher creep strength than Hastelloy X.

Inconel 618 appears to be a much simpler alloy than either Inconel 617 or Hastelloy X. This manifests itself as very good thermal stability during long-term aging. The lowest impact values for Inconel 618 welds and base metal were about 100 J even after 20,000 h of aging. The creep strength is almost equivalent to that of Hastelloy X. Although Inconel 618 is carburized by exposure to HTR-He, the creep properties in air and HTR-He environments appear identical.

Work is nearly completed on Inconel 617 and Inconel 618. Some samples of both materials are being aged, and samples of Inconel 617 have reached 53,000 h.

Considerable creep work has been done on Inconel 718 by other programs, and the main purpose of our work has been to determine whether the carburization which occurs in HTR-He results in changes in behavior. Creep tests to 10,000 h do not show detectable differences in creep behavior in air and HTR-He environments. Aging of 10,000 h at 600 or 650°C

did not cause detectable changes in short-term tensile or creep properties, but aging at 650°C did reduce the impact energy from almost 50 J to 10 J.

Incoloy 802 and HD 556 were evaluated in a brief program and the results have been presented in a topical report.[13] Incoloy 802 was suitably welded using Inconel 617 filler wire. The weld metal was stronger in this case than the base metal. Even though the heat of material which we studied contained 0.3% carbon, it carburized significantly in HTR-He. Carburization had no detectable effect on the creep behavior, but the large amount of carbide precipitate in the alloy led to creep and tensile fracture strains of only a few percent at ambient temperature. Incoloy 802 has excellent creep strength, but it is questionable whether the complications of low ductility and poor weldability are tolerable.

Alloy HD 556 had excellent weldability, and its creep strength was about the same as that of Inconel 617. This alloy has aging characteristics similar to those observed in Inconel 617 and Hastelloy X. Aging of 1000 h at 870°C reduced the ambient temperature elongation in short-term tensile tests to a few percent and the impact energy to 10 J. This alloy seemed to be relatively more resistant to carburization in HTR-He than others studied; this might be important in the very long term. However, the embrittlement from aging may be so severe that the improved resistance to carburization would not be a compensating factor.

7.3.2 High-Cycle Fatigue of Hastelloy X - J. P. Strizak

High-cycle fatigue testing of Hastelloy X has continued. Results of tests on solution-annealed Hastelloy X at 760°C in air were presented in the 1983 annual progress report.[14] Tests are currently being conducted on solution-annealed material in air at 650°C. The limited data at 650°C are compared in Fig. 7.10 with cyclic lifetimes at 750 and 760°C obtained at ORNL, General Electric (GE) and GA Technologies Inc. (GA). The scatter in the data at 750 and 760°C is attributed to heat-to-heat variations. As expected, cyclic life times obtained at 650°C tend to be somewhat higher than for 760°C.

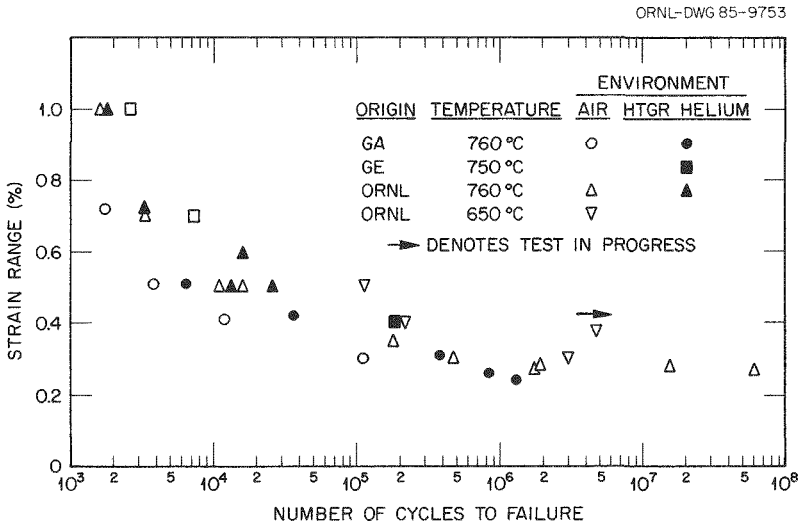

Fig. 7.10. Strain-cycling fatigue data on Hastelloy X at 750°C to 760°C.

7.3.3 Creep-Fatigue Interactions in Hastelloy X — (J. P. Strizak)

Strain-controlled fatigue testing on Hastelloy X at 760°C in air and HTR-He continued throughout 1984. Low-cycle fatigue testing employed a triangular waveform with a strain rate of 4×10^{-3}/s. Creep-fatigue tests were conducted with hold periods of 0.1 to 1.0 h introduced at either the peak tensile or compressive strain amplitudes; thus, creep damage occurred during each cycle via stress relaxation. The typical waveforms employed for strain-controlled fatigue testing are shown in Fig. 7.11. Fatigue testing was performed in air and in a typical service environment for gas-cooled reactors, i.e., impure helium. The impure helium environment included 30.39 Pa H_2, 3.04 Pa CO_2, 2.02 Pa Co, and 0.20 Pa H_2O at an environmental chamber pressure of 83 kPa.

Continuous cycle data for solution annealed Hastelloy X at 760°C are shown in Fig. 7.12 where total strain range and related elastic and plastic strain components are plotted against cycles to failure. Comparing the data generated in HTR-He with that obtained in air shows that the helium environment was not detrimental to fatigue life. Previously reported data at 540°C and 870°C support this observation.

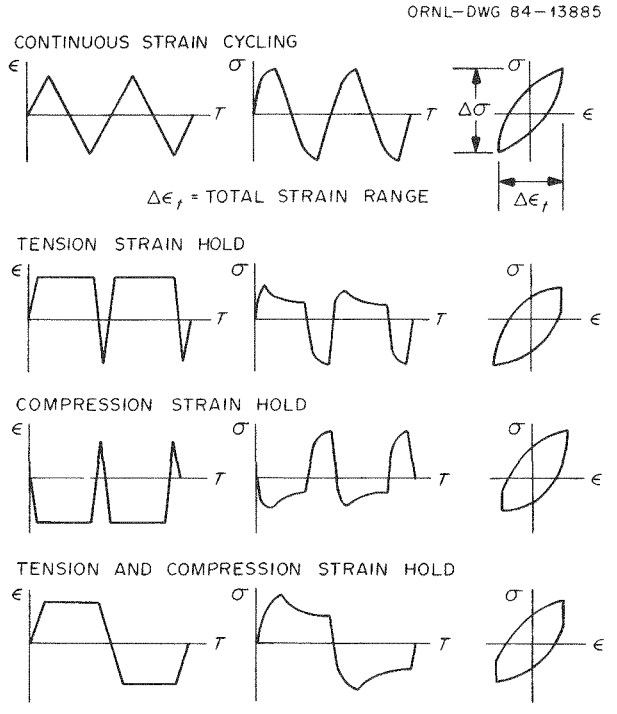

Fig. 7.11. Typical waveforms for strain-controlled fatigue.

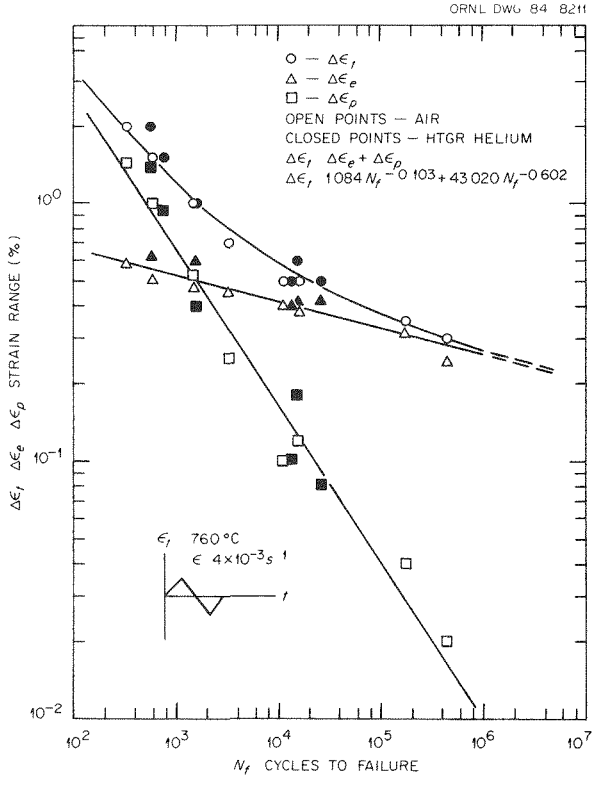

Fig. 7.12. Strain range vs. cycles to failure for Hastelloy X at 760°C.

The introduction of a hold period at the peak tensile or compressive strain amplitudes of the strain cycling waveform significantly reduced the low-cycle fatigue life of Hastelloy X at 760°C. As shown in Fig. 7.13, life reduction was most pronounced at low strain ranges. Resultant cyclic lives for hold period tests conducted at strain ranges of 0.5 and 0.4% were around an order of magnitude lower than for tests with no hold period. Figure 7.13 shows that compressive hold periods are somewhat more damaging to the fatigue life of Hastelloy X than tensile holds. Generally, the most damaging effect occurred when a hold period was introduced at both the tensile and compressive strain amplitudes of the cyclic waveform.

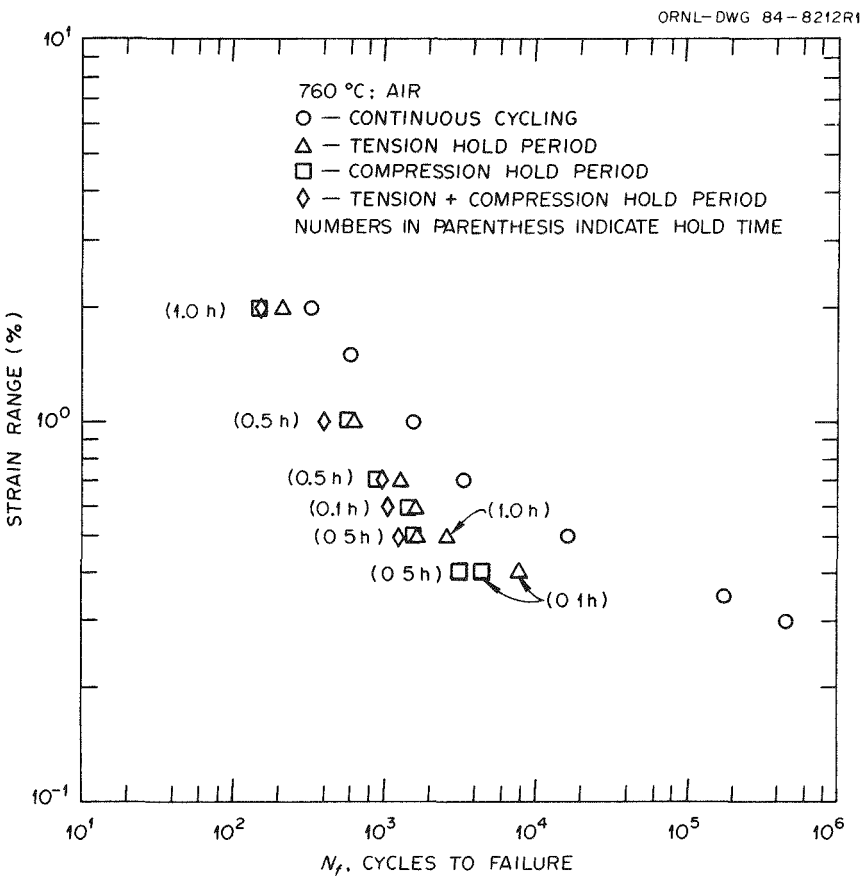

Fig. 7.13. Both tension and compression hold periods are deleterious to the fatigue life of Hastelloy X at 760°C.

Figure 7.14 is a plot of the tensile vs compressive stress amplitudes from the creep-fatigue tests conducted at 760°C. As stress amplitudes decreased, corresponding to the lower strain ranges more applicable to design conditions, mean tensile stresses were developed in tests with compressive hold periods and mean compressive stresses were developed in tests with tensile hold periods. Investigations of mean stress influence on fatigue strength have generally shown that, compared to fully reversed cyclic loading, tensile mean stresses are detrimental to fatigue life and compressive mean stresses result in increased fatigue life. The development of tensile mean stresses when compressive hold times are imposed explains why compressive hold periods are more damaging to the fatigue life of Hastelloy X than are corresponding tensile hold periods in either air or HTR-He environments.

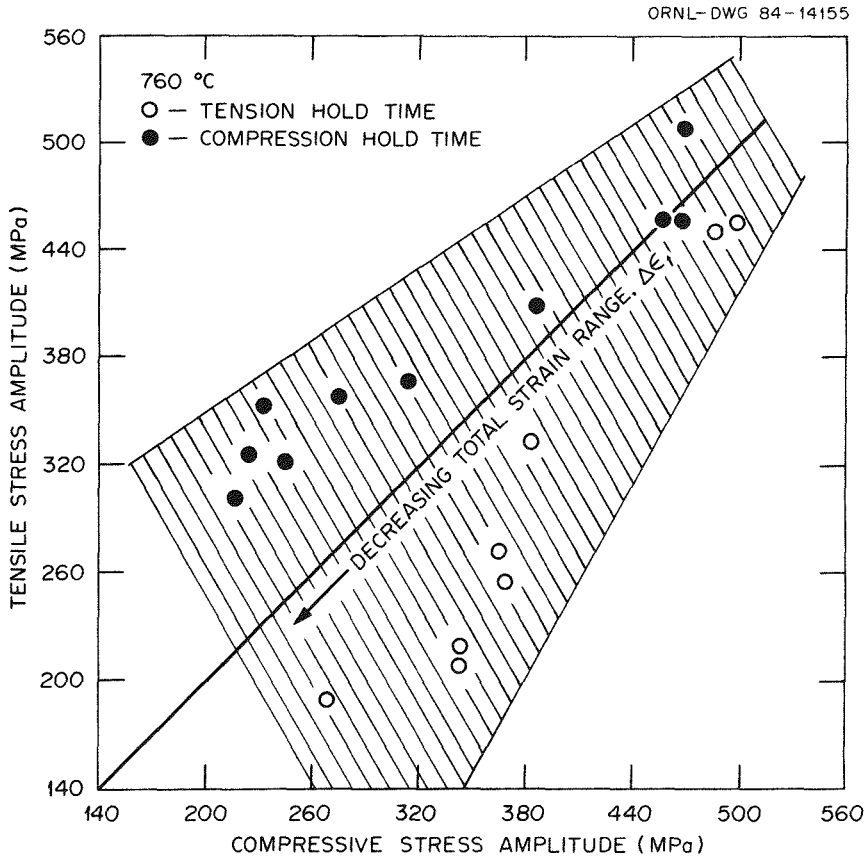

Fig. 7.14. Half-cycle life ($N_f/2$) tensile stress amplitude as a function of compressive stress amplitude for fully reversed fatigue tests conducted at several strain ranges and hold periods.

Of the many methods which have been employed to extrapolate creep-fatigue data or to estimate time dependent fatigue life of materials, linear damage summation is perhaps the most widely known and simplest, and is recommended by the American Society of Mechanical Engineers, Code Case N-47. Generally, linear damage summation is stated as:

$$D_c + D_f = 1 \text{ (at failure)} \tag{1}$$

where D_c and D_f are the creep and fatigue damage values, respectively.

The damage values determined for the creep-fatigue tests conducted on Hastelloy X at 760°C are plotted in Fig. 7.15. It is apparent that a unique damage sum value D does not exist and that a linear damage summation (i.e., D=1) is not appropriate. Similar conclusions have been made for other structural materials including 2 1/4 Cr-1 Mo steel, type 304 stainless steel, and alloy 800H.

A limited number of creep-fatigue tests were conducted at 760°C in air on thermally aged Hastelloy X. Prior to specimen machining, solution

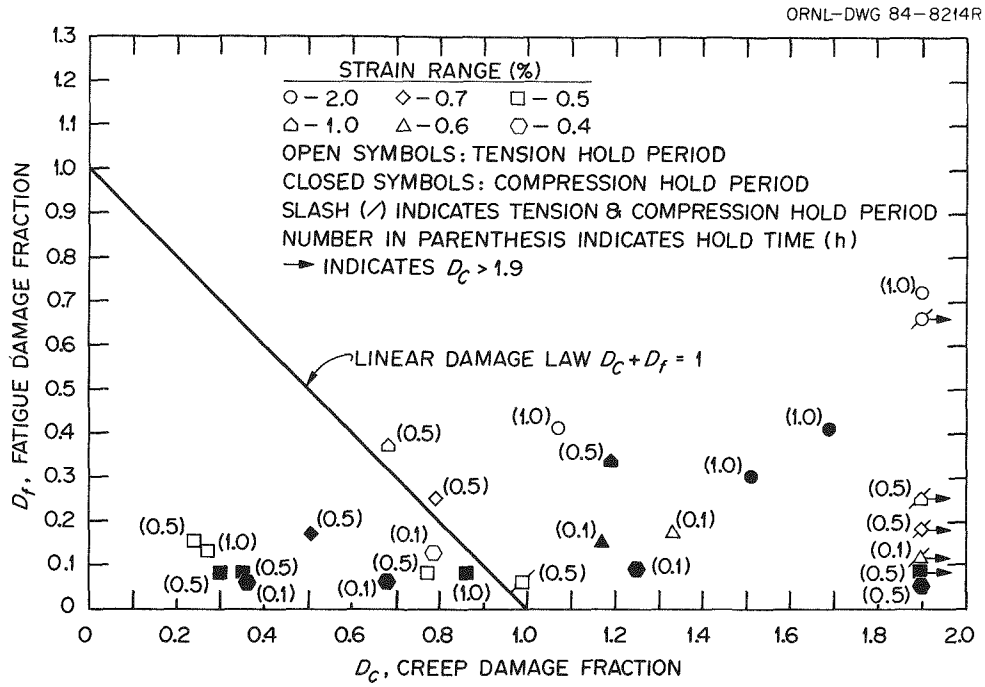

Fig. 7.15. Fatigue damage fractions vs. creep damage fractions for Hastelloy X tested in strain control at 760°C with various hold.

annealed material was aged in an argon environment for 20,000 h at temperatures of 700 and 870°C. Figure 7.16 shows the fatigue lives of continuous cycling, tension hold period, and compressive hold period tests conducted at a strain range of 2% on solution annealed and thermally aged materials. For each of the three cyclic loading conditions, resultant fatigue lives for the thermally aged material were lower than those for solution annealed material. Reduced continuous cycle fatigue strength due to thermal aging of Hastelloy X has been previously observed.

Creep-fatigue testing of Hastelloy X is continuing. Test results will be analyzed using some of the other methods for estimating time-dependent behavior of materials (e.g., strain-range partitioning, the frequency modified approach, and the damage rate model).

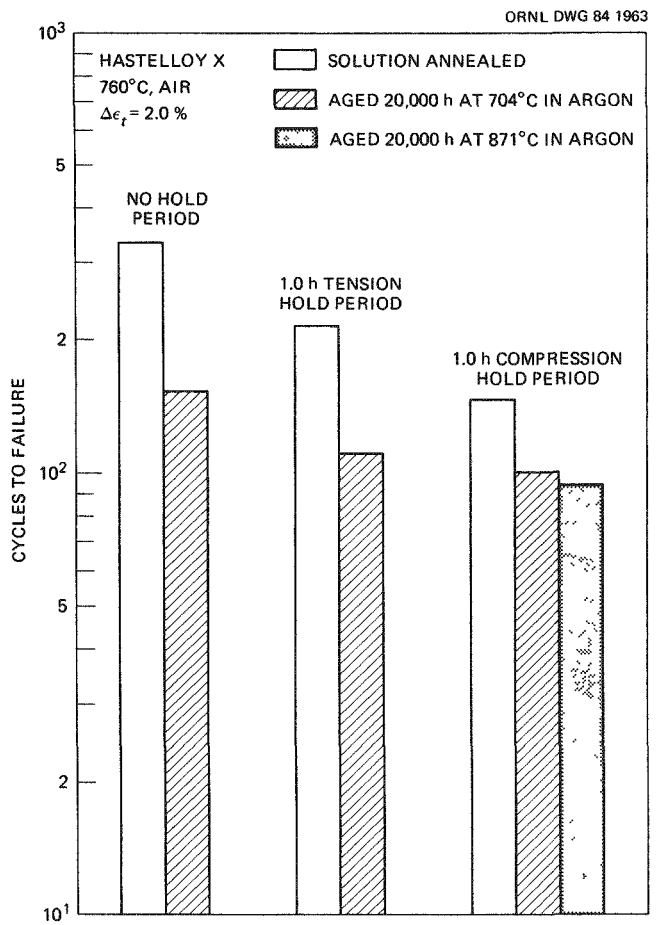

Fig. 7.16. Resultant fatigue lifetimes for tests on solution annealed and thermally aged Hastelloy X employing various fully reversed strain-controlled cyclic waveforms.

7.4 HEAT TRANSPORT MATERIALS (WBS 1603.04)

7.4.1 Tube-to-Tubesheet Joining - J. F. King

The HTR Joining Technology Program has been developing a procedure for joining the steam generator superheater tubing to the tubesheet by internal bore welding. These weld joints are required between a weld clad alloy 800H forging and alloy 800H superheater tubing as shown in Fig. 7.17. Internal bore welds will need to be made from the inside diameter (nominally 23.2 mm) of the tubing through matching drilled holes in the 356 mm-thick tubesheet. The weld must be made in a tube wall thickness of 4.4 mm. This report presents the results on the joining development for this weld which is the base line configuration of the Mark IV steam generator of the 2240 MW(t) plant. This internal bore welding development program was discontinued at the end of 1984 because of redirection of project priorities.

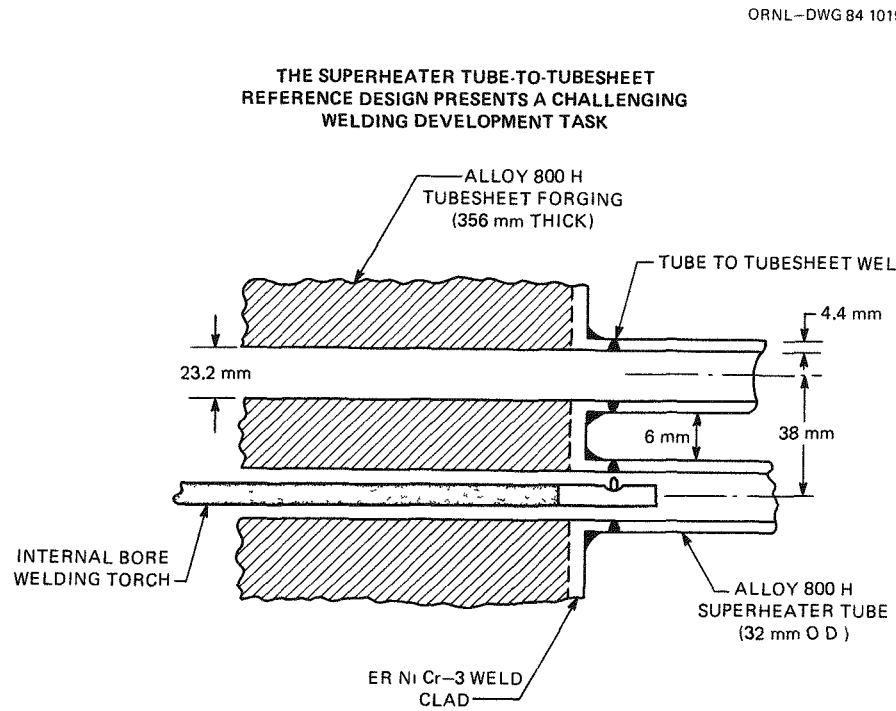

Fig. 7.17. The internal bore tube-to-tubesheet welds will be made between alloy 800H tubing and a weld clad alloy 800H tubesheet forging.

7.4.1.1 Recent Welding Development Studies

An internal bore welding (IBW) head was obtained earlier for use in the laboratory welding development program to study tube-to-tubesheet joining. The IBW head, shown in Fig. 7.18, consists of the welding torch, automatic voltage control, wire feeder, and heat rotating mechanism. This welding system and early results were described previously.[15]

Work on the multipass welding procedure was conducted near the end of the program. It was found that a problem existed with locating the filler wire guide in the proper location for welding while still retaining

Y-194739

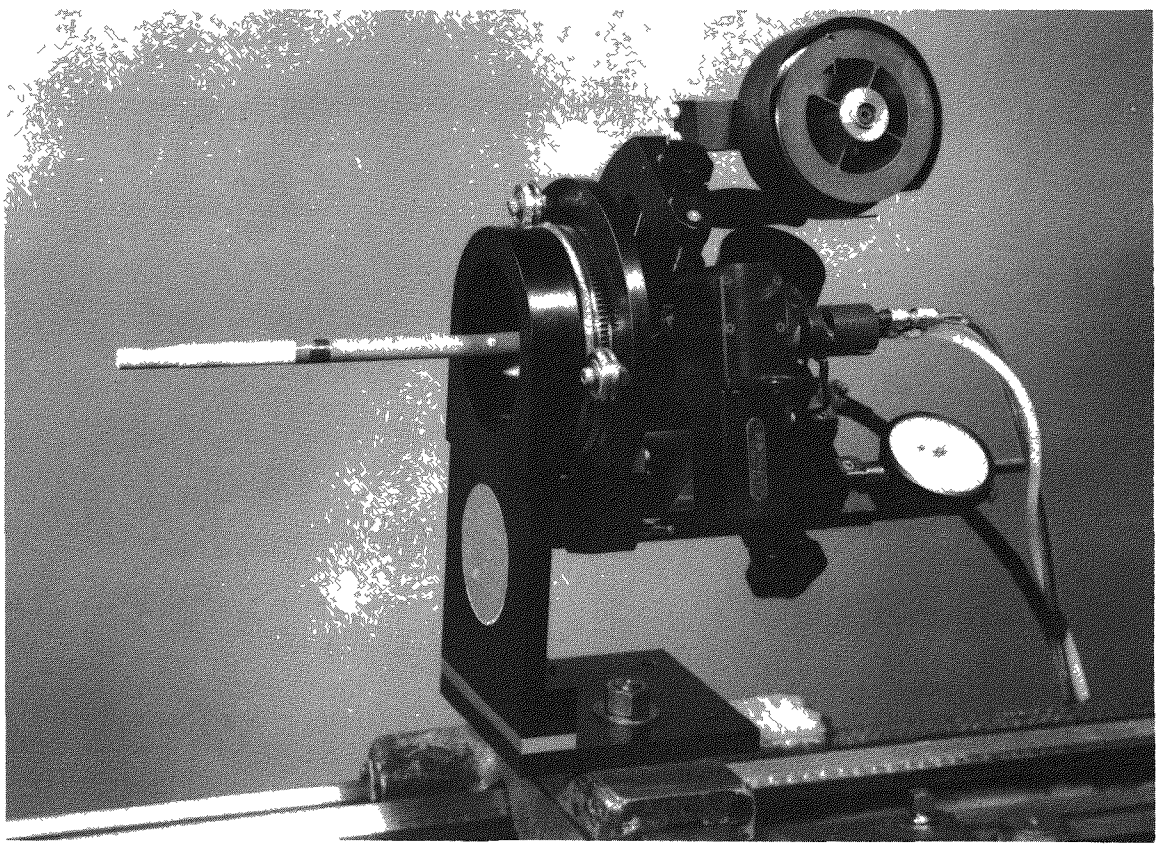

Fig. 7.18. The internal bore welding head for the development program consists of a welding torch with automatic voltage control wire feeder, and a head rotating mechanism.

clearance with the tube inside surface and maintaining weld joint geometry. Various wire guide tubes and weld joint geometries were tried. Filler wire of 0.64 mm diameter appears to be the largest which can be reliably fed using the guide tube shown in Fig. 7.19. (The filler wire is the ERNiCr-3 composition.) Reasonably good root weld passes have been made with this technique in a V-groove weld joint design. Considerably more work is needed, however, in optimizing the welding torch configuration and joint geometry, determining weld pass positioning, and cleaning between passes. Although the multipass welding technique introduces additional fabrication problems to the internal bore welded tube-to-tubesheet joints, it does offer a solution which now shows promise.

Y-200808

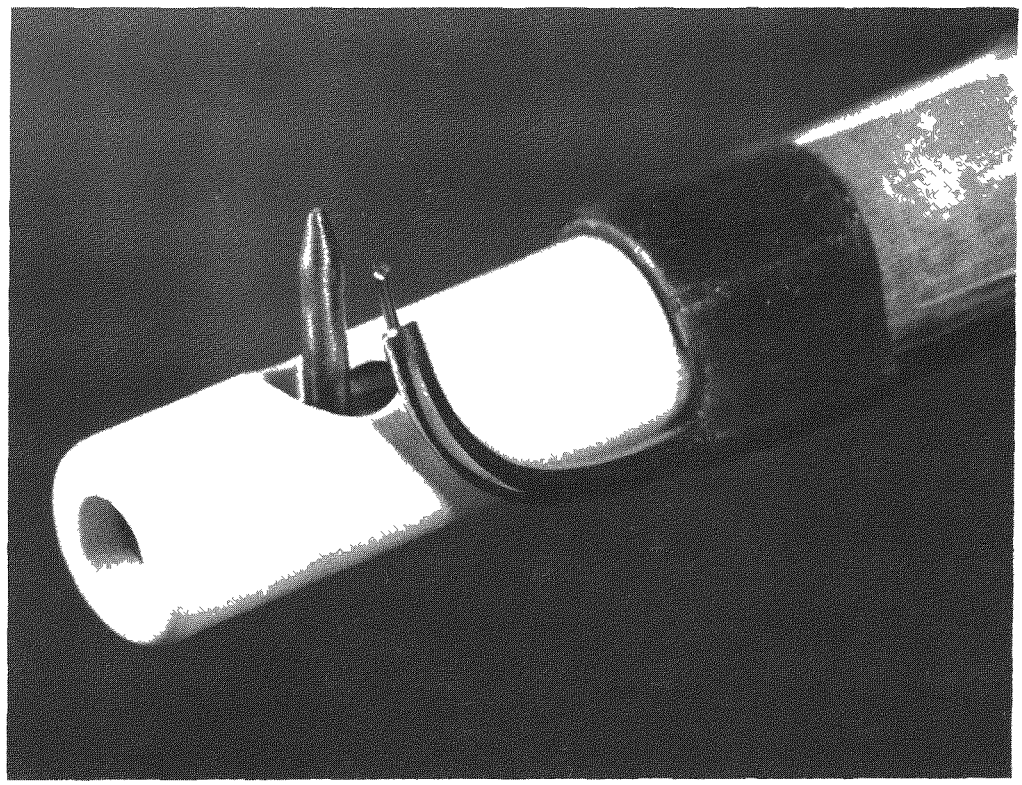

Fig. 7.19. Filler metal guide tube in position to feed 0.64 mm wire into weld puddle.

7.4.1.2 Overall Program Summary and Conclusions

The internal bore welding of HTR superheater tube-to-tubesheet joints presents a challenging welding development task. An internal bore welding head consisting of a gas tungsten arc welding torch, automatic voltage control, wire feeder, and head rotating mechanism was obtained for the laboratory welding development. This welding head was installed with aligning fixtures, shielding chamber, and a programmable welding power supply to produce an experimental welding station.

Our assessment of the welding problem indicated an autogenous welding procedure would present the least fabrication problems for production of these joints. Numerous experiments were conducted to examine current wave forms, electrode geometries, shielding gases, and consumable inserts. None of these variables produced suitable weld penetration characteristics for making autogenous welds in the 4.4-mm thick tubing.

Recent studies have indicated that a multipass welding technique with filler wire addition appears to be the best procedure for making the tube-to-tubesheet welds. This introduces new complications since filler wire must now be accurately fed into the weld joint inside a relatively small diameter tube. Weld bead placement from pass to pass and the cleaning of the joint surface between passes becomes important. Although this technique will be somewhat more difficult in production it appears to be a feasible approach to this joining problem.

Future designs of steam generator tube-to-tubesheet joinings could reduce the welding difficulty of this critical joint by changing one or more dimensions. It is recognized that certain changes are impractical due to the impact on the overall design or efficiency of the steam generator. Dimensional changes for consideration to reduce the welding difficulty include reduced tube wall thickness, increased tube inside diameter, and increased tube-to-tube outside diameter spacing. The reduction of tube wall thickness could eliminate the need for a multipass weld requiring filler metal addition. An increase in the tube inside diameter would provide more clearance for the welding torch and allow for better positioning of the filler wire guide tip. Increasing the spacing between tubes may

permit welding from the OD and ID. An autogenous weld pass which penetrates approximately half the tube wall thickness from each side would be relatively simple and reproducible.

7.4.2 Creep and Aging of 2 1/4 Cr-1 Mo Steel (H. E. McCoy)

Creep and aging tests are being performed in four heats of 2 1/4 Cr-1 Mo steel. Three of the heats have been studied rather extensively in the past and the fourth, in the form of 2-in. diameter bar, was added recently. The materials are being aged at 600 and 650°C in HTR-He and are being tested in air and in HTR-He. Samples of the fourth heat are being held at 670°C in sodium to remove part or all of the carbon. Many of the details of creep testing were reported previously.[16]

All four heats of material have been given an "isothermal" anneal consisting of 30 min. at 925 ±15°C, cooling to 705 ±15°C at a maximum rate of 83°C/h, holding at 705 ±15°C for 2 h, and cooling to room temperature at maximum rate of 6°C/min. After this treatment the creep properties of the heats are equivalent.

The gas/metal equilibrium in our test environment (see •7.3.1.) is such that 2 1/4 Cr-1 Mo is carburized at 480°C, decarburized at 650 and 595°C, and unchanged in carbon content at 540°C. The kinetics of carburization at the lowest temperature are very slow, and the creep properties do not seem to be affected. At 650°C the kinetics of decarburization are rather rapid and samples tested in HTR-He creep slightly faster than those tested in air.

Samples have been aged in HTR-He at 595°C for 12,500 h and tests run thus far on these samples do not indicate any effect of the aging on creep properties. Other samples have been aged nearly 10,000 h at 650°C; these may possibly have altered creep properties.

The fourth heat of material is being decarburized in sodium, and the creep effects are being evaluated. A first group of samples was exposed for 522 h at 670°C; this treatment removed about one-third of the carbon. These samples ruptured in one-tenth the times of equivalently tested specimens of as-received material. Samples were also aged 522 h in Ar at 670°C to evaluate thermal effects. This treatment also reduced rupture

life, but not nearly to the extent noted for decarburized material. A second group of samples is being exposed to sodium for a longer time to remove more of the carbon.

7.4.3 Fracture Mechanics of 2 1/4 Cr-1 Mo Steel (R. K. Nanstad and J. J. McGowan)

Study of the fracture mechanics behavior of 2 1/4 Cr-1 Mo steel is a new task initiated at the start of FY 1985. In meetings with GA designers and materials specialists, it was determined that the material form of primary interest is annealed tubing for the steam generator. Also important is the heat-affected zone of bimetallic (2 1/4 Cr-1 Mo to alloy 800H) tube welds. Of secondary interest are plates and forgings which may be manufactured of normalized and tempered 2 1/4 Cr-1 Mo.

The design temperature range of 2 1/4 Cr-1 Mo steam generator tubing is about 450 to 550°C. Properties of primary interest are initiation toughness (e.g., J_{Ic}), fatigue crack growth (da/dN), and creep crack growth (da/dt) as functions of temperature. Both thermal aging and HTR-He environment will be necessary conditions in the study.

Fracture mechanics technology is considered to be of the utmost importance in assessment of the integrity of the steam generator. In addition to the materials data, a methodology for applying the data at elevated temperatures is needed. This will also be part of the ORNL work.

Work was initiated on development of high-speed data acquisition computer interface to allow for uninterrupted collection of data during da/dN and J-R curve testing of the 2 1/4 Cr-1 Mo steel.

7.4.4 Creep-Fatigue Behavior of 2 1/4 Cr-1 Mo Steel (J. P. Strizak)

Available information on the creep-fatigue behavior of 2 1/4 Cr-1 Mo steel is being assembled and examined. Comparison of the compilation with creep-fatigue data needs for the HTR will permit selection of a matrix for additional testing.

Review of available data indicated that low-oxygen environments, including low-oxygen sodium and HTR-He, improved the continuous cycling fatigue behavior of 2 1/4 Cr-1 Mo steel over the temperature range 490 to

595°C. It is apparent in Figs. 7.20–7.22 that a low-oxygen environment is beneficial in increasing fatigue life, particularly in the low-cycle end of the fatigue curve where crack propagation dominates cycle life. The increased fatigue life is attributed to the low-oxygen environment rather than to decarburization, which can occur in HTR-He during prolonged exposure at high temperatures as shown in Fig. 7.23.

Cyclic lives of strain-controlled fatigue tests conducted in HTR-He and air are compared in Fig. 7.24 for several strain-time waveforms. All tests were conducted at a strain range of 0.5% and at temperatures of either 480 or 540°C. In comparing the cyclic lives of the specimens tested in air, it is apparent that (1) hold periods reduce the cyclic lives below

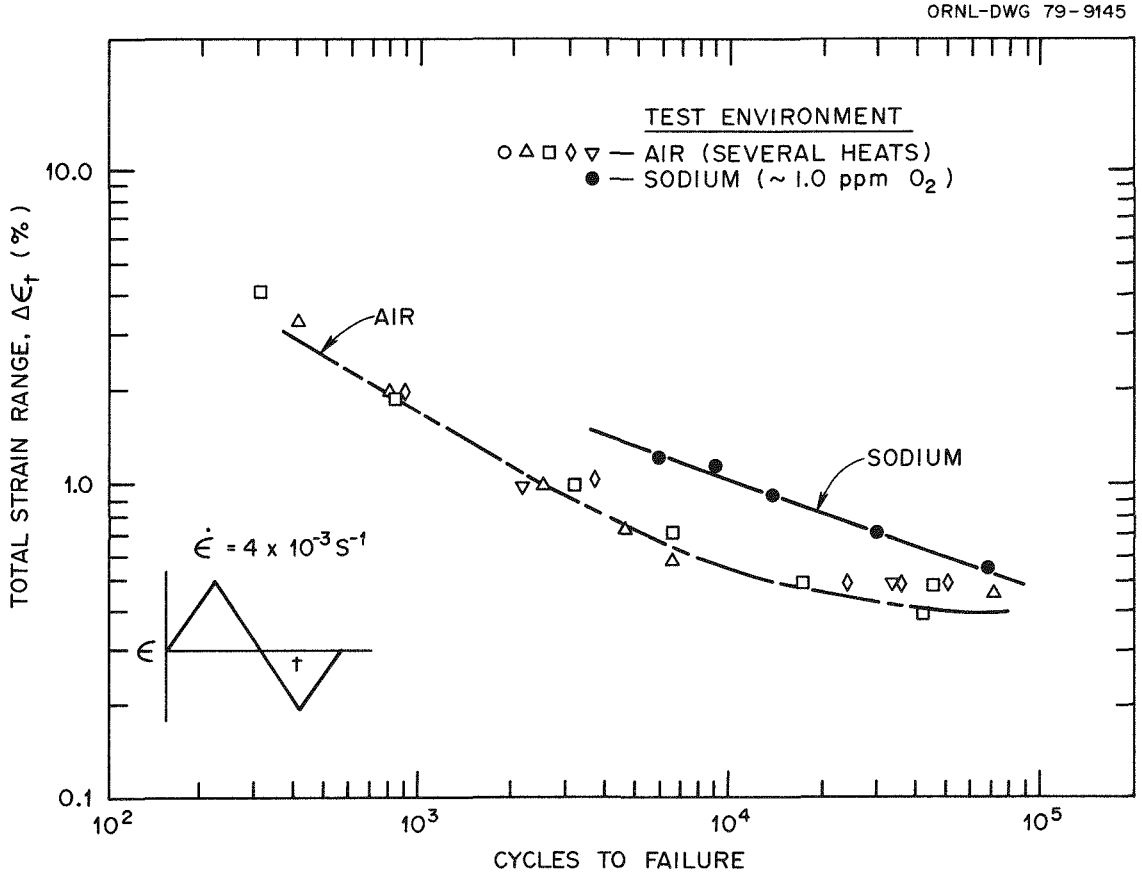

Fig. 7.20. A sodium environment improves the continuous cycling fatigue properties of 2 1/4 Cr-1 Mo steel at 480°C.

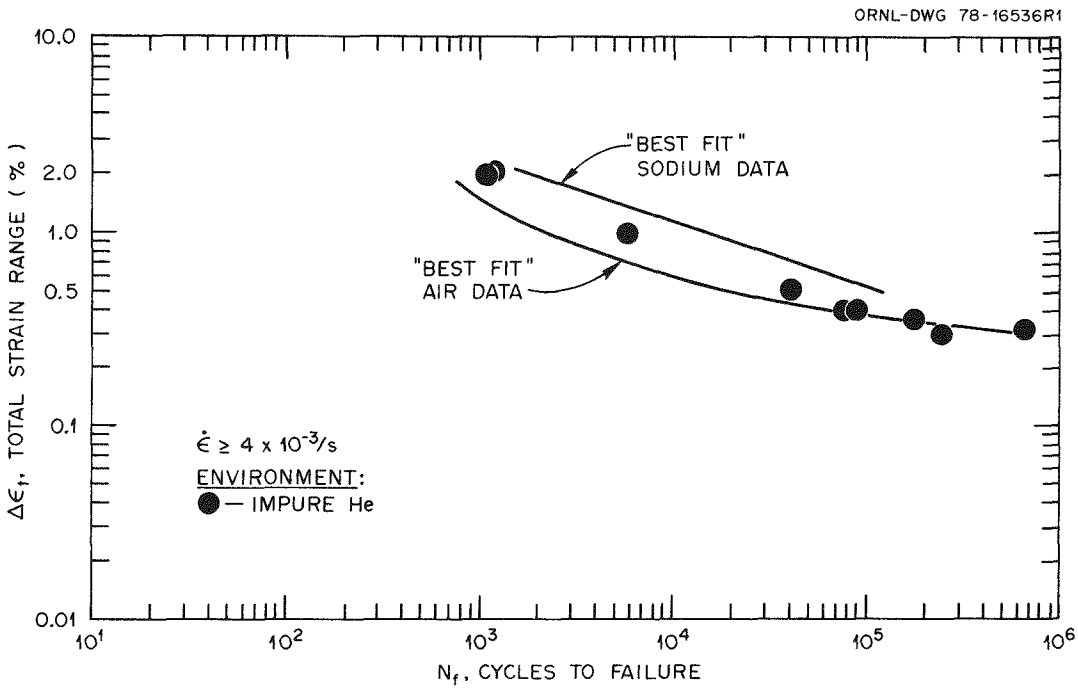

Fig. 7.21. Comparison of continuous cycling strain-controlled fatigue data from tests conducted on 2 1/4 Cr-1 Mo at 540°C.

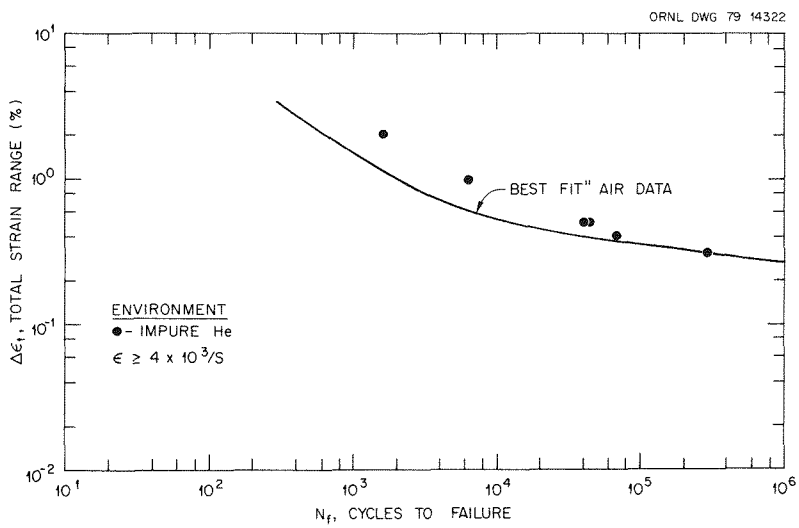

Fig. 7.22. Continuous cycling strain-controlled fatigue data on 2 1/4 Cr-1 Mo at 595°C in impure helium compared with a best-fit line of data obtained in air.

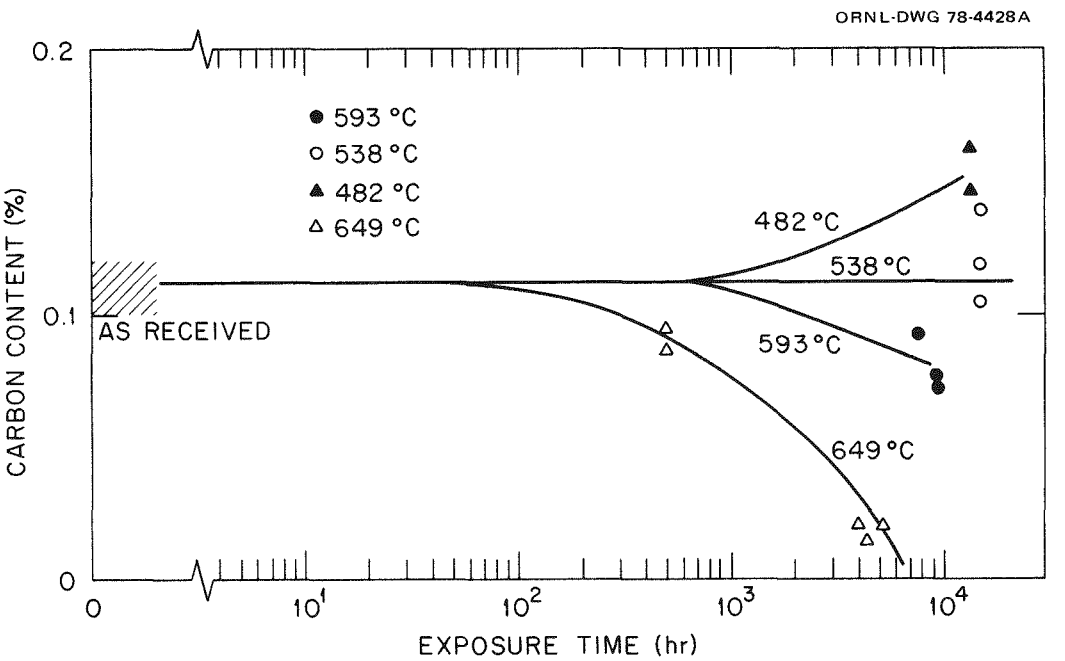

Fig. 7.23. Carbon contents of 2 1/4 Cr-1Mo steel exposed to high-temperature gas-cooled reactor helium.

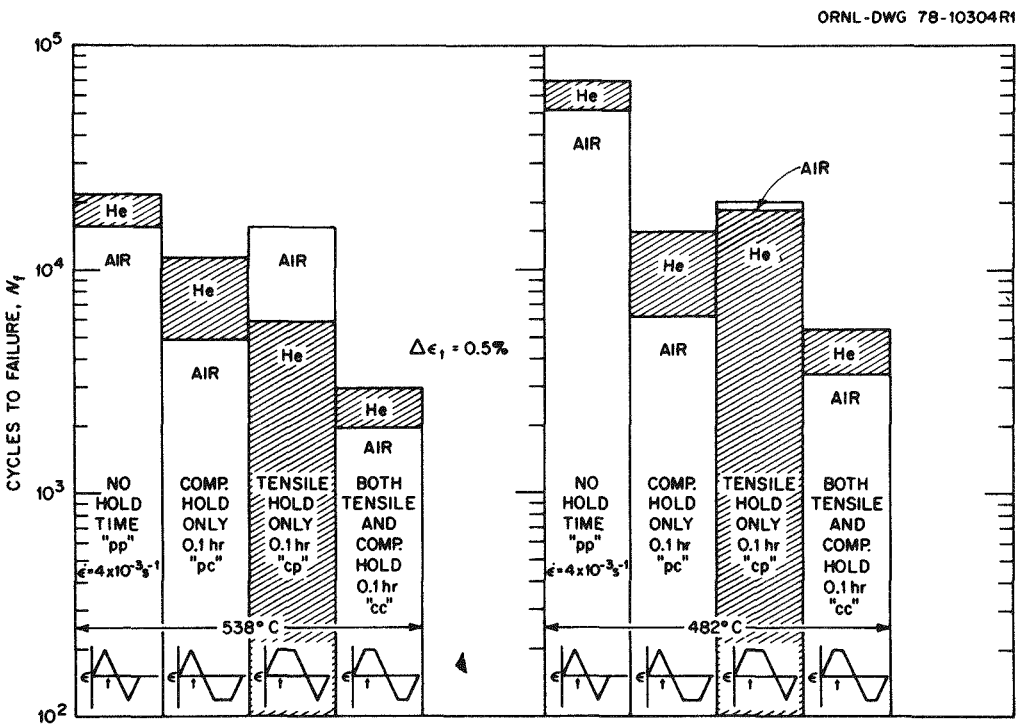

Fig. 7.24. Tests conducted in He with controlled impurities show improved cyclic lifetimes for several waveforms in comparison to air. Tensile hold times only, however, appear to be an exception.

those of continuous cycle (i.e., no hold time) tests; (2) compressive holds are more damaging than tensile holds; and (3) combined tension and compression holds of equal duration are more damaging than either tensile or compressive hold periods. Similarly, hold period tests conducted in HTR-He showed reductions in cyclic lives in comparison with continuous cycle tests.

The HTR-He environment was beneficial in improving the fatigue life for all waveforms in comparison with tests in air except for the tensile hold only tests. These results clearly indicate that environment plays an important role in conjunction with waveform in determining the time-dependent fatigue behavior of 2 1/4 Cr-1 Mo steel.

7.4.5 Decarburization Kinetics of 2 1/4 Cr-1 Mo Steel (H. Inouye)

Bar specimens of 3.18 and 6.35 mm-diam. with a length of 51 mm were machined from a commercial plate of 2 1/4 Cr-1 Mo steel and then exposed to simulated wet HTR-He containing partial pressures (Pa) of 10.1 H_2, 1.01 CH_4, 5.05 CO, 1.52 CO_2, 1.52 H_2O for times to 2.52×10^7s at temperatures of 430, 510, 580, and 650°C. Carbon analyses of the exposed specimens showed that the test gas was only slightly decarburizing at 430 and 510°C, moderate at 580°C, but severe at 650°C.

The expression that describes the decarburization for exposure to this environment is:

$$C_m - C_o/(C_s - C_o) = 2.256(Dt)^{1/2}/L \qquad [7.2]$$

where

C_m = mean carbon concentration (ppm)
C_o = initial carbon concentration (ppm)
C_s = surface carbon concentration (ppm)
D = carbon diffusivity (cm^2/s)
t = exposure time (s)
L = radius of bar specimen (cm)

The D values for Eq. 7.2 vs. $1/T$ are plotted in Fig. 7.25 and are compared with those also calculated by Eq. 7.2 for specimens exposed to other environments. The convergence of these plots at the higher temperatures

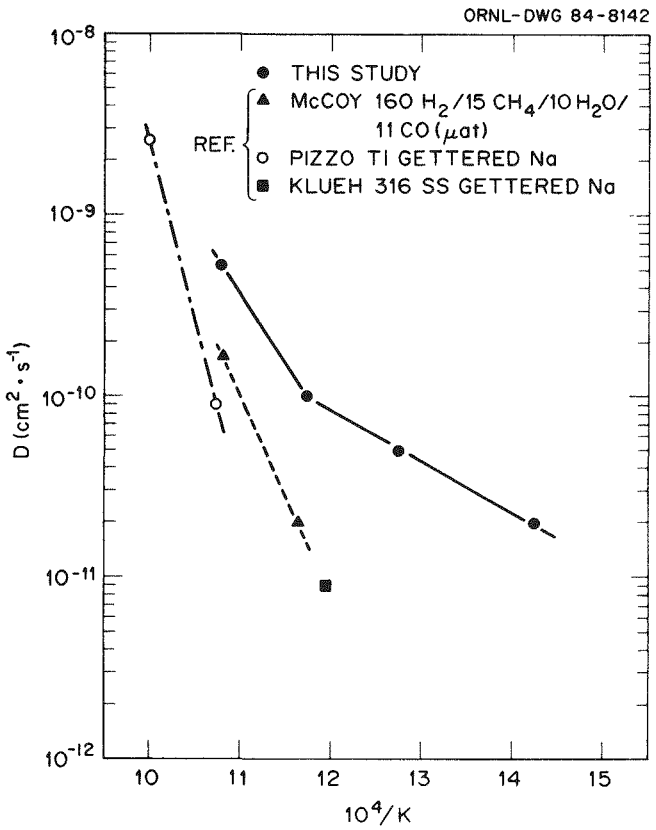

Fig. 7.25. Carbon diffusivities in 2 1/4 Cr-1 Mo steels tested in various environments.

and their divergence at the lower temperatures suggest that the carbon activity of the environment is the main variable governing the decarburization rates at the lower temperatures but has a smaller influence as the exposure temperature is increased. Further details are reported in ORNL/TM-9171 (January 1985).

7.5. ADVANCED METALLIC MATERIALS (WBS 1603.06)

7.5.1 Creep of GASM and Advanced Ni-Base Alloys - H. E. McCoy

Small quantities of bar stock of GASM alloy GA 911 (Ni-8% Cr-10% Mo-2% Al-2% Ti) and GA 912 (Ni-8% Cr-10% W-2% Al-2% Ti) were provided for

testing. Small heats of three modifications of Inconel 617 containing from 12 to 22% Cr and 2% Ti were obtained commercially as 1/2-in. thick plate.

Only limited amounts of the GA 911 and GA 912 alloys were provided; about 12 creep samples of each were prepared. Creep tests were run at 850, 900, and 950°C and all but one test is complete. The three modified heats of Inconel 617 were available in 1/2-in. thick plate, so weldability tests were also performed. All three alloys welded well and passed bend testing. Some of the modified Inconel 617 specimens have been aged to 12,500 h and creep tested for 10,000 h at to 870°C. The lower-chromium modification of Inconel 617 does have improved resistance to carburization.

The GASM Alloys (911 and 912) were quite strong at the lowest test temperature (850°C), but they rapidly declined in strength with increasing test temperature. The modified Inconel 617 alloys were weaker than standard Inconel 617, they had creep strengths about equivalent to that of Hastelloy X. At the highest test temperature (950°C), the creep strengths of all wrought Ni-base alloys that we have tested to date appear essentially equivalent. This suggests, then, that new classes of materials are desirable for service at temperatures above 900°C.

7.5.2 Nickel Aluminide Alloys (H. Inouye and C. T. Liu)

Three experimental nickel aluminide alloys with nominal compositions Ni-24% Al-0.24% B, Ni-23.5% Al-0.5% Hf-0.24% B, and Ni-20% Al-10% Fe-0.5% Hf-0.5% Mn-0.24% B were fabricated to rods and specimens 6.35 mm-diam. × 51 mm-long were exposed to simulated dry HTR-He containing partial pressures (Pa) of 50 H_2, 5 CH_4, 5 CO, for 2500 h at 950°C. Flow in the recirculating loop was 9 L/min. at 150 kPa. The corrosion and carburization resistance of the three alloys are compared with the commercial alloy Inconel 617 in Table 7.5.

These data show that weight change and carbon pickup in the nickel aluminides depend on the alloying elements even though the corrosion product is principally an adherent Al_2O_3 film. As an example, the presence of only 0.5 a/o Hf in IC-50 results in a carbon increase of 757 ppm compared

Table 7.5. Weight change and carbon increase of alloys exposed to HTR-He for 2500 h at 950°C

Alloy	Composition (a/o)	Weight gain[a] (mg/cm^2)	Carbon increase[b] (ppm)
IC-15	Ni-24% Al-0.25% B	0.19	42
IC-50	Ni-23.5% Al-0.5% Hf-0.24% B	1.60	757
IC-63	Ni-20% Al-10% Fe-0.5% Mn-0.5% Hf-0.24% B	0.30	146
IN 617	Ni-22.8% Cr-12% Co-5.2% Mo	7.00	1176

[a]Average of 6 specimens.

[b]Duplicate analyses by LECO combustion-gas chromatograph method.

to a carbon increase of only 42 ppm in the Hf-free alloy IC-15. The apparent adverse influence of Hf on carburization, however, was virtually neutralized by the Fe and/or Mn in IC-63.

All experimental aluminides were more corrosion and carburization resistant than Inconel 617.

7.5.3 High Temperature Code Development (J. J. Blass)

The objective of this task is to perform an assessment of the applicability of ASME Code Case N-47 to very high-temperature reactor (VHTR) components and to identify shortcomings and development needs.

The current design methodology for Class-1, HTR system components is embodied in the criteria of ASME Code Case N-47 (ref. 17) and in the design requirements and guidance of DOE standards F 9-4T (ref. 18) and F 9-5T (ref. 19). This methodology is currently limited primarily to Liquid Metal Fast Breeder Reactor (LMFBR) materials and to temperatures not exceeding 815°C (1500°F) for types 304 and 316 stainless steels, 760°C (1400°F) for alloy 800H, and 650°C (1200°F) for 2 1/4 Cr-1 Mo steel. In general, the methodology is based on a design-by-analysis concept addressing the several possible failure modes in high-temperature service: (1) ductile rupture from short-term loadings, (2) creep rupture from long-term loadings,

(3) creep-fatigue failure, (4) gross distortion due to incremental collapse and ratchetting, (5) loss of function due to excessive deformation, (6) buckling due to short-term loadings, and (7) creep buckling due to long-term loadings. The methodology includes many contributions in terms of both development and validation from the High-Temperature Structural Design Technology Program of Oak Ridge National Laboratory.

The approach taken in this task is to develop further the existing LMFBR high-temperature design methodology for the particular alloys and conditions of interest in the very high-temperature gas-cooled reactor (VHTR). This will be accomplished in concert with the Task Force on Very High Temperature Design (TF-VHTD) established in March 1983 within the ASME Code organization. The Task Force is to formulate design rules and procedures for Class-1 components of helium-cooled nuclear reactor plants operating at temperatures to 950°C (1742°F). A draft compilation of design rules is scheduled for completion by October 1989.

The rules will cover metal pressure boundary components designed for 20–40 year service. The materials receiving primary emphasis are alloy 800H, Hastelloy X, and Inconel 617. Secondary emphasis will be given to Inconel 618 and Nimonic 86. The rules will be consistent with applicable guidelines, will recognize inherent HTR characteristics (e.g., slow temperature changes), will differentiate between safety goals and economic goals, will avoid non-pertinent precedents, and will establish margins on a rational basis.

Two informal reports[20,21] were prepared during 1984 for subsequent presentation to the Task Force. These reports will serve as the basis for a formal ORNL report to be issued in 1985. The first report[20] provided an assessment of the applicability of ASME Code Case N-47 to VHTR components. This assessment served to focus Task Force attention on a number of technical issues. Prominent among these was the tensile and creep ductility of Hastelloy X weldments. This led to preparation of the second report,[21] a survey of mechanical properties of Hastelloy X and Hastelloy XR weldments.

Based on Task Force deliberations thus far, significant departures from the ASME high-temperature Code Case N-47 are expected. Among these are inclusion of effects of aging on strength and ductility, elimination

of the tertiary creep criterion from the time-dependent stress allowable, establishment of strain limits based on analysis of experimental data, modification of elastic ratchetting and creep fatigue rules to include rapid stress relaxation effects, consideration of mechanical behavior exhibiting little strain hardening, and explicit coverage of the effects of pernicious environments.

7.6 REFERENCES

1. G. F. Smolik and G. E. Korth, "Reference Heat of Alloy 718 for Department of Energy Programs," TREE-1253, Idaho National Engineering Laboratory, EG&G Idaho, Inc., April, 1978.

2. H. A. Ernst, "Material Resistance and Instability Beyond J-Controlled Crack Growth," *Elastic Plastic Fracture: Second Symposium Volume I - Inelastic Analysis*, ASTM STP-803, 1983, pp. I-191—I-213.

3. F. L. Loss, ed. "Structural Integrity of Water Reactor Pressure Boundary Components," Annual Report, FY 1979, USNRC, Report NUREG/CR-1128, 1979.

4. J. J. McGowan and R. K. Nanstad, "A Direct Comparison of Unloading Compliance and Potential Drop Techniques in J-Integral Testing," *Computer-Aided Testing and Model Analysis*, Society for Experimental Mechanics, November 1984.

5. L. A. James and W. J. Mills, "Effect of Heat Treatment and Heat-to-Heat Variations in the Fatigue-Crack Growth Response of Alloy 718 - Part 1: Macroscopic Observations, Hanford Engineering Development Laboratory, HEDL-TME 80-9, April 1980.

6. P. F. Tortorelli, "Compatibility of Alloys with B_4C Compacts, pp. 199—200, *High-Temperature Gas-Cooled Reactor Technology Development Program Annual Progress Report for Period Ending December 31, 1983*, ORNL-6053, June 1984.

7. S. Baba, et al., "Compatibility of Heat Resistant Alloys with Boron Carbide," JAERI-M-82-196, Japan Atomic Energy Research Institute December 1982.

8. B. Fleischer, J. H. DeVan, and J. H. Coobs, "Graphite-Stainless Steel Compatibility Studies," ORNL/TM-338, Oak Ridge National Laboratory, September 1962.

9. H. E. McCoy, "Creep Behavior of Hastelloy X, 2 1/4 Cr-1 Mo Steel, and Other Alloys in Simulated HTGR Helium," ORNL/TM-6822, June 1979.

10. H. E. McCoy and J. F. King, "Evaluation of Hastelloy X for Gas-Cooled Reactor Applications," ORNL/TM-8499, November 1982.

11. H. E. McCoy, J. P. Strizak, and J. F. King, "Hastelloy X for High-Temperature Gas-Cooled Reactor Applications," Nuclear Technology, **66**, July 1984, pp. 161–174.

12. H. E. McCoy and J. F. King, "Mechanical Properties of Inconel 618 and 618," ORNL/TM-9337, February 1985.

13. H. E. McCoy and J. F. King, "Evaluation of HD556 and Incoloy 802 for High-Temperature Gas-Cooled Reactor Applications," ORNL/TM-9382, January 1985.

14. J. P. Strizak, "High-Cycle Fatigue Behavior of Hastelloy X," p. 193, *High-Temperature Gas-Cooled Reactor Technology Development Program Annual Progress Report for Period Ending December 31, 1983*, ORNL-6053, June 1984.

15. J. F. King, "Joining Technology," pp. 200–207, *High-Temperature Gas-Cooled Reactor Technology Development Program Annual Progress Report for Period Ending December 31, 1983*, ORNL-6053, June 1984.

16. H. E. McCoy, "Creep Behavior of Hastelloy X, 2 1/4 Cr-1 Mo Steel, and Other Alloys in Simulated HTGR Helium," ORNL/TM-6822, June 1979.

17. Case N-47-22, Class 1 Components in Elevated Temperature Service," Sect. III, Div. 1, *Cases of ASME Boiler and Pressure Vessel Code*, American Society of Mechanical Engineers, New York, April 5, 1984.

18. NE Standard F 9-4T, *Requirements for Design of Class 1 Elevated Temperature Nuclear System Components (Supplement to ASME Code Case N-47)*, U.S. Dept. of Energy, February 1984.

19. NE Standard F 9-5T, *Guidelines and Procedures for Design of Class 1 Elevated Temperature Nuclear System Components*, U. S. Dept. of Energy, March 1981.

20. K. Hada, *An Assessment of the Applicability of ASME Code Case N-47 to VHTR Components*, presented to ASME Task Force on Very High Temperature Design, June 24, 1984.

21. K. Hada, *A Comparative Survey of Mechanical Property Data for Hastelloy X and XR Weldments*, presented to ASME Task Force on Very High Temperature Design, February 25, 1985.

8. CERAMICS (WBS 1604.01)

D. J. Naus and P. L. Rittenhouse

8.1 INTRODUCTION — D. J. Naus

The function of the HTGR thermal barrier is to protect the Prestressed Concrete Reactor Vessel (PCRV) liner and adjacent concrete from overheating due to high temperature helium. This protection is provided by a system of fibrous insulation blankets plus cover plates, seals, and hard structural ceramics. In the bottom head region of the core outlet plenum, the thermal barrier also dissipates hot gas streaks and provides structural support for the reactor core. The present testing program is concerned with this last aspect of the thermal barrier; it is an evaluation of the hard ceramic pad and interface materials that are used to support the graphite posts, which support the core.

8.1.1 Ceramic Material Testing

During the past year, structural response tests were conducted on pads that were fabricated from a fused-silica, hard ceramic material. The pads, which were supplied to ORNL by GA Technologies Inc., were in the form of right circular disks having a centrally located hole extending vertically through each disk as shown in Fig. 8.1. Through the use of specially designed test fixture shown in Fig. 8.2, which incorporated either flat or conical platen sets, we subjected these pads to mechanical loading conditions to provide a parametric representation of loads that would be induced in the ceramic pads due to thermal gradients. This phase of testing, which is part of an overall series of tests,[1] was conducted only at room temperature and followed procedures similar to those used in the previous series of tests involving Grades 85 and 995 Alumina and fused-silica, hard ceramic materials.[2]

ORNL PHOTO 7290-84

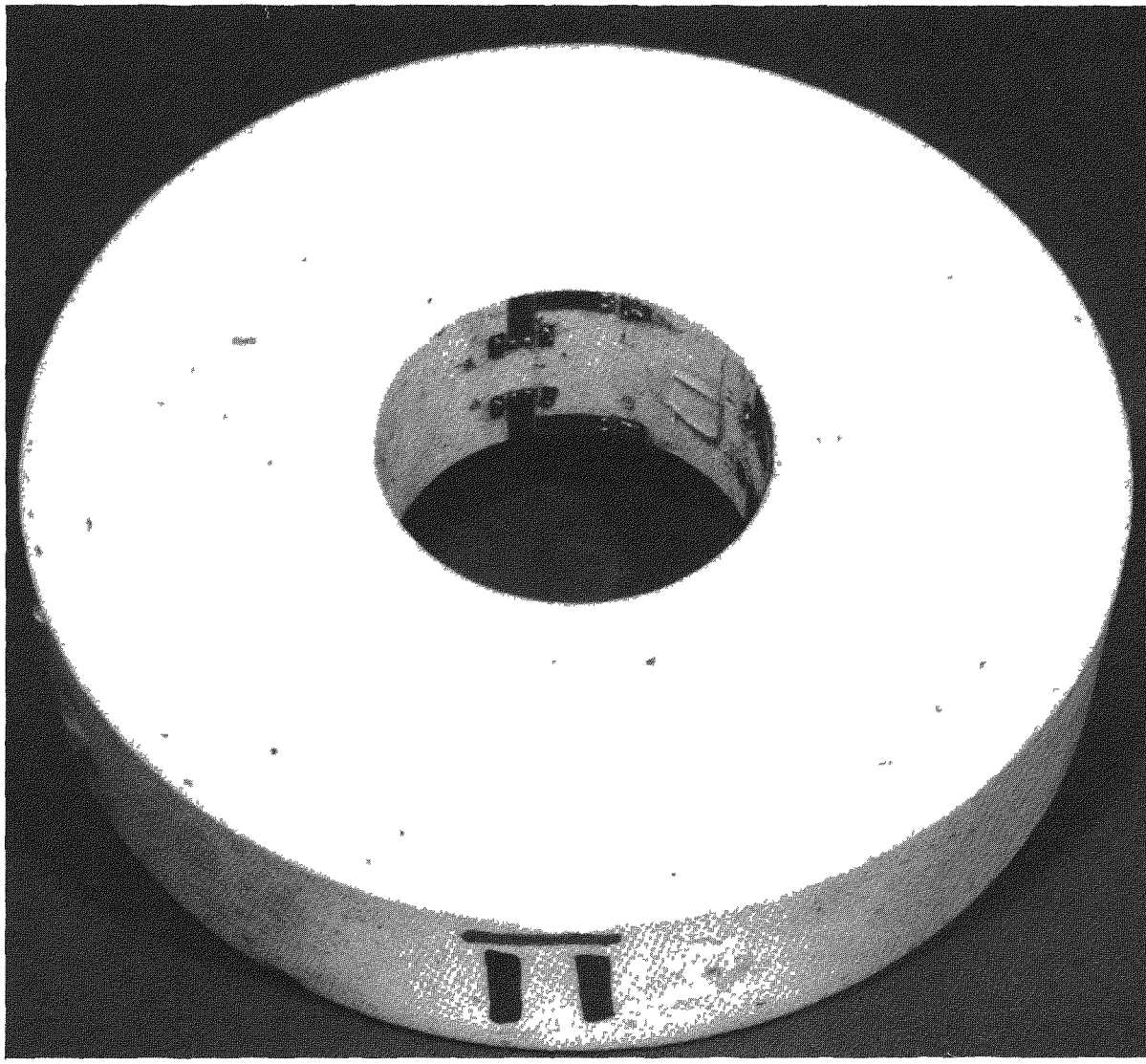

Fig. 8.1. Typical fused-silica pad for structural response tests.

ORNL PHOTO 8289-82R

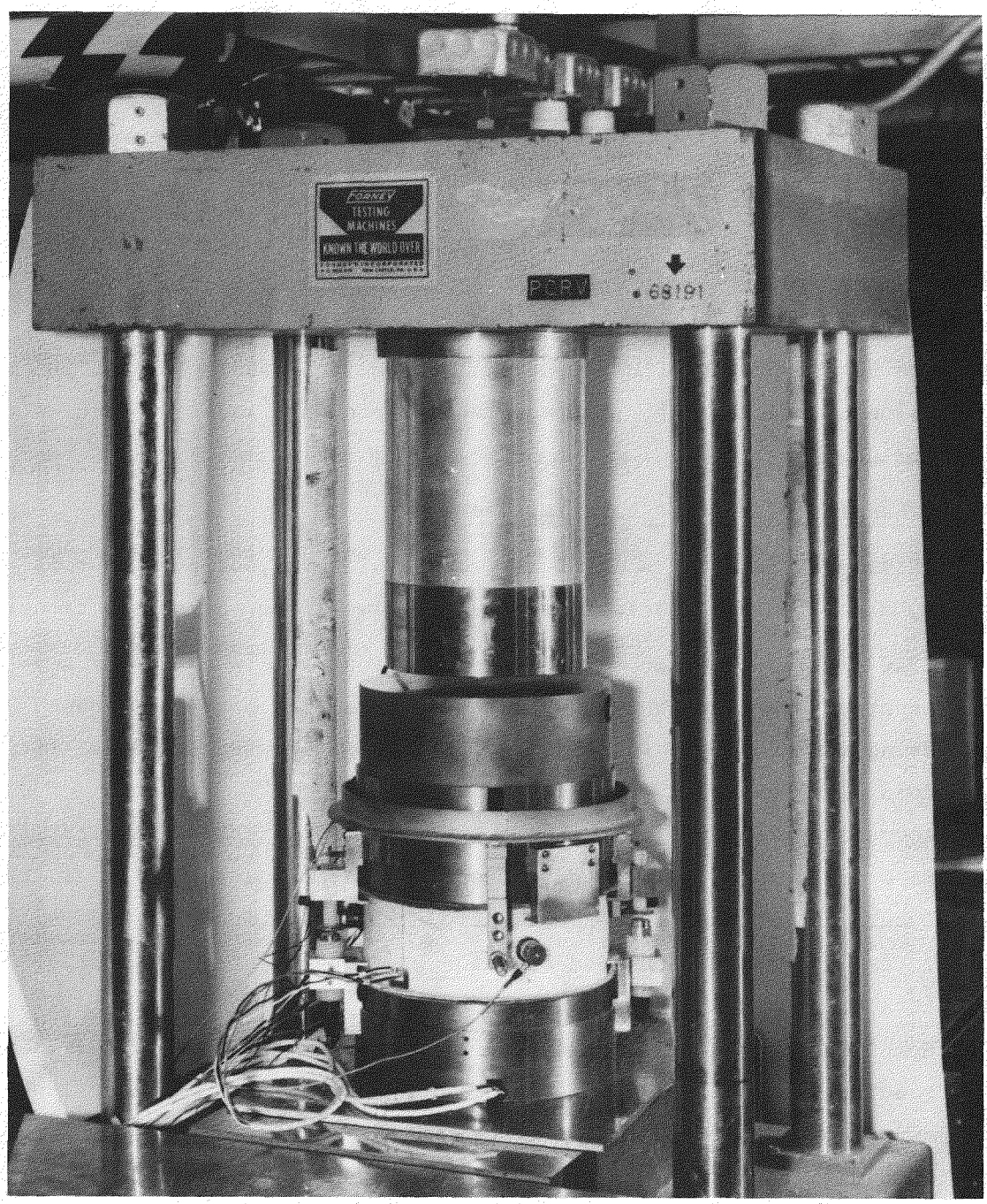

Fig. 8.2. Test fixture used to load thermal barrier hard ceramic pads mechanically.

We conducted 15 tests in which the fused-silica ceramic pads were mechanically loaded with the test fixture shown in Fig. 8.2. The pads were initially loaded with flat platens to 890 kN. At the conclusion of the flat platen loading, the flat platens were replaced by conical platen sets having the required taper, and the loading cycle was repeated. Platen offsets used in the investigation ranged from 0 mm (flat) to 0.254 mm. Table 8.1 presents the number of interface layers, platen offset, maximum applied load, and final condition of the specimen for each of the 15 tests. Strain, displacement, and acoustic emission data were obtained as a function of applied load during each loading cycle. At the conclusion of the testing, posttest radiographs were made for each of the 6 specimens.

8.1.2 Results of Ceramic Material Tests

Although a detailed analysis of the results was not part of this procedure, a few general conclusions can be derived from our observations:

- Flat platens (no induced specimen rotations) did not produce any apparent specimen cracking for the fused silica materials loaded using either two or four layers of Siltemp interface material for the load level examined [890 kN (200 kips)].
- Acoustic emission (AE) activity obtained from the fused silica materials exhibited a trend to decrease as the number of layers of interface material increased. Also, as the number of interface layers increased, the load at which cracking occurred increased. (Cracking noted by increased AE activity.)
- Specimen to specimen consistency with respect to AE activity was very good for specimens tested under similar conditions. However, specimen 13 was significantly more active than either of the other two specimens (specimens 11 and 14) tested under similar conditions.
- AE results correlated well with discontinuities (sudden changes) in the strain-versus-load curves, which were obtained for each test.

More details on this series of tests are contained in internal reports.[3]

Table 8.1. A summary of test results for the fused-silica, thermal barrier hard ceramic pads

Specimen designation	Number Siltemp layers[a]	Platen offset (mm)	Maximum applied load (kN)	Cracking[b]
026568-001-1	2	0	891.0	No
-1	2	0.152	891.0	Yes
-3	2	0	890.5	No
-3	2	0.152	890.5	Yes
-10	2	0	891.4	No
-10	2	0.152	890.5	Yes
-11	4	0	890.5	No
-11	4	0.152	890.5	Yes
-11	4	0.254	890.5	Yes
-13	4	0	891.9	No
-13	4	0.152	891.0	Yes
-13	4	0.254	890.5	Yes
-14	4	0	891.0	No
-14	4	0.152	891.0	Yes
-14	4	0.254	891.0	Yes

[a]Layers per loaded face.

[b]As detected by a discontinuity in the strain, displacement or acoustic emission response.

8.2 CERAMIC TECHNOLOGY PLANNING — P. L. Rittenhouse

An effort on the preparation of a Technology Development Program Plan was scheduled to begin in the final quarter of 1984. It was decided subsequently to combine this work into the Plan for metallic materials (see Section 7.1).

8.3 CREEP TESTING OF DENSE CERAMICS — H. E. McCoy

Four ceramic materials have been creep tested in helium atmospheres typical of HTRs. The materials are grade 7941 SiO_2 made by Corning, grade 11981 SiO_2 made by Thermo Materials, grade AD 85 Al_2O_3 made by Coors, and grade AD 995 Al_2O_3 made by Coors. Some microscopic characterization studies of these materials were performed by Lauf.[4] The mechanical testing methods included the compression of right circular cylinders and four-point bend tests in which rectangular bars were tested. The test environment

was helium containing small amounts of H_2, CH_4, CO, and H_2O. Details of the test environment and testing procedure were described previously.[5]

Creep in all four materials was characterized by an initial high creep rate decelerating to a near steady-state rate. Only in two tests was the amount of strain sufficient to cause the specimen diameter to increase significantly. There is considerable scatter in the test results for grade 7941 SiO_2, and this is illustrated well by the duplicate tests at 871°C and 14 MPa that differ in creep rate by about two orders of magnitude. There does seem to be a marked change in behavior between 871 and 927°C, and the creep rate at 927°C is significantly higher than that at 871°C.

The Thermo Materials SiO_2 (11981) was tested at lower temperatures and higher stresses than the Corning SiO_2 (7941), so it is not possible to make a comparison of relative strengths. Two tests show that the problem of reproducibility of test results also exists for TM 11981 material. These two tests have stresses that differ by a factor of 2, but the creep rates vary by a factor of 2 in the opposite direction.

The two tests on the two grades of Al_2O_3 have shown very little creep response under the test conditions being used. This is the type behavior expected for Al_2O_3 at 750°C.

Some results were obtained in four-point bending. In this type test, one side of the specimen is in tension and the other in compression. (In the compression tests, the entire specimen is loaded in compression.) Since ceramic materials are generally weaker in tension than in compression, it is not surprising that they would exhibit more creep in the four-point bend configuration than in simple compression. This expected pattern was borne out by the test results.

8.4 REFERENCES

1. R. K. Luci, GA Technologies, San Diego, Calif., unpublished data, Dec. 23, 1982.

2. D. J. Naus, unpublished data, March 1983.

3. C. B. Oland and D. J. Naus, unpublished data, August 1983.

4. R. J. Lauf and H. E. McCoy, "Characterization of Core Support Ceramics," *Gas-Cooled Reactor Programs High-Temperature Gas-Cooled Reactor Technology Development Program Annual Progress Report for Period Ending Dec. 31, 1983*, ORNL-6053 (June 1984) p. 117—121.

5. H. E. McCoy and J. F. King, *Evaluation of Hastelloy X for Gas-Cooled Reactor Applications*, ORNL/TM-8499 (Nov. 1982).

9. CONCRETE MATERIALS QUALIFICATION (WBS 1605.01)

D. J. Naus

9.1 INTRODUCTION

Design optimization studies by GA Technologies Inc.[1] (GA) have indicated that a significant size reduction (≈1.3 m) can be effected in the Prestressed Concrete Reactor Vessel (PCRV) for a 2240-MW(t) HTGR through the use of 55-MPa concrete in conjunction with 13.3-MN capacity vertical prestressing tendons. This can lead to substantial cost savings (≈$5.7 M) in both the PCRV and the containment structure. However, in order to realize this cost savings it must be demonstrated that concrete mix designs can be developed that have the required mechanical and thermal properties.

9.2 OBJECTIVE AND SCOPE OF THE TEST PLAN

The objective of the overall test program is to develop and evaluate high-strength concretes (>63.4-MPa)* using materials that are in close proximity to areas representing potential sites for an HTGR plant. The program is to be conducted in three phases. Phase I involves the selection and evaluation of materials, identification of optimum cement contents, evaluation of the selected aggregate materials plus the effects of partial cement replacement by fly ash, and final mix selection and determination of strength and elastic properties.

Phase II is concerned with an evaluation of the effect of temperatures to 316°C on both sealed and unsealed specimens fabricated from the mix designs developed under Phase I.

---

*The ASME Code[2] requires that an average compressive strength at least 8.3 MPa greater than the specified strength be produced in the laboratory.

Phase III involves a determination of the creep characteristics of the concretes developed under Phase I when subjected to loadings representing either 30%, 45%, or 60% or their control strengths at temperatures to 71°C. Thermal properties and the effects of thermal cycling on strength and elastic properties will be evaluated under this phase. The detailed test plan[3] presents more information on the overall test program, and the detailed procedures[4] of Phase I presents a description of activities that were conducted during this year.

9.3 FACTORS RELATED TO THE PRODUCTION OF HIGH-STRENGTH CONCRETE

To achieve high-strength concrete, optimization of the following factors is required: (1) characteristics of the cementing medium; (2) characteristics of the aggregate; (3) proportions of the paste; (4) paste-aggregate interaction; (5) mixing, consolidation and curing; and (6) testing procedures. Choice of type and brand of cement is probably one of the most important factors in the selection of materials and should be on the basis of long-term strength development. Durable aggregate materials, free of deleterious substances and having good thermal and mechanical properties, must be utilized.

Development of high strengths requires use of the lowest possible water-cement ratio (0.30-0.40) and high cement factors (>450 kg/m^3). Appropriate procedures must be followed to ensure that the concrete is thoroughly mixed, adequately consolidated, and properly cured. By employing these considerations in conjunction with a comprehensive quality assurance and quality control program, we can achieve consistent production and placement of ready-mix concretes having compressive strengths in excess of 75 MPa.

9.4 MATERIAL SELECTION AND EVALUATION

Representative concrete-making materials, conforming as closely as possible to requirements presented in the previous section, have been selected for use in this study. These materials include cement, fly ash, water reducing and retarding admixtures, and aggregates.

ASTM Type II moderate heat of hydration and low alkali content Portland cement having a 7-d mortar cube strength >29 MPa was selected.

ASTM Class C fly ash having a loss of ignition (<3%) and a high pozzolanic activity index (>100% at 28-d) was chosen for use as a partial replacement for cement.

Selection of Pozzolith 300-R as the admixture was based on its compatibility with the three ASTM Type D water reducing-retarding admixtures evaluated with the type and brand of cement procured. Strength and workability results from a series of trial mixes were utilized to evaluate cement compatibility and to determine the dosage.

Since aggregate materials generally occupy 60 to 80% of the volume of concrete, their availability and quality represent a key ingredient in the production of high-strength concrete. Results of a survey conducted in conjunction with this program indicate that high-strength concretes can be produced anywhere in the U.S., but certain areas (e.g., Florida) may require the use of imported aggregate at a cost penalty of $\$52/m^3$.

In order to establish bounds on concrete properties obtainable from aggregate materials available in the U.S., four sites were selected corresponding to areas that are candidate locations for the HTGR plant, and local aggregate materials from these areas were obtained. These sites included: the Pennsylvania-Delaware border area; Florida City-Turkey Point, Florida; Port Arthur, Texas; and Blythe, California area.

An interim report[5] presents particulars on the selection and evaluation of materials for use in the investigation.

9.5 OPTIMUM CEMENT CONTENT DETERMINATIONS

As noted by Mead,[6] there is an optimum cement factor for concrete mixes of equal workability and the same consistency that uses a specific aggregate of a certain maximum size. The optimum cement factor used in this study was evaluated through a series of laboratory mixes utilizing the Pennsylvania-Delaware border area aggregate materials [38-mm and 9.5-mm maximum size aggregate (MSA)]. Cementitious materials contents (90% cement plus 10% fly ash, by weight) ranged from 7 to 12 sacks/cu. yd. (390 to 670 kg/m^3). In the mixes, the MSA was held constant, the water

content was adjusted to maintain the slump at 80 ± 13 mm, and the fine aggregate content was adjusted to account for the changing cement and water contents. Cement contents of 586 kg/m^3 and 530 kg/m^3 were selected for the 38-mm and 9.5-mm MSA, respectively, based on results present in Figs. 9.1 and 9.2

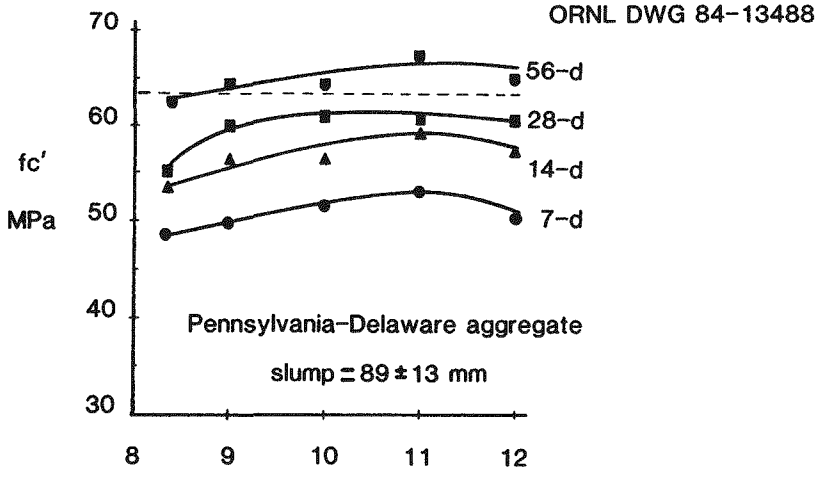

Fig. 9.1. Test results for optimum cement content determination for 38-mm maximum size aggregate.

9.6 AGGREGATE AND FLY ASH EVALUATION TESTING

In this series of tests, each of the four aggregate sources was evaluated as well as the effect of partial replacement of cement with fly ash. Using results from the optimum cement content test series, concrete mixes were fabricated for each of the aggregate sources. Cement replacement by fly ash in the mixes varied from 0 to 40%, by weight, and each mix was designed for equal workability by adjusting the water content to maintain the slump at 89 ± 13 mm. Fine aggregate contents were adjusted to account for the changing volume from mix to mix of the cement, fly ash and water. Tables 9.1.1 through 9.4.2 present basic mix designs, mix properties, and test results obtained to date for the four aggregate sources being evaluated.

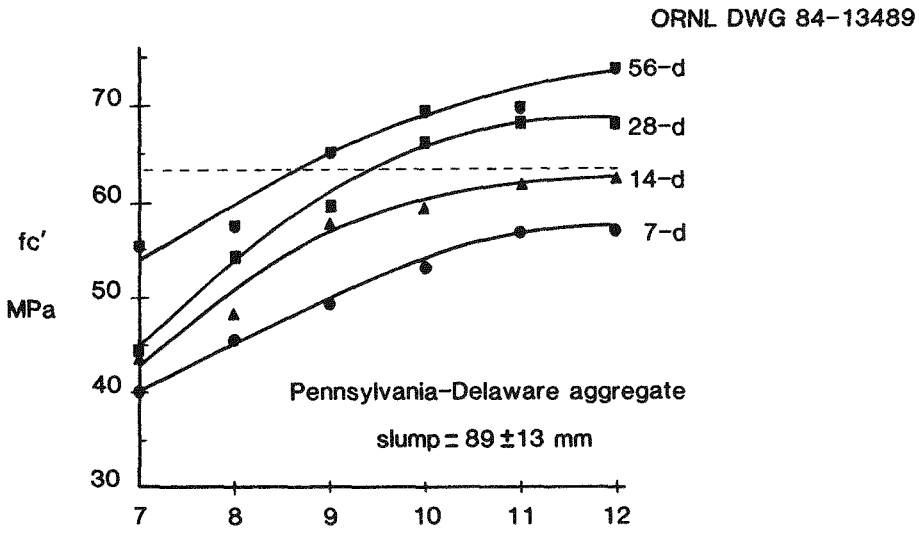

Fig. 9.2. Test results for optimum cement content determination for 9.5 mm maximum size aggregate.

9.7 FINAL AGGREGATE SELECTION FOR DETAILED PROPERTY DETERMINATION

Compressive strength test results demonstrate that the target compressive strength of >63.4 MPa can be achieved using materials from each of the four aggregate sources selected for evaluation. In order to acquire a representative range of concrete properties that can be obtained from potential aggregate sources in the U.S., the Pennsylvania-Delaware border area and the Florida City-Turkey Point, Florida materials were selected for use in the balance of the investigation. The Pennsylvania-Delaware border area aggregate was selected on the basis that it had been used in the development of 45-MPa mix designs for the previous generation PCRVs (Fulton and Summit plants).[7] Selection of the Florida City-Turkey Point, Florida aggregate was on the basis that it produced concrete mixes having the lowest modulus of elasticity. Compressive strength, tensile strength, modulus of elasticity and Poisson's ratio values will be established from specimens which have been fabricated using materials from these sources. Tests will be conducted on both moist-cured and sealed specimens at concrete ages to 182 d. These materials will also be used in subsequent Phases II and III of the overall study.

Table 9.1.1. Fly Ash Content Evaluation: 38-mm maximum size aggregate[a]

Batch No.[b]	21A	21B	22A	22B	23A	23B	24A	24B	25A	25B	26A[d]	26B[d]
	Fly ash content - % of cementitious materials											
Materials (per cu yd)	0	0	10	10	20	20	30	30	40	40	30	30
Cement, lb	994	987	894	893	795	795	690	689	588	588	681	682
Fly ash, lb	0	0	100	100	198	198	293	292	392	393	289	290
Coarse aggregate, lb (SSD)	1896	1882	1906	1904	1900	1900	1896	1894	1884	1887	1874	1876
Fine aggregate, lb (SSD)	937	931	927	926	959	959	969	967	951	952	957	958
Water, lb	287	285	279	279	270	270	265	265	264	265	262	262
Admixture, oz.	40	39	40	40	40	40	40	40	40	40	60	60
Mix Properties												
Slump, in.	3 1/2	3 3/8	3 1/4	3 1/8	4	4	4	5 1/2	5	5 3/4	6	7 1/4
Unit wt., lb/ft^3	152.4	151.4	152.2	152.0	152.8	152.8	152.4	152.2	151.2	151.4	150.6	150.8
Air Content, %	1.80	1.80	1.60	1.85	1.55	1.60	1.60	1.60	1.40	1.45	2.25	2.20
W/C, lb/lb	0.289	0.289	0.281	0.281	0.272	0.272	0.270	0.270	0.269	0.270	0.270	0.270
Workability	good[c]	good[c]	good[c]	good[c]	very good[c]	very good[c]	very good[c]	very good[c]	very good[c]	very good[c]	very good[c]	very good[c]
Compressive Strength, psi (Moist cure)												
7-day average	-	7665	-	7685	-	8330	-	8415	-	6985	-	6060
14-day average	8040	-	7385	-	8145	-	9745	-	8795	-	9485	-
28-day average	-	9090	-	9140	-	9525	-	9995	-	10140	-	9900
56-day average	9275	9320	8525	10105	10595	10790	10715	11710	10710	10185[e]	11180	11770
91-day average	9915	9545	9900	10205	10895	11205	11820	12635	12930	12930	11565	10925
182-day average	10535	-	11185	-	12060	-	13220	-	13435	-	13590	-
Compressive Strength, psi (Sealed)												
7-day average	-	6760	-	6800	-	6390	-	5595	-	6225	-	4910
14-day average	8050	-	7645	-	7090	-	6050	-	6760	-	6290	-
28-day average	-	7855	-	6135	-	7410	-	6625	-	8145	-	8345
56-day average	7720	-	8390	-	8455	-	7925	-	6805	-	8835	-
91-day average	-	9340	-	7725	-	8695	-	8660	-	9040	-	8445
182-day average	10125	-	9905	-	9050	-	9095	-	8395	-	9585	-

[a] Pozzolith 300R admixture. Pennsylvania/Delaware border area aggregate.

[b] Two batches are required for each fly ash content to provide sufficient materials to cast strength cylinders and obtain mix properties.

[c] Lost workability as casting process progressed. Mix still placeable and compactable with vibration at end of casting process. (Workability maintained with agitation, however).

[d] 150% WRA (6 oz/100 lb).

[e] One specimen only, other specimens split.

Table 9.1.2. Fly ash content evaluation: 9.5-mm maximum size aggregate[a]

Batch No.[b]	27A	27B	28A	28B	29A	29B	30A	30B	31A	31B
	Fly ash content - % of cementitious materials									
Materials (per cu yd)	0	0	10	10	20	20	30	30	40	40
Cement, lb	895	895	803	799	710	715	623	622	538	538
Fly ash, lb	0	0	89	89	177	179	267	267	358	359
Coarse aggregate, lb (SSD)	1735	1735	1733	1724	1724	1735	1730	1725	1740	1742
Fine aggregate, lb (SSD)	1182	1182	1186	1180	1191	1199	1211	1208	1218	1219
Water, lb	295	295	289	288	272	274	265	265	259	259
Admixture, oz.	36	36	36	36	36	36	36	36	36	36
Mix Properties										
Slump, in.	3 5/16	3 1/8	3 5/8	3 5/8	3 3/16	3 3/8	3 1/4	2 7/8	3 3/4	3 3/8
Unit wt., lb/ft^3	152.2	152.2	152.0	151.2	151.0	152.0	151.8	151.4	152.4	152.6
Air Content, %	1.75	2.05	1.80	2.65	3.20	2.65	2.60	2.90	2.00	2.05
W/C, lb/lb	0.330	0.330	0.324	0.324	0.306	0.306	0.298	0.298	0.289	0.289
Workability	very good	very good	very good	very good	very[c] good	very[c] good	very[c] good	very[c] good	very[c] good	very[c] good
Compressive Strength, psi (moist cure)										
7-day average	-	7190	-	7095	-	7600	-	6895	-	5335
14-day average	7505	-	8230	-	7910	-	9325	-	8275	-
28-day average	-	8220	-	8810	-	9700	-	10290	-	10000
56-day average	9085	8385	9995	9480	9465	10480	10725	11155	11585	11210
91-day average	9815	9915	10325	9920	10745	11600	12355	12255	12330	11840
182-day average	10680	-	11445	-	11285	-	13355	-	13825	-
Compressive Strength, psi (sealed)										
7-day average	-	6300	-	6325	-	6230	-	6935	-	4805
14-day average	7680	-	6400	-	7445	-	7300	-	6390	-
28-day average	-	7870	-	7640	-	8140	-	7820	-	7870
56-day average	8443	-	8990	-	7425	-	9180	-	8990	-
91-day average	-	7915	-	8565	-	10040	-	9825	-	9740
182-day average	9845	-	9480	-	10115	-	10145	-	9990	-

[a]Pozzolith 300R admixture. Pennsylvania/Delaware border area aggregates.

[b]Two batches are required for each fly ash content to provide sufficient materials to cast strength cylinders and obtain mix propertis.

[c]Lost workability as specimen casting progressed.

Table 9.2.1. Fly ash content evaluation: 38-mm maximum size aggregate[a]

Batch No.[b]	32A	32B	33A	33B	34A	34B	35A	35B	36A	36B	37A	37B
	Fly ash content = % of cementitious materials											
Materials (per cu yd)	0	0	0	0	10	10	20	20	30	30	40	40
Cement, lb.	978	975	979	980	884	891	785	788	682	691	589	588
Fly ash, lb.	0	0	0	0	99	100	196	196	293	296	393	392
Coarse aggregate, lb (SSD)	2016	2010	2018	2018	2009	2023	2007	2012	1991	2017	2005	2002
Fine aggregate, lb (SSD)	781	779	782	783	768	772	789	790	769	780	778	777
Water, lb.	267	267	268	268	261	262	260	261	259	263	261	261
Admixture, oz.	39	39	39	39	39	39	39	39	39	39	39	39
Mix Properties												
Slump, in.	3 1/2	3 1/2	3 5/8	4	3 5/8	3	3 3/4	3 1/8	3 1/4	4	3 1/2	5 1/2
(Δt, minutes)[e]	(14)	(21)	(18)	(17)	(20)	(24)	(25)	(25)	(32)	(33)	(40)	(32)
Unit wt., lb/ft^3	149.8	149.4	150.0	150.2	149.0	150.0	149.6	150.0	148.0	150.0	149.2	149.0
Air content, %	1.65	1.80	1.60	1.60	1.80	1.65	1.60	1.55	1.65	1.55	1.05	1.35
W/C, lb/lb.	0.273	0.271	0.274	0.273	0.266	0.264	0.265	0.265	0.266	0.266	0.266	0.266
Workability	very good	very good	very good	very good	very good	very good	very good	very good	very good	very good	very good	very good
Compressive Strength, psi (moist cure)												
7-day average	-	-	-	6075	-	-	-	6700	-	7540	-	3940
14-day average	-	-	7605	-	7370	7225	7500	-	8660	-	8005	-
28-day average	-	-	-	8760	-	8473	-	8180	-	10180	-	
56-day average	-	-	9130	8830	8700	9125	8480	10125	10470	10675	10945	10515
91-day average	-	-	9325	9240	9110	9595	9455	10450	11235	11845	11235	11410
182-day average	-	-	10245	-	9810	-	10060	-	12150	-	11010	-
Compressive Strength, psi (sealed)												
7-day average	-	7040	-	6600	-	-	-	6465	-	6115	-	4265
14-day average	6350	-	6450	-	7260	6460	6925	-	6860	-	6250	-
28-day average	-	7810	-	8590	-	7920	-	7915	-	7685	-	7430
56-day average	8515	-	8615	-	8480	-	7530	-	7625	-	7360	-
91-day average	-	8835	-	9470	-	9035	-	8715	-	8455	-	9920
182-day average	10065	-	9885	-	9240	-	8715	-	8760	-	8260	-

Table 9.2.1. Fly ash content evaluation: 38-mm maximum size aggregate[a] (Cont'd)

Batch No.[b]	32A	32B	33A	33B	34A	34B	35A	35B	36A	36B	37A	37B
	Fly ash content = % of cementitious materials											
	0	0	0	0	10	10	20	20	30	30	40	40
Compressive Strength, psi (limewater cure)[d]												
7-day average	-	7330	-	-	-	-	-	-	-	-	-	-
14-day average	7140	-	-	-	-	-	-	-	-	-	-	-
28-day average	-	8190	-	8585	-	8395	-	8820	-	10420	-	9845
56-day average	9230	9065	-	9150	-	9400	-	9065	-	10475	-	11065
91-day average	9415	9300	-	9635	-	9990	-	9455	-	11645	-	11955
182-day average	9915	-	-	9945	-	10195	-	11490	-	12300	-	c

[a] Pozzolith 300R admixture. Port Arthur, Texas aggregate materials.

[b] Two batches are required for fly ash content to provide sufficient materials to cast strength cylinders and obtain mix properties.

[c] To be determined.

[d] Extra specimens cast to investigate effect of moist cure versus line saturated water cure.

[e] Elapsed time since contact of cement and water when slump was determined.

Table 9.2.2. Fly ash content evaluation: 9.5 mm-maximum size aggregate[a]

Batch No.[b]	38A	38B	39A	39B	40A	40B	41A	41B	42A	42B
	Fly ash content = % of cementitious materials									
Materials (per cu yd)	0	0	10	10	20	20	30	30	40	40
Cement, lb.	898	895	807	806	715	714	623	623	535	535
Fly ash, lb.	0	0	90	90	179	179	267	267	356	356
Coarse aggregate, lb (SSD)	1822	1817	1826	1827	1828	1826	1819	1819	1821	1821
Fine aggregate, lb (SSD)	974	972	983	984	1005	1003	1008	1007	1009	1009
Water, lb.	268	267	256	255	239	239	238	239	239	239
Admixture, oz.	36	36	36	36	36	36	36	36	36	36
Mix Properties										
Slump, in.	3 5/8	3	3 5/8	3	3 1/8	2 1/2	3	3 1/8	3 1/4	3 3/4
(Δt, minutes)[c]	13	22	18	21	16	20	25	25	34	26
Unit wt., lb/ft^3	146.8	146.4	146.8	146.8	147.0	146.8	146.6	146.6	146.8	146.8
Air content, %	2.70	2.70	2.60	2.90	2.85	2.85	3.00	3.15	2.10	2.50
W/C, lb/lb.	0.298	0.298	0.285	0.285	0.267	0.268	0.267	0.269	0.268	0.268
Workability	very good	very good	very good	very good	good	good	good	good	very good	very good
Compressive Strength, psi (moist cure)										
7-day average	-	6990	-	7875	-	7910	-	7710	-	5850
14-day average	8525	-	8065	-	8285	-	8678	-	7850	-
28-day average	-	8370	-	9440	-	10020	-	9540	-	9520
56-day average	9570	9385	9785	9795	10010	10945	11085	10660	11055	10785
91-day average	9860	9860	10375	10525	10600	11895	11655	11245	11605	12075
182-day average	10935	-	11100	-	11260	-	10950	-	12730	-
Compressive Strength, psi (sealed)										
7-day average	-	7425	-	7480	-	7545	-	6885	-	5445
14-day average	8065	-	8320	-	7920	-	7500	-	7075	-
28-day average	-	8655	-	9160	-	9645	-	8755	-	8410
56-day average	9290	-	9635	-	9410	-	9160	-	8830	-
91-day average	-	9525	-	10775	-	10400	-	9625	-	10310
182-day average	10820	-	10715	-	10410	-	9785	-	10085	-

Table 9.2.2. Fly ash content evaluation: 9.5-mm maximum size aggregate[a] (Cont'd)

Batch No.[b]	38A	38B	39A	39B	40A	40B	41A	41B	42A	42B
	Fly ash content = % of cementitious materials									
Materials (per cu yd)	0	0	10	10	20	20	30	30	40	40
Compressive Strength, psi (limewater cure)[d]										
7-day average	-	-	-	-	-	-	-	-	-	-
14-day average	-	-	-	-	-	-	-	-	-	-
28-day average	-	8290	-	9605	-	10275	-	9375	-	9610
56-day average	-	9380	-	10315	-	10440	-	11630	-	11045
91-day average	-	9480	-	10950	-	11695	-	12200	-	12055
182-day average	-	10000	-	11420	-	11765	-	12045	-	c

[a] Pozzolith 300R admixture. Port Arthur, Texas aggregate materials.

[b] Two batches are required for fly ash content to provide sufficient materials to cast strength cylinders and obtain mix properties.

[c] To be determined.

[d] Extra specimens cast to investigate effect of moist cure versus line saturated water cure.

[e] Elapsed time since contact of cement and water when slump was determined.

Table 9.3.1. Fly ash content evaluation: 38-mm maximum size aggregate[a]

Batch No.[b]	43A	43B	44A	44B	45A	45B	46A	46B	47A	47B
	Fly ash content = % of cementitious materials									
Materials (per cu yd)	0	0	10	10	20	20	30	30	40	40
Cement, lb	975	985	885	887	791	795	688	690	586	592
Fly ash, lb	0	0	99	98	197	198	295	296	391	395
Coarse aggregate, lb (SSD)	1817	1833	1829	1835	1829	1837	1819	1825	1811	1827
Fine aggregate, lb (SSD)	958	966	972	975	982	988	986	989	976	985
Water, lb	277	279	267	268	260	261	259	259	257	259
Admixture, oz.	39	39	39	39	39	39	39	39	39	39
Mix Properties										
Slump, in.	3 1/8	2 3/4	3 7/8	3 1/8	3 1/2	4	3 3/8	3 1/4	2 1/2	3 3/4
Unit wt., lb/ft^3	149.2	150.6	150.2	150.6	150.4	151.2	150.0	150.4	149.0	150.4
Air content, %	1.50	1.60	1.55	1.75	1.45	1.50	1.50	1.50	1.30	1.25
W/C, lb/lb	0.284	0.283	0.271	0.272	0.263	0.263	0.263	0.263	0.263	0.262
Workability	good	good	good	good	good →poor	good →poor	very good	very good to good	very good to poor	very good to good
Compressive Strength, psi (Limewater Cure)										
14-day average	7550	-	7965	-	7890	-	8865	-	8685	-
28-day average	-	8120	-	8305	-	9300	-	10015	-	9865
56-day average	8215	8205	9085	8945	9750	10335	10640	11055	10515	11000
91-day average	9050	8300	9710	9695	9870	10340	11165	11480	11350	11345
182-day average	10000	9135	10010	9375	10570	10485	11595	12415	c	c
365-day average	-	c	-	c	-	c	-	c	-	c
730-day average	-	c	-	c	-	c	-	c	-	c
Compressive Strength, psi (sealed)										
14-day average	7510	-	7795	-	7440	-	7395	-	6290	-
28-day average	-	8045	-	8100	-	8230	-	7655	-	8110
56-day average	8780	-	8825	-	8640	-	8905	-	7770	-
91-day average	-	8645	-	8640	-	8815	-	8850	-	9060
182-day average	9265	9245	10050	9510	9620	9795	10165	9090	c	c
365-day average	-	c	-	c	-	c	-	c	-	c
730-day average	-	c	-	c	-	c	-	c	-	c

[a]Pozzolith 300R admixture. Blythe, California area aggregates.

[b]Two batches are required for each fly ash content to provide sufficient materials to cast strength cylinders and obtain mix properties.

[c]To be determined.

Table 9.3.2. Fly ash content evaluation: 9.5-mm maximum size aggregate[a]

Batch No.[b]	48A	48B	49A	49B	50A	50B	51A	51B	52A	52B
	Fly ash content = % of cementitious materials									
Materials (per cu yd)	0	0	10	10	20	20	30	30	40	40
Cement, lb.	899	895	802	801	712	716	627	624	535	536
Fly ash, lb.	0	0	89	89	178	179	269	268	536	357
Coarse aggregate, lb (SSD)	1693	1686	1698	1695	1696	1705	1706	1697	1695	1699
Fine aggregate, lb (SSD)	1145	1141	1147	1145	1153	1159	1164	1157	1177	1180
Water, lb.	278	277	269	269	255	256	249	248	242	242
Admixture, oz.	36	36	36	36	36	36	36	36	36	36
Mix Properties										
Slump, in.	3	3	3 1/2	3 3/8	3 1/4	3 1/2	3 5/8	3 7/8	3 1/2	3 1/2
(Δt, minutes)[d]	(16)	(8)	(13)	(7)	(12)	(7)	(8)	(8)	(15)	(13)
Unit wt., lb/ft^3	148.8	148.2	148.4	148.2	148.0	148.8	148.8	148.0	148.4	148.8
Air content, %	2.10	2.20	2.00	2.20	2.30	2.10	2.20	2.25	1.85	2.10
W/C, lb/lb.	0.309	0.309	0.302	0.302	0.287	0.286	0.278	0.278	0.272	0.271
Workability	Good	Good	Very Good	Very Good	Very Good	Very Good →Good	Good →Poor	Good →Poor	Very Good →Good	Very Good →Good
Compressive Strength, psi (limewater cure)										
7-day average	-	7775	-	8445	-	9105	-	8730	-	6130
14-day average	8890	-	9295	-	9975	-	10080	-	9830	-
28-day average	-	8950	-	c	-	c	-	11010	-	11240
56-day average	9915	10255	11220	10870	12250	11970	12085	12175	12265	12085
91-day average	10270	9910	11360	11135	12815	12515	12280	12370	13620	12780
182-day average	c	-	c	-	c	-	c	-	c	-
Compressive Strength, psi (sealed)										
7-day average	-	8055	-	7290	-	8315	-	7875	-	5885
14-day average	8720	-	9015	-	9300	-	9150	-	7900	-
28-day average	-	8810	-	9475	-	10315	-	9790	-	9385
56-day average	9840	-	10610	-	10735	-	10470	-	10065	-
91-day average	-	10185	-	10645	-	11635	-	10965	-	10505
182-day average	c	-	c	-	c	-	c	-	c	-

[a] Pozzolith 300R admixture. Blythe, California area aggregate materials.

[b] Two batches are required for fly ash content to provide sufficient materials to cast strength cylinders and obtain mix properties.

[c] To be determined

[d] Elapsed time since contact of cement and water when slump was determined.

Table 9.4.1. Fly ash content evaluation: 38-mm maximum size aggregate[a]

Batch No.[b]	53A	53B	54A	54B	55A	55B	56A	56B	57A	57B
	Fly ash content = % of cementitious materials									
Materials (per cu yd)	0	0	10	10	20	20	30	30	40	40
Cement, lb.	988	988	887	891	788	786	687	688	591	591
Fly ash, lb.	0	0	99	99	197	197	294	295	394	394
Coarse aggregate, lb (SSD)	1592	1592	1594	1601	1595	1591	1589	1591	1595	1595
Fine aggregate, lb (SSD)	997	997	997	1001	997	994	993	994	997	997
Water, lb.	277	277	270	271	270	269	269	269	270	270
Admixture, oz.	39	39	39	39	39	39	39	39	39	39
Mix Properties										
Slump, in.	3	3 1/2	3 1/2	3	4	3 1/2	3 3/4	3	3	3 1/8
(Δt, minutes)[d]	(18)	(10)	(7)	(17)	(16)	(23)	(24)	(29)	(36)	(33)
Unit wt., lb/ft^3	142.8	142.8	142.6	143.2	142.6	142.2	142.0	142.2	142.6	142.6
Air content, %	2.30	2.95	2.80	2.50	2.60	2.80	2.50	2.40	2.00	2.10
W/C, lb/lb.	0.280	0.280	0.274	0.274	0.274	0.274	0.274	0.274	0.274	0.274
Workability	Good→ Fair	Good→ Fair	Good→ Poor	Good→ Poor	Very Good→ Fair	Very Good→ Fair	Very Good→ Good	Very Good→ Good	Very Good	Very Good
Compressive Strength, psi (limewater cure)										
7-day average	-	8200	-	8100	-	8090	-	7470	-	5615
14-day average	8985	-	8815	-	8850	-	8900	-	8720	-
28-day average	-	8885	-	8860	-	8990	-	9470	-	9880
56-day average	9385	8485	9040	9005	8760	9585	9905	9525	10435	10320
91-day average	9865	8925	9835	9585	9705	10655	10090	9750	10240	10350
182-day average	c	-	c	-	c	-	c	-	c	-
Compressive Strength, psi (sealed)										
7-day average	-	8205	-	7630	-	7725	-	8010	-	6050
14-day average	8995	-	8820	-	8895	-	8220	-	8050	-
28-day average	-	9070	-	8645	-	9220	-	8585	-	9485
56-day average	9665	-	9050	-	9375	-	9600	-	9690	-
91-day average	-	8605	-	9065	-	10175	-	9525	-	10355
182-day average	c	-	c	-	c	-	c	-	c	-

[a] Pozzolith 300R admixture. Florida City - Turkey Point, Florida aggregate materials.

[b] Two batches are required for fly ash content to provide sufficient materials to cast strength cylinders and obtain mix properties.

[c] To be determined.

[d] Elapsed time since contact of cement and water when slump was determined.

Table 9.4.2. Fly ash content evaluation: 9.5-mm maximum size aggregate[a]

Batch No.[b]	58A	58B	59A	59B	60A	60B	61A	61B	61A	62B
	Fly ash content = % of cementitious materials									
Materials (per cu yd)	0	0	10	10	20	20	30	30	40	40
Cement, lb.	924	911	810	810	724	716	632	629	538	534
Fly ash, lb.	0	0	90	90	181	179	271	270	358	356
Coarse aggregate, lb (SSD)	1431	1411	1435	1435	1443	1428	1446	1440	1440	1430
Fine aggregate, lb (SSD)	1168	1151	1174	1174	1221	1208	1241	1235	1250	1241
Water, lb	304	299	280	280	259	256	253	253	247	245
Admixture, oz.	36	36	36	36	36	36	36	36	36	36
Mix Properties										
Slump, in.	3 5/8	3 3/4	3 7/8	3 7/8	3 3/8	2 3/4	2 3/4	3 7/8	3 1/2	3 1/2
(Δt, minutes)[d]	(19)	(19)	(12)	(8)	(17)	(7)	(16)	(7)	(11)	(11)
Unit wt., lb/ft^3	141.8	139.8	140.4	140.4	141.8	140.4	142.4	141.8	142.0	141
Air content, %	2.45	3.20	3.20	3.20	2.60	3.80	3.20	2.85	2.80	3.50
W/C, lb/lb.	0.329	0.328	0.311	0.311	0.286	0.286	0.280	0.280	0.276	0.275
Workability	Very Good	Very Good	Very Good	Very Good	Very Good→ Good	Fair→ Poor	Fair→ Poor	Fair→ Poor	Good→ Fair	Good→ Fair
Compressive Strength, psi (limewater cure)										
7-day average	-	6985	-	7845	-	8250	-	8300	-	6010
14-day average	8945	-	8685	-	9400	-	9975	-	9070	-
28-day average	-	8705	-	9160	-	9625	-	10025	-	9995
56-day average	10150	split	10165	10295	10805	10295	11105	11405	11170	11155
91-day average	10420	9225	10410	10295	11185	10400	11570	11410	11280	11395
182-day average	c	-	c	-	c	-	c	-	c	-
Compressive Strength, psi (sealed)										
7-day average	-	6750	-	7640	-	8085	-	8525	-	6860
14-day average	8810	-	8190	-	9005	-	9360	-	8750	-
28-day average	-	split	-	8830	-	9380	-	10410	-	9740
56-day average	10425	-	10110	-	9720	-	11130	-	10880	-
91-day average	-	9940	-	9710	-	10570	-	11395	-	11525
182-day average	c	-	c	-	c	-	c	-	c	-

[a]Pozzolith 300R admixture. Florida City-Turkey Point, Florida aggregate materials.

[b]Two batches are required for fly ash content to provide sufficient materials to cast strength cylinders and obtain mix properties.

[c]To be determined.

[d]Elapsed time since contact of cement and water when slump was determined.

9.8 REFERENCES

1. K. C. Cheung, (unpublished data), GA Technologies Inc., San Diego, Ca., December 17, 1982.

2. "Code for Concrete Reactor Vessels and Containments," Section III — Division 2 (ACI Standard 359-77), ASME Boiler and Pressure Vessel Code, July 1983.

3. D. J. Naus, Oak Ridge National Laboratory, unpublished data, May 1983.

4. D. J. Naus, Oak Ridge National Laboratory, unpublished data, Dec. 1983.

5. D. J. Naus, Oak Ridge National Laboratory, unpublished data, Dec. 1984.

6. A. R. Mead, Discussion of paper — "Effects of Aggregate Size on Properties of Concrete," by S. Walker and D. L. Bloem, *Am. Concr. Inst. J., Proc.* **57**, 1961.

7. M. Polivka et al., "Study of Concrete properties for Prestressed Concrete Reactor Vessels, Final Report — Part I," Report No. UC SESM 75-2, Department of Civil Engineering, University of California (Berkeley), March 1975.

10. REACTOR INTERNALS SUBSYSTEM DESIGN (WBS 5210.03)

D. L. Moses and C. O. Slater

10.1 INTRODUCTION

Work concerning the internals of HTR designs has included both analytical and experimental studies. The Tower Shielding Reactor (TSR) was used to determine the radiation transmission through the HTGR lower core support structure including the backscattering from the lower plenum structure and concrete. Results were compared with calculated values obtained from the DOT-IV and MORSE codes.

Preliminary calculations for the lower plenum of modular HTR designs indicated a significant contribution from fissions in the pebble removal system. Potential problem areas were identified for both the vertical in-line and the side-by-side designs.

Available computational procedures that include both neutronic and thermal analyses were used to evaluate performance parameters for the 2240-MW(t) HTGR core and for the 1170-MW(t) annular HTR design.

Methods for representing the neutronic response of the hexagonal core were evaluated, and methods used for the evaluation of the neutronic response of low enriched cores with a graphite moderator were examined.

10.2 SHIELDING STUDIES — C. O. Slater

The bulk of the shielding work was devoted to the second phase of the HTGR bottom reflector and core support block neutron streaming experiment. Reports on the first phase were issued during this period.[1,2] The remainder of the work was devoted to a preliminary analysis of the shielding designs for small HTR's.

10.2.1 HTGR Bottom Reflector and Core Support Block Neutron Streaming Experiment — C. O. Slater and F. J. Muckenthaler

The HTGR bottom reflector and core support block neutron streaming experiment was designed to verify calculations of neutron streaming through large coolant holes in the lower core support structure of the 2240-MW(t) HTGR and of thermal neutron streaming through the boronated graphite pin arrays providing shielding for the lower regions.

The experiment was divided into two phases. Phase I, performed in 1983, emphasized thermal neutron streaming through the boronated graphite pin arrays and some neutron streaming through the large coolant holes. Phase II, performed in 1984, mainly emphasized neutron streaming through the large coolant holes, although minor emphasis was placed on the shielding effects of the boronated graphite pin layers.

10.2.2 Description of Experiment

A sketch of the experimental configuration is shown in Fig. 10.1. It consisted of a spectrum modifier followed by seven segments (labeled A-G) representing a seven-hex-column cell from the HTGR lower core support structure. The seven-hex-column cell is shown in Fig. 10.2 and is one of many as shown in a horizontal cross section form a large HTGR in Fig. 10.3.

The source for the experiment was provided by the ORNL Tower Shielding Facility reactor, TSR-II, and the spectrum modifier preceding the experimental configuration was designed so that the TSR-II source spectrum incident on it would, on leaving, be altered to represent the spectrum impinging on the HTGR lower core support structure. The spectrum modifier consisted of slabs of 5.08-cm carbon steel and 30.5-cm graphite.

Sections A-G of Fig. 10.1 represented various portions of the HTGR lower core support structure and were segmented so that measurements could be made at key locations within the configuration. Section A contained the first boronated graphite pin layer. Reference and full pin patterns were studied to determine the shield pin effectiveness as a function of pin density within the layer. Section B contained only small coolant holes, representing the section of the reflector where the small coolant holes merge into larger ones. Section C represented the region where the

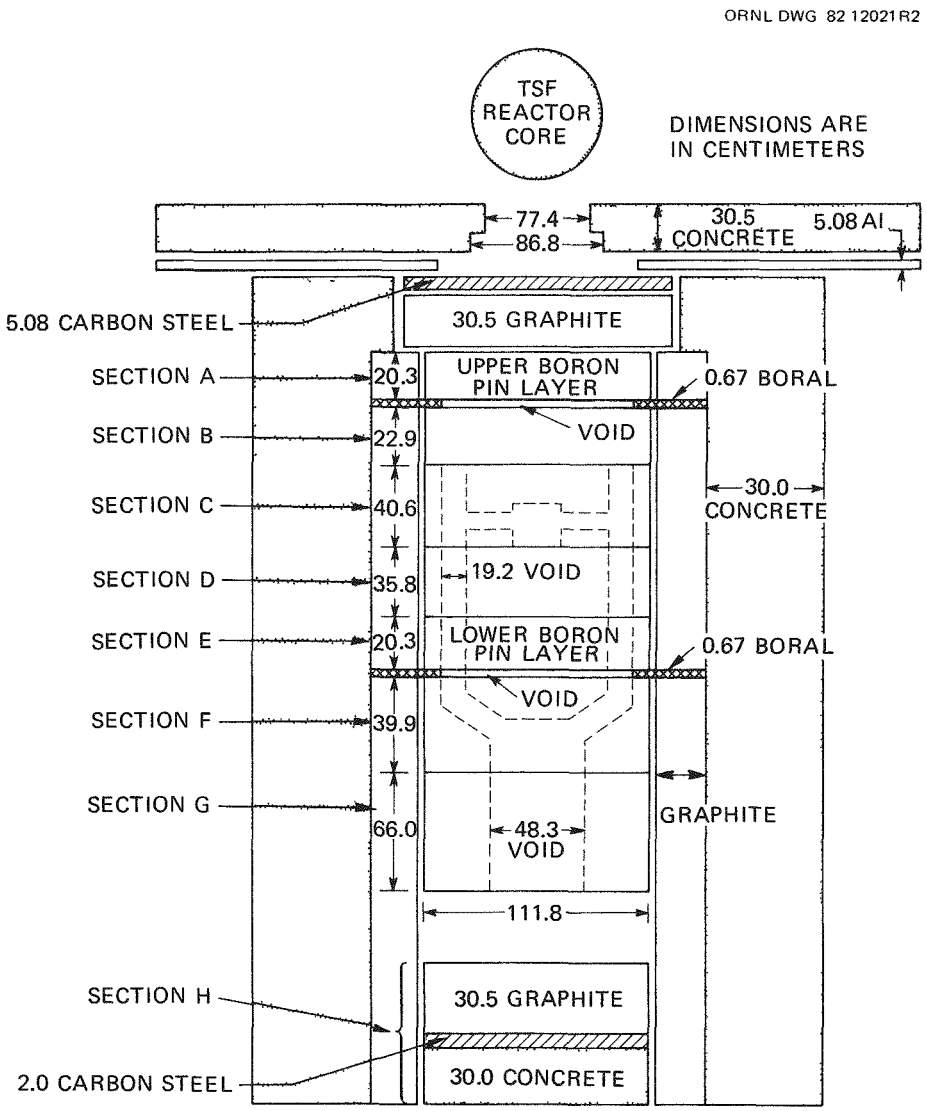

Fig. 10.1. Plan view of the full configuration for the HTGR bottom reflector and core support block neutron-streaming experiment.

ORNL–DWG 84-13406

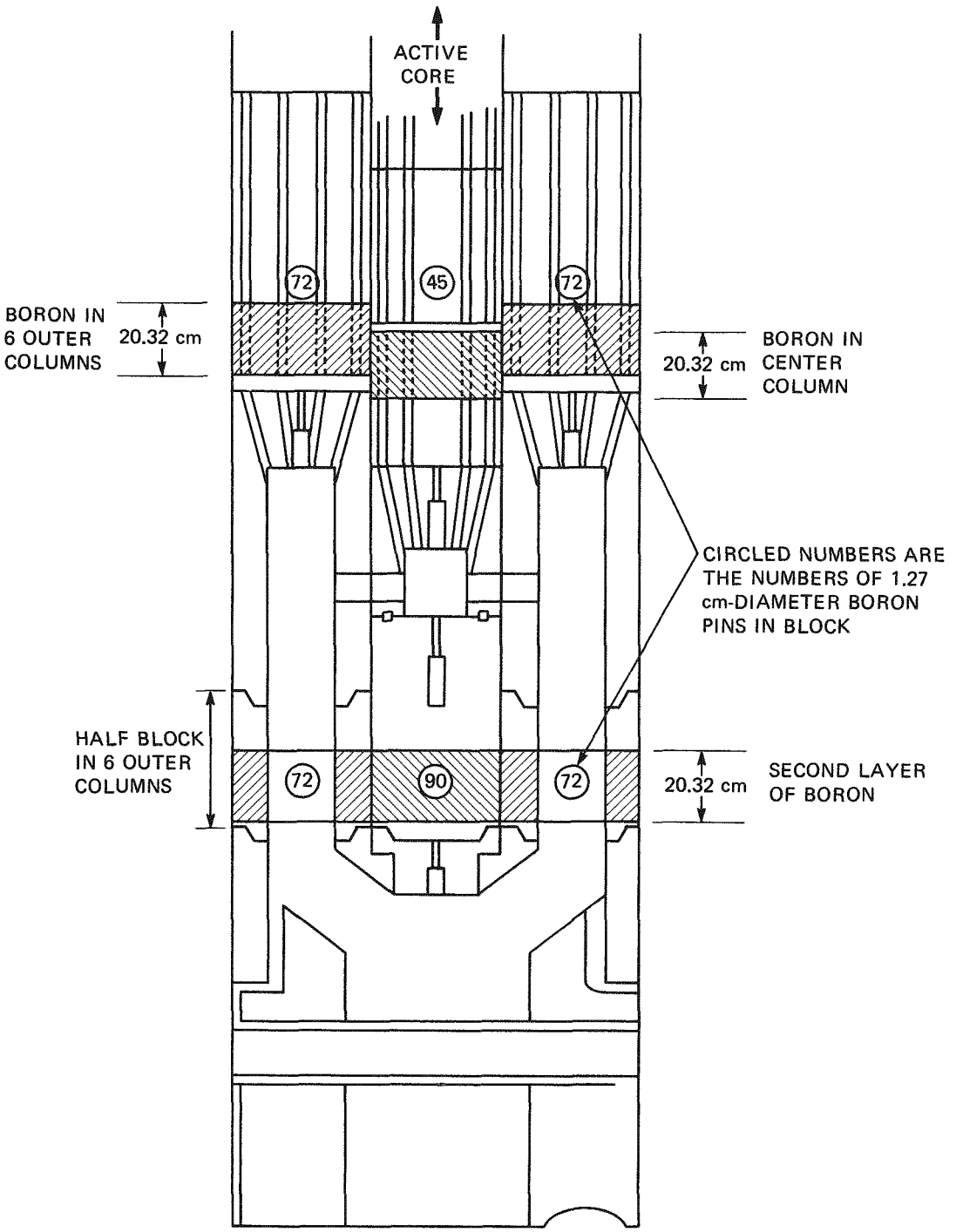

Fig. 10.2. HTGR core, bottom reflector, and support block arrangement in a typical seven column region.

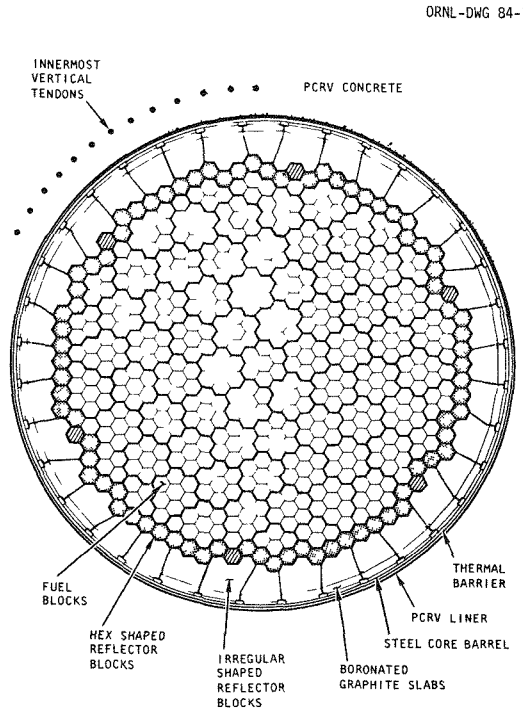

Fig. 10.3. Horizontal slice through the large HTGR core showing the layout of the many seven hex column regions.

coolant from the central hex column merged with the flow from the outer six hex columns. Section D represented the reflector block section that contained large coolant holes in the six outer hex columns and a solid graphite central hex column. Section E represented the second boronated graphite pin layer and sections F and G represented the support block upper (transition) and lower layers, respectively. Each boronated graphite pin layer was followed by a boral slab with a seven hex column cut-out to make the layers effectively infinite laterally and thus prevent thermal neutron transport around the pin layers. The pin layers of the surrounding cells serve the same purpose in the HTGR.

A simplified support post/PCRV mockup was included in the configuration to estimate the effect of neutron reflection from lower plenum structures on neutron leakage from the support block. Fig. 10.1 shows the

mockup as section H, with 30.5-cm graphite followed by 2.0-cm carbon steel and 30.0-cm concrete. The graphite thickness represented the full-density equivalent of the graphite support posts, and the carbon steel and concrete were representative of the reactor cavity liner plus a portion of the PCRV. However, due to the limited availability of graphite and the need to use materials that were available at the Tower Shielding Facility, the mockup was altered to one containing 22.9-cm graphite followed by 2.6-cm carbon steel and 30.5-cm concrete. In addition, a boronated graphite layer was substituted for the graphite layer to study the effects of boronating the support floor beneath the core support posts.

Measurements for Phase II mainly involved sections D through H. However, because of alterations to the TSR-II control plate system following Phase I, repeat measurements were made behind sections A and D, since the reactor alterations affected the neutron source from the TSR-II. Besides the measurements behind each layer as was done in Phase I, measurements were made to determine the effect of changing the location of the second boronated graphite pin layer. Sections D and E were interchanged to move the second layer closer to the first. All measurements were made with Bonner balls, since flux levels were not high enough for reliable flux spectrum measurements. The four detectors selected allow general inferences to be made about various portions of the neutron spectrum.

The measurements are reported in an ORNL report.[3]

10.2.3 Analysis of the Experiment

A detailed analysis of the experiment was performed and is reported in a separate report.[4] As was done in the Phase I analysis,[2] selected configurations were calculated using the DOT-IV two-dimensional discrete ordinates code[5] and the MORSE Monte Carlo code.[6] Results from the DOT-IV code were adjusted for streaming and geometric modelling effects with results from the MORSE code, and the adjusted results were compared with measured results. The comparisons led to certain implications for the HTGR design.

The effect of changing the spacing between the two boronated graphite pin layers was studied by comparing results for the reference spacing with

results at a different spacing. The alternate spacing was represented by interchanging layers D and E. The configurations were labeled II.B and II.C for the reference pin pattern and I.C and I.D for the full pin pattern. Calculated leakages and measured count rates were used to estimate the effects of moving the second boronated graphite pin layer 36 cm closer to the first. The results are shown in Table 10.1.

Table 10.1. Estimated percent changes in neutron leakages when the second boron pin layer is moved closer to the first

	DOT-IV	MORSE	Measured[a]
Measured pin pattern			
Thermal neutrons	−20.2	−31.4	−25.0
Total	−12.5	−24.5	
Full pin pattern			
Thermal neutrons	−19.9	−14.4	−23.0
Total	−13.1	−12.0	

[a]Obtained by comparing bare BF_3 detector count rates at the radial traverse peaks 30 cm behind a large coolant hole.

All results show a lowering of the thermal neutron flux when the two pin layers are closer together. As indicated, the measured result was obtained by comparing bare BF_3 detector count rates at the radial traverse peak and 30 cm behind a large coolant hole. On the centerline, the count rates are much lower than those near the coolant hole, however, the count rates are slightly higher with the two pin layers closer together due to a diffusion of thermal neutrons from the coolant holes toward the center of the layer D block. Conventional wisdom was that the second pin layer should be placed as far down in the support structure as possible so as to capture thermal neutrons produced by the thermalization of epithermal neutrons in the graphite.

The calculation-to-experiment ratios for the configurations are shown in Table 10.2. Generally, the best ratios were near the large coolant holes for the bare BF_3 detector and near both the centerline and the large coolant holes for the other detectors. The worst ratios generally were found at the periphery of the configuration. Agreement is good to excellent at certain locations and very poor at others. The geometric modelling for the DOT-IV code is a contributing factor to the discrepancy.

Table 10.2. Calculation-to-experiment ratios for detector radial traverses behind configurations I.C, I.D, II.B, and II.C

Detector description	Pattern configurations			
	Reference boron pin		Full boron pin	
	II.B	II.C	I.C	I.D.
Bare BF_3 at ~4 cm	0.85—21.4	0.37—0.93	0.47—9.66	0.32—0.86
Bare BF_3 at 30 cm	0.49—0.98	0.59—1.16	0.51—1.04	0.61—0.88
Cd-covered BF_3 at ~4cm	0.14—0.89	0.30—1.01	0.17—1.06	0.24—0.97
Cd-covered BF_3 at 30 cm	0.50—1.07	0.49—0.95	0.48—1.01	0.51—0.97
5-in. Bonner ball at 30 cm	0.58—1.09	0.58—1.01	0.58—1.05	0.56—0.92
10-in. Bonner ball at 30 cm	0.50—0.85	0.51—0.85	0.46—0.83	0.46—0.73

Calculations through the full experimental configuration gave results sometimes in reasonably good agreement with measured results as indicated in Table 10.3. Here, the worst results are at the periphery of the configration. Calculation-to-experiment ratios behind sections of the experimental configuration overall got progressively lower from the spectrum modifier through the support block as shown in Table 10.4. The agreement for the Cd-covered BF_3 detector remained about the same throughout the configuration.

Calculated streaming factors for the experiment are shown in Table 10.5. The factors computed with MORSE are most accurate, since the MORSE results were below but closer to the measured results than were the DOT-IV results. The MORSE-calculated streaming factors for the

Table 10.3. Calculation-to-experiment ratios for Bonner ball count rate radial traverses behind configurations II.F and I.G

Detector traverse	Ratio ranges	
	Configuration II.F	Configuration I.G
Bare BF_3 detector at 4 cm	0.63—0.96	0.61—0.79
Bare BF_3 detector at 30 cm	0.61—0.80	0.61—0.76
Cd-covered BF_3 detector at 4 cm	0.73—1.03	0.72—1.06
Cd-covered BF_3 detector at 30 cm	0.73—0.99	0.78—0.99
5-in. Bonner ball at 7.5 cm	0.25—0.86	0.32—0.88
5-in. Bonner ball at 30 cm	0.45—0.91	0.52—0.88
10-in. Bonner ball at 30 cm	0.32—0.72	0.33—0.69

Table 10.4. Calculated neutron streaming correction factors for the HTGR core support structure experimental mockups

Energy range	Calculated factors		Ratio: $\frac{\text{MORSE}}{\text{DOT-IV}}$
	DOT-IV	MORSE	
	Configuration II.F		
1.1 — 20.0 MeV	866	1301	1.5
0.1 — 1.1 MeV	1492	1964	1.3
3.05 eV — 0.1 MeV	2945	4657	1.6
1.0-5[a] — 3.05 eV	652	1038	1.6
1.0-5 eV —20.0 MeV	686	1909	1.6
	Configuration I.G		
1.1 — 20.0 MeV	693	1107	1.6
0.1 — 1.1 MeV	1272	1770	1.4
3.05 eV — 0.1 MeV	2711	4328	1.6
1.0-5 — 3.05 eV	532	804	1.5
1.0-5 eV — 20.0 MeV	565	856	1.5

[a]Read as 1.05×10^{-5}.

Table 10.5. Calculation-to-experiment ratios behind various sections of the full boron pin pattern experimental configurations

Detector	Ratio ranges			
	Spectrum modifier	Section B	Section D	Support block
Bare BF_3 detector	0.84—1.06	0.65—0.95	0.46—0.87	0.61—0.79
Cd-covered BF_3 detector	0.89—1.05	0.74—1.11	0.41—1.12	0.72—1.06
5-in. Bonner ball	0.83—1.09	0.82—1.01	0.71—0.92	0.32—0.88
10-in. Bonner ball	0.79—0.97	0.69—0.87	0.55—0.77	0.33—0.69

reference pin pattern experimental configuration (II.F) are about two-thirds those calculated for the HTGR design. This is attributed to the mockup of only one seven-hex-column region for the experiment. Neutrons from adjacent cells contribute significantly to flux levels in a given cell. The surrounding regions of the experiment were essentially homogeneous media. A second observation is that the MORSE streaming factors are only 1.3 to 1.6 times the DOT-IV streaming factors. For the HTGR design seven-hex-column cell, the MORSE streaming factors were 10 to 15 times the DOT-IV streaming factors. The differences could only be attributed to (1) the limited experimental mockup, (2) the streaming-corrected source used in the experiment calculation, and (3) a source at the start of the large coolant holes rather than about 12 cm into the preceding reflector as was done in the design analysis.

As in the Phase I analysis, the bare BF_3 detector count rate, being indicative of the thermal neutron flux behavior, was compared behind the support block for the two pin patterns in section A of the configuration. The shielding advantage of the full pin pattern was found to have dropped from a factor of 2.2 behind the boronated graphite pin layer to factors of 1.3 and 1.26 behind section D and the support block (section G), respectively. Obviously, little additional shielding effectiveness is gained by using nearly twice the number of pins. Hence, it would be prudent to use the reference pin pattern unless the thermal neutron fluence in the lower plenum were marginal.

The effect of neutron reflection from lower plenum structures was examined by using the core support post/PCRV mockups behind the support block mockup. The experimental results showed about a factor of two increase in the bare BF_3 detector count rate (thermal neutron flux) along the centerline and a factor of eight increase at the edge of the cell when the support post/PCRV mockup was placed 15 cm behind the support block mockup. Replacing the graphite with boronated graphite in the mockup lead to only a factor of 1.15 increase along the centerline and 3.9 at the cell edge. The results indicate a possible factor of 2.0 reduction in the thermal neutron fluence at the HTGR lower plenum sidewall with boronation of the floor beneath the support posts. However, no account is taken of

the support posts, which will precede the boronated region and will provide scattering centers for thermal neutrons to reach the sidewall without encountering the boronated layer.

Instead of calculations of the experimental configurations with the support post/PCRV mockups following, calculations were made on mockups of the HTGR lower plenum with and without boronated graphite pins in the floor beneath the support posts. The first calculations were performed with DOT-IV using a streaming-corrected source incident on a homogenized region representing the support posts. The results from this calculation indicated a factor of 1.2 reduction in the thermal neutron flux at the lower plenum sidewall due to a homogeneous boronation of the support floor. MORSE Monte Carlo calculations with an exact mockup of the support post region showed a factor of 1.85 decrease in the thermal neutron fluence at the lower plenum sidewall with homogeneous boronation of the support floor when compared to the case without boronation. This, of course, is an upper bound factor since the discrete arrangement of boronated graphite pins in the support floor would lead to higher thermal neutron back leakage from the floor and thus a higher thermal neutron flux at the sidewall.

Finally, the methods for applying streaming correction factors to fluxes leaving the support block were examined for their effects on neutron flux levels in regions following the support block. Three methods were tested on the reference pin pattern configuration by (1) applying streaming factors to fluxes leaving the support block, (2) calculating the resulting detector responses behind the configuration, and (3) comparing the results with the measured results and results from the other two calculations. Method 1, used in most of the experiment analysis,[2,4] involved the application of discrete space- and energy- and continuous direction-dependent scale factors to boundary fluxes from a DOT-IV heterogeneous calculation of the configuration. Method 2 used the BSPREP[7] code to apply discrete energy- and functional space-dependent scale factors to boundary fluxes from a DOT-IV heterogeneous calculation. Method 3, used in the design analysis, also used the BSPREP code but applied factors to boundary fluxes from a DOT-IV homogeneous calculation.

Calculated bare BF_3 detector count rate traverses 30 cm behind the support block for the reference pin pattern configuration (II.F) are compared with the measured traverse in Fig. 10.4. Note that Methods 1 and 2 give essentially the same results and give traverse curves the shapes of which are in good agreement with the measured curve shape. Method 1 gave slightly to significantly better results for the other detectors for the central portion of the traverse and slightly worse results toward the edge of the cell mockup. Method 3 greatly underestimates the bare BF_3 detector count rate near the center of the traverse and greatly overestimates the count rate in the peripheral regions of the configuration. Similar results were obtained for the other detectors.

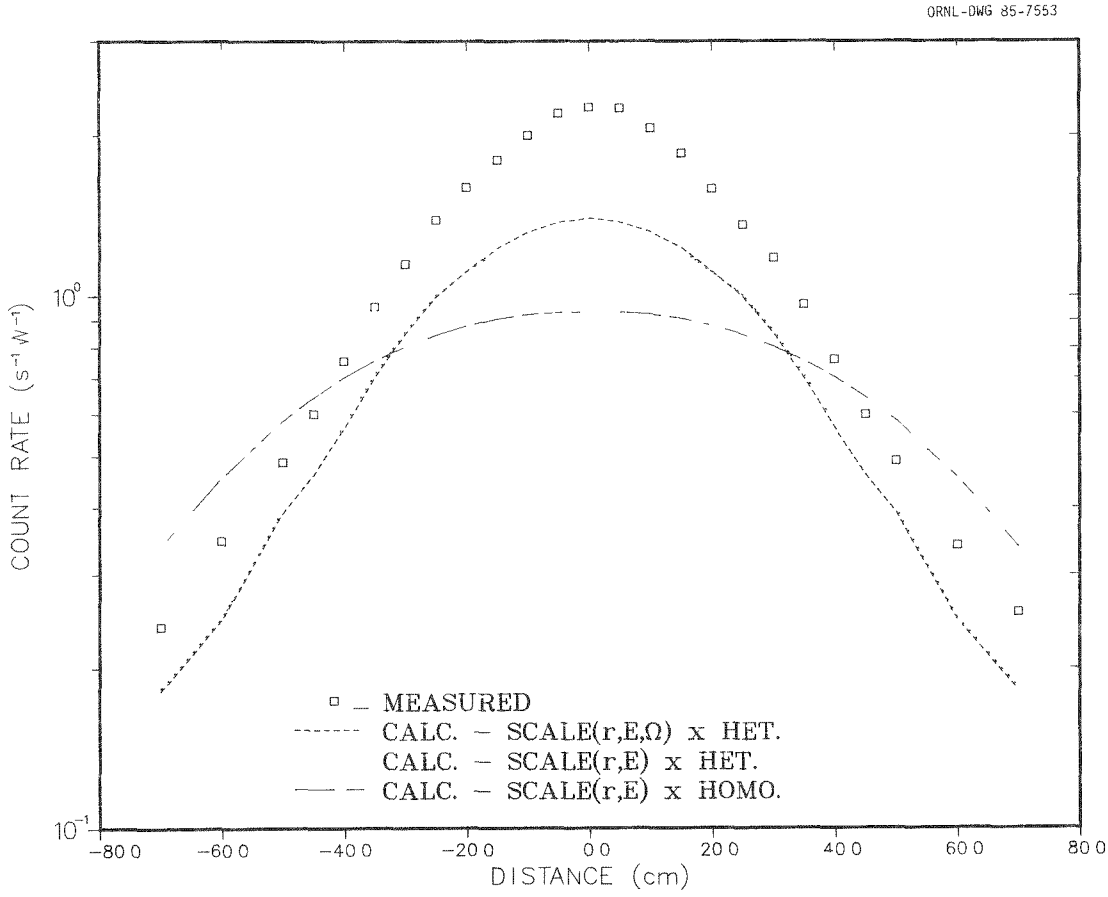

Fig. 10.4. Comparison of measured and three calculated bare BF_3 detector count rate radial traverses 30 cm behind the support block of the reference boronated graphite pin pattern configuration II.F.

Of main interest is the effect that the method of applying the streaming factors has on the thermal neutron fluence at the lower plenum sidewall. Since the fluence at the sidewall was obtained using a source computed by Method 3, the effect is estimated by the degree to which Method 3 either overpredicts or underpredicts detector responses toward the outer boundaries of the experimental configuration. First, all calculated curves in Fig. 10.4 were adjusted upward (to account for any underprediction caused by an underestimation of the TSR-II source) by the ratio of the measured centerline count rate to the centerline count rate calculated using Method 1. Then the count rate calculated by Method 3 at the cell edge was compared with the measured count rate and was found to be a factor of 2.3 higher. Thus the thermal neutron source directed at the sidewall and hence the thermal neutron fluence at the sidewall could be overestimated by a factor of 2.3, leaving the calculated fluence at 4.6×10^{17} cm^{-2}, rather than 10.5×10^{17} cm^{-2} as previously calculated.[8] The fluence would still be well above the design limit of 10^{17} cm^{-2}. For conservatism, it is recommended that the higher fluence be used for designing any shield to reduce the thermal neutron fluence in the lower plenum, since the overestimation for a design cell calculation should be much less than that for the experimental configuration.

10.2.4 Design Implications

Implications for the HTGR design are based on how well the calculated results agree with the measurements and thus the degree to which the calculational methods are verified by the experiment. First, since calculated results were in reasonably good agreement with the measured results and streaming factors were two-thirds those calculated for the design, one can conclude that the large streaming factors computed for the design are reasonably accurate and that severe flux levels exist in the HTGR lower plenum. Second, it is more economical and nearly as effective to use the reference pattern of boronated graphite pins in the first layer, since an additional shielding effectiveness factor of only 1.26 is gained by going to the full pin pattern. The use of the full pin pattern could be justified if the thermal neutron fluence were marginal. Third, a major

shield redesign will be required to lower the thermal neutron fluence to acceptable levels. Fourth, repositioning of the second pin layer relative to the first and boronation of the support floor offers significant fluence reductions but still leaves the thermal neutron fluence well above the design limit.

No alternate shielding concepts were studied, but one might consider lengthening the pins in the first layer and/or going to boron steel pins to reduce both high-energy and low-energy neutron fluxes.

10.3 SMALL HTR STUDIES — C. O. Slater

During December 1984, a preliminary analysis was made of the shielding designs for the vertical in-line and side-by-side steel vessel small HTR concepts. Each had a rated power of 250 MW(t). Crude estimates were made of radiation levels and dose rates within and surrounding the vessels. Prompt neutron and gamma-ray, fission-product gamma-ray, and plateout gamma-ray sources were considered.

Since both concepts contained fuel discharge chutes penetrating the lower reflector, an estimate was also made of the effect of fissions in the discharge chutes on radiation levels in the lower regions. It was found that the flux could increase several orders of magnitude as a result of the fissions. Also, the thermal neutron flux in the lower plenum of the side-by-side concept was increased to such an extent that a very high thermal neutron source into the steam-generator crossduct is likely. Again, only crude estimates of the fissions in the chutes were made.

For the side-by-side concept, a relatively high maintenance dose rate was observed for the circulator because it was located near the core mid-height and the concrete shielding between the reactor cavity and the steam-generator cavity was not sufficient to reduce the dose from the core fission-product gamma rays to acceptable levels. The dose would be reduced after shutdown in proportion to the decay of the fission products. Here again, the fission-product source was a crude estimate, being assumed to have the same relative spectrum as that determined for the large HTGR.[8]

There was insufficient time for an analysis based on the fuel mixture for the small HTR. Other maintenance dose rates within the steam-generator cavity were also found to be relatively high due to:

- direct transmission of fission-product gamma-rays through the concrete wall between the reactor and steam-generator cavities,
- radiation streaming from the lower core support plenum through the cross duct and into the steam-generator cavity,
- radiation streaming around the steam-generator vessel in its cavity, and
- the resultant activation of the steam-generator components.

Most of the dose estimates around the side-by-side steam-generator cavity were hand estimates obtained by using sources from one-dimensional discrete ordinates transport calculations and applying estimates of attenuations through shields, void ducts, and void annuli. Obviously, more detailed calculations are needed to obtain accurate dose estimates within the steam-generator cavity. At the same time, changes in the shielding design should permit attainment of acceptable radiation dose rates.

10.4 HTR PHYSICS STUDIES — D. R. Vondy

Some reactor analysis methods development has been supported in this program. Continuing enhancement of the modular core system for reactor core analysis has been of considerable utility in the local effort.[9] Capability was added for three-dimensional modeling of the heat removal by coolant flow through cylindrical holes, complete with adjustable orificing serving blocks of prismatic fuel assemblies.[10] Techniques are in routine use for the study of the prismatic and pebble bed gas cooled thermal reactor cores regarding performance, fuel requirements, heat removal, and stability.

A study was made of the effect of the design power density on the performance of the reference 2240-MW(t) core.[11] The subject is somewhat involved due to more than one proposed prismatic fuel assembly design. Calculations were made to assess the performance with highly enriched

fuel. Considering a somewhat simple fuel assembly design involving coolant and fuel holes bored straight through, the following coolant pressure losses shown in Table 10.6 were obtained.

Table 10.6. Coolant pressure loss in a 2240-MW(t) HTGR core

Power density (W/cm^3)	Pressure loss (atm)		
	Partial core		Total system
	Idealized	Degraded	
5	0.28	0.34	0.93
6	0.37	0.44	1.09
7	0.49	0.59	1.30

The penalty for higher coolant pumping requirements at the higher power density was found to be compensated by the lower capital cost of a smaller core and reduced fuel indirect costs if highly enriched fuel were used. (GA Technologies results indicate a lower power density is preferred economically for low enrichment fuel that would inhibit misappropriation of the fuel.) A higher power density does lead to higher fuel temperatures and less favorable cooling conditions following shutdown.

Calculations were done to evaluate the performance of an annular cylinder pebble bed core. Emphasis was on a 1170-MW (t) plant, one of sufficient size to have economic commercial potential. It was found that adequate control shutdown capability could be provided in the inner and outer reflectors.[12] However, there are a number of factors that affect the design choices regarding water ingress, the design for after-shutdown conditions including the capability to limit fuel temperatures with an after-heat load and desirable performance considering load following. Of some interest is the ability to reduce the power density peaking and decreasing the level of exposure to high energy neutrons by recirculating the pebbles a number of times as shown in Table 10.7.

Table 10.7. Effect of recirculating pebbles in annular core on performance characteristics

Variables	Pebble passes	
	4	8
Fissile inventory (kg)	622	621
Fissile feed (kg/FP day)	0.937	0.918
Peak pebble power density (w/cm^3)	19.6	18.2
Reflector flux peak (E > 0.2 MeV)	4.1×10^{13}	3.5×10^{13}
Peak fuel temperature (°C)	1048	1053

The annular 1170-MW(t) core was found to be stable against xenon-driven oscillation at reasonable power density and core radii. The worth of control rods in the inner and outer radial reflectors was studied. For a power density of 4 w/cm^3 and an outer radius of 4 m, the control worth is shown in Table 10.8 for 7.5-cm diameter rods in the inner reflector and 12.5 cm diameter rods in the outer reflector.

Table 10.8. Worth of inner and outer rods in the 1170-MW(t) annular HTR design

Rods inserted		Rod worth ($-\Delta k/k$)
Inner	Outer	
20		0.0275
	20	0.0272
20	20	0.0676
30	30	0.0877

Some flexibility in design comes from the ability to adjust the thickness of the annular core. (Decreasing the thickness reduces the distance that heat would have to be removed following a loss of forced convective coolant flow.) The results shown in Table 10.9 were obtained.

Table 10.9. Rod worth varying annular core thickness for the 1170-MW(t) annular HTR design

Power density (w/cm^3)	Core annulus thickness (m)	Rod worth ($-\Delta k/k$) for number of rods inserted		
		40	50	60
4	2.193	0.068	0.080	0.088
5	1.863	0.092	0.109	0.121
6	1.624	0.118	0.141	0.156

Toward the end of this year, the effort in this project has been devoted primarily to the evaluation of nuclear cross sections derived from ENDF data in application to the German AVR reactor. Recent calculations yield the results given in Table 10.10 for the spherical fuel cell using revised ^{232}Th and graphite data.

Table 10.10. Results for the spherical AVR fuel cell using revised ^{232}Th and graphite data

Temperature (°k)	Resonance integral (barns)	k	$\Delta k/\Delta T \times 10^5$ $T_{n-1} \rightarrow T_n$
300	52.99	1.5377	
500	56.14	1.5255	−6.1
800	59.09	1.5127	−4.3
1000	60.48	1.5068	−3.0
1200	61.60	1.5040	−1.4
2000	64.64	1.4954	−1.07

The data is of interest in evaluating reactivity response and extending experimental results. We continue to evaluate the results and test the data before communicating with the Federal Republic of Germany (FRG) under the existing technical exchange agreement.

Local core analysis methods were also tested by application to a benchmark pressurized water reactor exposure problem involving refueling and fuel element replacement.[13] Some effort is currently being devoted

to understanding and interpreting the results and assessing the implications with regard to the core analysis methods in local use. Comparisons can be made with other evaluations of the fully defined mathematical problem, including that from KWU in the FRG where the problem originated. Testing of the newer nodal methods should be of wide interest in comparison with our use of a finite difference diffusion theory model.

10.5 COOPERATIVE EFFORTS IN SUPPORT OF GA TECHNOLOGIES — J. R. White (University of Lowell) and D. L. Moses

The University of Lowell was under subcontract to ORNL during 1984 to assist in the development and application of computational tools of interest to GA Technologies for the physics analysis of HTGR designs. The main thrusts of this interaction during 1984 were:

- The investigation of "fast" 3-D hexagonal methods for HTGR large core physics calculations and
- The development and implementation of a generalized/depletion perturbation theory method for GA's FEVER-M1 code.[14]

The work on the first project was completed, and a draft report summarizing this overall effort has been sent to GA for review and comment. The second task is continuing into calendar year 1985, but considerable progress was made, and the project was nearing completion at the end of 1984.

10.5.1 Hexagonal Nodal Methods

The purpose of this work was to provide an overview of the status and availability of hexagonal nodal methods for potential application to HTGR neutronic design. This work was motivated in part by the tremendous impact that nodal methods have had on the LWR industry and, more recently, in the area of hexagonal LMFBR design computations. In addition, GA's inhouse nodal code, which had been under development for several years, was providing less than satisfactory results.

The overall investigation was broken into two separate phases. The first phase involved a relatively detailed survey of the pertinent literature, and the second part consisted of the full benchmark testing and evaluation of a particular code. For the first phase, several nodal-related documents were obtained and reviewed, where emphasis was on hexagonal geometry techniques because of their applicability to HTGR prismatic core design. Several of the major code methodologies investigated included DEGEN, SIXTUS, HEXAN, HEXBU-3D, N3D, and DIF3D. These codes can be grouped into three broad classes: early methods, hex-plane methods, and transverse integration methods. A more detailed discussion of this classification scheme will be provided in the final report of this project when published following completion of the GA review of the draft document.

During this investigation, particular attention was given to the N3D[15,16] and DIF3D[17,18] code methodologies, since these techniques represent U.S. developments in the field of hexagonal nodal methods. The N3D code (under development at GA) belongs to the early methods class, and DIF3D is based on the more rigorous transverse integration technique that has become the primary focus of LWR nodal methods. The DIF3D nodal option is currently in production use at ANL, and reported results indicated potential order of magnitude savings relative to standard finite difference techniques for LMFBR applications. On the other hand, N3D has been plagued with accuracy problems, and our review has isolated several approximations (e.g., the leakage treatment and the flat source fixup) that appear to be inherent limitations within the current N3D code methodology.

Because of its availability and previously reported success for LMFBR applications, the DIF3D nodal option was chosen for further detailed study and active hands-on experience. A stand-alone version of DIF3D was obtained from ANL and implemented on IBM 3033 system at ORNL. A series of 2-D and 3-D LMFBR and HTGR benchmarks were run to gain some experience with the code and to evaluate its potential as a cost-effective 3-D neutronics tool for prismatic HTGR applications.

For the HTGR applications, the reactor model selected was the 4-group HTGR benchmark specified by Steinke.[19] The physical core model has a radial dimension of approximately 380.1 cm and a height of 634.4 cm. The

lattice pitch is 36.2 cm. The large dimensions were expected to provide an adequate testing ground for the nodal methods in DIF3D. Identical finite difference models were run in VENTURE[20] and DIF3D, using both the finite difference and nodal options, on the IBM 3033 system. In two dimensions, the finite difference runs were made using 6, 24, and 54 points per hexagonal fuel element. The nodal method used one node per hexagon. In 3 dimensions, finite difference runs were made in VENTURE using 6 points per hexagon and 8 and 16 axial nodes and in DIF3D using 6 points per hexagon and 8, 16, and 32 axial mesh points. Also, a reference finite difference case was run in DIF3D using 24 points per hexagon and 64 axial nodes. The DIF3D nodal option used one node per hexagon and 8, 16, and 32 axial nodes. The results of these analyses are summarized in Table 10.11.

Table 10.11. Comparison of nodal and finite difference methods for an HTGR benchmark

Code	Method	K-effective	Total run time IBM 3033 CPU-sec	Maximum error in assembly power (%)
VENTURE	2-D 6	1.12028	12	4.0
	2-D 24	1.11891	73	0.7
	2-D 54	1.11860	141	0.0
DIF3D	2-D 6	1.12028	7	4.0
	2-D 24	1.11891	20	0.7
	2-D 54	1.11860	55	Ref.
DIF3D	2-D nodal	1.11857	7	1.6
				17.
VENTURE	3-D 6/8	1.09069	131	10.
	3-D 6/16	1.09063	234	
DIF3D	3-D 6/8	1.09069	45	17.
	3-D 6/16	1.09063	85	10.
	3-D 6/32	1.09137	162	6.
	3-D 24/64	1.09033	2471	Ref.
DIF3D	3-D nodal/8	1.08992	47	3.
	3-D nodal/16	1.09028	114	2.
	3-D nodal/32	1.09032	230	2.

First, it should be noted that both the VENTURE and DIF3D finite difference methods give exactly the same results, as is expected. However, DIF3D ran 2-3 times faster than VENTURE, but this difference is apparently because VENTURE's solution methods have been developed to handle more challenging problems, such as asymmetric, skewed-flux distributions for which DIF3D may not be able to converge. The primary observations to be made, however, lie in the area of accuracy versus cost of the nodal method versus the finite difference. In two dimensions, the nodal method is seen to be equivalent to the 54 pt./hex finite difference model in terms of k-effective, and the assembly averaged power is nearly as accurate as a 24 pt./hex model. The time taken for the nodal run is the same as a 6 pt./hex finite difference model.

A similar pattern is seen in the three-dimensional results, where accuracy is quite sensitive to the number of axial nodes. The nodal method is shown to be considerably more accurate than the finite difference model using the same number of axial nodes. A finite difference model of a 634.4-cm tall core with only 8 axial mesh points cannot be expected to be nearly as accurate as the fine-mesh calculation. However, the nodal method using 8 axial nodes is much more accurate, and in terms of accuracy versus cost, the nodal method with 16 axial nodes provides an accurate solution to this problem at a considerably reduced cost relative to the reference finite difference solution (24 pts./hex and 64 axial nodes).

10.5.2 Generalized/Depletion Perturbation Theory

The second task in the overall effort this year was the implementation of a generalized/depletion perturbation theory (GPT/DPT) capability that is directly compatible with GA's FEVER-M1 fuel-cycle analysis code. The primary incentive for this work is to provide GA a GPT/DPT computational tool that may have potential applications in the analysis of the axial zoning of HTGR cores. Thus, a code system that meets these goals is currently under development.

This new GPT/DPT capability is being implemented as the NIFDE-HAREM code (for New Improved FEVER-DEPTH/CHARGE-HAREM). The system has a set of code modules (FEVERA, HAREMF, CHARGF, and DEPTHF) for generalized static

and time-dependent perturbation/sensitivity computations in one-dimensional HTGR cores. Initially, the code system performs reference 1-D HTGR fuel-cycle computations and saves the appropriate data for subsequent adjoint calculations. In the adjoint mode, the various codes prepare the required adjoint sources, solve the adjoint nuclide (N*), adjoint power (P*), and generalized adjoint (Γ^*) equations of depletion perturbation theory,[21,22] and calculate static and/or time-dependent nuclide derivatives for a variety of response functionals.

The FEVERA module is used to perform the reference calculations. FEVERA uses a modified Wielandt iteration scheme to solve the neutron diffusion equation, and a conventional burnup scheme is used to perform depletion calculations. HAREMF is a module that analytically solves several forms of the one-dimensional diffusion equation, including the reference forward and adjoint forms and the generalized fixed-source problem, which is of prime interest in the DPT methodology. Its primary purpose in the current system is to solve the Γ^* problem, but it is also necessary to calculate reference exact flux (ϕ) and adjoint (ϕ^*) solutions for subsequent use in the fundamental mode "decontamination" procedure used in the Γ^* calculation. The analytic HAREM methodology is relatively new and unique.[23]

The DEPTHF module (for DEpletion Perturbation THeory with FEVER) is the calculational code for the DPT section of the NIFDE-HAREM system. It uses a straight-forward series expansion method for the matrix exponential solution of the forward and adjoint nuclide density equations, and a numerical integration technique is utilized to evaluate the time integrals appearing in the formulations for several of the adjoint functions.

The NIFDE-HAREM system being developed is similar to the original VENTURE-DEPTH/CHARGE[24] GPT/DPT capability, where the VENTURE/BURNER forward depletion capability has been replaced with the FEVER methodology and the VENTURE Γ^* solution has been replaced by the analytic HAREM technique. The system is undergoing checkout testing on a CYBER 170/825 at the University of Lowell, and it is written completely in FORTRAN-77.

10.6 HTGR PHYSICS METHODS AND DATA TESTING — R. D. Timmerman and D. L. Moses

An analysis of Hanford graphite-moderated pin-in-block exponential lattices[25] was performed to facilitate the evaluation of ENDF/B-V cross-section data for simple graphite-moderated systems using low enriched uranium (LEU) fuel. A trend of increasing values of k-effective was calculated with increasing fuel rod pitch. This behavior has cast doubt on the utility of the exponential measurements. As shown in Table 10.12, the trend of k-effective values obtained with ENDF/B-V and the ORNL 123-group (early ENDF) libraries was very close for the 2.97-cm diameter natural uranium fuel rod. An initial set of calculations had shown a more significant decrease between the older library and ENDF/B-V, but that difference was apparently due in part to the initial use of a geometrical cell model that had been used in early British calculations of the same lattices[26] rather than the more exact geometry subsequently employed in the ORNL calculations.

The trend with pitch is very close to a 1966 set of British calculations using an early version of WIMS.[27] This behavior has been observed in all of the British analyses of the graphite-moderated, single-pin

Table 10.12. Lattice cell eigenvalues for Hanford 2.97-m natural uranium pin in graphite (dry lattice)

Lattice pitch (cm)	ORNL[a] 123-group	ORNL ENDF/B-V	Winfrith[b] WIMS (1966)
13.176	0.98292 (0.98327)	0.98190	0.960 (0.982)
15.716	0.98433	0.98578	0.970 (0.989)
17.780	0.98706	0.99017	0.977
19.05	0.98968	0.99328	0.981
26.353	1.00295 (1.00082)	1.00646	0.986
$\Delta\lambda$:13.176→26.353	0.02003 (0.01755)	0.02456	0.026

[a]Parenthetical values are provided for the case using ENDF/B-V graphite in 123 groups.

[b]Winfrith used a Uranium-235 number density ~1% too low and used a graphite capture cross section which was 4.066 mb compared to 3.83 mb deduced from later Hanford data. Parenthetical values are for a 10% reduction in uranium-238 resonance capture which the British argue is the source of the observed trend with pitch.

exponential experiments performed both at Hanford and Winfrith, and the British have taken the position that the trend results from the differential data for Uranium-238 resonance capture.[28] In fact, the British WIMS-E computer code uses two different sets of data for uranium-238 (ref. 29). One set is employed for thin pin light water lattices and agrees with U.S. data. The other "adjusted" set is applied only to graphite-moderated lattices. However, biases observed in analyzing exponential experiments are not limited to just graphite-moderated systems. Studies performed at the Savannah River Laboratory (SRL) over the past 20 years have also found significant biases in both light and heavy water moderated exponential experiments.[30,31] As part of the ORNL study, calculations have also been performed for the endpoints of Hanford 93 weight percent enriched uranium-aluminum alloy pins, and, as shown in Table 10.13, the projected trend with pitch is even more severe than for the natural uranium pins even though uranium-238 capture could not be a significant factor. It should be noted that the primary exponential pile dimension was only 1.2 m for the enriched fuel pins rather than the 2.4 m used for the natural uranium lattices. This dimension impacts the distance over which the data for the buckling fit can be taken, and it appears that the results for enriched uranium lattices support a conclusion that the buckling measurement and not the cross-section data for the uranium-238 capture resonance is the major source of error in the exponential lattices.

Table 10.13. Lattice cell eigenvalues for Hanford 3.411 cm enriched uranium (93 weight percent)-aluminum alloy pins in graphite (dry lattice)

Weight fraction of uranium in aluminum alloy	Lattice pitch (cm)	ORNL ENDF/B-V
0.0446	10.636	0.98078
0.0446	26.353	1.03064
	$\Delta\lambda$:10.636→26.353	0.0499
0.0750	10.636	0.96811
0.0750	26.353	1.01348
	$\Delta\lambda$:10.636→26.353	0.0454

Since as shown in Table 10.14, ORNL methods can do a reasonably good job in calculating heavy water moderated "critical" lattices of nearly the same fuel pin dimension and spacings,[32] the conclusion is that the American and British exponential experiments share a similar common error or bias in the measured bucklings. Further research on this matter has indicated that the nature of this error is possibly characterized by difficulties encountered and noted by experimentors at Atomics International (AI). The AI experimentors attempted to infer material bucklings on both subcritical and critical graphite-moderated lattices as part of the Advanced Sodium Graphite Reactor project.[33,34] In that study, the experimentors measured erroneous material bucklings from the exponential (subcritical) lattices apparently due to diffusion anisotropy caused by streaming and assembly heterogeneity as well as the use of calculated rather than measured radial bucklings. When diffusion anisotropy exists, the measured material buckling is not a unique property of the lattice.

Table 10.14. Lattice cell eigenvalues for Chalk River (3.256-cm) natural uranium pin in heavy water (critical experiment)

Lattice pitch (cm)	ORNL 123-group	ORNL ENDF/B-V	AECL[a] ENDF/B-V
12.06	0.99748	0.99532	0.99821
13.97	0.99855	0.99905	0.99767
19.68	0.99654	1.00076	
20.00			0.99858
20.57	0.99206	0.99656	
22.00	0.99513	0.99955	

[a]Chalk River used a point energy, discrete ordinates resonance integral calculation. ORNL results used the Nordheim Integral Method to calculate resonance shielding.

The observed bias in the Hanford lattices appears to be consistent since the calculated results are very similar for both the dry and water-flooded can measurements that produce different values of bucklings for the same lattice configuration (Table 10.15). Similar results have also

Table 10.15. Dry and wet lattice eigenvalues for the Hanford 2.97-cm natural uranium pin in graphite

Lattice pitch (cm)	Dry buckling (10^{-6} cm^{-2})	ORNL ENDF/B-V	Wet buckling (10^{-6} cm^{-2})	ORNL ENDF/B-V
13.176	−76	0.98190	−11	0.98248
15.716	77	0.98578	84	0.98820
17.780	116	0.99017	100	0.99297
19.05	122	0.99328	99	0.99507
26.353	57	1.00646	15	1.00902
Δλ:13.176→26.353		0.0246		0.0265

been obtained for a lattice of natural uranium rods with a diameter of 2.35 cm. Aside from the cited British analyses and the recent calculations at ORNL, there has apparently been only one other attempt to analyze any of the cited graphite exponential experiments. This analysis was performed by Brookhaven National Laboratory (BNL) using a Monte Carlo method for several of the Winfrith experiments.[35] No trend with pitch was noted in the BNL analysis; however, no set of experiments of similar rod and clad dimensions were analyzed at significantly different pitches so as to allow seeing such a trend.

These results are disappointing since those kinds of lattice physics experiments are much easier and less expensive to analyze than the large, nonrepetitive lattice critical experiments that have been performed by GA Technologies Inc. in the U.S. and by Winfrith and Berkeley in the U.K. The resulting lack of confidence in the utility of the exponential experiments may also eliminate the LEU particulate fuel HTR exponential lattices[36] from Winfrith as a possible benchmark. British data from plutonium-graphite experiments are also suspect since they incorporate oscillation measurements that were "verified" against exponentials.[37,38] This is most unfortunate since data for graphite-moderated plutonium lattices are already limited, and the plutonium will be produced in significant quantities as LEU fuels are burned in HTRs. The separate effects analysis of the exponential experiments at ORNL has been useful, however, in resolving problems with

our local processing of graphite data and in developing an understanding of the problems and limitations in using much of the available graphite-moderated integral experiments.

10.7 REFERENCES

1. F. J. Muckenthaler et al., *Phase I Measurements for the HTGR Bottom Reflector and Core Support Block Neutron-Streaming Experiment*, ORNL/TM-8977, Oak Ridge National Laboratory, July 1984.

2. C. O. Slater, *Analysis of Phase I of the HTGR Bottom Reflector and Core Support Block Neutron Streaming Experiment*, ORNL/TM-9252, Oak Ridge National Laboratory, July 1984.

3. F. J. Muckenthaler et al., *Phase II Measurements for the HTGR Bottom Reflector and Core Support Block Neutron-Streaming Experiment*, ORNL/TM-9484, Oak Ridge National Laboratory, May 1985.

4. C. O. Slater, *Analysis of Phase II of the HTGR Bottom Reflector and Core Support Block Neutron-Streaming Experiment*, ORNL/TM-9485, Oak Ridge National Laboratory, to be published.

5. W. A. Rhoades et al., *The DOT-IV Two-Dimensional Discrete Ordinates Transport Code with Space-Dependent Mesh and Quadrature*, ORNL/TM-6529, Oak Ridge National Laboratory, January 1979.

6. M. B. Emmett, *The MORSE Monte Carlo Radiation Transport Code System*, ORNL-4972, Oak Ridge National Laboratory, February 1975.

7. C. O. Slater, internal correspondence, 1980.

8. C. O. Slater and S. N. Cramer, *Survey Analysis of Radiation Levels in the HTGR Lower Regions*, ORNL/TM-8141, Oak Ridge National Laboratory, February 1982.

9. D. R. Vondy et al., *The Bold Venture Computation System for Nuclear Reactor Core Analysis, Version III*, ORNL-5711, Oak Ridge National Laboratory, June 1981.

10. D. R. Vondy, *THR-TH: A High Temperature Gas-Cooled Nuclear Reactor Core Thermal Hydraulics Code*, ORNL-5951, Oak Ridge National Laboratory, July 1984.

11. D. R. Vondy, *2240 MW(t) High-Temperature Reactor Core Power Density Study*, ORNL/TM-9099, Oak Ridge National Laboratory, September 1984.

12. D. R. Vondy, *Characteristics of an Annular Pebble Bed Reactor Core [1170 MW(t)]*, ORNL/TM-9188, Oak Ridge National Laboratory, in publication.

13. D. R. Vondy, "Solution of a Two-Dimensional PWR Benchmark Problem Modeling Two Cycles with Refueling and Fuel Assembly Repositioning by Finite Difference Method," ANS Knoxville M&C Division Topical Meeting, April 1985 (in publication).

14. F. Todt, *FEVER/M1, A One-Dimensional Depletion Program for Reactor Fuel Cycle Analysis*, GA-9780, General Atomic Co., San Diego, California, 1969.

15. D. Mathews and P. Koch, unpublished report, GA Technologies Inc., San Diego, California, 1983.

16. D. Mathews and P. Koch, unpublished report GA Technologies Inc., San Diego, California, 1982.

17. K. L. Derstine, *DIF3D: A Code to Solve One-, Two-, and Three-Dimensional Finite Difference Diffusion Theory Problems*, ANL-82-64, Argonne National Laboratory, April 1984.

18. R. D. Lawrence, *The DIF3D Nodal Neutronics Option for Two- and Three-Dimensional Diffusion Theory Calculations in Hexagonal Geometry*, ANL-83-1, Argonne National Laboratory, March 1983.

19. R. G. Steinke, "Benchmark Source Situation — Multi-Dimensional (Hex-Z) HTGR Model," in *Benchmark Problem Book*, ANL-7416 Supplement No. 2, 1977.

20. D. R. Vondy, et al., *The BOLD VENTURE Computation System for Nuclear Reactor Core Analysis, Version III*, ORNL-5711, Oak Ridge National Laboratory, 1981.

21. M. L. Williams, "Development of Depletion Perturbation Theory for Coupled Neutron/Nuclide Fields," *Nucl. Sci. Eng.*, **70**, p. 20, (1979).

22. J. R. White, *The Development, Implementation, and Verification of Multicycle Depletion Perturbation Theory for Reactor Burnup Analysis*, ORNL/TM-7305, Oak Ridge National Laboratory, 1980.

23. J. R. White, B. R. Frank, and J. Pappas, "Analytic Solution for the Fundamental and Higher Harmonics of the 1-D Diffusion Equation," *Trans. Am. Nucl. Soc.*, **46**, 408 (1984).

24. J. R. White, *The DEPTH-CHARGE Static and Time-Dependent Perturbation/Sensitivity System for Nuclear Reactor Core Analysis*, ORNL/CSD-78, Oak Ridge National Laboratory, 1981.

25. D. E. Wood, *Material Buckling Measurements on Graphite-Uranium Systems at Hanford: A Summary Tabulation*, HW-69525, Hanford Atomic Products Operation, Richland, Washington, May 1961.

26. R. G. Harper, *An Analysis of Experiments on Graphite Moderated Assemblies Fueled with Uranium, Plutonium and Uranium-Plutonium Metal*, AEEW-R325, Atomic Energy Establishment Winfrith, England, July 1964.

27. F. R. Barclay, *An Analysis of Uranium Metal-Graphite System Using the Multigroups Code WIMS*, AEEW-R473, Atomic Energy Establishment Winfrith, England, June 1966.

28. J. R. Askew, *Current UK Position on Uranium-238 Resonance Capture in Thermal Reactors*, AEEW-R1006, Atomic Energy Establishment Winfrith, England, June 1975.

29. J. R. Askew et al., *WIMS-E*, AEEW-R1315, Atomic Energy Establishment Winfrith, England, 1982.

30. W. E. Graves and E. J. Hennelly, "Comparison of the Worth of Critical and Exponential Measurements for Heavy-Water-Moderated Reactors," IAEA-SM-42/42, *Exponential and Critical Experiments, Vol. II*, International Atomic Energy Agency, Vienna, 1964.

31. D. R. Finch and W. E. Graves (Dupont-SRL), "Quantitative Consistency Testing of Thermal Benchmark Lattice Experiments," *Trans. Am. Nucl. Soc.* **27**, 888–890, (December 1977).

32. D. S. Craig, *Testing ENDF/B-V Data for Thermal Reactors*, AECL-7690, Chalk River Nuclear Laboratory, Canada, October 1982.

33. O. R. Hillig and D. W. Latham, *Material Bucklings of Critical and Subcritical Uranium Carbide Fueled Graphite Assemblies, Part I, Experiment*, NAA-SR-9771, Atomics International, Canoga Park, California, December 1964.

34. E. R. Specht, *Material Bucklings of Critical and Subcritical Uranium Carbide Fueled Graphite Assemblies, Part II, Theoretical Interpretation*, NAA-SR-9772, Atomics International, Canoga Park, California, August 1964.

35. R. L. Hellens et al., *Comparative Analysis of Some Graphite and Water Moderated Reactor Lattices*, BNL-11353, Brookhaven National Laboratory, Upton, New York, 1967 (also CONF-670607-2, *International Conference on the Physics Problems in Thermal Reactor Design*, London, June 1977).

36. *Experimental Results from the UKAEA Reactor Physics Programme on Low Enriched HTR Lattices at AEE Winfrith*, Dragon Project Report 730, Atomic Energy Establishment Winfrith, England, August 1970.

37. J. R. Askew and H. H. W. Pitcher, "Concerning the Analysis of Single Channel Substitution Measurements," *J. Brit. Nucl. Energy Soc.*, **6**, 260–270 (1967).

38. W. N. Fox, D. C. King, H. H. W. Pitcher and J. E. Sanders, "Reactor Physics Measurements on ^{235}U and ^{239}Pu Fuels in an Intermediate Spectrum Assembly," *J. Brit. Nucl, Energy Soc.*, **9**, 15–27 (1970).

GAS-COOLED REACTOR PROGRAMS

FEBRUARY 1 1985

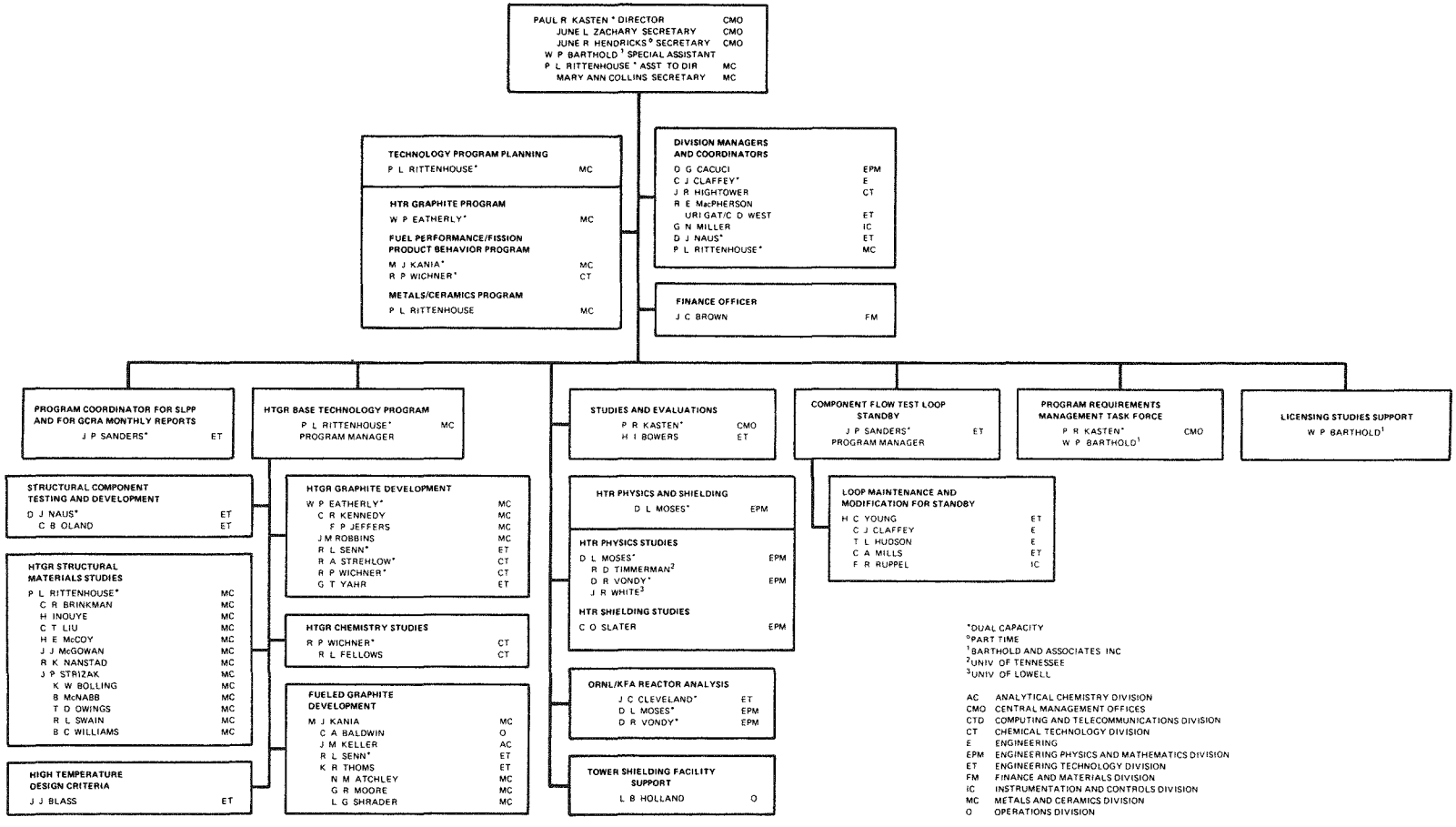

*DUAL CAPACITY
°PART TIME
[1]BARTHOLD AND ASSOCIATES INC
[2]UNIV OF TENNESSEE
[3]UNIV OF LOWELL

AC	ANALYTICAL CHEMISTRY DIVISION
CMO	CENTRAL MANAGEMENT OFFICES
CTD	COMPUTING AND TELECOMMUNICATIONS DIVISION
CT	CHEMICAL TECHNOLOGY DIVISION
E	ENGINEERING
EPM	ENGINEERING PHYSICS AND MATHEMATICS DIVISION
ET	ENGINEERING TECHNOLOGY DIVISION
FM	FINANCE AND MATERIALS DIVISION
IC	INSTRUMENTATION AND CONTROLS DIVISION
MC	METALS AND CERAMICS DIVISION
O	OPERATIONS DIVISION

217/218

HTGR-85-062
ORNL-6192
Distribution
Category UC-77T

INTERNAL DISTRIBUTION

1—2. Central Research Library
3. Document Reference Section
4—5. Laboratory Records Department
6. Laboratory Records, ORNL RC
7. ORNL Patent Section
8. J. J. Blass
9. H. I. Bowers
10. D. G. Cacuci
11. C. J. Claffey
12. W. R. Clark
13. J. C. Cleveland
14. J. M. Corum
15—17. W. P. Eatherly
18. R. L. Fellows
19. U. Gat
20. J. R. Hightower
21. L. B. Holland
22. T. L. Hudson
23. D. T. Ingersoll
24. J. E. Jones, Jr.
25—29. M. J. Kania
30—39. P. R. Kasten
40. C. R. Kennedy
41. J. F. King
42. D. A. Lee
43. F. C. Maienschein
44. R. W. McClung
45. H. E. McCoy
46. D. L. Moses
47. F. R. Mynatt
48. D. J. Naus
49. C. B. Oland
50. H. Postma
51—55. P. L. Rittenhouse
56. G. C. Robinson
57—61. J. P. Sanders
62. R. L. Senn
63. C. O. Slater
64. G. M. Slaughter
65. J. O. Stiegler
66. R. A. Strehlow
67. J. P. Strizak
68—71. P. T. Thornton
72. H. E. Trammell
73. D. B. Trauger
74. D. R. Vondy
75. C. D. West
76. G. D. Whitman
77. R. P. Wichner
78. R. G. Wymer
79. G. T. Yahr

EXTERNAL DISTRIBUTION

80—84. DOE, DIVISION OF HTR DEVELOPMENT, NE-15, Washington, DC 20545

R. Ng, Director
J. E. Fox
I. L. Helms
A. S. Mehner
A. C. Millunzi

85. DOE, OFFICE OF CONVERTER REACTOR DEPLOYMENT, NE-10,
Washington, DC 20545

Director

86. DOE, SAN-SAN DIEGO,

L. Lanni

87. DOE, OAK RIDGE OPERATIONS OFFICE, P.O. Box E, Oak Ridge, TN 37831

Office of Assistant Manager for Research and Development
ATTN: S. W. Ahrends/M. J. Rohr

88–146. DOE, TECHNICAL INFORMATION CENTER, P.O. Box 62, Oak Ridge, TN 37831

For distribution as shown in TID-4500 Distribution Category,
UC-77T (Gas-Cooled Reactor Technology)